Endoscopic Fluorescence Imaging: Spectral Optimization and in vivo Characterization of Positive Sites by Magnifying Vascular Imaging

THÈSE N^{O} 4797 (2010)

PRÉSENTÉE LE 17 SEPTEMBRE 2010

À LA FACULTÉ SCIENCES DE BASE

INSTITUT DES SCIENCES ET INGENIERIE CHIMIQUES

PROGRAMME DOCTORAL EN PHOTONIQUE

ÉCOLE POLYTECHNIQUE FÉDÉRALE DE LAUSANNE

POUR L'OBTENTION DU GRADE DE DOCTEUR ÈS SCIENCES

PAR

Blaise LOVISA

acceptée sur proposition du jury:

Prof. J.-E. Moser, président du jury
MER, Dr G. Wagnières, directeur de thèse
Dr W. Blondel, rapporteur
Prof. C. Depeursinge, rapporteur
Prof. P. Jichlinski, rapporteur

ÉCOLE POLYTECHNIQUE
FÉDÉRALE DE LAUSANNE

Suisse
2010

C'est le propre des grands voyageurs que de ramener tout autre chose que ce qu'on allait chercher.
Nicholas Bouvier

A mes parents, Denise et Raoul
A Sophie et Timothée

Résumé

Depuis plusieurs décennies, les médecins peuvent accéder aux organes creux avec des méthodes endoscopiques, qui remplissent à la fois la fonction d'outil diagnostique et chirurgical dans nombre de disciplines de la médecine moderne (par ex. en urologie, pneumologie, gastroentérologie). Malheureusement, l'endoscopie conventionnelle en lumière blanche (LB) montre une sensibilité limitée pour les lésions cancéreuses précoces. Par conséquent, plusieurs méthodes endoscopiques utilisant l'imagerie de fluorescence ont été développées pour surmonter cette limitation. La fluorescence endogène et exogène-induite a été étudiée, menant à des produits commercialisés. En effet, la bronchoscopie en autofluorescence, et la cystoscopie utilisant la fluorescence des porphyrines sont maintenant sur le marché.

Les méthodes de dépistage endoscopiques utilisant la fluorescence montrent une sensibilité très élevée pour les lésions pré-cancéreuses, souvent invisibles en LB, mais elles souffrent encore d'une spécificité limitée, principalement due au taux élevé de faux-positifs. Bien que la plupart de ces faux-positifs puissent être facilement rejetés en observation LB, il est plus difficile d'identifier des anomalies tissulaires telles que les zone inflammatoires, les hyperplasies et les métaplasies. Cela se traduit souvent en des biopsies supplémentaires, péjorant encore la spécificité. Par conséquent, le but de cette thèse est d'étudier une méthode novatrice, rapide et commode pour caractériser *in situ* les zones positives en fluorescence pendant l'endoscopie et, plus généralement, pour optimiser l'appareillage endoscopique existant. Dans cette thèse, plusieurs évaluations cliniques ont été effectuées soit dans l'arbre trachéo-bronchique, soit dans la vessie.

Dans la vessie, l'imagerie de fluorescence pour la détection des tumeurs superficielles utilise la production et l'accumulation sélective dans les tissus cancéreux de porphyrines fluorescentes, principalement la protoporphyrine IX (PpIX), après une instillation de Hexvix® pendant une heure. Dans cette thèse, nous avons adapté un cystoscope rigide pour observer la muqueuse vésicale avec un grossissement élevé (GE), ceci afin de distinguer les vrais- des faux-positifs détectés par fluorescence. L'optique permettant le GE peut-être utilisée soit avec lumière blanche, soit en fluorescence, avec un grossissement variant entre 30× – pour l'observation standard – et 650×. Une molette permet l'ajustement continu *in situ* du grossissement pendant la cystoscopie. Dans le régime élevé de grossissement, le plus petit diamètre du champ visuel est de 600 microns et la résolution est de 2.5 microns, le cystoscope étant dans ce cas précis au contact avec la muqueuse vésicale. Avec ce cystoscope CGE, nous avons caractérisé – avec un éclairement en lumière blanche 370–700 nm – la vascularisation superficielle des zones positives en fluorescence afin de distinguer les tissus cancéreux des non-cancéreux. Ce procédé nous a permis d'établir une classification utilisant les motifs vasculaires observés. 72 patients examinés avec la cystoscopie de fluorescence Hexvix® ont été inclus dans l'étude. La comparaison de la classification GE avec les résultats d'histopathologie a confirmé 32/33 (97%) de biopsies cancéreuses, et a rejeté 17/20 (85%) de lésions non-cancéreuses. Aucun changement vasculaire n'a pu être visualisé sur la seule lésion positive qui était négative GE, parce que ce carcinome sarcomatoïde trouvait son origine ailleurs que dans l'urothélium. Nous avons montré avec cette étude qu'un grossissement de l'ordre de 80–100× pouvait constituer un bon compromis entre l'endoscopie macroscopique en fluorescence et microscopie en réflectance. Afin de rendre cette approche plus quantitative, des algorithmes de traitement d'images (segmentation, extraction de squelette, extraction de l'information globale) ont été également implémentés dans cette thèse.

Afin de mieux visualiser les vaisseaux, nous avons augmenté leur contraste par rapport à l'arrière-plan par des méthodes optiques. Puisque l'hémoglobine est un absorbeur puissant, nous avons visé ses deux pics d'absorption en plaçant deux filtres passe-bande (405±50 nm

bleu, 550±50 nm vert) dans la fontaine de lumière. La cystoscopie CGE a été alors exécutée séquentiellement avec l'illumination blanche, bleue et verte. Les deux dernières ont montré un contraste plus élevé des vaisseaux par rapport au fond, mettant en évidence la vascularisation à plusieurs profondeurs grâce à la pénétration différenciée des longeurs d'onde utilisées.

Pendant la cystoscopie de fluorescence, nous avons souvent observé que les images sont floutées par un écran bleu-vert entre l'extrémité de l'endoscope et la muqueuse vésicale. Puisque cet effet est augmenté par la production d'urine, il est encore plus marqué avec les endoscopes flexibles (qui disposent d'un rinçage limité) et les imageurs qui utilisent seulement l'autofluorescence comme arrière-plan. En effet, quand la vessie n'est pas rinsée régulièrement, on observe facilement des écoulements bleu-vert sortant des uretères. Pour cette raison, on a supposé que quelques fluorophores contenus dans l'urine sont excités par la lumière d'excitation, et apparaissent bleu-vert à l'écran. Cet effet peut altérer la visualisation de la muqueuse vésicale et les lésions cancéreuses. Par conséquent, la sensibilité de la cystoscopie de fluorescence est diminuée. Dans cette thèse, nous avons identifié les principaux produits responsables de la fluorescence du liquide, et avons optimisé la conception spectrale en conséquence.

Dans l'arbre trachéo-bronchique, le contraste de fluorescence utilise la forte diminution d'autofluorescence (AF) de la bande spectrale verte (environ 500 nm) sur les lésions cancéreuses précoces et une diminution relative moins importante de la bande spectrale rouge (> 600 nm), lorsque la muqueuse bronchique est excitée avec de la lumière bleu violet (environ 410 nm). Il a été montré au cours des dernières années que ce contraste peut être attribué à un effet combiné de l'épithélium épaissi et à une concentration plus élevée d'hémoglobine dans le tissu sous-jacent des lésions cancéreuses précoces.

Dans cette thèse, nous avons contribué à la conception de plusieurs nouveaux prototypes, qui ont été plus tard évalués en clinique. En premier lieu, nous avons prouvé que l'excitation à bande étroite dans le bleu-violet pourrait augmenter le contraste tumeur-tissu sain dans la bande spectrale verte. Puis, nous avons mesuré les variations en intensité d'AF intra- et inter-patients afin d'optimiser la réponse spectrale de l'imageur endoscopique. A cette fin, nous avons développé une référence endoscopique à placer près de la muqueuse bronchique pendant la bronchoscopie. Finalement, nous avons évalué sur 144 patients un bronchoscope AF nouvellement équipé avec la lumière bleu-rétrodiffusée. Ce nouveau dispositif a montré une sensibilité augmentée pour les lésions pré-néoplasiques.

A l'instar de ce que nous avons observé dans la vessie, il est très probable que les nouveaux développements en imagerie (y compris l'imagerie vasculaire) facilitent la distinction des vrais et faux-positifs dans la bronchoscopie en AF. Dans cette étude, nous avons montré que le grossissement permettait de résoudre des vaisseaux d'un diamètre d'environ 30 microns. Cette résolution est probablement suffisante pour identifier les critères vasculaires de Shibuya (boucles, mailles, vaisseaux pointillés) sur les lésions positives en AF. Ces critères lui permettent d'identifier les lésions précancéreuses, et potentiellement permettrait d'abaisser le taux de faux-positifs avec notre imageur AF. Ce grossissement a également amélioré la bronchoscopie de routine, puisqu'il fournit des images plus structurées à l'opérateur.

Mots-clés: tumeurs vésicales, cystoscopie de fluorescence, endoscopie à grossissement, imagerie vasculaire, Hexvix®, Cysview^{TM}, hexylester d'acide aminolévulinique, motifs vasculaires, angiogenèse, cancer bronchique, bronchoscopie, autofluorescence, imagerie et spectroscopie de fluorescence, phantomes optiques, évaluation clinique.

Abstract

Since several decades, the physicians are able to access hollow organs with endoscopic methods, which serve both as diagnostic and surgical means in a wide range of disciplines of the modern medicine (*e.g.* urology, pneumology, gastroenterology). Unfortunately, white light (WL) endoscopy displays a limited sensitivity to early pre-cancerous lesions. Hence, several endoscopic methods based on fluorescence imaging have been developed to overcome this limitation. Both endogenous and exogenously-induced fluorescence have been investigated, leading to commercial products. Indeed, autofluorescence bronchoscopy, as well as porphyrin-based fluorescence cystoscopy, are now on the market.

As a matter of fact, fluorescence-based endoscopic detection methods show very high sensitivity to pre-cancerous lesions, which are often overlooked in WL endoscopy, but they still lack specificity mainly due to the high false-positive rate. Although most of these false positives can easily be rejected under WL observation, tissue abnormalities such as inflammations, hyperplasia, and metaplasia are more difficult to identify, often resulting in supplementary biopsies. Therefore, the purpose of this thesis is to study novel, fast, and convenient method to characterize fluorescence positive spots *in situ* during fluorescence endoscopy and, more generally, to optimize the existing endoscopic setup. In this thesis, several clinical evaluations were conducted either in the tracheo-bronchial tree and the urinary bladder.

In the urinary bladder, fluorescence imaging for detection of non-muscle invasive bladder cancer is based on the selective production and accumulation of fluorescing porphyrins, mainly protoporphyrin IX (PpIX), in cancerous tissues after the instillation of Hexvix® during one hour. In this thesis, we adapted a rigid cystoscope to perform high magnification (HM) cystoscopy in order to discriminate false from true fluorescence positive findings. Both white light and fluorescence modes are possible with the magnification cystoscope, allowing observation of the bladder wall with magnification ranging between 30× – for standard observation – and 650×. The optical zooming setup allows adjusting the magnification continuously *in situ*. In the high magnification regime, the smallest diameter of the field of view is 600 microns and the resolution is 2.5 microns, when in contact with the bladder wall. With this HM cystoscope, we characterized the superficial vascularization of the fluorescing sites in WL (370–700 nm) reflectance imaging in order to discriminate cancerous from non-cancerous tissues. This procedure allowed us to establish a classification based on observed vascular patterns. 72 patients subject to Hexvix® fluorescence cystoscopy were included in the study. Comparison of HM cystoscopy classification with histopathology results confirmed 32/33 (97%) cancerous biopsies, and rejected 17/20 (85%) non-cancerous lesions. No vascular alteration could be observed on the only positive lesion that was negative in HM mode, probably because this sarcomatoid carcinoma was not originating in the bladder mucosa. We established with this study that a magnification ranging between 80× and 100× is an optimal tradeoff to perform both macroscopic PDD and HM reflectance imaging. In order to make this approach more quantitative, different algorithms of image processing (vessel segmentation and skeletonisation, global information extraction) were also implemented in this thesis.

In order to better visualize the vessels, we improved their contrast with respect to the background. Since hemoglobin is a very strong absorber, we targeted the two hemoglobin absorption peaks by placing appropriate bandpass filters (blue 405±50 nm, green 550±50 nm) in the light source. HM cystoscopy was then performed sequentially with WL, blue and green illumination. The two latter showed higher vessel-to-background contrast, identifying different layers of vascularization due to the light penetration depth.

During fluorescence cystoscopy, we often observed that the images are somehow "blurred" by a greenish screen between endoscope tip and bladder mucosa. Since this effect is enhanced by the urine production, it is more visible with flexible scopes (lower flushing capabilities) and imaging systems that collect only autofluorescence as background. Indeed, when the bladder is not flushed regularly, greenish flows coming out of the ureters can easily be observed. For this reason, it is supposed that some fluorophores contained in the urine are excited by the photodetection excitation light, and appear greenish on the screen. This effect may impair the visualization of the bladder mucosa, and thus cancerous lesions, and lowers sensitivity of the fluorescence cystoscopy. In this thesis, we identified the main metabolites responsible for the liquid fluorescence, and optimized the spectral design accordingly.

In the tracheo-bronchial tree, the fluorescence contrast is based on the sharp autofluorescence (AF) decrease on early cancerous lesions in the green spectral region (around 500 nm) and a relatively less important decrease in the red spectral region (> 600 nm) when excited with blue-violet light (around 410 nm). It has been shown over the last years, that this contrast may be attributed to a combined effect of epithelium thickening and higher concentration of hemoglobin in the tissues underneath the (pre-)cancerous lesions.

In this thesis, we contributed to the definition of the input design of several new prototypes, that were subsequently tested in the clinical environment. We first showed that narrow-band excitation in the blue-violet could increase the tumor-to-normal spectral contrast in the green spectral region. Then, we quantified the intra- and inter-patient variations in the AF intensities in order to optimize the spectral response of the endoscopic fluorescence imaging system. For this purpose, we developed an endoscopic reference to be placed close to the bronchial mucosa during bronchoscopy. Finally, we evaluated a novel AF bronchoscope with blue-backscattered light on 144 patients. This new device showed increased sensitivity for pre-neoplastic lesions.

Similar to what we observed in the bladder, it is likely that developing new imaging capabilities (including vascular imaging) will facilitate discriminating true from false positive in AF bronchoscopy. Here, we demonstrated that this magnification allowed us to resolve vessels with a diameter of about 30 μm. This resolution is likely to be sufficient to identify Shibuya's vascular criteria (loops, meshes, dotted vessels) on AF positive lesions. This criteria allow him to recognize pre-cancerous lesions, and thus can potentially decrease the false-positive rate with our AF imaging system. This magnification was also showed to be better for routine bronchoscopy, since it delivers sharper and more structured images to the operator.

Keywords: bladder cancer, fluorescence cystoscopy, high magnification, vascular imaging, Hexvix®, Cysview^{TM}, hexaminolevulinate, vessel patterns, angiogenesis, bronchial cancer, autofluorescence, bronchoscopy, fluorescence imaging and spectroscopy, optical phantoms, clinical evaluation.

List of Abbreviations

AF	AutoFluorescence
AFB	AutoFluorescence Bronchoscopy
AFS	AutoFluorescence Spectroscopy
ALA	AminoLevulinic Acid
ASD	Angiogenic Squamous Dysplasia
BBS	Blue-BackScattered Light
BC	Bladder Cancer
BCG	Bacillus Calmette-Guérin
CAM	ChorioAllantoic Membrane
CCD	Charge-Coupled Device
CCW	Counter Clock-Wise
CI	Confidence Interval
CIS	Carcinoma *in situ*
CMOS	Complementary Metal-Oxide-Semiconductor
CMYG	Cyan-Magenta-Yellow-Green
CoC	Circle of Confusion
CRT	Cathode Ray Tube
CT	Computed Tomography
CW	Clock-Wise
DAFE	Diagnostic AutoFluorescence Endoscopy
DMSO	DiMethylSulfOxyde
DOF	Depth Of Field
EAU	European Association of Urology
EBUS	EndoBronchial UltraSound
EEM	Excitation-Emission Matrix
EFI	Endoscopic Fluorescence Imaging
EM	Electromagnetic
ENT	Ear-Nose-Throat, equivalent as otorhinolaryngology
EORTC	European Organization for Research and Treatment of Cancer
FAD	Flavin Adenine Dinucleotide
FDA	Food and Drug Administration
FFT	Fast-Fourier Transformation
FICE	Fujinon Intelligent Color Imaging
FITC	Fluorescein IsoThioCyanate
FN	False-Negative
FOV	Field Of View
FP	False-Positive
FWHM	Full-Width Half Maximum
GBS	Green-BackScattered Light
H&E	Hematoxylin and Eosin
HAL	Hexyl-ester of AminoLevulinic acid or HexAminoLevulinate
HIF	Hypoxia-Inducible Factor
HM	High Magnification
HP	Hydroxylysyl Pyridinoline
HpD	HematoPorphyrin Derivatives
IASLC	International Association for the Study of Lung Cancer
IC	Internal Conversion
iCB	intelligent Color Balance
ICG	IndoCyanine Green
IR	Infrared
ISC	InterSystem Crossing
LED	Light Emitting Diodes
LP	Long-Pass
LP	Lysyl Pyridinoline

MEMS	MicroElectroMechanical System
mfp	Mean Free Path
MPE	MultiPhoton Endoscopy
MPM	MultiPhoton Microscopy
MRI	Magnetic Resonance Imaging
MVD	MicroVascular Density
N/C	Nuclear-to-Cytoplasm ratio
NA	Numerical Aperture
NAD	Nicotinamide Adenine Dinucleotide
NBI	Narrow Band Imaging
NDA	New Drug Application
NMIBC	Non-Muscle Invasive Bladder Cancer
NPV	Negative Predictive Value
NSCLC	Non-Small-Cell Lung Cancer
OBI	Optimal Band Imaging
OCT	Optical Coherence Tomography
OR	Odds Ratio
OTDR	Optical Time-Domain Reflectometry
PAP	PhotoActive Porphyrin
PDD	PhotoDynamic Diagnosis
PDT	PhotoDynamic Therapy
PET	Positron Emission Tomography
PFC	Percentage of False-Classification
pp	per patient
PpIX	ProtoPorphyrin IX
PPV	Positive Predictive Value
PS	PhotoSensitizer
PUNLMP	Papillary Urothelial Neoplasm of Low Malignant Potential
RGB	Red-Green-Blue
ROI	Region-Of-Interest
S/N	Signal-to-Noise ratio
SCC	Squamous Cell Carcinoma
SCLC	Small Cell Lung Carcinoma
SEM	Scanning Electron Microscopy
SHG	Second Harmonic Generation
T/N	Tumor-to-Normal ratio
TBNA	TransBronchial Needle Aspiration
TN	True-Negative
TNM	Tumor-node-metastasis
TP	True-Positive
TUR	TransUrethral Resection
TURB	TransUrethral Resection of the Bladder
TURP	TransUrethral Resection of the Prostate
UICC	Union Internationale Contre le Cancer
UV	UltraViolet
VEGF	Vascular Endothelial Growth Factor
VOC	Volatile Organic Compounds
WHO	World Health Organization
WL	White Light
WLC	White Light Cystoscopy

Contents

Foreword

This manuscript is the final report about my research activity as a PhD student in the Biomedical Photonics Group of Prof. Hubert van den Bergh, under the supervision of Dr. Georges Wagnières, at the Ecole Polytechnique Fédérale de Lausanne in Switzerland. Some parts of this report have been published or submitted during the course of my Ph.D. thesis. I therefore included the text of the publications with a brief introduction instead of an original chapter whenever relevant. In such a case, the reference is clearly stated.

As will be seen in the author's list of the published sections of this work, many studies has been done in close collaboration with other people. Whenever relevant (i.e. whenever I don't appear as the first author of a paper that has been include in my report), I stated in the introduction what my exact contribution was. It should be understood that those papers have been included in my report with full knowledge and agreement from my co-authors and supervisor.

This work is the result of multidisciplinary research approaches intended to contribute to improved management of a major heath problem: cancer. In this report, we will focus on the lesions of the tracheo-bronchial tree and the urinary bladder. They are frequent cancers but, unfortunately, they are still difficult to diagnose in the early stages of development with conventional detection methods. Interestingly, over the last decades, several endoscopic methods based on fluorescence imaging have been reported. Both endogenous and exogenously-induced fluorescence have been investigated, leading to commercial products. Indeed, autofluorescence bronchoscopy, as well as porphyrin-based fluorescence cystoscopy, are now commercialized.

Both methods have been reported to have a high sensitivity, but still suffer from a limited specificity, mainly attributed to the high rate of false-positive lesions. This thesis is focused on the optimization of endoscopic visual contrast between cancerous lesions and healthy tissue, and on the rejection of false-positive in both organs, mainly with the help of high magnification vascular imaging.

Chapter 1 gives a brief overview on tissue optics, describing the light-tissue interactions (dispersion, absorption, and scattering). It also introduces some fluorescence basic concepts.

Chapter 2 deals with the issue of clinical cancer detection by optical imaging. It describes the principles of reflectance and fluorescence endoscopic imaging, and their applications to cancer diagnostic. After a short technical review about instrumentation aspects, we describe the state-of-the-art in high magnification imaging. The special case of confocal endoscopy is discussed separately. Finally, we explain some statistical concepts that often intervene in clinical studies (sensitivity, specificity, likelihood and odds ratios).

Part I (Chapter 3, 4, 5 and 6) deals with bladder cancer. **Chapter 3** is a brief summary of some facts about bladder cancer, the current methods of detection and their limits, as well as the current methods of management of the disease. It also summarizes the development of porphyrin-based photodetection of bladder cancer. It reviews the methods of false-positive characterization, and describes the mechanisms underlying angiogenesis in bladder cancer. **Chapter 4** describes the optimization of the spectral design for fluorescence cystoscopy, with a dedicated interest to the fluorescing metabolites present in the liquid filling the bladder.

Chapter 5 deals with the development of high magnification (HM) reflectance imaging in the bladder. After the optical characterization of the dedicated cystoscope, we present the results of a clinical study, evaluating the potential to reject false-positive lesions with the help of HM cystoscopy. In order to make this approach more quantitative, the next sections deal

with different algorithms of image processing (vessel segmentation and skeletonisation, global information extraction). **Chapter 6** sums up all the contributions related to bladder cancer, and outlooks some future prospects.

Part II (Chapter 7, 8, 9, 10, 11, and 12) deals with bronchial cancer. **Chapter 7** is a brief summary of some facts about bronchial cancer, as well as the current methods of management of the disease. It also summarizes the development of autofluorescence photodetection of bronchial cancer, and describes the mechanisms underlying angiogenesis in the bronchi.

Chapter 8 evaluates if narrow-band imaging improves the spectral contrast in autofluorescence imaging. **Chapter 9** quantifies the inter-patients variations in autofluorescence intensity in order to scale the dynamic range of future endoscopic setup accordingly. For this purpose, it also describes the development and characterization of an endoscopic reference, that can be placed close to the bronchial mucosa.

Chapter 10 summarizes a clinical study evaluating the performance of a new autofluorescence bronchoscope prototype on 147 patients. This new device has shown a high sensitivity for (pre-)neoplasia. **Chapter 11** introduces the high magnification imaging concept in the bronchi with preliminary clinical tests, providing a proof-of-concept of vascular imaging in the tracheo-bronchial tree. **Chapter 12** sums up all the contributions related to bronchial cancer.

Some appendices have been added to this manuscript summarizing some minor contributions. **Appendix A** reviews a clinical study with autofluorescence bronchoscopy showing a great benefit for Head&Neck cancer patients. **Appendix B** lists the morphological criteria for bladder cancer classification. It also reviews an interesting scoring system, that predicts prognosis and recurrence in bladder cancer patients. **Appendix C** introduces narrow-band excitation in the bladder to improve tumor-to-healthy contrast. **Appendix D** illustrates the development of a fluorescence validation sample to assess the correct functioning of endoscopic instrumentation. **Appendix E** deals with the color presentation of optical contrasts in endoscopy and its influence on tumor detectability. Finally, **Appendix F** presents some attempts of spectral optimization in HM endoscopy.

As stated above, the common thread of all these studies is the use of fluorescence imaging with the addition of reflectance high magnification imaging. We showed that the combination of these two techniques allows a higher sensitivity and a better rejection of false-positive lesions.

Finally, I would like to apologize to the native English speaker reader for my less that perfect command of their language.

Introduction

Chapter 1

Introduction to Tissue Optics

The first part of this chapter gives an introduction to the physical basics of tissue optics (dispersion, absorption, scattering, and diffusion). The second part gives an overview of the optical properties of biological tissues, dominated by absorption, scattering and fluorescence emission.

Interactions of light with biological tissues and structures was at the origin of all optical diagnostic or therapeutic tool, leading to the common topic of *photomedicine*. Light propagation in a turbid medium (*e.g.* in a biological tissue) is ruled by reflection and refraction, absorption, and scattering. These four interaction mechanisms define the optical properties of the medium. In the framework of photomedicine, the study of these interactions allows to find how much light energy per unit area per unit time reaches a target chromophore, and, thus, to develop characterization and therapeutic methods based on the tissue optical properties.

The absorption coefficient μ_a, the scattering coefficient μ_s, the index of refraction n and the phase function Φ are referred to as the fundamental or "microscopic" optical parameters. Each type of tissue has its specific optical parameters, which can lead to specialized diagnostic and therapeutic applications. The macroscopic parameters, μ_{eff}, δ, R, and T are generally measured from thick tissue samples. The microscopic parameters can be evaluated from the macroscopic ones using theoretical models for light propagation. Table 1.1 summarizes the tissue optical parameters.

1.1 Dispersion

The present section will treat microscopic origin of the dispersion. The *refractive index* n of a medium is defined to be the ratio between light velocity in the vacuum c_o (2.99793×10^8 m/s) and in the medium c. The refractive index n is frequency-dependent, and thus wavelength-dependent.

$$n = c_o/c \text{ with } c = \lambda \cdot \nu$$

If one applies an external electric field onto a molecule, its surrounding electron cloud is distorted. The internal charge distribution is thus modified and a dipole moment is generated. In case of an incident harmonic electromagnetic (EM) wave, time-varying forces and torques act upon internal charge distribution and generate oscillating dipoles. When excited by a light wave, the electron will oscillate at the driving frequency, and emit light at this frequency. If one considers

Fundamental microscopic parameters			
μ_a		Absorption coefficient	$[cm^{-1}]$
μ_s		Scattering coefficient	$[cm^{-1}]$
n		Refraction index	dimensionless
g		Anisotropy factor	dimensionless
Dependent microscopic parameters			
a	μ_s/μ_a	Optical albedo	
μ_t	$\mu_a + \mu_s$	Total extinction coefficient	$[cm^{-1}]$
L_t	$1/\mu_t$	Free optical path length	$[cm]$
μ_s'	$(1-g)\mu_s$	Reduced scattering coefficient	$[cm^{-1}]$
Macroscopic parameters			
μ_{eff}	$\sqrt{3\mu_a \cdot (\mu_a + \mu_s')}$	Effective attenuation coefficient	$[cm^{-1}]$
δ	$1/\mu_{\text{eff}}$	Effective penetration depth	$[cm]$
R		Diffuse reflectance	
T		Diffuse transmittance	

Table 1.1: ***Tissue optical parameters.*** *The fundamental optical parameters are the absorption coefficient μ_a, the scattering coefficient μ_s, and the refraction index n. The other parameters can be deduced from these parameters.*

the electron to be elastically bound to the nucleus, like a harmonic oscillator with a natural or resonant frequency ω_o, the restoring force F is linear for small displacement, according to Hooke's law, with k being a positive constant, and m_e the electron mass (9.109×10^{-31} kg):

$$F = -k \cdot x$$

The resonance frequency will be

$$\omega_o = \sqrt{\frac{k}{m_e}}$$

In this model, one assumes that the electron cloud is elastically bound to the nucleus *isotropically* (i.e. with the same force in all directions), and one only considers the harmonic response of the electron cloud to the driving force of the incident E-field. Assuming such a linear response is correct, while the induced displacements are small. Conversely, larger EM fields (*e.g.* high intensity laser pulses) can induce larger displacements, and non-linear restoring forces. Thus, higher order, anharmonic terms should be added to this expression, leading to *non-linear optics*. In complex materials, the molecular spring constant can change for different polarization of the E-field. This will lead to different indices of refraction for different E-field polarizations ($n_{\|}$,$n_{\perp}$), defined as *birefringence*.

If one considers an electron with position $x_e(t)$ and driven by a light wave, $E_o e^{-i\omega t}$:

$$\sum_i \overrightarrow{F_i} = \text{driving force} + \text{restoring force} \quad = \quad \text{mass} \cdot \text{acceleration}$$

$$eE_o e^{-i\omega t} - m_e \omega_o^2 x_e \quad = \quad m_e \frac{d^2 x_e}{dt^2} \tag{1.1}$$

The solution is :

$$x_e(t) = \left[\frac{e/m_e}{\omega_o^2 - \omega^2}\right] E_o e^{-i\omega t} \tag{1.2}$$

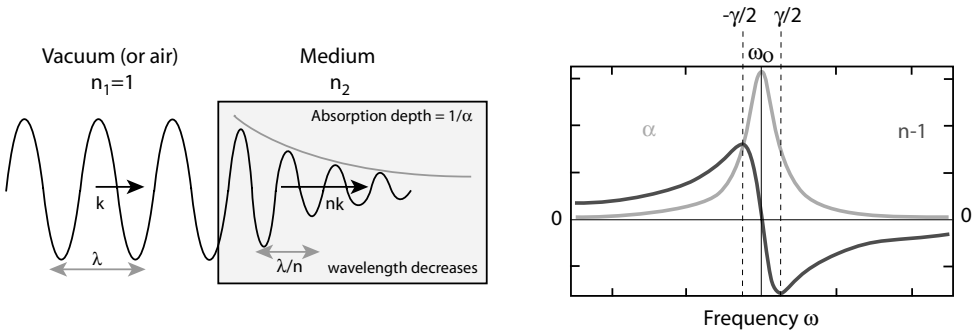

Figure 1.1: *Light propagation between two different media and resonance peaks*

The amplitude of oscillation is frequency-dependent, with the maximum displacement occurring at ω_o, the resonance frequency. $x_e(t)$ is the displacement of each charge vs. time, e is the electron charge (1.602×10^{-19} coulombs), m_e the electron mass, and ω the oscillating frequency.

In this context, a damped forced oscillator would fit as a more realistic model though. The harmonic oscillator experiences thus a sinusoidal force and viscous drag γ (friction). One should add a viscous drag term $m_e \gamma dx_e/dt$ to Equation 1.1:

$$m_e \frac{d^2 x_e}{dt^2} + m_e \gamma \frac{dx_e}{dt} + m_e \omega_o^2 x_e = e E_o e^{-i\omega t}$$

The solution is now:

$$x_e(t) = \frac{1}{\omega_o^2 - \omega^2 - i\omega\gamma} \frac{e}{m_e} E_o e^{-i\omega t} \tag{1.3}$$

The electron still oscillates at the driving frequency of the light wave, but with an amplitude and a phase that depend on the relative frequencies. It can be rewritten as:

$$\begin{aligned} x_e(t) &= x_o e^{-i(\omega t - \phi)} \\ \text{where } x_o &= E_o \frac{e}{m_e} \frac{1}{\sqrt{(\omega_o^2 - \omega^2)^2 + \gamma^2 \omega^2}} \text{ , the amplitude} \qquad (1.4) \\ \text{and } \phi &= \arctan\left(\frac{\gamma\omega}{\omega_o^2 - \omega^2}\right) \text{ , the phase lag} \qquad (1.5) \end{aligned}$$

The incident light wave will induce a polarization in the medium defined as

$$P(t) = N \cdot e \cdot x_e(t)$$

where N is the number density of charges.
It can be shown (as illustrated in Figure 1.1) that the electric field in the vacuum is given by

$$E(z,t) = E_o e^{i(kz - \omega t)}$$

and in the medium

$$E(z,t) = E_o e^{(-\alpha/2)z} e^{i(nkz - \omega t)}$$

We can also show that absorption causes attenuation of the field:

$$\alpha = \frac{N e^2}{4 m_e \epsilon_o c_o} \frac{\gamma/2}{(\omega_o - \omega)^2 + (\gamma/2)^2}$$

Refractive index n changes the k-vector:

$$n - 1 = \frac{Ne^2}{4m_e\epsilon_o}\frac{\omega_o - \omega}{(\omega_o - \omega)^2 + (\gamma/2)^2}$$

Figure 1.1 illustrates the influence of the incident light frequency ω on the absorption coefficient α and the refractive index n:

$\omega_o \gg \omega$ $\Rightarrow$ n hardly depends on λ $\rightsquigarrow$ transparency of the medium (i.e. colorless)
$\omega \to \omega_o$ $\Rightarrow$ n increases with λ $\rightsquigarrow$ normal dispersion
$\omega \approx \omega_o$ $\Rightarrow$ n is dominated by absorption & viscous drag
$\rightsquigarrow$ anomalous dispersion between $-\gamma/2$ and $\gamma/2$

1.2 Absorption

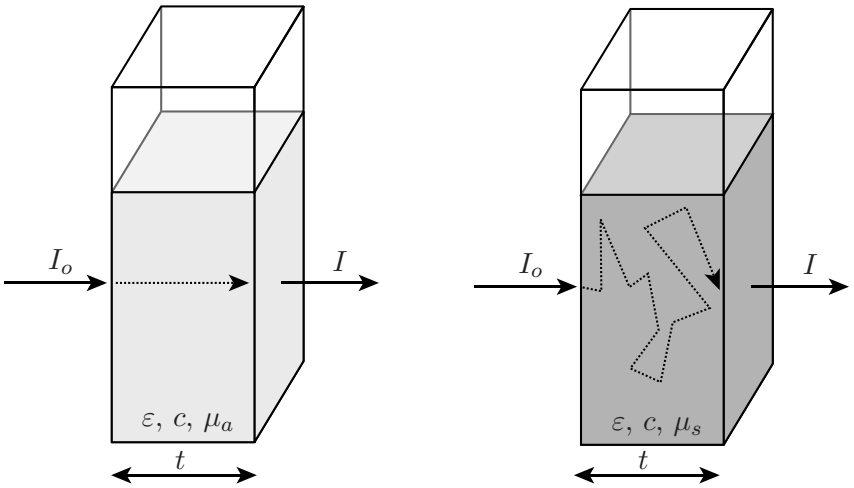

Figure 1.2: *Absorption and scattering through a turbid medium*

In tissue optics, one calls *absorption* the extraction of energy from light by matter. The absorption of light energy is the primary mechanism that allows light from a source (*e.g.* laser) to produce physical effects on tissue in light-based therapeutic applications. Since numerous chromophores lie in the tissue and act as light absorbers, one can often link them to the physiological status of the tissue. Transitions between two energy levels of a molecule could serve as spectral fingerprint of the molecule in diagnostic applications [Tuch02]. These energy transitions are quantized (i.e. discrete) and correspond to specific wavelengths. The Planck-Einstein equation links these quantities:

$$\Delta E = E_2 - E_1 = h(\nu_2 - \nu_1) = h\nu = \frac{h}{2\pi}\omega = \hbar\omega = h \cdot \frac{c}{\lambda} \tag{1.6}$$

with h the Planck constant (6.626×10^{-34} J s), ν the frequency, ω the angular frequency, λ the wavelength, and c the speed of light.

The *absorption coefficient* $\mu_a[cm^{-1}]$ is defined as $\mu_a = N_a \cdot \sigma_a$ where σ_a is the effective cross-section $[m^2]$ and N_a is the amount of absorbers per volume unit $[m^{-3}]$. This definition is valid with the assumptions that (i) the cross section is independent of the relative orientation of the incident light and absorbers, and (ii) that the distribution of identical absorbing particles

is uniform. The average travel distance of a photon before being absorbed is defined as the *absorption mean free path* $l_a = 1/\mu_a$ $[m]$.

An absorbing medium is characterized by the absorption coefficient μ_a, the transmission coefficient T, and the absorbance A (also called *optical density* OD). The Lambert-Beer[1] law describes the effect of either thickness or concentration of the sample on absorption:

$$\begin{aligned} I &= I_o e^{-\mu_a \cdot t} \\ A &= \varepsilon \cdot c \cdot t \end{aligned} \tag{1.7}$$

c is the chromophore concentration $[mol\ l^{-1}]$, t is the sample thickness $[cm]$, and ε the molar extinction coefficient given in $[l\ mol^{-1} cm^{-1}]$. I_o and I are the intensities entering or leaving the sample, respectively (see Figure 1.2). Equation 1.7 can be combined using these definitions:

$$A = -\log(\frac{I}{I_o}) \text{ with } \ln(x) = \frac{\log(x)}{\log(e)} = 2.303 \cdot \log(x) \tag{1.8}$$

$$T = \frac{I}{I_o} = 10^{-A} = 10^{-\varepsilon \cdot c \cdot t} \tag{1.9}$$

$$\ln(\frac{I}{I_o}) = \ln(10^{-\varepsilon \cdot c \cdot t}) = -2.303 \cdot \varepsilon \cdot c \cdot t = -\mu_a \cdot t \tag{1.10}$$

$$\mu_a = 2.303 \cdot \varepsilon \cdot c \tag{1.11}$$

By measuring the transmission T or the absorbance A for a given c, we can obtain ε usually *ex vivo*. If ε is known, and if we can measure μ_a *in vivo*, we can quantify the concentration of the chromophores.

1.3 Scattering and Diffusion

Diffusion assumes that the quantity that is diffusing (*e.g.* optical or radiant energy) does not have a preferential direction of travel. Light *scattering* arises from the presence of heterogeneities, resulting in non-uniform temporal/spatial distribution of refractive index n within a bulk medium. Incident EM wave sets electric charges into oscillatory motion and can excite vibrational modes. Scattered light is re-radiated by acceleration of these charges and/or relaxation of vibrational transition. The scattering is said to be *elastic* if the energy (and therefore the wavelength) of the incident photon is conserved and only its direction is changed (*e.g.* Rayleigh, Mie). Conversely, the scattering is said to be *inelastic* where the scattered photon either gives energy to or takes energy from the medium (*e.g.* fluorescence or Raman, respectively). The main parameters that affect scattering: (i) wavelength, (ii) relative refractive index, (iii) particle radius and (iv) shape and orientation.

The *scattering coefficient* $\mu_s[cm^{-1}]$ is defined as $\mu_s = N_s \cdot \sigma_s$ where σ_s is the effective cross-section $[m^2]$ and N_s is the amount of scatterers per volume unit $[m^{-3}]$. The scattering *mean free path* (mfp), defined as $l_s = 1/\mu_s$ [m], is the average distance a photon travels between scattering events.

Rayleigh scattering arises from very small particles ($\approx \lambda/10$). Scattering at right angles is half the forward intensity (see Figure 1.3). The strong wavelength dependence enhances the

[1] Pierre Bouguer (1698-1758), Johann Heinrich Lambert (1728-1777), and August Beer (1825-1863) are at the origin of these equations.

short wavelengths. It depends on the size, morphology, and structure of the components in tissues. The scattered intensity is equal to:

$$I = I_o \frac{8\pi^4 N\alpha^2}{\lambda^4 R^2}(1+\cos^2\theta) \propto \frac{1}{\lambda^4} \tag{1.12}$$

Rayleigh scattering is inversely related to the fourth power of the wavelength of the incident light $I \propto 1/\lambda^4$.

Mie scattering predominates if the encountered particles is comparable or larger than the wavelength. Because of the relative particle size, Mie scattering is poorly wavelength dependent, but is rather forward directional scattering.

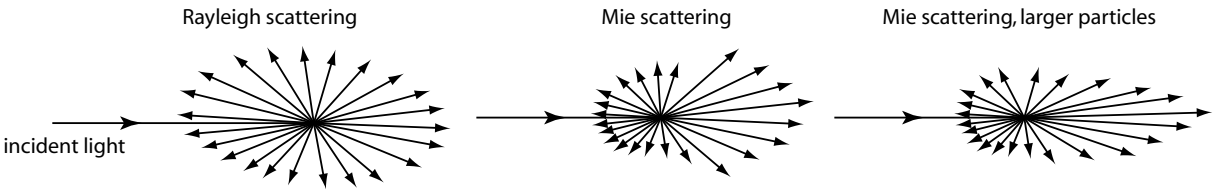

Figure 1.3: *Direction of propagation in Rayleigh and Mie scattering*

Due to various size of scatterers in biological tissues, neither Rayleigh nor Mie theories completely describe scattering in biological tissue. Therefore, one needs to establish a new model for scattering calculation. One assumes that a photon is scattered by a particle so that its trajectory is deflected by an angle θ (see Figure 1.4). The projection of its new trajectory on the direction of original traveling path is $\cos\theta$.

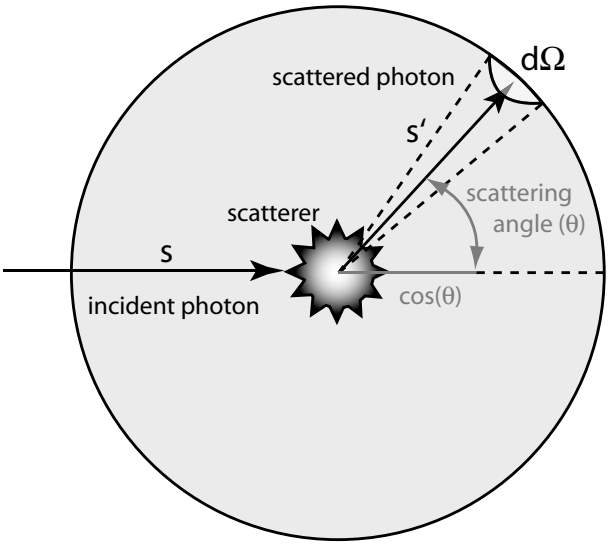

Figure 1.4: *Scattering anisotropy g*

The *anisotropy g* is defined as the mean cosine $\langle\cos\theta\rangle$ of the deflection angle and is a measure of the forward direction retained after a single scattering event.

The proper definition for g is the expectation value of $\cos(\theta)$:

$$g = \langle \cos\theta \rangle = \frac{\int p(\mathbf{s}\cdot\mathbf{s}')\mathbf{s}\cdot\mathbf{s}'d\Omega}{\int p(\mathbf{s}\cdot\mathbf{s}')d\Omega} = \int_0^\pi p(\theta)2\pi\cos\theta\sin\theta d\theta$$

The angular dependence of scattering is called the *scattering phase function*, $p(\theta)$, which has units of $[sr^{-1}]$. It describes the probability of a photon to be scattered into a unit solid angle, oriented at an angle θ relative to the original trajectory. An *isotropic* scattering function would scatter light with equal efficiency into all possible directions. Such a scattering function has the form:

$$p(\theta) = \frac{1}{4\pi} \text{ , such that } \int_0^\pi p(\theta)2\pi\cos\theta\sin\theta d\theta = 1$$

The Heyney-Greenstein scattering phase function is an analytical expression which mimics the angular dependence of light scattering by small particles and is based on the anisotropy factor g (see Figure 1.5).

$$p(\theta) = \frac{1}{4\pi}\frac{1-g^2}{(1+g^2-2g\cos\theta)^{3/2}} \tag{1.13}$$

$$g = \begin{cases} -1 & \text{totally backward scattering} \\ 0 & \text{isotropic scattering} \\ 1 & \text{totally forward scattering} \end{cases}$$

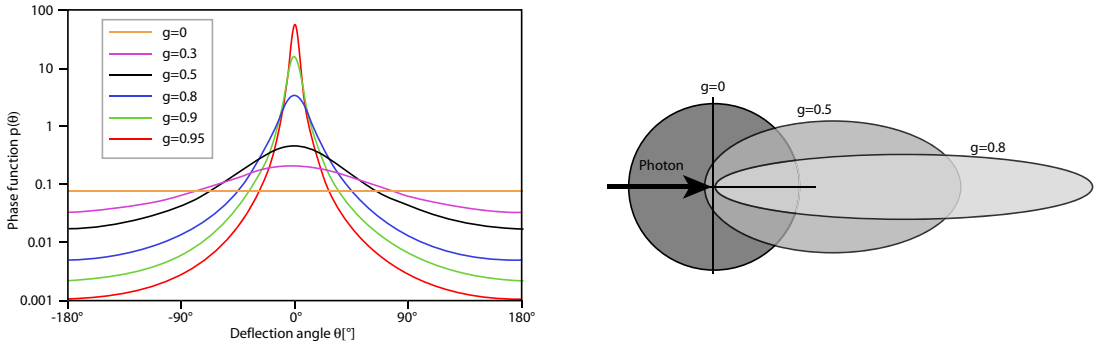

Figure 1.5: *Heyney Greenstein approximation of the scattering anisotropy g*

The function does not represent true scattering phase functions in biological tissues, but it is a fairly good approximation. Typical values for g are ranging between 0.65 and 0.95 [Niem07]. The absorption and scattering coefficients, μ_a and μ_s, are the probability of absorption and scattering occurring per unit path length. The other microscopic parameters listed in Table 1.1 can all be deduced from the three fundamental ones.

The optical *albedo* a is defined by the ratio $a = \mu_s/\mu_t$. For $a = 0$, attenuation is exclusively due to absorption, whereas only scattering occurs in the case of $a = 1$.

The *effective scattering coefficient* μ_s' is a lumped property incorporating the scattering coefficient μ_s and the anisotropy g:

$$\mu_s' = \mu_s(1-g)$$

The purpose of μ_s' is to describe the diffusion of photons in a random walk of step size of $1/\mu_s'$, where each step involves isotropic scattering. Such a description is equivalent to description of photon movement using many small steps $1/\mu_s$, that each involves only a partial deflection angle

if there are many scattering events before an absorption event, i.e. $\mu_a \ll \mu_s'$. This situation of scattering-dominated light transport is called the *diffusion regime*. μ_s' is commonly encountered when treating how visible and near-infrared light propagates through biological tissues.

$\mu_s' < 10\mu_a$	Strong absorption regime $\rightsquigarrow$ Lambert-Beer Law ($\lambda < 300nm$; $\lambda > 2000nm$)
$\mu_s' \gg \mu_a$	Diffusion approximation regime ($600nm < \lambda < 1000nm$)
$\mu_a \cong \mu_s'$	Equation of radiative transfer ($300nm < \lambda < 600nm$; $1000nm < \lambda < 2000nm$)

The *total extinction coefficient* μ_t is the inverse of the *mean free optical path* L_t of incident photons in turbid media and is given by

$$\mu_t = \frac{1}{L_t} = \mu_a + \mu_s'$$

The *optical penetration depth* δ is the depth at which the incident spatial irradiance has decreased to $1/e$ in the tissue. The *effective attenuation coefficient* μ_{eff} is the inverse of δ. The relation between μ_{eff} and the microscopic parameters μ_a and μ_s' can be derived from photon transport theory:

$$\mu_{\text{eff}} = \frac{1}{\delta} = \sqrt{3\mu_a\mu_t} = \sqrt{3\mu_a \cdot (\mu_a + \mu_s')} \tag{1.14}$$

1.4 Fluorescence Basics

Most of the biological tissues do fluoresce when they are excited by visible or ultraviolet (UV) light. This fluorescence is emitted by numerous bio-molecules. In this section, one will describe the physical mechanisms underlying fluorescence emission.

Luminescence occurs as a light emission during electronic transitions of a physical system, i.e. atoms or molecules, from its excited states back to a lower state. Various excitation ways lead an electron into an excited state: chemically, biologically, electronically, light-based, etc...

Chemoluminescence: chemical reactions provides the necessary excitation energy. An example would be a "glow-in-the-dark" plastic tube. Zinc Sulfide and Strontium Aluminate are the two most commonly used phosphors.

Bioluminescence: the excitation energy is provided by biochemical, mainly enzymatical, reactions in living organisms. Examples for bioluminescence are the glow of lightning bugs *lampyridae* and sea plankton *dinoflagellat noctiluca scintillans* observed in summer nights.

Electroluminescence is activated by electrical current. Examples are numerous : fluorescence tubes, light emitting diodes (LED), auroras (polar lights) and lightening. The same phenomenon is observed in cathode ray tube (CRT) screens, where electrons are accelerated towards a light-emitting screen.

Photoluminescence is the luminescence from systems excited with ultraviolet (UV), visible (VIS) or infrared (IR) light. Depending on the nature of the system's excited state, two forms of photoluminescence are defined : *fluorescence* and *phosphorescence*. Fluorescence is the emission resulting from the decay of an excited singlet state, while phosphorescence is the emission resulting from the decay of an excited triplet state. Molecules showing fluorescence and phosphorescence behavior are also called *fluorochromes* or *fluorophores*.

The electronic transitions occurring in a molecule are schematically illustrated with the classical Jablonski diagram, first proposed by Professor Alexander Jabłoński in 1935 [Jabl35] to

describe absorption and emission of light (see Figure 1.6). The energy levels of a molecule are shown as horizontal lines on a vertical, schematic energy scale. Each of these electronic levels is subdivided in a number of vibrational sublevels, which themselves consist of different rotational sublevels (not shown here). The total intrinsic energy of a molecule state is the sum of the electronic, vibrational, and rotational contributions. Transitions between the energy levels are depicted by vertical arrows. Prior to excitation, the electronic configuration of the molecule is described as being in the ground state, i.e. the most stable energy configuration, typically a singlet state (S_0). Upon absorbing a photon of excitation light, usually of short wavelengths (i.e high energy), electrons may be raised to a higher vibrational energy level in the first excited state (S_1) in about a femtosecond (10^{-15} s) before rapidly relaxing to the lowest energy level. This event depicted in Figure 1.6 as a transition from the upper to lower bars in S_1, is termed *vibrational relaxation* and occurs in about a picosecond (10^{-12} s) or less. Because of this rapid relaxation, emission spectra are usually independent of the excitation wavelength. Fluorescence lifetimes (10^{-9} s) are typically four orders of magnitude slower than vibrational relaxation. This gives the molecules sufficient time to achieve a thermally equilibrated lowest-energy excited state (i.e. the lowest vibrational level of S_l) prior to fluorescence emission. Except for atoms in the vapor phase, one invariably observes a shift to lower wavelength (i.e. a loss of energy) of the emission relative to the absorption. This phenomenon is called *Stokes' shift*, and is named after Irish physicist George G. Stokes, who observed it first in 1852. Internal conversion (IC) can occur between two excited states (*e.g.* $S_2 \rightarrow S_1$) under certain conditions [Lako06].

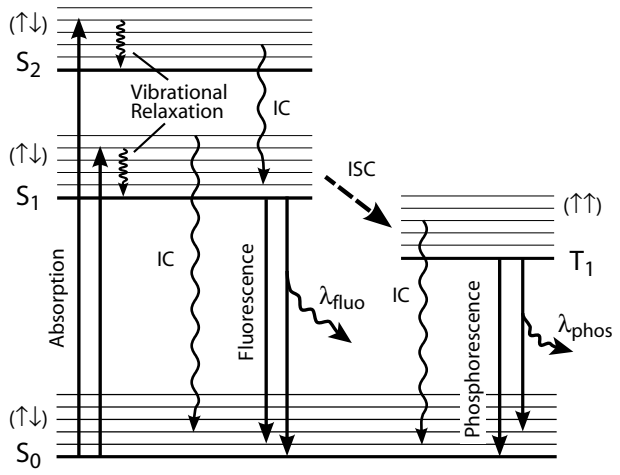

Figure 1.6: *Jablonski diagram shows the ground (S_0), first (S_1) and second (S_2) excited electronic singlet states of a molecule, as well as the first excited triplet state (T_1) with fluorescence and phosphorescence emission.*

Phosphorescence decay is similar to fluorescence, except that the electron undergoes a spin conversion ($\downarrow\uparrow \rightsquigarrow \uparrow\uparrow$) into a "forbidden" triplet state T_1 instead of S_0. This process is known as *intersystem crossing* (ISC) . Emission from the triplet state occurs with lower energy relative to fluorescence, hence emitted photons have longer wavelengths. Typical phosphorescence lifetimes are in the order of millisecond ($10^{-3}s$), thus much longer than fluorescence lifetimes.

It is interesting to note that the emission spectrum of a fluorophore is typically a mirror image of the S_0 to S_1 absorption spectrum transition. According to the Franck-Condon principle, all electronic transitions are vertical. Thus, electronic excitation does not seriously alter the geometry of the nucleus and the spacing of excited state vibrational levels is similar to that of the ground state, that is, they occur without change in the position of the nuclei. As a result,

if a particular transition probability between the 0^{th} and 2^{nd} vibrational levels is largest in absorption, the reciprocal transition is also most probable in emission. Consequently, fluorescence emission spectra often display similar, but reversed, vibrational structures to those observed in the absorption spectra. This is called the *mirror image rule*

The *quantum yield* of a fluorophore describes the number of emitted photons divided by the number of absorbed photons. Consequently, fluorochromes with large quantum yields display the brightest emissions.

Bibliography

[Born99] M. Born and E. Wolf. *Principles of Optics: Electromagnetic Theory of Propagation, Interference and Diffraction of Light (7th Edition)*. Cambridge University Press, 7th edition, 1999.

[Gard96] C. Gardner, A. Welch, and S. Jacques. Fluorescence spectroscopy of tissue: Recovery of intrinsic fluorescence from measured fluorescence. *Applied Optics*, 35(10):1780–1792, 1996.

[Guib90] G. G. Guibault, editor. *Practical Fluorescence (Modern Monographs in Analytical Chemistry)*. CRC Press, 1990.

[Jabl35] A. Jablonski. Über den Mechanismus der Photolumineszenz von Farbstoffphosphoren. *Zeitschrift fur Physik*, 94:38–46, 1935.

[Lako06] J. R. Lakowicz. *Principles of Fluorescence Spectroscopy*. Springer, 3rd edition, 2006.

[Niem07] M. H. Niemz. *Laser-Tissue Interactions: Fundamentals and Applications (Biological and Medical Physics, Biomedical Engineering)*. Springer, 3rd edition, 2007.

[Sale07] B. E. A. Saleh and M. C. Teich. *Fundamentals of Photonics*. Pure and Applied Optics. Wiley-Interscience, 2nd edition, 2007.

[Tuch02] V. V. Tuchin. *Handbook of Optical Biomedical Diagnostics (SPIE Press Monograph Vol. PM107)*. SPIE Publications, 2002.

Chapter 2

Clinical cancer detection and tissue characterization by optical imaging

In this chapter, we will address the optical tissue characterization, leading us to introduce the clinical cancer detection by optical methods. In Section 2.1, we will focus on *reflectance imaging*, where only scattering and absorption play a significant role. In this context, we will present shortly the main non-fluorescing absorbers, called *chromophores*. The latter are either contained in the biological tissue – the *endogenous* chromophores –, or applied externally – the *exogenous* chromophores. In Section 2.2, we will address the fluorescence photodetection. In this context, we will present the main fluorophores involved, and the instrumentation aspects. In Section 2.3, we will review the technical concepts of high magnification shortly, and present their implementation in the endoscopic imaging apparatus. In Section 2.4, we will focus on *confocal endoscopy*. In the last Section 2.5, we will introduce some basic statistical concepts that underly our clinical studies.

2.1 Reflectance endoscopic imaging

2.1.1 Major absorbing chromophores

2.1.1.1 Endogenous chromophores

As described thoroughly in Section 1.2, absorption plays an important role in photomedical applications. The major light absorbing molecules in mammalian tissues are oxy- and deoxyhemoglobin, melanin, myoglobin and water. The absorption spectra of these molecules are shown in Figure 2.1 adapted from [Boul86]. We can observe a lower absorption between 600 nm and 1000 nm. In this so-called *therapeutic window*, scattering predominates over absorption and light is deep-penetrating into the tissue. Since we are working in hollow organs (i.e. not skin), we will focus on the main absorbers in soft tissue for visible light, namely hemoglobin.

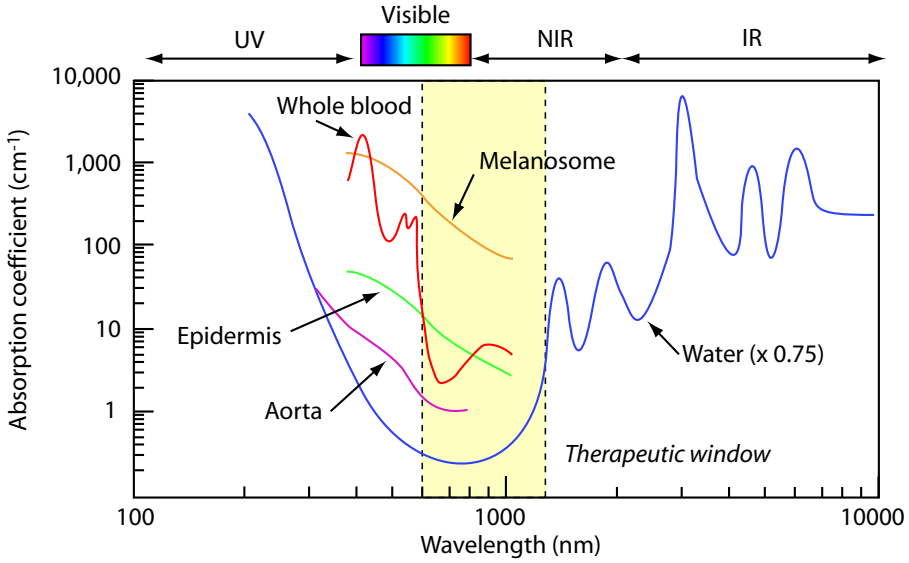

Figure 2.1: *Major light absorbing molecules in soft mammalian tissues.*

Hemoglobin absorption Healthy functioning of all tissues depends on an adequate blood supply, and thus sufficient oxygen delivery. In the normal adult, blood is composed of (i) plasma ($\sim 55\%$ by volume), (ii) red blood cells ($\sim 44\%$ by volume for an adult, 1 cm^3 blood = 5 billion rbc), and (iii) white blood cells and platelets ($< 1\%$ by volume, leucocytes - 1 per 100 rbc).

Red blood cells can be considered simply as small sacks containing hemoglobin. They attach oxygen in the lungs, becoming oxyhemoglobin (HbO_2), and then deliver oxygen to tissues. At the tissue, the oxygen dissociates to leave deoxyhemoglobin (Hb). Figure 2.2 shows oxy- and deoxy- hemoglobin absorption spectra (adapted from [Grat60], cited by Scott Prahl[1]). The circulating blood is almost fully saturated with oxygen ($\approx 98\%$), so that the hemoglobin absorption spectrum is dominated by the oxyhemoglogin component.

Hemoglobin has a normal concentration of 150g/liter of blood, which permits the whole blood to carry 65 times more oxygen than does plasma at a pO_2 of 100 mmHg. The hemoglobin molecule can bind up to four oxygens molecules. The oxygen *saturation* gives the statistical average of all oxygen bound to hemoglobin molecules relative to the total amount that can be bound. One gram of functional hemoglobin can combine with 1.34ml O_2, yielding

$$150\text{g Hb/liter} \times 1.34\text{ml } O_2\text{/ g Hb} = 200\text{ml } O_2\text{/liter}$$

Then to convert the molar extinction coefficient $\varepsilon(\lambda)$ to an absorption coefficient μ_a:

$$\mu_a(\lambda) = 2.303 \cdot \varepsilon(\lambda) \cdot \frac{150 \text{ g Hb/liter}}{64500 \text{ g Hb/mole}} = 0.0054 \cdot \varepsilon(\lambda)$$

In vascular imaging, one may either use an intravenous contrast agent (*e.g.* ICG or FITC) or target hemoglobin absorption peaks to maximize the contrast between blood vessels and surrounding tissue. Narrow-band imaging (NBI) has been developed over the last decade [Gono03] to exploit this latter property (see Section 2.1.2). In this thesis, we will present a spectral design optimization of our high-magnification setup also based on these properties.

[1] `http://omlc.ogi.edu/spectra/hemoglobin/`

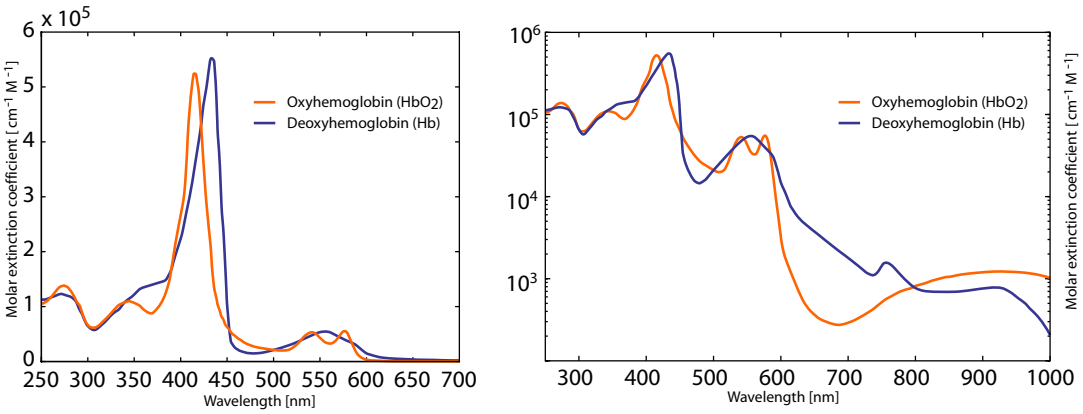

Figure 2.2: *Hemoglobin absorption in the near ultraviolet, visible and near infrared (NIR) range. Normal and logarithmic scales are presented.*

2.1.1.2 Exogenous chromophores

In the unstained mucosa, meticulous attention is required for the initial detection of abnormalities, looking for subtle changes in color, topography, and vasculature [DaCo05]. With the development of endoscopy, new techniques have been implemented to enhance the detection of early cancers. The use of a chromogenic contrast agent that accumulates (or not) in cancerous tissues helps to determine the boundary of the lesion and to determine whether it is elevated, flat, or depressed. As a common term, one calls this imaging procedure *chromoendoscopy*, based on the Greek words *chromo* (color), *endon* (within), and *skopein* (to examine).

Intravital staining techniques are not new. In fact, it dates back to Schiller (1933), who used Lugol's solution to improve diagnosis in the uterine cervix [Schi33]. In the 1960s and 1970s, endoscopic staining techniques were employed for oropharyngeal and esophageal tumors [Voeg66, Endo72]. However, since then, the knowledge about the different dyes has increased dramatically [Kies04a, Eise04]. Furthermore, the renaissance of chromoendoscopy was accelerated by the rapid improvement of endoscopic image resolution. In the last decade, a significant increase in published data about chromo- and high resolution endoscopy has been observed.

Chromoendoscopy means to stain certain areas with several dyes. Generally, the dye is distributed in a homogenous fashion by the help of a spraying catheter which is passed through the working channel of the endoscope [Jung99]. Intravital staining of suspected lesions in the colon offers the possibility to define the macroscopic type and to delineate the exact borders. Additionally, the surface structure can be analyzed by the help of magnifying endoscopes. The efficiency of magnifying endoscopy is often determined in conjunction with intravital staining techniques. Chromoendoscopy first helps to identify small, circumscribed lesions. Subsequent surface analysis is done by the help of magnifying endoscopy [Kies03].
The different dyes are categorized according to their staining mechanisms :

Absorbtive dyes are taken up by specific epithelial cells, thereby making it possible to specifically characterize the mucosa, *e.g.* Lugol's solution (0.5-3%), methylene blue (0.1-1%), toluidine blue and Cresyl violet (0.2%).

Contrast dyes are not absorbed but accumulate in pits and valleys between cells, highlighting mucosal architecture, *e.g.* indigo carmine (0.1-0.4%).

Reactive stains induce a chemical reaction at the cell level, *e.g.* Congo red (0.3%) and phenol red react to changing conditions of acid secretion and carry a potential with regard to the early detection of gastric cancer and *helicobacter pylori* infection [Jung99, Brun03].

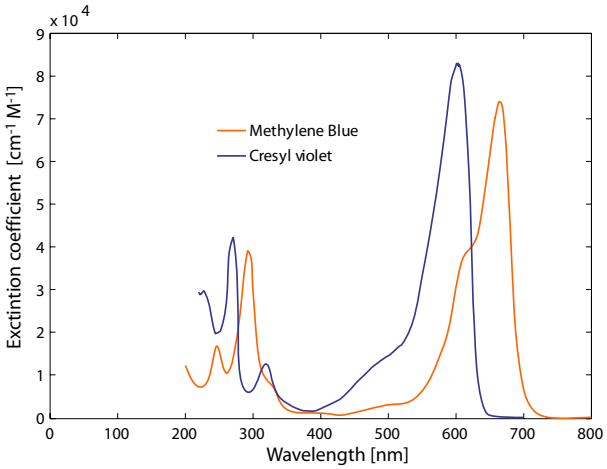

Figure 2.3: *Extinction coefficients of two absorptive dyes: Methylene blue and Cresyl violet [Du98].*

In the following, one will describe the main exogenous chromophore and their applications:

Methylene blue is a heterocyclic aromatic compound with molecular formula $C_{16}H_{18}N_3SCl$. At room temperature it appears as a solid, odorless, dark green powder, that yields a blue solution when dissolved in water. Usually a concentration of 0.5% of methylene blue is used. It requires a mucus clearance prior to examination with *e.g.* acetic acid. A lot of results have been obtained in the gastrointestinal (GI) tract to highlight metaplasia on Barret's esophagus. Tests have also been performed in the urinary bladder. Mufti *et al.* used *in vivo* staining of the bladder mucosa with 0.1% methylene blue in normal saline in 23 randomly selected patients, with known and previously treated transitional cell tumors of the bladder, in whom routine check cystoscopy failed to demonstrate any mucosal abnormality. Cold cup biopsies were obtained from stained ($n = 21$) as well as unstained areas ($n = 2$). Although positive staining did not prove the presence of a pre-malignant or malignant area, lack of staining was more likely to exclude mucosal abnormalities [Muft90]. Creagh *et al.* studied 39 patients newly diagnosed with bladder tumors and followed for a minimum of 2 years. Potential biopsy sites were identified by staining intravesically with a 1% methylene blue solution and compared with random biopsy sites. Biopsy directed by methylene blue staining detected carcinoma *in situ* more often than random biopsy, but rates of recurrence were similar in both stained and unstained groups. These authors concluded that methylene blue staining does not add significantly to the management of patients presenting with bladder tumors [Crea95].

Toluidine blue is an acidophilus metachromatic nuclear stain that colors sites of squamous cell carcinoma, but not adjacent normal mucosal surfaces. Whether or not toluidine blue actually stains tumor nuclei is still not proven, but dye may diffuse into larger intercellular canaliculi present in the tumor cells.

Cresyl violet is also an absorptive dye, that is used to visually emboss the relief of planar polyps [Jung99]. It is often used in combination with indigo carmine. Regular staining

patterns are often seen in hyperplastic polyps or normal mucosa, whereas unstructured surface architecture was associated with malignancy [Kudo94]. Also the kind of adenoma (tubular vs. villous) can be seen by detailed inspection. This experience has lead to a categorization of the different staining patterns in the colon. The so-called *pit-pattern classification* differentiated 5 types and several subtypes of colonic mucosa [Kudo96]. With the help of this classification, the endoscopist is allowed to predict histology with good accuracy [Huan04].

Indigo carmine is a contrast stain that is not taken up by cells. Instead, it accumulates in pits and valleys between cells highlighting the mucosal architecture that becomes even more apparent with the use of magnification or high resolution endoscopy, or both. In general, a concentration of 0.5% to 1% is used. It contributes to contrasting and accentuating changed mucosal processes [Fu04]. It has been used to diagnose Barrett's esophagus [Aman05, Curv08], and diagnose and discriminate polypoid and non-polypoid lesions in the colon [Kudo97]. Endo *et al.* have developed an outpatient procedure to resect urinary bladder cancer using a blue dye-mixed local anesthetic (2% xylocaine:indigo carmine 8:2), that was injected into the tumor base prior to resection [Endo10].

Lugol's solution contains potassium iodine and iodine that reacts with glycogen in non-keratinized squamous epithelium. Usually a concentration of 2% to 3% is used. Normal squamous epithelium stains deeply brown giving the esophagus a snake skin-like appearance while areas with inflammation, dysplasia, or (early) cancer lack appropriate staining because of a depletion of glycogen. Lugol's solution has been used to delineate the extent of Barrett's esophagus [Wool89], to screen for squamous cell cancer in the esophagus in high risk populations [Inou01], and to detect (standard) endoscopy negative reflux disease in combination with high resolution endoscopy [Tam02].

2.1.2 Narrow-band imaging, FICE and Chromoendoscopy

Since the initial development of white light endoscopy, several attempts have been made to improve sensitivity. Among them, Hürzeler placed some color filter in front of the light source to better delineate the tumor margins [Hürz75]. Other optical modifications were investigated to develop the so-called *virtual* chromoendoscopy, i.e. staining without the need of any dyes. Two main technologies have been developed by two distinct Japanese groups.

Narrow-Band Imaging (NBI) has been in use since 1999 and was developed as a part of the joint research between the Japanese National Cancer Center Hospital East and Olympus Medical Systems Corporation (Tokyo, Japan). Gono *et al.* revealed that the use of 415 nm narrowband light could improve the capillary images, which are difficult to observe under conventional white light cystoscopy (WLC) [Gono03, Gono04]. The NBI technology is an optical image enhancement technique designed for endoscopy to enhance the contrast between mucosal surfaces and microvascular structures without the use of dyes. With NBI, the tissue surface is illuminated with light of a narrow bandwidth, with center wavelengths in the blue (415 nm) and green (540 nm) spectrum of light (see Figure 2.4). The penetration depth for these wavelengths is 170 μm, and 240 μm, respectively. Since these specific wavelengths are strongly absorbed by hemoglobin (see Section 2.1.1), the vascular structures appear dark brown or green against a pink-whitish mucosal background. Several investigators have demonstrated that this modification of spectral features emphasizes the contrast of both the capillary pattern and the pit pattern, so providing imaging features additional to those of both conventional endoscopy and chromoendoscopy [Kara05, Sano09].

Systems that have integrated NBI and WLC are already commercially available. With the push of a button, the NBI mode is activated by mechanical insertion of the narrow-band filter in front of the white-light source.

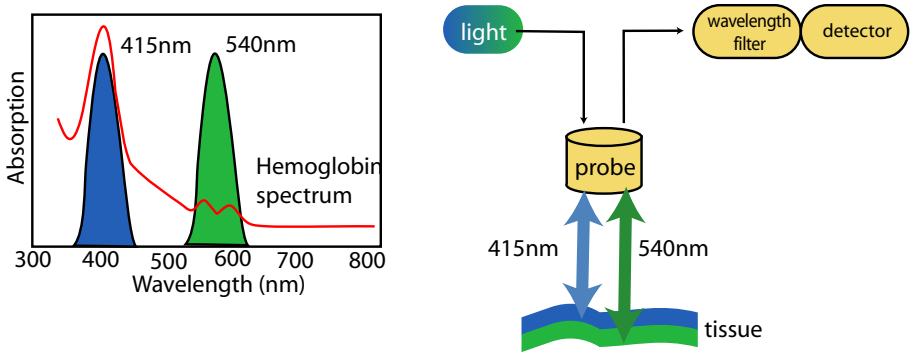

Figure 2.4: *Narrow-band imaging (NBI) is based on the phenomenon that the depth of light penetration increases with wavelength. The blue light (415 nm) enhances the superficial capillary network, whereas the green light (540 nm) enhances the visibility of deeper vessels [Caub09].*

Fujinon Intelligent Color Enhancement (FICE) was invented by Yohishi Miyake (Faculty of Engineering, Chiba University Japan) [Miya89, Shio95] and introduced by Fujinon Inc. in 2005. Like NBI, the FICE technology (sometimes called *Optimal Band Imaging*, OBI) is based on the selection of spectral transmittance with a dedicated wavelength. In contrast to NBI, in which the bandwidth of the spectral transmittance is narrowed by optical filters, this system is based on a new spectral estimation technique that replaces the need for optical filters. The FICE system takes an ordinary endoscopic image from the video processor and arithmetically processes the reflected photons to reconstitute virtual images for a choice of different wavelengths. Because the spectra of pixels are known, it is possible to implement imaging on a single wavelength. Such single-wavelength images are carefully selected, and assigned to red, green, and blue to build and display an enhanced color image. There are 10 pre-programmed filters which are switched on the keyboard, each of which has different settings for estimated RGB channels (see Table 2.1). Although each spectral image is a monochromatic image, their combination brings a view similar to a color image produced under conventional video endoscopy and improves visibility in the spectral image [P.-B09, Pohl07, Pohl08, Osaw09, Camm08]. Figure 2.5 shows an evaluation of the vascular patterns with the help of FICE virtual filters (adapted from [P.-B09]). FICE emphasizes increased vascular density, which can be appreciated as a darkening of the mucosal pattern, or as a fine meshwork of brown/bluish vessels.

The FICE design has not been yet implemented in the urinary tract, whereas the NBI system has been adapted to cystoscopy [Brya07, Herr08, Herr09, Nase10]. These authors concluded that NBI cystoscopy improved the detection of recurrent non-muscle-invasive bladder tumors as compared to standard WLC. NBI cystoscopy also provided a much clearer view of papillary tumors than with WLC, in particular their delicate capillary architecture. Moreover, NBI better defined the margins of carcinoma *in situ* (CIS) lesions with surrounding normal appearing mucosa. Since NBI can be implemented in magnification or high resolution endoscope, it is also possible to visualize small vessel structures on detected carcinomas. For instance, Shibuya *et al.* revealed vascular patterns on squamous cell carcinoma in the bronchi [Shib10], but nothing similar has been up-to-now implemented in the bladder.

NBI 1st generation	
NBI-blue filter	395-445nm
NBI-green filter	530-550nm
NBI 2nd generation	
R	500 ± 15nm
G	445 ± 15nm
B	415 ± 15nm

FICE virtual set of filters	R	G	B
set 0	500	445	415
set 1	550	470	580
set 2	550	500	470
set 3	400	450	480
set 4	520	500	405
set 5	500	480	420
set 6	580	520	460
set 7	650	550	450
set 8	540	415	415
set 9	550	500	400

Table 2.1: *NBI optical filters and FICE virtual filters*

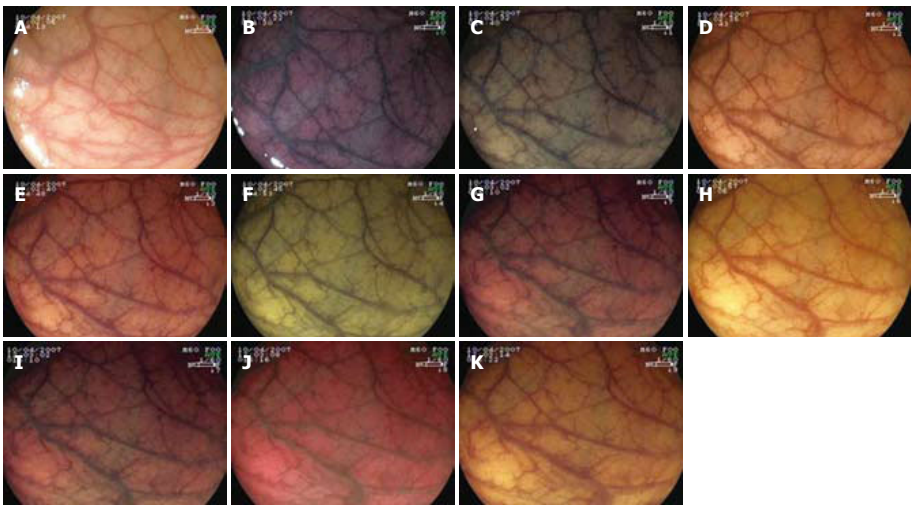

Figure 2.5: *Evaluation of the vascular pattern without magnification with the FICE system. [A] Conventional WL endoscopy [B] Filter 0 [C] Filter 1 [D] Filter 2 [E] Filter 3 [F] Filter 4 [G] Filter 5 [H] Filter 6 [I] Filter 7 [J] Filter 8 [K] Filter 9.*

Similarly, as NBI is a reflectance imaging technology, it cannot be implemented on the same detector with fluorescence detection at the present time, because the latter requires a filter in front of the CCD, that blocks *e.g.* the blue backscattered light.

We present here some results obtained in the urinary bladder. Bryan *et al.* performed flexible WLC and subsequent NBI cystoscopy in 29 patients with recurrent non-muscle invasive bladder cancer (NMIBC) [Brya07]. NBI cystoscopy revealed 15 additional tumors in 12 patients.

Herr *et al.* performed WLC with subsequent NBI cystoscopy in 427 consecutive patients with a history of NMIBC [Herr08]. Recurrence was found in 103 patients. In 58/103 (56%) patients with a recurrence, additional tumors were detected by NBI, and in 13/103 (12%) patients, the bladder tumors were detected only due to NBI. A limitation of this study is the possible observer bias, since WLC and NBI were performed subsequently by the same urologist. Whether the specificity of NBI will be negatively influenced by previous intravesical instillation, inflammation, or scarring, was not known in this study.

Naselli *et al.* reviewed 47 consecutive patients with newly diagnosed high-grade NMIBC in a prospective observational study [Nase10]. About one month after the first transurethral resection (TUR), NBI cold-cup biopsies were taken from areas suspicious for urothelial cancer at the end of an extensive white-light second TUR protocol including: (i) resection of the scar of the primary tumor; (ii) resection of any overt or suspected urothelial lesions; and (iii) six random cold-cup biopsies of healthy mucosa. Nine patients (19%) had macroscopic or microscopic high-grade NMI urothelial cancer, whereas one was reassessed as having muscle-invasive disease at the white-light second TUR plus the six random biopsies. NBI biopsies were taken in 40 of the 47 patients and detected six more patients with high-grade cancerous tissue (13%).

Summarily, these studies shows that NBI and FICE endoscopy are superior in sensitivity to white-light endoscopy. However, since these technologies are quite new, the surgeons often need to get trained by "typical" images, because often they don't have any feeling about how to interpret the presented colorized patterns.

The size of the observed vascular patterns highly depends on the model of endoscope. Obviously, in the GI tract, the large diameter of the scopes ($\approx$ 15 mm) allows to integrate an optical zooming setup (up to 150×), whereas in urology and pneumology, the small scope diameter ($\approx$ 5–6 mm) does not leave much space for a mechanical zoom. Therefore, high resolution scope are preferred because it is possible to perform electronic zoom on the regions of interest. For instance, in a recent study, Shibuya *et al.* used a high-resolution endoscope (850 kPixels), and observed vascular patterns down to 30 μm [Shib10]. Section 2.3 will treat *high-magnification endoscopy* in details.

2.2 Cancer detection by endoscopic fluorescence imaging

The fundamental principle of tissue characterization or cancer detection by fluorescence is to exploit the optical contrast between the (cancerous) lesions and their surrounding healthy tissue. As the lesions often remain invisible in conventional white light (WL) examination, one needs an additional method to produce a better contrast. The fluorescence contrast is said to be *intrinsic* in case one exploits the inherent tissue optical properties (i.e autofluorescence) or *induced* if the fluorescence comes from a selective accumulation of an exogenous or exogenously-induced fluorophore. The contrast itself may originate from the fluorescence brightness, spectral shape, lifetime or a combination of them. Spectroscopic measurements (space or time-resolved) or imaging are of great help in order to visualize this contrast quantitatively or qualitatively.

In this thesis, we will concentrate on two applications of the photodetection in hollow organs: bronchial and urinary bladder cancers. We left intentionally detection and treatment of cancers

of the GI tract, the gynecological tract, the skin, the liver, the pancreas, and affections of the eye aside.

2.2.1 Endogenous fluorophore

All biological tissues emit fluorescence when excited by ultra-violet (UV) or visible light. This fluorescence is emitted by naturally-occurring fluorophores and is therefore often called *autofluorescence* (AF) . This phenomenon has been intensively studied in the last decades, whereas pioneering work was performed in the beginning of 20th century by Policard *et al.* [Poli24]. The main endogenous fluorochromes in human tissue are listed in Table 2.2. Figure 2.6 shows the fluorescence absorption and emission spectra of the main tissue fluorochromes (adapted from [Wagn98b]). It can easily be seen, that the absorption maxima of endogenous fluorochromes predominately lay in the UV and the blue-violet visible wavelength range.

Chromophore	Absorption maxima	Excitation maxima	Emission maxima	Molar extinction coefficient	Fluorescence quantum yield
Tryptophan	280	280	350	5.6×10^{-3}	0.2
Tyrosine	275	275	300	1.4×10^{-3}	0.1
Phenylalanine	260		280	2×10^{-4}	0.04
NADH	260 340	290 340	440 450	14.4×10^{-3} 6.2×10^{-3}	
NAD+	260	not fluorescing		18×10^{-3}	
FAD		450	515		
FADH		not fluorescing			
HP, collagen, elastin LP, collagen, elastin	325	325 325	400 400		
4-Pyridoxic acid	307	315	425		
Hematoporphyrin derivatives (HpD)		405 544	610 675		0.11 0.32
Protoporphyrin IX (PpIX)		415,582	634		

Table 2.2: *Endogenous fluorophores at physiologic pH adapted from [R.-K96]*

A biological tissue is containing fluorescing and absorbing molecules. Intrinsic fluorescence spectra emitted from the tissue are often distorted by scattering and absorption. Most of the proteins exhibiting fluorescence are those containing the aromatic amino acids tryptophan, tyrosine, and phenylalanine, or a combination thereof [Wolf93]. Their chemical structure is depicted in Figure 2.7. The excitation maxima for those molecules all lay in the UV wavelength region below 295 nm and their maximal fluorescence emission occurs between 280 nm and 350 nm.

Most endogenous fluorochromes are involved in cellular metabolic processes or are constituents of the structural matrix of the tissues [Utzi01, R.-K96], and thus are under certain conditions affected by environmental factors. They can be classified in four groups, namely the aromatic amino acids and proteins, the pyridine nucleotides, the flavins, and the porphyrins. The principal fluorescing proteins are collagen and elastin, which are both involved in the structural matrix of numerous tissues. Their fluorescence stems from cross-links between their composing amino-acids. In load-bearing tissues, two types of cross-links are found: hydroxylysyl pyridinoline (HP) , and lysyl pyridinoline (LP). Both HP and LP are emitting autofluorescence with an excitation maximum at 325 nm and an emission maximum at 400 nm [Eyre84]. Collagen has an inextensible fibrous structure and is the main protein in connective tissue (cartilage, ligaments,

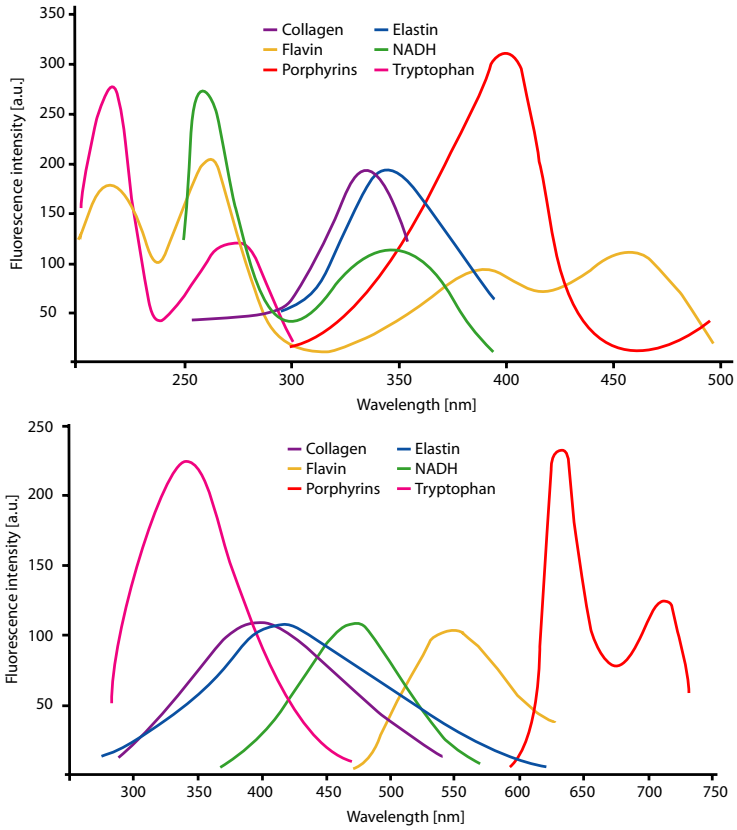

Figure 2.6: *Excitation and emission spectra of the main tissue fluorophores (adapted from [Wagn98b])*

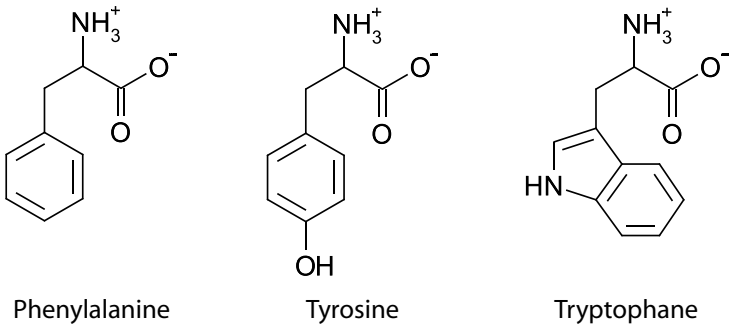

Figure 2.7: *Most of the fluorescing proteins contains phenylalanine (Phe), tyrosine (Tyr), tryptophan (Trp), or a combination thereof.*

tendons, bones). The absorption maximum of collagen fibres is around 325 nm with a maximal fluorescence emission around 400 nm [Kirk07].

Flavins and pyridine nucleotides are strong electron acceptors and play an important role in cellular energy metabolism. Flavin adenine dinucleotide (FAD) is the major flavin-related electron carrier. Its oxidized form (FAD) is fluorescent, while its reduced form (FADH) is not. The fluorescence excitation maximum of FAD lies around 450 nm and the emission maximum around 530 nm [R.-K96]. The other main electron acceptors are nicotinamide adenine dinucleotide (NAD). This molecule emits fluorescence in its reduced form, NADH. Fluorescence excitation and emission maxima can be found around 340 nm and 450 nm, respectively. Oxidization plays an important role over their respective fluorescence yield. Their relative fluorescence intensities, often defined as *redox ratio*, can be used as a metabolic indicator, and thus as a diagnostic mechanism in case of cancerous lesions [Brew02].

2.2.1.1 Autofluorescence in Pneumology

In the 1970's, Hürzeler *et al.* carried out some theoretical, then practical tests in order to heighten the contrast observed in endoscopy [Hürz75]. Filters (red, green, yellow and light blue) were placed in front of the light source and the subjective perceptible changes in contrast were examined. These tests showed that the light blue filter gave a heightened contrast between light and dark red as well as between yellow and red. With this illumination, pre-cancerous lesions were more visible in the mucous membrane.

In the early 1980's, Alfano *et al.* developed laser-induced autofluorescence spectroscopy to differentiate normal from tumor tissues. This work was initiated on rat tissues [Alfa84], and later extended to human breast and lung tissues [Alfa91] and eventually to the gynecological tract (uterus, cervix, ovary) [Glas92]. In these studies, 300 nm appeared to be the most appropriate excitation wavelength, while the ratio of the emitted fluorescence at 340 and 440nm provided the most prominent differences between the normal and malignant tissues.

Several papers report a sharp autofluorescence decrease on early cancerous lesions in the bronchi around 500 nm and/or a relatively less important decrease after 600 nm when excited between 400 and 450 nm [Anth89, Palc91, Hung91]. This serve as a basis for most autofluorescence imaging systems. Indeed, the authors observed a sharp decrease (around a factor of 10) in the green tissue autofluorescence on the CIS with respect to healthy mucosa. However, the spectral shape of the signal is not changed.

Anthony *et al.* reported autofluorescence spectra of bronchial tissue in vivo [Anth89]. They showed that the tissue, when excited around 410±5 nm displays an emission peak around 500 nm and a monotonically decreasing spectrum for $\lambda > 500$ nm. Moreover, they reported that the spectra of the tumor and the healthy tissue were, after normalization, very well overlapped between 500 and 600 nm but then the spectrum from the tumor displayed an increase in the red region that could not be found in the spectrum of the healthy tissue.

Zellweger *et al.* studied the autofluorescence of human healthy, metaplastic and dysplastic/CIS bronchial tissue, covering excitation wavelengths from 350 to 480 nm [Zell01a]. Typical spectra of bronchial mucosa are depicted in Figure 2.8. These measurements were performed with a spectrofluorometer whose distal end is designed to simulate the spectroscopic response of an imaging system using routine bronchoscopes. They also maximized the tumor vs. healthy and the tumor vs inflammatory/metaplastic contrast in detecting pre-/early malignant lesions. They found that the excitation wavelengths yielding the highest contrast are between 400 and 480 nm with a peak at 405 nm [Zell01b]. In a more recent publication, Tercelj *et al.* mentioned similar results obtained with an integrated endoscopic imaging and spectroscopy system [Terc05].

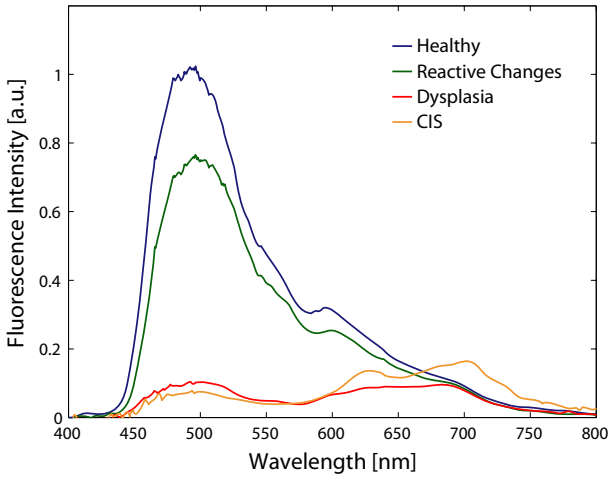

Figure 2.8: *Typical* in vivo *AF spectra from healthy bronchial mucosa, reactive changes and pre-neoplastic lesions (dysplasia and CIS). The spectra were measured with a non-contact optical fibre based spectrofluorometer using a 405 nm wavelength for excitation. These data were adapted from [Zell01a].*

At the beginning of the 2000's, several authors hypothesized the differences in the AF spectra between normal and abnormal tissues due to the variations of the following parameters :

1. the intrinsic fluorochrome concentration
2. the metabolic status of the fluorochromes [R.-K96, Wolf93]
3. the biochemical and biophysical micro-environment [Uehl09]
4. the loss of tissue layered architecture, due to *e.g.* mucosal thickening [Qu95]
5. the wavelength-dependent light attenuation due to the concentration and distribution of (non-fluorescent) chromophores, particularly hemoglobin [Qu95, Qu94, Gabr07]

In the next paragraphs, we will review the literature that shows that the latter two mechanisms are most likely to be at the origin of the contrasts.

Bard *et al.* developed a fiberoptic instrument allowing the measurement of autofluorescence spectroscopy (AFS) , diffuse reflectance spectroscopy, and differential path length spectroscopy during bronchoscopy [Bard05, Bard06]. Autofluorescence and reflectance spectra were analyzed in ranges from 435 to 700 nm and 435 to 900 nm, respectively. These authors commented about the variations in the autofluorescence spectra. Large natural variations in fluorophore concentrations seem to have less relevance for tissue diagnostics. Scattering modifications are related to changes in tissue architecture such as thickening of the epithelial layer and to cellular changes such as an increase of the nucleus chromatin content, variations in the nucleus-cytoplasmic ratio. Qu *et al.* described parallel changes in the mean thickness of the bronchial epithelium from 46±3 μm in normal epithelium, to 70±7 μm in a dysplasia to 116±16 μm for CIS [Qu95].

Absorption modifications are mostly related to modifications of the concentration and distribution of light absorbers such as hemoglobin. Such increased blood content is related to the increased density of microvessels and the blood stasis occurring in tumoral tissue [Shij03]. Shibuya *et al.* identified an marked increase of the microvessel density observed first on angiogenic squamous dysplasia (ASD) [Shib02, Shib03], and then on every type of early squamous cell carcinoma [Shib10].

Kobayashi *et al.* observed a clear blue peak located at around 483 nm along with a green peak at around 560 nm in the normal tissue excited at 400nm with a gallium-nitride (GaN)

based UV-laser diode [Koba02, Koba03]. Weak intensities were observed on the tumor tissues. The AF imaging and spectrum analysis were performed along with a histopathological study. The spatial distribution of the elastin in the bronchial tissue affected the intensity of the AF whereas the spectrum shape was not affected.

Bourg-Eckly *et al.* modified the Cellvizio® confocal system adding spectroscopic analysis capability with 488 nm excitation [Jean07, B.-H08]. They simultaneously acquired images and emission spectra using a flexible miniprobe. In the normal bronchi, reproducible images were obtained, characterized by a highly organized fibrous network. Precancerous lesions exhibited alterations of this fibrous network. Microscopic and spectral analysis showed that the signal mainly originates from the elastin component of the bronchial subepithelial layer.

Uehlinger *et al.* performed time-resolved measurements of bronchial tissue AF excited at 405 nm with an optical-fiber-based spectrometer [Uehl09]. These authors analyzed whether the fluorescence lifetime could serve as a new tumor/normal (T/N) tissue contrast parameter. A secondary end-point was to explain the origin of the contrasts observed when using AF-based cancer detection imaging systems. No significant change in the AF lifetimes was found. These results suggest that the spectral contrast might be due to an enhanced blood concentration just below the epithelial layers of the lesion. The intensity contrast probably results from the thickening of the epithelium in the lesions. The absence of T/N lifetime variations indicates that the quenching is not at the origin of the fluorescence intensity and spectral contrasts. These lifetimes were consistent for all the examined sites. It is very likely that there is only one dominant fluorophore since the measured lifetimes were the same for different emission domains ranging between 430 and 680 nm. The measured lifetimes suggest that this fluorophore is elastin, which is in good agreement with Bourg-Eckly *et al.*

In a recent study, Gabrecht *et al.* compared spectral measurement acquired *in vivo* during bronchoscopy and *ex vivo* on samples fixed in formalin [Gabr07]. These authors showed that the spectral contrast between healthy and cancerous bronchial tissue observed *in vivo* disappears completely when the samples are fixed in formalin (10% buffered). Indeed, the normalized spectra acquired *ex vivo* on healthy, pre-neoplastic lesions (squamous metaplasia, mild dysplasia, CIS, invasive SCC) and invasive lesions can be fairly superposed. In contrast to this, the mechanisms responsible for the intensity contrast are altered, but not destroyed by tissue death and/or the formalin fixation process. The thickening of the epithelium in the measured tissue samples is likely to be the cause of this intensity decrease on pre-neoplastic lesions. These results indicate that epithelial thickening and blood supply in the adjacent lamina propria are likely to play a key role in the generation of the AF contrast in bronchial tissues.

In a later study, Gabrecht *et al.* [Gabr08] investigated the potential of using blue backscattered light to reduce the numbers of false-positive in AF bronchial photodetection. These authors showed (pre-)neoplastic mucosa displays a clear wavelength dependence of the blue-violet light backscattering properties, whereas the reflectivity of normal, metaplastic and hyperplastic autofluorescence positive mucosa was wavelength independent. Again, this may be attributed to the higher hemoglobin content in the pre-neoplastic mucosa as compared to the normal tissue due to the neoangiogenesis.

2.2.1.2 Autofluorescence in Urology

The normal urothelium thickness of the bladder is estimated to be 150 μm [Reut92], and the 300-400 nm light is able to excite bladder tissue layers on the order of 500 μm. As a result, tissue autofluorescence (AF) signals from bladder tissue include contributions not only from the urothelium but also from deeper tissue layers, such as the collagen located in the lamina

propria and the NADH in muscle layers. In contrast to the lamina propria and muscle, there is no collagen and only a small amount of NADH compounds in the urothelium [Koen96]. The increased thickness of the urothelium in malignant lesions thus led to the decrease of the collagen and NADH signals (390 nm and 470 nm, respectively) by attenuating the autofluorescence from deeper tissue layers.

In a study about bladder tissue autofluorescence following excitation at 308, 337 or 480 nm, Anidjar *et al.* reported a marked decrease in autofluorescence for CIS with respect to normal bladder mucosa when excited at 337 or 480 nm [Anid96, Anid98], whereas the spectral shape of the autofluorescence underwent no change. At 308 nm excitation wavelength, they observed not only a change in intensity but also a change in spectral shape between the normal bladder mucosa and the CIS. They related these changes to the emission of oxidized flavoproteins (480 nm), tryptophan (selectively excited by 308 nm) and NADH (337 nm). They report that these results make it possible to distinguish normal bladder mucosa from CIS.

This is in partial agreement with Koenig *et al.* , who also used 337 nm as an excitation wavelength (N_2 laser) but found a spectrum with a different shape. Indeed, these authors found not only a difference in fluorescence intensity but also a modification of the spectral shape between the healthy mucosa and the CIS [Koen98]. The disagreements might be due to differences in data manipulation. Indeed, Anidjar *et al.* provided no explanation on how and whether their spectra were corrected for background fluorescence, the spectral response of their setup. They were also differences in their acquisition system, as Anidjar used a long pass filter centered at 400 nm whereas Koenig used a gated intensifier [Koen96, Koen98]. Moreover, Koenig's results rely on a larger series of random biopsies. Their explanation about the autofluorescence changes is that the spectrum is influenced by the epithelial thickness. Their idea is that the AF photons are reabsorbed on their way out by the thicker tissues. Their imaging system combined AF and blue backscattered light to enhance the contrast, as originally proposed by Hürzeler, although without the use of fluorescence [Hürz75].

Zaak *et al.* carried out AF excitation with a xenon chloride (XeCl) excimer laser operating at 308 nm [Zaak02]. For the evaluation of the AF spectra, an intensity ratio (335/430 nm) was calculated and correlated with the histologic results of the biopsies taken. They also highlighted a spectral distortion between spectra of the healthy mucosa, the inflammatory bladder mucosa and the CIS. They analyzed the AF spectra of 114 biopsies (21 malignant, 93 benign). The AF intensity ratios for the benign lesions were a factor of 2 to 7 higher than CIS and neoplastic tissue. Therefore, 20 of 21 neoplastic lesions were detected as true positive by AF. They combine it to the photodetection of 5-ALA induced fluorescence to improve its specificity.

Zheng *et al.* determine the optimal excitation and emission wavelengths for AF diagnosis of bladder cancer [Zhen03]. A total of 52 bladder tissue specimens were analyzed *ex vivo* from samples obtained with cystoscopic biopsy or surgical resection. The tissue specimens were rinsed, placed in bottles with physiologic saline solution (pH = 7.4) and delivered for spectroscopic measurements immediately. Fluorescence excitation wavelengths varying from 220 to 500 nm (10 nm step) were used to induce tissue AF, and emission spectra were measured in the 280–700 nm range (5 nm step). These spectra were then combined to construct 2-dimensional fluorescence excitation-emission matrices (EEMs). Significant changes in fluorescence intensity of EEMs were observed between normal and tumor bladder tissues, the most marked differences being at the excitation wavelengths of 280 and 330 nm. Their diagnostic algorithm is based on the combination of the fluorescence peak intensity ratios of I_{350}/I_{470} at 280 nm excitation and I_{390}/I_{470} at 330 nm excitation. One threshold per ratio was set to 3.5 and 1.18, respectively, and the combination of the two ratios yielded a sensitivity of 100% [95% confidence interval (CI) 0.95-1.0] and specificity of 100% (95% CI 0.90-1.0). This study is not fully comparable

with the studies described above, as the spectra were acquired *ex vivo*. Indeed, the hemoglobin absorption doesn't play a significant role anymore, since the samples are rinsed with saline before EEMs acquisition. Nevertheless, their results demonstrate increased fluorescence at 350 and 635 nm emission and a decrease at 390, 470 and 520 nm emission associated with bladder tumors (see Figure 2.9). The fluorescence peaks observed in fluorescence EEMs are close to the emission spectra of pure tryptophan (emission peak approx. 340 nm), collagen (emission peak approx. 385 nm), NADH (emission peak approx. 460 nm), FAD (emission peak approx. 510-530 nm) and porphyrins (emission peak 635 nm) as listed in Table 2.2.

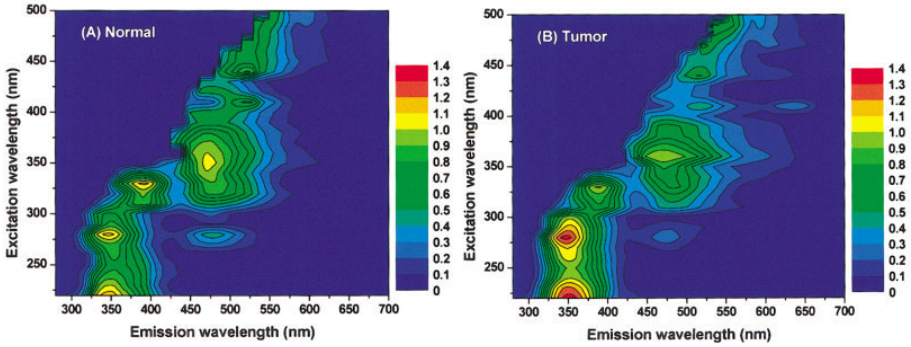

Figure 2.9: *Contour plots of the average fluorescence EEMs of (a) normal and (b) tumor bladder tissues [Zhen03].*

2.2.2 Exogenous fluorochromes

The use of fluorescence imaging and spectroscopy for *in vivo* and *ex vivo* characterization of biological materials has been well established for several decades, based on the specific localization of administered fluorescent molecules (fluorophores) in tissue or cell structures. Techniques frequently used clinically include fluorescein angiography to image the retinal vasculature and for guidance of surgical resections. Most exogenously administered fluorochromes currently being investigated for endoscopic oncologic applications have been developed primarily as photosensitizers (PS) for the photodynamic therapy (PDT). Therefore, most compounds have been designed with specific PDT characteristics, such as strong absorption at longer red wavelengths (and thus high penetration depth) and high triplet state quantum yield. These properties are not relevant for fluorescence detection. Furthermore, the selectivity of these PS has been rather poor for detection of pre-neoplastic and early cancerous lesions. Consequently, over the last years, one has designed exogenous fluorochromes with better targeting strategies, since they can be characterized *in vitro* regarding their photophysical and pharmacokinetics properties.

The fluorescence originating from an exogenous fluorophore has often a higher intensity than autofluorescence. This results in a simpler instrumentation (*e.g.* no need of image intensifier) and thus reduces the manufacturing costs. In contrast, the use of exogenous fluorochromes for detection raises concerns about safety and toxicity, whereas the time delay between administration and light delivery, defined as *drug-time interval*, has to be optimized, since the fluorescence brightness and contrasts often do not peak at the same time in different tissues.

Some existing non- or weakly phototoxic drugs are already available clinically. Fluorescein (FITC) and Indocyanine Green (ICG) have well-known applications in ophthalmology, but also explorative results in endoscopy [Kimu08]. Specifically, fluorescein (often coupled to dextran, FITC-dextran) has been reported to be suitable for tumor imaging [Brag93], but this seems unlikely because it is highly water soluble and very rapidly cleared in vivo. On the other

hand, coupling of fluorescein to a monoclonal antibody makes it quite useful for fluorescence diagnostics [Foll92] and the same may be true for ICG and similar compounds [Ball97].

2.2.2.1 PpIX : build-up and spectroscopy

Under certain circumstances, a non-fluorescing exogenous substance, that will be *activated* inside the cancerous tissue with the help of a biochemical modification, is used as a *precursor* of a fluorescing photosensitizer. In this case, one speaks of *exogenously induced* fluorescence. Aminolevulinic acid (ALA) derivatives belong to this category, since they are not fluorescent in themselves, but they are part of the biosynthetic pathway of heme as shown in Figure 2.10. In this biochemical reaction chain, the protoporphyrin IX (PpIX) is fluorescing. PpIX belong to the group of porphyrins which play an important role in the formation of key macromolecules like hemoglobin, myoglobin,and cytochromes. The PpIX precursor is delta- or 5-aminolevulinic acid (5-ALA) or one of its derivatives. Certain types of cells have a large capacity to synthesize PpIX when exposed to an adequate concentration of exogenous ALA. The systemic administration of an adequate dose of ALA to experimental animals leads to the development of strong PpIX fluorescence in certain tissues but not in others [Kenn92, Kenn90]. In particular, it was observed by fluorescence microscopy, that skin, bladder, and uterus showed strong fluorescence in the epidermis, endometrium, and urothelium without significant fluorescence in the dermis, the elastic cartilage of the ear, the myometrium, or the muscles of the bladder [Diva90].

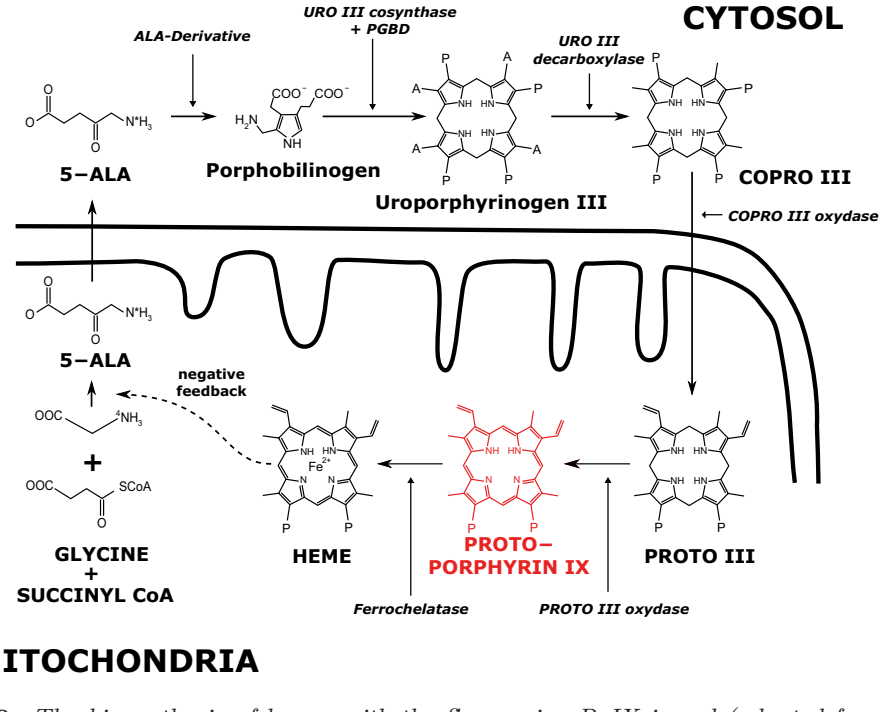

Figure 2.10: *The biosynthesis of heme, with the fluorescing PpIX in red (adapted from [Foti06]).*

Figure 2.10 shows the biosynthesis of heme. The initial step in this process is the condensation of glycine and succinyl coenzyme A (succinyl CoA) to 5-aminolevulinic acid (5-ALA) in the mitochondrion. 5-ALA production is regulated by heme in a negative feedback mechanism, i.e. the presence of heme in the cell inhibits the production of 5-ALA. The 5-ALA molecule passes into the cytoplasm where it undergoes several chemical reactions regulated by various enzymes to produce the so-called coproporphyrinogen III. The latter re-enters the mitochondrion and is

converted to protoporphyrinogen IX and finally to the PpIX. The last step is the chelation of an iron ion into the porphyrin ring, resulting in the non-fluorescent heme molecule. This chelation is enabled by the ferrochelatase. The heme molecule is then transformed into hemoglobin.

In 1951, Berlin *et al.* demonstrated that excess administration of exogenous ALA bypasses the cellular feedback control mechanism in normal organisms and leads to abnormally large quantities of protoporphyrin IX (PpIX) in humans [Berl56a, Berl56b]. Thus, the external application of 5-ALA (or one of its derivatives) can lead to a temporary accumulation of PpIX. In cancerous cells, one observes a higher accumulation of PpIX after administration of exogenous 5-ALA, because (i) the up-take of ALA is increased so that one finds ALA in excess into the cell, and (ii) the ferrochelatase activity is reduced, so that PpIX can accumulate within the cell. It results a fluorescence intensity contrast between healthy tissues and lesions, which can be used in ALA-induced PpIX fluorescence detection of dysplasia and early neoplasia.

The excitation and emission properties of PpIX are well known (see Figure 2.11), but are strongly dependent on the medium (solution, cell culture, *in vivo* organs). One excites its fluorescence between 405 nm and 632 nm (depending on the applications, i.e. desired penetration depth), resulting in a typical red emission in the 625nm-725 nm region. ALA-induced PpIX fluorescence detection has been used for various cancerous and non-cancerous conditions, including port-wine stains treatment [Li10], actinic keratosis and basal cell carcinoma [Foti06] endometriosis [Mali98, Hill00], ovarian carcinoma metastases [Löni04, Lüdi03], Barrett's esophagus [Fell03, Bran02], and bladder [Jich97].

In section 3.6.2, we will discuss in details the development of ALA-derivatives for the detection of non-muscle invasive bladder cancer. Pioneering research has been performed by our group in Lausanne in order to enhance the porphyrin production inside the cancer cells. In the next section, we will introduce some other exogenous fluorophores that have also been used for cancer photodetection.

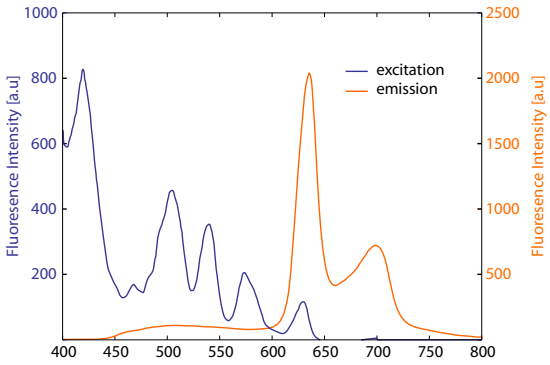

Figure 2.11: *PpIX excitation and emission spectrum with maximum at 405 nm and 632 nm, respectively.*

2.2.2.2 Various photosensitizers used in photodetection

Hematoporphyrin derivatives The accumulation of hematoporphyrin (HP) in various types of cancers was discovered and exploited during the 1950's [Peck55]. In attempting to purify commercially available HP-hydrochloride, Schwartz *et al.* found that the fraction containing impurities accumulated preferentially in tumors better than the partially purified, HP-rich material [Schw92]. This so-called *hematoporphyrin derivative* (HpD) was evaluated subsequently for localization of cancers in various organs, including the esophagus, tracheo-bronchial tree and cervix, and for characterizing suspicious head and neck lesions [Wagn98a].

The first cystoscopic observations of HpD fluorescence in urinary bladder tumors were reported by Kelly and Snell in 1976, but indicated that the fluorescence was too weak for effective direct-viewing endoscopy [Kell76]. Subsequently, Profio and Doiron [Prof77] and Kinsey *et al.* [Kins78] pioneered the development of dedicated fluorescence instrumentation using photoelectronic detectors. This, and the initial clinical and animal model studies of HpD-mediated PDT by Dougherty *et al.* [Doug78], led to fluorescence diagnostic studies by many other groups using this drug or its later commercial Photofrin (QLT Phototherapeutics, Vancouver, Canada).

Hypericin-based photodetection The botanical St. John's wort *Hypericum perforatum* is native to Europe, West Asia, and North Africa, and has been naturalized to North and South America and Australia. The Greeks and the Romans documented its medicinal use in the treatment of nerve-related disorders. St. John's wort has been used to treat a variety of conditions. Several brands are standardized for content of hypericin and hyperforin, which are among the most researched active components of St. John's wort [Lawv05].

Hypericin, a hydroxylated phenanthroperylenequinone, is widely used in photomedicine. It exhibits a high fluorescence quantum yield, and its presence in the tissue can easily be visualized. Interestingly, when instilled into the human bladder, hypericin selectively accumulates in bladder carcinoma lesions. Hence, the compound is now used as a fluorescent diagnostic tool for superficial bladder cancer [Kamu04]. However, hypericin is also a photosensitizer with a potent photocytotoxic activity. Indeed, it produces singlet oxygen efficiently upon light irradiation with a quantum yield of 0.73 [Raci88].

d'Hallewin *et al.* determined the sensitivity and specificity of detecting flat bladder CIS through fluorescent detection after intravesical hypericin instillation [D'Ha00]. Their study included 40 patients, of whom 26 presented with macroscopic visible tumor, 9 had a positive cytology without visible tumor and 5 underwent cystoscopy after bacillus Calmette-Guerin instillations (n=4) or radiotherapy (n=1). A solution of hypericin (40 ml 8 μM) was instilled intravesically for at least 2 hours. Fluorescence excitation with blue light was effective up to 16 hours after termination of the instillation. All visible papillary tumors showed red fluorescence. In addition, 134 flat fluorescent areas were detected. Analysis of 281 biopsies from flat bladder wall indicated 93% sensitivity and 98.5% specificity for detecting CIS. These data were confirmed in a larger series of 87 patients, where the sensitivity and specificity for detecting CIS were found to be 94 and 95%, respectively [D'Ha02]. In both studies, there were no signs of photobleaching of hypericin during inspection of the bladder and resection of the tumors. Inflammatory reactions resulting from radiotherapy, chemotherapy or immunotherapy did not induce fluorescence or false positive readings.

Kubin *et al.* evaluated an hypericin derivative (PVP-hypericin), and they reach a comparable sensitivity, but their specificity was markedly lower (53%) than that reported in other studies (98-100%), because no biopsies were taken from healthy tissues [Kubi08a, Kubi08b].

In comparison, both hypericin and ALA-induced PpIX show similar sensitivities for detecting CIS, but hypericin shows much higher specificity (93%). However, before a final conclusion can be reached, the data on sensitivity and specificity for hypericin should first be confirmed by multicentric trials, which presently have not been carried out [Kamu04].

2.2.3 Instrumentation aspects

2.2.3.1 Video system

CCD-sensor (charge-coupled device) is a device that moves the electrical charges from within the device to an area where the charge can be manipulated, for example conversion into a digital

value. This is achieved by "shifting" the signals between stages within the device one at a time. Technically, CCDs are implemented as shift registers that move charge between capacitive bins in the device, with the shift allowing for the transfer of charge between bins. Often the device is integrated with an image sensor, such as a photoelectric device to produce the charge that is being read, thus making the CCD a major technology for digital imaging. Although CCDs are not the only technology to allow for light detection, CCDs are widely used in professional, medical, and scientific applications where high-quality image data are required.

CMOS-sensor (complementary metal-oxide-semiconductor) is an image sensor consisting of an integrated circuit containing an array of pixel sensors, each pixel containing a photodetector and an active amplifier. CMOS-sensors solve the speed and scalability issues of the passive-pixel sensor. They consume far less power than a CCD, have less image lag, and can be fabricated on much cheaper and more available manufacturing lines. Unlike CCDs, CMOS sensors can combine the image sensor function and image processing functions within the same integrated circuit.

Historical CCD have been designed for 1-color imaging. Therefore, to reproduce color image in a video system, one used to need 3-CCD cameras, assembled within a complex setup of prisms and optical filters. With the development of mosaic filters to be placed in front of the CCD, only one CCD chip is required, and missing pixels are interpolated. First "color" CCD were equipped with primary RGB filters, whereas most of the current endoscopic cameras are equipped with complementary CMYG filters.

Image quality depends on its *resolution* and *contrast* [Muto09]. Resolution is the capacity to visualize minute patterns and is determined by the pixel number of each CCD. To enhance resolution, the number of pixels in the CCD has to be increased. However, a CCD with a higher number of pixels increases the size of the videoendoscope by expanding its outer diameter. On the other hand, if a thinner endoscope is made, the CCD must be smaller, thereby decreasing the number of pixels with a resulting reduction of image resolution. Contrast is the ratio of brightness between a pattern and its background, and can be increased by modifying spectral design or electronic amplification.

Over the years, clip-on cameras have been designed so that they remain outside of the patient. It worked perfect with the rigid endoscopes, but during flexible endoscopy, fiberoptic bundles create a honeycomb appearance. Additionally, over the time, major drawbacks and pitfalls due the nature of optical fibers (loss of transmission, breakage, ...) have encouraged the manufacturers to move towards videoendoscopy, that mounts the imaging device on the tip of the endoscope. Flexible endoscopy requires only local anesthesia, which can save costs (examination time and involved people) in the clinical routine. Nowadays, CCDs detectors are used almost exclusively, but in CMOS detectors may be implement in the future (smaller size, smaller cost, higher speed). High resolution endoscopes achieve very good image quality, that is similar or even better than rigid endoscopes. However, rigid endoscopy is still preferred for surgery, because the surgical tools (*e.g.* high-frequency resectoscope for transurethral resection of the bladder) are available only on the rigid platform yet.

2.2.3.2 Light sources, filters and spectral design

Over the last century, the world of endoscopy had a great evolution. The ability to reflect light in deeply located organs was a central problem in designing open tubes. The early version developed by Nitze used a platinum wire in a glass jacket with water-cooling. The wire was

heated and lit by a battery for illumination. Needless to say, this was a very clumsy and cumbersome approach, but it was modified after Edison's invention of the filament globe (1879). Nitze and his team were able to miniaturize the Edison-type globe to a size small enough to fit into the tip of a cystoscope.

To address the limitations of the Nitze optical system, H. Hopkins, a London physicist, devised the prototype of a new optical system in 1954 [Hopk54]. He replaced the previous lens and air-interspace optical relays using glass rods instead of interspersed air. He also cemented better lenses on both ends. Hopkins created a system that had the following distinct advantages over the Nitze system :

1. The light transmission was significantly greater, yielding a brighter image enabled the examiner to distinguish the features more easily and recognize slight changes more clearly. In general, perception was improved.

2. The viewing angle, which was small with the previous optics, was wider. Therefore, the examiner could see a larger part of the object in a single viewing field; thus, as soon as the telescope was introduced, orientation was faster.

3. The system included several improved optical parameters (*e.g.* natural color reproduction, image quality at the edge, higher resolution).

4. The system was smaller in diameter, resulting in easier and safer introduction. With further miniaturization, it was possible to produce telescopes measuring 2-3 mm in diameter, including fiber light transmission. This improvement opened up a new chapter in pediatric endoscopy.

5. Thanks to the brighter image and increased light transmission, the examiners were able to document their findings by attaching 35-mm still cameras, and, later on, video systems.

Nowadays, one often uses high-pressure xenon or mercury short arc lamp as an external light source, which is connected to the endoscope via a flexible light cable. The first prototype using light-emitting diodes (LEDs) are now commercialized. That will allow the manufacturers to design stand-alone wireless endoscope, since any fluid light cable won't be required anymore.

Spectral design In this thesis, we used several commercial devices as light source for the endoscopic fluorescence imaging. Figure 2.12 shows the excitation spectra of the systems measured at the distal end of the light cable with a portable spectrometer (USB2000, Ocean Optics, Duiven, NL) :

1. DAFE (Diagnostic Autofluorescence Endoscopy, Richard Wolf GmbH) for pneumology

2. Combilight system (Photodynamic Diagnostic, Richard Wolf GmbH) for urology

3. D-Light system (Photodynamic Diagnostic, Karl Storz GmbH), which has a larger excitation spectrum to overlap with the long-pass filter in the blue spectral region, to allow blue backscattered background for urology.

Both systems (Storz and Wolf) do have a yellow long-pass (LP) in the detection path to reject the excitation light. This allows collecting autofluorescence in the bronchi and porphyrins fluorescence in the urinary bladder. The LP filter (cut-on wavelength 450nm) is integrated either in the endoscope (Storz) or directly into the camera objective (Wolf).

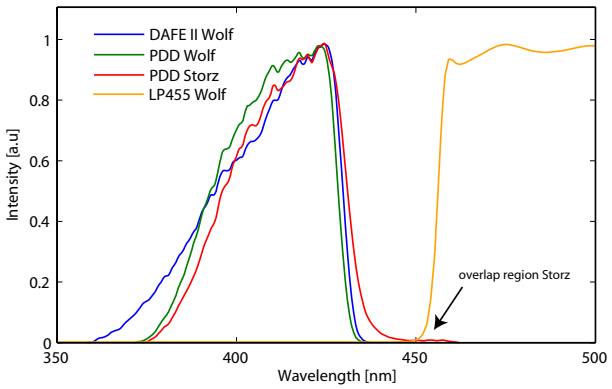

Figure 2.12: *Excitation spectra of the DAFE, PDD and Storz systems normalized at their maximum.*

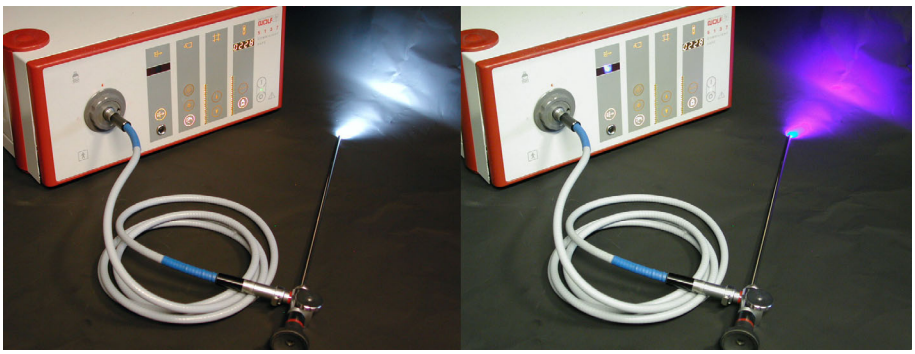

Figure 2.13: *The commercial version of the Xenon light source delivering white/blue light for endoscopic examination*

2.3 High magnification technical concepts and state-of-the-art

Magnification endoscopes have high zooming capability (allowing small areas to be magnified), whereas high resolution endoscopes have a high pixel density (allowing small details to be visualized in the overview image). A non-exhaustive literature review is presented in Table 2.3 in different organs.

In large GI endoscopes, an optical zooming setup located in the tip of scope (typically a motor driven movable lens) allows high magnification examination. By controlling the focal distance, the scope can move very close to the mucosal surface providing the magnified image [Brun03]. In smaller devices (*e.g.* bronchoscope), due to space limitations, one cannot implement an active zooming setup. One solution that was implemented was the combination of two optical systems in the same device : (i) a video observation system for high magnification observation, and (ii) a fiber observation system for orientation of the endoscope tip within the organ [Yama07].

One of the most promising aspects of the use of high-resolution endoscopes lies in their superior ability to discriminate details in the non-magnified overview image. New generation video endoscopes are equipped with CCD-chips of more than 850 Kpixels and can distinguish points that are several tens of μm apart (as compared to about 150 μm for the naked eye) [Brun03].

Several applications of high magnification endoscopy in gastroenteroscopy and colonoscopy are nowadays well implemented, making use of the newly observable features that can be visualized with these new scopes: pit patterns, neo-vessels morphology, and nuclear morphometry. Sugano *et al.* have diagnosed gastric cancer and inflammatory changes in ulcerative colitis [Suga04, Suga06]. Fortun *et al.* have studied diagnostic improvement of Barrett's esophagus with this particular technique [Fort06].

In bronchoscopic studies, Shibuya *et al.* stated that conventional white light bronchovideoscopy observe only increased redness and local swelling, while high magnification bronchovideoscopes enable visualization of the vascular network [Shib02, Shib03]. Observing increased vessel growth and complex networks of tortuous vessels of various sizes, these authors were able to discriminate between inflammatory reactions and angiogenic squamous dysplasia (ASD) in the bronchi. Indeed, they observed the complex neo-vessels structure and tortuosity in the bronchial mucosa (magnification of up to 110×), visualizing dotted vessels (size 25–53 μm), in full agreement with capillary blood vessel diameters in ASD as observed during histopathology analysis (size 35–62.5 μm).

Yamada *et al.* developed a dual-channel bronchoscope. This flexible bronchovideoscope is equipped with a prism at the distal end, allowing the images of the bronchial mucosa to be captured by the CCD through a magnifying objective lens. The bronchial mucosa were visualized with a magnification power of 55–110 × according to the distance between the objective lens and the bronchial surface. The view angle was 40°, but little distortion is seen. In addition, a forward-viewing optical fiberscope was attached to act as a guide. By using this front-viewing system, we confirmed the orientation and approached the endobronchial destinations while obtaining a high-magnification view [Yama05].

In the lower GI tract, Oba and co-workers characterized the colorectal tumors using narrow-band imaging magnification, combining diagnosis with both pit pattern and microvessel features [Oba10].

2.4 Confocal endoscopy

Over the last years, several groups attempted to transfer the on-bench microscope into a dedicated clinical micro-endoscope to assess histopathological status *in vivo* with either reflectance

Author	Year	Organ	Endoscope	Magnification	Remarks
Warnecke et al. [Warn10]	2010	Larynx	Storz contact endoscopes	60× and 150×	Observation also with methylene blue.
Galli et al. [Gall07]	2007	Larynx	Pentax+Fujinon 850kPixels	2× elec zoom	DOF 8-100mm (wide) and 4-7mm (narrow)
Yamada et al. [Yama07]	2007	Broncho	XBF-200HM5 Olympus NBI	100× optical	Calculation of vessel parameters
Yamada et al. [Yama06]	2006	Broncho	XBF-200HM3 Olympus NBI	100× optical	Microvessels 800 μmbelow epithelial surface
Shibuya et al. [Shib03]	2003	Broncho	XBF-200HM2		Vessel diameter 35–50 μm
Tanaka et al. [Tana03]	2003	Broncho	XBF 200HM3	105×	focal distance <1mm. vessel area density, vessel length density
Shibuya et al [Shib03]	2002	Broncho	XBF-200HM2	110×	Observation of capillary vessels.
Oba et al. [Oba10]	2010	Lower GI	CF-H260AZI Olympus	80×	pit patterns and microvessel features
Cammarota et al. [Camm08]	2008	Upper GI	FICE 850kPixels	100× opt. 2× elect.	R/G/B set
Gono et al. [Gono04]	2004	Upper GI	GIF-Q240Z, Olympus.	80× optical	
Katayama et al. [Kata00]	2000	Lower GI	TCE-3680MH, Toshiba	elect. 1.5–2×	25×@3mm,60×@2mm

Table 2.3: *Magnification endoscopes dedicated to early cancer detection.*

images or fluorescence images.

2.4.1 Motivation and technology

The *endo-cytoscopy* was suggested by observations made using the contact endoscope (Karl Storz GmbH). In the 1980s, Hamou *et al.* reported observations of the surface of the genital tract under high magnification using a microhysteroscope [Hamo81, Hamo83, Hamo84]. Since then, several studies involving *in vitro* and *in vivo* magnified observations by contact endoscopy have been reported in the field of otorhinolaryngology. These studies used methylene blue to stain the surface epithelium during observation, and succeeded in making cells on the surface epithelium visible [Andr95a, Andr95b]. However, the contact endoscope used in these studies was a rigid endoscope, which precluded observations of most organs (*e.g.* GI tract).

Therefore, a new *flexible* endo-cytoscopy system, which could be inserted into the digestive tract, was developed by Olympus Inc. This system consisted of two flexible endoscopes : (i) the low-magnification type (XEC300, 380 cm long, 3.2 mm in diameter) provided 450× magnification and a field of view (FOV) of 300×300 μm, (ii) the high-magnification type (XEC120) that provided 1125× magnification and a FOV of 120×120 μm. These flexible probes could be passed through the instrument channel of the Olympus gastroscope (GIF1T-240). For magnified observation, vital staining, such as with methylene blue or toluidine blue, was necessary. The most evident feature of the observation using this system is the real-time diagnosis of abnormalities of the cell nuclei [Kuma06]. Sasajima *et al.* also performed real-time virtual histology of colorectal lesions using vital staining [Sasa06].

Confocal *microendoscopes* provide high resolution cellular imaging *in vivo* in a relatively small package. This minimally invasive technique provides instant visualization of tissue and allows pathologists to make a diagnosis *in situ* without having to use traditional biopsy methods [Makh08]. Therefore, this technology has often been named *optical biopsy*, since it replaces the conventional tissue sampling. Confocal microendoscopy can be performed in reflectance or fluorescence modes [Flus05], and has been used for the detection and diagnosis of diseases in a broad variety of organs such as cervix [Sung02, Carl05], colon [Kies04b], oral cavity [Thon07], lung [Thib07, Thib09b], esophagus [Goet06], bladder [Sonn09a], and ovary [Brew04].

Two companies are currently on the market with a microendoscopic confocal device [Dunb08]:

Optiscan Pty Ltd. licenses its tip-integrated confocal laser endomicroscope to Pentax Corp., so that the confocal probe is fully integrated into an endoscope. Optiscan miniaturized the microscope and integrates the whole xy-scanning device at the distal tip of the endoscope, which contains a rigid part of 5 cm at the distal tip. Images have a lateral resolution of 0.7 μm and an axial resolution of 7 μm within a field of view of 475×475 μm. The setup only achieves a slow speed (0.7 frame/sec). The excitation light (488-nm laser) is coupled into a single optical fiber that acts as both a point source and a point detection pinhole for confocal imaging. z-sectioning can be achieved by rotating a knob on the handle, which moves the entire scanning mechanism (including both magnetic coils and the tuning fork) axially along the tube. This provides a mechanical range of almost 300 μm below the surface [Thon07]. For optimum image contrast, the laser power can be adjusted between 0 to 1000 mW at the distal tip of the probe in contact with the tissue.

MaunaKea Technologies Inc. licenses its flexible fiber-based confocal miniprobe to Leica for the small animal applications, and market it on its own for human clinical applications. The Cellvizio® probe is inserted into the working channel of any standard endoscope

and is thus not device-dependent. The ultrafast xy-scanning device is located outside the patient within the laser light source (488nm or 660 nm). A coherent multi-core fiber (30'000 cores) is scanned with the laser device and collects the fluorescence image back from the tissue [Laem04]. The software associated with the probe is providing rapid image capture and *stitching* of adjacent images to create an image mosaic in real-time. Three mini-probes are available with different imaging depth, field of view, and lateral resolution. A quasi video rate (12 frames/s) is achieved with a lateral resolution depending on the probe (1-3.5 μm). The imaging depth (0-120 μm), as well as the field of view (130×130 μm- 600×600 μm), can be obtained thanks to a set of flexible optical microprobes whose diameters vary from 0.16 to 1.5 mm, but no z-sectioning is possible yet [Verc08].

Bhuvaneswari *et al.* used the last generation of the Optiscan probe to acquire *in vivo* fluorescence microscopic imaging of tumor blood vessels [Bhuv10]. The images were acquired 30 min. after intravenous administration of FITC dextran. The new Optiscan FIVE 1 system features the same basic design with improved specifications. They demonstrated that by using laser confocal endomicroscopy, responses to antiangiogenic therapies can be evaluated successfully by *in vivo* imaging of tumor vasculature.

An interesting clinical study was recently reported by Thiberville *et al.* who imaged bronchial wall microstructure using a fibered confocal fluorescence microscope [Thib07]. They used the Cellvizio® optical microprobe to image the autofluorescence up to the alveoli [Thib09a]. They observed specific basement membrane alterations associated with premalignant bronchial lesions *in vivo*. The technique may also be useful to study the bronchial wall remodeling in nonmalignant chronic bronchial diseases (e.g fibrosis).

Sonn *et al.* used the same device in the urinary bladder [Sonn09a, Sonn09b]. After standard cystoscopy, fluorescein was administered intravesically and/or intravenously as a contrast dye. A 2.6 mm probe based confocal laser endomicroscope was passed through a 26 Fr resectoscope to image normal and abnormal appearing areas. The endomicroscopic images were compared with standard hematoxylin and eosin (H&E) analysis of transurethral resection of bladder tumor specimens. Endomicroscopic images demonstrated clear differences between normal mucosa, and low and high grade tumors. In normal urothelium larger umbrella cells are seen most superficially followed by smaller intermediate cells and the less cellular lamina propria (as to be seen in Figure 2.14 adapted from [Sonn09a]). In contrast, low grade papillary tumors demonstrate densely arranged but normal-shaped small cells extending outward from fibrovascular cores. High grade tumors show markedly irregular architecture and cellular pleomorphism.

2.4.2 Limitations of current confocal endoscopy

This MaunaKea approach suffers several limitations. The shape of an object is a morphological quantification. However, images in the field of view, smaller than the pixel resolution of the microprobe can only be viewed as accurately as this resolution permits. In terms of intensity, the signal is directly proportional to the amount of light detected (if below the detector saturation limit). If the detector is saturated, the linear relationship is not valid anymore. In terms of temporal analysis, since the frame rate is fixed, the time elapsed between two frames is constant. Thus the absolute acquisition time is indelibly associated with each frame.

In addition, image acquisition is extremely sensitive to motion introduced by the subject (ie diaphragmatic motion or arterial pulsation) or the operator. Also, the used probe (2.6 mm size) necessitates the use of a 26 Fr rigid resectoscope instead of a flexible cystoscope. The rigid cystoscope offers less options to manipulate the probe tip. Therefore, the required perpendicular contact with the tissue is impossible in cases where the area of interest resides on the anterior

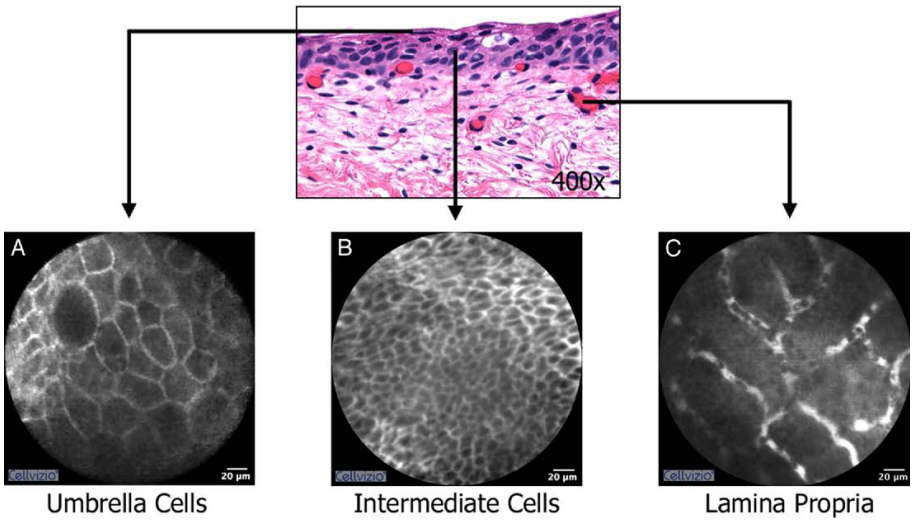

Figure 2.14: *Comparison of H&E and confocal endomicroscopic images of normal human bladder mucosa with fluorescein staining [A] large, polygonal superficial cells consistent with umbrella cells [B] smaller, deeper urothelial cells consistent with intermediate cells [C] less cellular lamina propria containing blood vessels filled with erythrocytes adapted from [Sonn09a].*

bladder wall. Accordingly due to their location in the bladder some tumors could not be imaged. In addition, given the 2.6 mm probe tip size with a 240 μm field of view and the requirement for direct contact with the urothelium, imaging the entire bladder is not practical. Rather the proposed role of confocal laser endomicroscopy is to provide real-time histology of areas highlighted by white light cystoscopy or other imaging modalities such as fluorescence cystoscopy.

Two potential drawbacks explain why the Pentax system is not yet available for the respiratory and urinary tract imaging. First, because of the added sizes of the distal scan head, working channel, conventional light guide, and CCD camera, the diameter of the distal tip of the endoscope is currently larger than 12 mm. With this size, the exploration of the human trachea and large main bronchi (resp. urethra and bladder) is hardly possible. Second, the miniaturization of the distal scan head results in scanning rates of 1 frame/second, which needs a very efficient stabilization system of the distal tip of the endoscope onto the mucosae, to produce crisp microscopic images of the epithelium.

Both devices are working in fluorescence mode, and requires an exogenous contrast agent to acquire images (*e.g.* intravenous injection of fluorescein). Indeed, they are still unable to detect the autofluorescence of most tissues. Several experiments reported that only the very high level of autofluorescence in hair and adipose tissue has been detected. Therefore, the current Cellvizio® cannot be used for detection and imaging of autofluorescence. On the other hand, the autofluorescence of the tissue does not interfere with the imaging of specific targeting of cells by the fluorophores.

Even if fluorescein is widely used in ophthalmology, its clinical usage is not fully harmless. Severe allergic reactions to this dye are extremely rare, but occasional deaths have been reported (1/220'000). Anaphylactic shocks occur in 1/350 patients. Users of Pentax system reported an injection of 10 ml fluorescein (10%), whereas the Cellvizio®'s users reported an injection of 5 ml fluorescein (1%), which corresponds to a 50× lower dose[2].

Additionally, the confocal cystoscopy may have to be limited in time because approximately 10 minutes after i.v. administration, fluorescein is excreted into the bladder, potentially inter-

[2]More information is available on the web `www.optiscan.com` and `www.maunakeatech.com`

fering with cystoscopic visualization.

In contrast to most other hollow organs, the bladder offers a direct route for topical administration of medications. Sonn *et al.* demonstrates that intravesical fluorescein instillation adequately provides cellular resolution and micro-architecture comparable to intravenous administration [Sonn09a]. These authors also reported that quality does deteriorate after approximately 15 minutes likely due to repeated bladder irrigation. However, intravesical fluorescein instillation may be repeated if necessary. Finally fluorescein does not permit visualization of cell nuclei as noted in similar studies in the GI tract [Kies04b].

2.5 Statistical calculation for cancer detection

At this point, one should define some concepts to quantify the performance of a new diagnosis method. One usually refers to the result of an unknown test as compared to the result of a known reference. In this context, the reference is determined by a *gold standard*, which is defined in medicine as "a relatively irrefutable standard that constitutes recognized and accepted evidence that a certain disease exists" [Fouc97]. In cancer diagnosis, the gold standard is histopathology and cellular pathology. However, the objectivity and inerrability of histopathologic diagnosis, especially for early neoplastic pathologies, has been discussed in several scientific reports and reviews [Rams99, Jenk01, Cros98, Farm96].

		Gold standard	
		Positive	Negative
Test	Positive	**True Positive TP**	**False Positive FP** *Type I error*, α
	Negative	**False Negative FN** *Type II error*, β	**True Negative TN**
		↓ Sensitivity	↓ Specificity

→ Positive predictive value

→ Negative predictive value

Table 2.4: ***Test vs. Gold standard.*** *In endoscopic cancer detection, it corresponds to endoscopic appearance vs. histopathology result [Altm94].*

If the test and the reference agree on a positive or negative value, it is said to be a *true positive* (TP) or a *true negative* (TN), respectively. If the test is positive and the reference is negative, this is referred to a *false positive* (FP) result. Conversely, if the test is negative and the reference is positive, this is called a *false negative* (FN) result. A summary of these values is shown in Table 2.4.

The performance of a method is described by its *sensitivity*, its *specificity*, its *positive predictive value* (PPV), and its *negative predictive value* (NPV), generally expressed in percentage [%]. These numbers are defined in Table 2.5.

Statisticians speak of two significant sorts of statistical error. *Type I error* α occurs observing a difference when in truth there is none, thus indicating a test of poor specificity. An example of this would be if a test shows that a woman is pregnant when in reality she is not. Type I error can be viewed as the error of excessive credulity. *Type II error* β occurs when failing to observe a difference when in truth there is one, thus indicating a test of poor sensitivity. An example of this would be if a test shows that a woman is not pregnant, when in reality, she is. Type II error can be viewed as the error of excessive skepticism. Table 2.6 defines these quantities.

In many studies, one has to be cautious with the given sensitivity and specificity, because the number of true negative and false negative results are difficult to assess correctly. Indeed, the determination of these parameters would require extensive sampling from putative healthy tissues.

Sensitivity	Probability that an individual with the disease is screened positive.	$\frac{TP}{FN+TP}$
Specificity	Probability that an individual without the disease is screened negative.	$\frac{TN}{TN+FP}$
Positive Predictive Value (PPV)	Probability that an individual with a positive screening result has the disease.	$\frac{TP}{TP+FP}$
Negative Predictive Value (NPV)	Probability that an individual with a negative screening result does not have the disease.	$\frac{TN}{TN+TP}$

Table 2.5: *Main parameters that describe the quality of a detection and diagnostic method [Rama00].*

False positive rate (Type I error)	1 - specificity	$\alpha = \frac{FP}{FP+TN}$
False negative rate (Type II error)	1 - sensitivity	$\beta = \frac{FN}{TP+FN}$
Power	sensitivity	1 - $\beta = \frac{TP}{TP+FN}$
Likelihood-ratio positive LR+	sensitivity / (1 - specificity)	$\frac{TP}{FP+TP} \cdot \frac{TN+FP}{FP}$
Likelihood-ratio negative LR-	(1 - sensitivity) / specificity	$\frac{TN}{TN+FP} \cdot \frac{FN+TP}{FN}$

Table 2.6: *Error calculation and other related statistical values.*

In case of cancer detection, we need to take biopsies to analyze the tissue with histopathology and this procedure is considered to be invasive and not harmless for the patient. Therefore, biopsy sampling on healthy tissues is often not defendable for medical and ethical reasons. Consequently, one often prefers to speak of *relative* sensitivity and specificity when comparing two concurrent methods.

The *odds ratio* (OR) is the ratio of the odds of an event occurring in one group to the odds of it occurring in another group. The term is also used to refer to sample-based estimates of this ratio. These groups might be men and women, an experimental group and a control group, or any other dichotomous classification. If the probabilities of the event in each of the groups are p_1 (first group) and p_2 (second group), then the odds ratio is:

$$\frac{p_1/(1-p_1)}{p_2/(1-p_2)} = \frac{p_1/q_1}{p_2/q_2} = \frac{p_1 q_2}{p_2 q_1} \text{ where } q_x = 1 - p_x$$

An OR of 1 indicates that the condition or event under study is equally likely to occur in both groups. An OR greater than 1 indicates that the condition or event is more likely to occur in the first group, and an OR less than 1 indicates that the condition or event is less likely to occur in the first group.

To quantify statistical tests, one needs some more definitions. The *pre-test probability* (or population prevalence) is defined as $p_1 = (TP + FN)/(TP + TN + FP + FN)$, related to the *pre-test odds* $PrTO = p_1/(1 - p_1)$. The *post-test odds* are defined $p_2 = PrTO * LR$, related to the *post-test probability* $PoTP = p_2/(p_2 + 1)$.

Bibliography

[Alfa84] R. R. Alfano, D. B. Tata, J. Cordero, Tomashefsky, F. W. Philip, Longo, and M. A. Alfano. Laser induced fluorescence spectroscopy from native cancerous and normal tissue. *IEEE Journal of Quantum Electronics*, QE-20(12):1507–1511, 1984.

[Alfa91] R. R. Alfano, B. B. Das, J. Cleary, R. Prudente, and E. J. Celmer. Light sheds light on cancer–distinguishing malignant tumors from benign tissues and tumors. *Bull N Y Acad Med*, 67(2):143–150, 1991.

[Altm94] D. G. Altman and J. M. Bland. Diagnostic tests 2: Predictive values. *BMJ*, 309(6947):102, Jul 1994.

[Aman05] Y. Amano. Chromoendoscopic diagnosis of barrett's esophagus. *Nippon Rinsho*, 63(8):1416–1419, Aug 2005.

[Andr95a] M. Andrea, O. Dias, and A. Santos. Contact endoscopy during microlaryngeal surgery: a new technique for endoscopic examination of the larynx. *Ann Otol Rhinol Laryngol*, 104(5):333–339, May 1995.

[Andr95b] M. Andrea, O. Dias, and A. Santos. Contact endoscopy of the vocal cord: normal and pathological patterns. *Acta Otolaryngol*, 115(2):314–316, Mar 1995.

[Anid96] M. Anidjar, D. Ettori, O. Cussenot, P. Meria, F. Desgrandchamps, A. Cortesse, P. Teillac, A. L. Duc, and S. Avrillier. Laser induced autofluorescence diagnosis of bladder tumors: dependence on the excitation wavelength. *J Urol*, 156(5):1590–1596, Nov 1996.

[Anid98] M. Anidjar, O. Cussenot, S. Avrillier, D. Ettori, P. Teillac, and A. Le Duc. The role of laser-induced autofluorescence spectroscopy in bladder tumor detection. dependence on the excitation wavelength. *Annals of the New York Academy of Sciences*, 838:130–42, 1998.

[Anth89] D. J. Anthony, A. E. Profio, and O. J. Balchum. Fluorescence spectra in lung with porphyrin injection. *Photochem Photobiol*, 49(5):583–586, May 1989.

[B.-H08] G. Bourg-Heckly, L. Thiberville, C. Vever-Bizet, and B. Viellerobe. In vivo endoscopic autofluorescence microspectro-imaging of bronchi and alveoli. In *Proceedings of SPIE - The International Society for Optical Engineering*, volume 6851, 2008.

[Ball97] B. Ballou, G. W. Fisher, T. R. Hakala, and D. L. Farkas. Tumor detection and visualization using cyanine fluorochrome-labeled antibodies. *Biotechnol Prog*, 13(5):649–658, 1997.

[Bard05] M. P. L. Bard, A. Amelink, M. Skurichina, M. den Bakker, S. A. Burgers, J. P. van Meerbeeck, R. P. W. Duin, J. G. J. V. Aerts, H. C. Hoogsteden, and H. J. C. M. Sterenborg. Improving the specificity of fluorescence bronchoscopy for the analysis of neoplastic lesions of the bronchial tree by combination with optical spectroscopy: preliminary communication. *Lung Cancer*, 47(1):41–47, 2005.

[Bard06] M. P. L. Bard, A. Amelink, M. Skurichina, V. N. Hegt, R. P. W. Duin, H. J. C. M. Sterenborg, H. C. Hoogsteden, and J. G. J. V. Aerts. Optical spectroscopy for the classification of malignant lesions of the bronchial tree. *Chest*, 129(4):995–1001, Apr 2006.

[Berl56a] N. I. Berlin, A. Neuberger, and J. J. Scott. The metabolism of delta-aminolaevulic acid. 1. normal pathways, studied with the aid of 15n. *Biochem J*, 64(1):80–90, Sep 1956.

[Berl56b] N. I. Berlin, A. Neuberger, and J. J. Scott. The metabolism of delta-aminolaevulic acid. 2. normal pathways, studied with the aid of 14c. *Biochem J*, 64(1):90–100, Sep 1956.

[Bhuv10] R. Bhuvaneswari, P. S. P. Thong, Y.-Y. Gan, K. Soo, and M. Olivo. Evaluation of hypericin-mediated photodynamic therapy in combination with angiogenesis inhibitor bevacizumab using in vivo fluorescence confocal endomicroscopy. *J Biomed Opt*, 15(1):011114, 2010.

[Boul86] J.-L. Boulnois. Photophysical processes in recent medical laser developments: A review. *Lasers in Medical Science*, 1(1):47–66, 1986.

[Brag93] O. V. Braginskaja, V. V. Lazarev, I. N. Pershina, K. V. Petrov, L. B. Rubin, and O. V. Tikhonova. Sodium fluorescein accumulation in cultured cells. *Gen Physiol Biophys*, 12(5):453–464, Oct 1993.

[Bran02] S. Brand, T. D. Wang, K. T. Schomacker, J. M. Poneros, G. Y. Lauwers, C. C. Compton, M. C. Pedrosa, and N. S. Nishioka. Detection of high-grade dysplasia in barrett's esophagus by spectroscopy measurement of 5-aminolevulinic acid-induced protoporphyrin ix fluorescence. *Gastrointestinal endoscopy*, 56(4):479–487, 2002.

[Brew02] M. Brewer, U. Utzinger, Y. Li, E. N. Atkinson, W. Satterfield, N. Auersperg, R. Richards-Kortum, M. Follen, and R. Bast. Fluorescence spectroscopy as a biomarker in a cell culture and in a nonhuman primate model for ovarian cancer chemopreventive agents. *J Biomed Opt*, 7(1):20–26, Jan 2002.

[Brew04] M. A. Brewer, U. Utzinger, J. K. Barton, J. B. Hoying, N. D. Kirkpatrick, W. R. Brands, J. R. Davis, K. Hunt, S. J. Stevens, and A. F. Gmitro. Imaging of the ovary. *Technol Cancer Res Treat*, 3(6):617–627, Dec 2004.

[Brun03] M. J. Bruno. Magnification endoscopy, high resolution endoscopy, and chromoscopy; towards a better optical diagnosis. *Gut*, 52 Suppl 4:iv7–i11, Jun 2003.

[Brya07] R. T. Bryan, L. J. Billingham, and D. M. A. Wallace. Narrow-band imaging flexible cystoscopy in the detection of recurrent urothelial cancer of the bladder. *BJU Int*, 101(6):702–5; discussion 705–6, Mar 2007.

[Camm08] G. Cammarota, P. Cesaro, A. Cazzato, P. Fedeli, L. Sparano, F. M. Vecchio, L. M. Larocca, and G. Gasbarrini. Optimal band imaging system: a new tool for enhancing the duodenal villous pattern in celiac disease. *Gastrointest Endosc*, 68(2):352–357, Aug 2008.

[Carl05] K. Carlson, M. Chidley, K.-B. Sung, M. Descour, A. Gillenwater, M. Follen, and R. Richards-Kortum. In vivo fiber-optic confocal reflectance microscope with an injection-molded plastic miniature objective lens. *Appl Opt*, 44(10):1792–1797, Apr 2005.

[Caub09] E. C. C. Cauberg, D. M. de Bruin, D. J. Faber, T. G. van Leeuwen, J. J. M. C. H. de la Rosette, and T. M. de Reijke. A new generation of optical diagnostics for bladder cancer: technology, diagnostic accuracy, and future applications. *Eur Urol*, 56(2):287–296, Aug 2009.

[Crea95] T. A. Creagh, M. Gleeson, D. Travis, R. Grainger, T. E. McDermott, and M. R. Butler. Is there a role for in vivo methylene blue staining in the prediction of bladder tumour recurrence? *Br J Urol*, 75(4):477–479, Apr 1995.

[Cros98] S. Cross. Grading and scoring in histopathology. *Histopath*, 33:99–106, 1998.

[Curv08] W. Curvers, L. Baak, R. Kiesslich, A. V. Oijen, T. Rabenstein, K. Ragunath, J.-F. Rey, P. Scholten, U. Seitz, F. T. Kate, P. Fockens, and J. Bergman. Chromoendoscopy and narrow-band imaging compared with high-resolution magnification endoscopy in barrett's esophagus. *Gastroenterology*, 134(3):670–679, Mar 2008.

[DaCo05] R. DaCosta, B. Wilson, and N. Marcon. Optical techniques for the endoscopic detection of dysplastic colonic lesions. *Current Opinion in Gastroenterology*, 21(1):70–79, 2005.

[D'Ha00] M. A. D'Hallewin, P. A. D. Witte, E. Waelkens, W. Merlevede, and L. Baert. Fluorescence detection of flat bladder carcinoma in situ after intravesical instillation of hypericin. *J Urol*, 164(2):349–351, Aug 2000.

[D'Ha02] M.-A. D'Hallewin, A. R. Kamuhabwa, T. Roskams, P. A. M. D. Witte, and L. Baert. Hypericin-based fluorescence diagnosis of bladder carcinoma. *BJU Int*, 89(7):760–763, May 2002.

[Diva90] D. X. Divaris, J. C. Kennedy, and R. H. Pottier. Phototoxic damage to sebaceous glands and hair follicles of mice after systemic administration of 5-aminolevulinic acid correlates with localized protoporphyrin ix fluorescence. *Am J Pathol*, 136(4):891–897, Apr 1990.

[Doug78] T. J. Dougherty, J. E. Kaufman, A. Goldfarb, K. R. Weishaupt, D. Boyle, and A. Mittleman. Photoradiation therapy for the treatment of malignant tumors. *Cancer Res*, 38(8):2628–35, 1978.

[Du98] H. Du, R. A. Fuh, J. Li, A. Corkan, and J. S. Lindsey. Photochemcad: A computer-aided design and research tool in photochemistry. *Photochem Photobiol*, 68:141–42, 1998.

[Dunb08] K. Dunbar and M. Canto. Confocal endomicroscopy. *Curr Opin Gastroenterol*, 24(5):631–637, Sep 2008.

[Eise04] G. M. Eisen. Chromoendoscopy of the colon. *Gastrointest Endosc Clin N Am*, 14(3):453–60, vii, Jul 2004.

[Endo72] M. Endo, N. Sakakibara, and H. Suzuki. Observation of esophageal lesions with the use of endoscopic dyes. *Progress of Digestive Endoscopy*, 1:34, 1972.

[Endo10] F. Endo, Y. Shiga, M. Yashi, K. Hattori, and O. Muraishi. Office-based transurethral resection of multiple bladder tumors using blue dye-mixed local anesthesia: a descriptive cohort study. *J Endourol*, 24(2):267–270, Feb 2010.

[Eyre84] D. R. Eyre, M. A. Paz, and P. M. Gallop. Cross-linking in collagen and elastin. *Annu Rev Biochem*, 53:717–748, 1984.

[Farm96] E. Farmer, R. Gonin, and M. Hanna. Discordance in the histopathologic diagnosis of melanoma and melanocytic nevi between expert pathologists. *Human Pathology*, pages 528–531, 1996.

[Fell03] C. Felley, P. Jornod, G. Dorta, T. Stepinac, N. Lange, T. Gabrecht, H. Van Den Bergh, G. Wagnières, C. Fontolliet, P. Grosjean, P. Monnier, and G. VanMelle. Endoscopic fluorescence detection of intraepithelial neoplasia in barrett's esophagus after oral administration of aminolevulinic acid. *Endoscopy*, 35(8):663–668, 2003.

[Flus05] B. A. Flusberg, E. D. Cocker, W. Piyawattanametha, J. C. Jung, E. L. M. Cheung, and M. J. Schnitzer. Fiber-optic fluorescence imaging. *Nat Methods*, 2(12):941–950, Dec 2005.

[Foll92] S. Folli, G. Wagnières, A. Pélegrin, J.-M. Calmes, D. Braichotte, F. Buchegger, Y. Chalandon, N. Hardman, C. Heusser, J.-C. Givel, G. Chapuis, A. Châtelain, H. E. van den Bergh, and J.-P. Mach. Immunophotodiagnosis of colon carcinomas in patients injected with fluoresceinated chimeric antibodies against carcinoembryonic antigen. *Proc Natl Acad Sci USA*, 89:7973–7977, 1992.

[Fort06] P. J. Fortun, G. K. Anagnostopoulos, P. Kaye, M. James, S. Foley, S. Samuel, A. Shonde, R. Badreldin, E. Campbell, C. J. Hawkey, and K. Ragunath. Acetic acid-enhanced magnification endoscopy in the diagnosis of specialized intestinal metaplasia, dysplasia and early cancer in barrett's oesophagus. *Alimentary Pharmacology and Therapeutics*, 23(6):735–742, 2006.

[Foti06] N. Fotinos, M. A. Campo, F. Popowycz, R. Gurny, and N. Lange. 5-aminolevulinic acid derivatives in photomedicine: Characteristics, application and perspectives. *Photochem Photobiol*, 82(4):994–1015, 2006.

[Fouc97] E. Foucar. Do pathologists play dice? uncertainty and early histopathological diagnosis of common malignancies. *Histopathology*, pages 495–502, 1997.

[Fu04] K.-I. Fu, Y. Sano, S. Kato, T. Fujii, F. Nagashima, T. Yoshino, T. Okuno, S. Yoshida, and T. Fujimori. Chromoendoscopy using indigo carmine dye spraying with magnifying observation is the most reliable method for differential diagnosis between non-neoplastic and neoplastic colorectal lesions: a prospective study. *Endoscopy*, 36(12):1089–1093, Dec 2004.

[Gabr07] T. Gabrecht, S. Andrejevic-Blant, and G. Wagnières. Blue-violet excited autofluorescence spectroscopy and imaging of normal and cancerous human bronchial tissue after formalin fixation. *Photochem Photobiol*, 83(2):450–458, 2007.

[Gabr08] T. Gabrecht, A. Radu, P. Grosjean, B. Weber, G. Reichle, L. Freitag, P. Monnier, H. van den Bergh, and G. Wagnières. Improvement of the specificity of cancer detection by autofluorescence imaging in the tracheo-bronchial tree using backscattered violet light. *Photodiagnosis Photodyn Ther*, 5(1):2–9, Mar 2008.

[Gall07] J. Galli, G. Cammarota, M. Rigante, E. D. Corso, C. Parrilla, G. C. Passali, G. Almadori, and G. Paludetti. High resolution magnifying endoscopy: a new diagnostic tool also for laryngeal examination? *Acta Otorhinolaryngol Ital*, 27(5):233–236, Oct 2007.

[Glas92] W. Glassman, C. Liu, G. Tang, S. Lubicz, and R. Alfano. Ultraviolet excited fluorescence spectra from non-malignant and malignant tissues of the gynecological tract. *Lasers in the Life Sciences*, 5(1-2):49–58, 1992. cited By (since 1996) 50.

[Goet06] M. Goetz, A. Hoffman, P. R. Galle, M. F. Neurath, and R. Kiesslich. Confocal laser endoscopy: new approach to the early diagnosis of tumors of the esophagus and stomach. *Future Oncol*, 2(4):469–476, Aug 2006.

[Gono03] K. Gono, K. Yamazaki, Doguchi, N. T. N., T. Obi, M. Yamaguchi, N. Ohyama, H. Machida, Y. Sano, S. Yoshida, Y. Hamamoto, and T. Endo. Endoscopic observation of tissue by narrowband illumination. *Optical Review*, 10(4):211–215, 2003.

[Gono04] K. Gono, T. Obi, M. Yamaguchi, N. Ohyama, H. Machida, Y. Sano, S. Yoshida, Y. Hamamoto, and T. Endo. Appearance of enhanced tissue features in narrow-band endoscopic imaging. *J Biomed Opt*, 9(3):568–577, 2004.

[Grat60] W. B. Gratzer and G. H. Beaven. Transparent starch gels: preparation, optical properties and application to haemoglobin characterisation. *Clin Chim Acta*, 5:577–582, Jul 1960.

[Hamo81] J. Hamou. Microhysteroscopy. a new procedure and its original applications in gynecology. *J Reprod Med*, 26(7):375–382, Jul 1981.

[Hamo83] J. E. Hamou. Microhysteroscopy. *Clin Obstet Gynecol*, 26(2):285–301, Jun 1983.

[Hamo84] J. Hamou, J. Salat-Baroux, F. Coupez, and J. D. Brux. Microhysteroscopy: a new approach to the diagnosis of cervical intraepithelial neoplasia. *Obstet Gynecol*, 63(4):567–574, Apr 1984.

[Herr08] H. W. Herr and S. M. Donat. A comparison of white-light cystoscopy and narrow-band imaging cystoscopy to detect bladder tumour recurrences. *BJU Int*, 102(9):1111–1114, Nov 2008.

[Herr09] H. Herr, M. Donat, G. Dalbagni, and J. Taylor. Narrow-band imaging cystoscopy to evaluate bladder tumours - individual surgeon variability. *BJU Int*, Dec 2009.

[Hill00] P. Hillemanns, H. Weingandt, H. Stepp, R. Baumgartner, W. Xiang, and M. Korell. Assessment of 5-aminolevulinic acid-induced porphyrin fluorescence in patients with peritoneal endometriosis. *American Journal of Obstetrics and Gynecology*, 183(1):52–57, 2000.

[Hopk54] H. Hopkins and N. Kapany. A flexible fiberscope. *Nature*, 173:39, 1954.

[Hürz75] D. Hürzeler. Blue light endoscopy. *Laryngoscope*, 85(8):1374–1378, Aug 1975.

[Huan04] Q. Huang, N. Fukami, H. Kashida, T. Takeuchi, E. Kogure, T. Kurahashi, E. Stahl, Y. Kudo, H. Kimata, and S. ei Kudo. Interobserver and intra-observer consistency in the endoscopic assessment of colonic pit patterns. *Gastrointest Endosc*, 60(4):520–526, Oct 2004.

[Hung91] J. Hung, S. Lam, J. C. LeRiche, and B. Palcic. Autofluorescence of normal and malignant bronchial tissue. *Lasers Surg Med*, 11(2):99–105, 1991.

[Inou01] H. Inoue, J. F. Rey, and C. Lightdale. Lugol chromoendoscopy for esophageal squamous cell cancer. *Endoscopy*, 33(1):75–79, Jan 2001.

[Jean07] F. Jean, G. Bourg-Heckly, and B. Viellerobe. Fibered confocal spectroscopy and multicolor imaging system for in vivo fluorescence analysis. *Opt Express*, 15(7):4008–4017, 2007.

[Jenk01] D. Jenkins, E. Bentley, and K. Fleming. Evidence-based cellular pathology: a systematic framework for pathological diagnosis and clinical decisions. *Curr Diag Patho*, 7:272–280, 2001.

[Jich97] P. Jichlinski, M. Forrer, J. Mizeret, T. Glanzmann, D. Braichotte, G. Wagnières, G. Zimmer, L. Guillou, F. Schmidlin, P. Graber, H. D. Van Bergh, and H. J. Leisinger. Clinical evaluation of a method for detecting superficial transitional cell carcinoma of the bladder by light-induced fluorescence of protoporphyrin ix following topical application of 5-aminolevulinic acid: Preliminary results. *Lasers in Surgery and Medicine*, 20(4):402–408, 1997.

[Jung99] M. Jung and R. Kiesslich. Chromoendoscopy and intravital staining techniques. *Baillieres Best Pract Res Clin Gastroenterol*, 13(1):11–19, Apr 1999.

[Kamu04] A. Kamuhabwa, P. Agostinis, B. Ahmed, W. Landuyt, B. van Cleynenbreugel, H. van Poppel, and P. de Witte. Hypericin as a potential phototherapeutic agent in superficial transitional cell carcinoma of the bladder. *Photochem Photobiol Sci*, 3(8):772–780, Aug 2004.

[Kara05] M. A. Kara, F. P. Peters, W. D. Rosmolen, K. K. Krishnadath, F. J. ten Kate, P. Fockens, and J. J. G. H. Bergman. High-resolution endoscopy plus chromoendoscopy or narrow-band imaging in barrett's esophagus: a prospective randomized crossover study. *Endoscopy*, 37(10):929–936, Oct 2005.

[Kata00] O. Katayama, K. Namiki, K. Iwakoshi, H. Fujita, H. Yasuhara, I. Ohi, and S. Tomatsu. Magnified examination of small colorectal polyps using a prototype electronic endoscope. *Diagn Ther Endosc*, 6(2):77–82, 2000.

[Kell76] J. F. Kelly and M. E. Snell. Hematoporphyrin derivative: a possible aid in the diagnosis and therapy of carcinoma of the bladder. *J Urol*, 115(2):150–151, Feb 1976.

[Kenn90] J. C. Kennedy, R. H. Pottier, and D. C. Pross. Photodynamic therapy with endogenous protoporphyrin ix: basic principles and present clinical experience. *J Photochem Photobiol B*, 6(1-2):143–148, Jun 1990.

[Kenn92] J. C. Kennedy and R. H. Pottier. Endogenous protoporphyrin ix, a clinically useful photosensitizer for photodynamic therapy. *J Photochem Photobiol B*, 14(4):275–292, Jul 1992.

[Kies03] R. Kiesslich, J. Fritsch, M. Holtmann, H. H. Koehler, M. Stolte, S. Kanzler, B. Nafe, M. Jung, P. R. Galle, and M. F. Neurath. Methylene blue-aided chromoendoscopy for the detection of intraepithelial neoplasia and colon cancer in ulcerative colitis. *Gastroenterology*, 124(4):880–888, Apr 2003.

[Kies04a] R. Kiesslich, M. Jung, J. A. DiSario, P. R. Galle, and M. F. Neurath. Perspectives of chromo and magnifying endoscopy: how, how much, when, and whom should we stain? *J Clin Gastroenterol*, 38(1):7–13, Jan 2004.

[Kies04b] R. Kiesslich, J. Burg, M. Vieth, J. Gnaendiger, M. Enders, P. Delaney, A. Polglase, W. McLaren, D. Janell, S. Thomas, B. Nafe, P. R. Galle, and M. F. Neurath. Confocal laser endoscopy for diagnosing intraepithelial neoplasias and colorectal cancer in vivo. *Gastroenterology*, 127(3):706–713, Sep 2004.

[Kimu08] T. Kimura, N. Muguruma, T. Okahisa, T. Itagaki, H. Takeuchi, M. Kaji, S. Okamura, and T. Takayama. Infrared fluorescence endoscopy combined with indocyanine green injection for evaluation of severity in patients with ulcerative colitis. *Gastrointestinal Endoscopy*, 67(5):AB134, 2008. DDW Abstract Issue 2008, Digestive Disease Week 2008.

[Kins78] J. H. Kinsey, D. A. Cortese, and D. R. Sanderson. Detection of hematoporphyrin fluorescence during fiberoptic bronchoscopy to localize early bronchogenic carcinoma. *Mayo Clin Proc*, 53(9):594–600, Sep 1978.

[Kirk07] N. D. Kirkpatrick, M. A. Brewer, and U. Utzinger. Endogenous optical biomarkers of ovarian cancer evaluated with multiphoton microscopy. *Cancer Epidemiol Biomarkers Prev*, 16(10):2048–2057, 2007.

[Koba02] M. Kobayashi, K. Shibuya, H. Hoshino, and T. Fujisawa. Spectroscopic analysis of the autofluorescence from human bronchus using an ultraviolet laser diode. *J Biomed Opt*, 7(4):603–8, 2002.

[Koba03] M. Kobayashi, R. Sawada, and Y. Ueda. Spectroscopic imaging and the characterization of the autofluorescence properties of human bronchus tissues using uv laser diodes. *IEEE J Sel Top Quantum Electronics*, 9(2):142–147, 2003.

[Koen96] F. Koenig, F. J. McGovern, A. F. Althausen, T. F. Deutsch, and K. T. Schomacker. Laser induced autofluorescence diagnosis of bladder cancer. *J Urol*, 156(5):1597–1601, Nov 1996.

[Koen98] F. Koenig, F. J. McGovern, H. Enquist, R. Larne, T. F. Deutsch, and K. T. Schomacker. Autofluorescence guided biopsy for the early diagnosis of bladder carcinoma. *J Urol*, 159(6):1871–1875, Jun 1998.

[Kubi08a] A. Kubin, H. G. Loew, U. Burner, G. Jessner, H. Kolbabek, and F. Wierrani. How to make hypericin water-soluble. *Pharmazie*, 63(4):263–269, Apr 2008.

[Kubi08b] A. Kubin, P. Meissner, F. Wierrani, U. Burner, A. Bodenteich, A. Pytel, and N. Schmeller. Fluorescence diagnosis of bladder cancer with new water soluble hypericin bound to polyvinylpyrrolidone: Pvp-hypericin. *Photochem Photobiol*, 84(6):1560–1563, 2008.

[Kudo94] S. Kudo, S. Hirota, T. Nakajima, S. Hosobe, H. Kusaka, T. Kobayashi, M. Himori, and A. Yagyuu. Colorectal tumours and pit pattern. *J Clin Pathol*, 47(10):880–885, Oct 1994.

[Kudo96] S. Kudo, S. Tamura, T. Nakajima, H. Yamano, H. Kusaka, and H. Watanabe. Diagnosis of colorectal tumorous lesions by magnifying endoscopy. *Gastrointest Endosc*, 44(1):8–14, Jul 1996.

[Kudo97] S. Kudo, H. Kashida, T. Nakajima, S. Tamura, and K. Nakajo. Endoscopic diagnosis and treatment of early colorectal cancer. *World J Surg*, 21(7):694–701, Sep 1997.

[Kuma06] Y. Kumagai, M. Iida, and S. Yamazaki. Magnifying endoscopic observation of the upper gastrointestinal tract. *Digestive Endoscopy*, 18(3):165–172, 2006.

[Laem04] E. Laemmel, M. Genet, G. L. Goualher, A. Perchant, J.-F. L. Gargasson, and E. Vicaut. Fibered confocal fluorescence microscopy (Cell-viZio) facilitates extended imaging in the field of microcirculation. a comparison with intravital microscopy. *J Vasc Res*, 41(5):400–411, 2004.

[Lawv05] S. Lawvere and M. C. Mahoney. St. john's wort. *Am Fam Physician*, 72(11):2249–2254, Dec 2005.

[Lüdi03] F. Lüdicke, T. Gabrecht, N. Lange, G. Wagnières, H. V. D. Bergh, L. Berclaz, and A. L. Major. Photodynamic diagnosis of ovarian cancer using hexaminolaevulinate: a preclinical study. *Br J Cancer*, 88(11):1780–1784, Jun 2003.

[Li10] W. Li, I. Yamada, K. Masumoto, Y. Ueda, and K. Hashimoto. Photodynamic therapy with intradermal administration of 5-aminolevulinic acid for port-wine stains. *J Dermatolog Treat*, 21(4):232–239, Jul 2010.

[Löni04] M. Löning, W. Küpker, K. Diedrich, H. Diddens, and G. Hüttmann. Laparoscopic fluorescence detection of ovarian carcinoma metastases using 5-aminolevulinic acid-induced protoporphyrin ix. *Cancer*, 100(8):1650–1656, 2004.

[Makh08] H. Makhlouf, A. F. Gmitro, A. A. Tanbakuchi, J. A. Udovich, and A. R. Rouse. Multispectral confocal microendoscope for in vivo and in situ imaging. *J Biomed Opt*, 13(4):044016, 2008.

[Mali98] E. Malik, A. Meyhofer-Malik, D. Trutenau, H. Diddens, W. Kupker, and K. Diedrich. Photodynamic diagnosis of endometriosis using 5-aminolevulinic acid - a pilot study[pilotstudie zur photodynamischen diagnostik der endometriose mittels 5- aminolavulinsaure]. *Geburtshilfe und Frauenheilkunde*, 58(8):420–425, 1998.

[Miya89] Y. Miyake, T. Sekiya, S. Kubo, and T. Hara. A new spectrophotometer for measuring the spectral reflectance of gastric mucous membrane. *J Photogr Sci*, 37:134–8, 1989.

[Muft90] G. R. Mufti, P. J. Shah, M. C. Parkinson, and P. R. Riddle. Diagnosis of clinically occult bladder cancer by in vivo staining with methylene blue. *Br J Urol*, 65(2):173–175, Feb 1990.

[Muto09] M. Muto, T. Horimatsu, Y. Ezoe, S. Morita, and S. Miyamoto. Improving visualization techniques by narrow band imaging and magnification endoscopy. *J Gastroenterol Hepatol*, 24(8):1333–1346, Aug 2009.

[Nase10] A. Naselli, C. Introini, F. Bertolotto, B. Spina, and P. Puppo. Narrow band imaging for detecting residual/recurrent cancerous tissue during second transurethral resection of newly diagnosed non-muscle-invasive high-grade bladder cancer. *BJU Int*, 105(2):208–211, Jan 2010.

[Oba10] S. Oba, S. Tanaka, S. Oka, H. Kanao, S. Yoshida, F. Shimamoto, and K. Chayama. Characterization of colorectal tumors using narrow-band imaging magnification: combined diagnosis with both pit pattern and microvessel features. *Scand J Gastroenterol*, Mar 2010.

[Osaw09] H. Osawa, H. Yamamoto, N. Yamada, M. Yoshizawa, K. Sunada, H. Kita, H. Ajibe, K. Satoh, and K. Sugano. Diagnosis of endoscopic barrett's esophagus by transnasal flexible spectral imaging color enhancement. *J Gastroenterol*, 44(11):1125–1132, 2009.

[P.-B09] A. Parra-Blanco, A. Jiménez, B. Rembacken, N. González, D. Nicolás-Pérez, A. Z. Gimeno-García, M. Carrillo-Palau, T. Matsuda, and E. Quintero. Validation of fujinon intelligent chromoendoscopy with high definition endoscopes in colonoscopy. *World J Gastroenterol*, 15(42):5266–5273, Nov 2009.

[Palc91] B. Palcic, S. Lam, J. Hung, and C. MacAulay. Detection and localization of early lung cancer by imaging techniques. *Chest*, 99(3):742–743, Mar 1991.

[Peck55] G. C. Peck, H. P. Mack, W. A. Holbrook, and F. H. Figge. Use of hematoporphyrin fluorescence in biliary and cancer surgery. *Am Surg*, 21(3):181–188, Mar 1955.

[Pohl07] J. Pohl, A. May, T. Rabenstein, O. Pech, and C. Ell. Computed virtual chromoendoscopy: a new tool for enhancing tissue surface structures. *Endoscopy*, 39(1):80–83, Jan 2007.

[Pohl08] J. Pohl, M. Nguyen-Tat, O. Pech, A. May, T. Rabenstein, and C. Ell. Computed virtual chromoendoscopy for classification of small colorectal lesions: a prospective comparative study. *Am J Gastroenterol*, 103(3):562–569, Mar 2008.

[Poli24] A. Policard. Etudes sur les aspects offerts par les tumeurs expérimentales à la lumière de wood. *CR. Séances Soc. Biol. Fil.*, 91:1423, 1924.

[Prof77] A. E. Profio and D. R. Doiron. A feasibility study of the use of fluorescence bronchoscopy for localization of small lung tumours. *Phys Med Biol*, 22(5):949–57, 1977.

[Qu94] J. Qu, C. MacAulay, S. Lam, and B. Palcic. Optical properties of normal and carcinomatous bronchial tissue. *Applied Optics*, 33(31):7397–7405, 1994.

[Qu95] J. Qu, C. MacAulay, S. Lam, and B. Palcic. Laser-induced fluorescence spectroscopy at endoscopy: tissue optics, monte carlo modeling and in vivo measurements. *Optical Engineering*, 34(11):3334–3343, 1995.

[R.-K96] R. Richards-Kortum and E. Sevick-Muraca. Quantitative optical spectroscopy for tissue diagnosis. *Annu Rev Phys Chem*, 47:555–606, 1996.

[Raci88] H. Racinet. Formation d'oxzgène singulet 1-delta-g photosensibilisée par l'hypericine; étude cinétique en milieu micellaire non ionique. *J Chem Phys Chim Biol*, 85:971–976, 1988.

[Rama00] N. Ramanujam. Fluorescence spectroscopy of neoplastic and non-neoplastic tissues. *Neoplasia*, 2(1-2):89–117, 2000.

[Rams99] A. Ramsay. Errors in histopathology reporting: Detection and avoidance. *Histopathology*, pages 481–490, 1999.

[Reut92] V. R. Reuter. *Histology for pathologists.* Raven Press, 1992.

[Sano09] Y. Sano, H. Ikematsu, K. I. Fu, F. Emura, A. Katagiri, T. Horimatsu, K. Kaneko, R. Soetikno, and S. Yoshida. Meshed capillary vessels by use of narrow-band imaging for differential diagnosis of small colorectal polyps. *Gastrointest Endosc*, 69(2):278–283, Feb 2009.

[Sasa06] K. Sasajima, S. e. Kudo, H. Inoue, T. Takeuchi, H. Kashida, E. Hidaka, H. Kawachi, M. Sakashita, J. Tanaka, and A. Shiokawa. Real-time in vivo virtual histology of colorectal lesions when using the endocytoscopy system. *Gastrointestinal Endoscopy*, 63(7):1010–1017, 2006.

[Schi33] W. Schiller. Early diagnosis of carcinoma of the cervix. *Surgery, Gynecology and Obstetrics*, 56:210–222, 1933.

[Schw92] S. Schwartz. *Historical perspectives. ln Photodynamic Therapy: Basic Principles and Clinical Applications.* Marcel Dekker. New York., 1992.

[Shib02] K. Shibuya, H. Hoshino, M. Chiyo, K. Yasufuku, T. Iizasa, Y. Saitoh, M. Baba, K. Hiroshima, H. Ohwada, and T. Fujisawa. Subepithelial vascular patterns in bronchial dysplasias using a high magnification bronchovideoscope. *Thorax*, 57(10):902–7, 2002.

[Shib03] K. Shibuya, H. Hoshino, M. Chiyo, A. Iyoda, S. Yoshida, Y. Sekine, T. Iizasa, Y. Saitoh, M. Baba, K. Hiroshima, H. Ohwada, and T. Fujisawa. High magnification bronchovideoscopy combined with narrow band imaging could detect capillary looops of angiogenic squamous dysplasia in heavy smokers at high risk for lung cancer. *Thorax*, 58(11):989–995, 2003.

[Shib10] K. Shibuya, T. Nakajima, T. Fujiwara, M. Chiyo, H. Hoshino, Y. Moriya, M. Suzuki, K. Hiroshima, Y. Nakatani, and I. Yoshino. Narrow band imaging with high-resolution bronchovideoscopy: A new approach for visualizing angiogenesis in squamous cell carcinoma of the lung. *Lung Cancer*, in press:NA, Jun 2010.

[Shij03] N. Shijubo, H. Kojima, M. Nagata, T. Ohchi, A. Suzuki, S. Abe, and N. Sato. Tumor angiogenesis of non-small cell lung cancer. *Microsc Res Tech*, 60(2):186–198, Feb 2003.

[Shio95] T. Shiobara, H. Haneishi, and Y. Miyake. Color correction for colorimetric color reproduction in an electronic endoscope. *Opt Commun*, 114:57–63, 1995.

[Sonn09a] G. A. Sonn, S.-N. E. Jones, T. V. Tarin, C. B. Du, K. E. Mach, K. C. Jensen, and J. C. Liao. Optical biopsy of human bladder neoplasia with in vivo confocal laser endomicroscopy. *J Urol*, 182(4):1299–1305, Oct 2009.

[Sonn09b] G. A. Sonn, K. E. Mach, K. Jensen, P.-L. Hsiung, S.-N. Jones, C. H. Contag, T. D. Wang, and J. C. Liao. Fibered confocal microscopy of bladder tumors: an ex vivo study. *J Endourol*, 23(2):197–201, Feb 2009.

[Suga04] K. Sugano, K. Sato, and K. Yao. New diagnostic approaches for early detection of gastric cancer. *Digestive Diseases*, 22(4):327–333, 2004.

[Suga06] S. Sugano, S. Fujinuma, and Y. Sakai. Magnifying colonoscopy for the diagnosis of inflammatory changes in ulcerative colitis. *Digestive Endoscopy*, 18(3):173–180, 2006.

[Sung02] K.-B. Sung, C. Liang, M. Descour, T. Collier, M. Follen, and R. Richards-Kortum. Fiber-optic confocal reflectance microscope with miniature objective for in vivo imaging of human tissues. *IEEE Trans Biomed Eng*, 49(10):1168–1172, Oct 2002.

[Tam02] W. Tam, A. Edebo, and M. Bruno. Endoscopy negative reflux disease (enrd): High-resolution endoscopic and histological signs. *Gastroenterology*, 122:A74, 2002.

[Tana03] H. Tanaka, G. Yamada, T. Saikai, M. Hashimoto, S. Tanaka, K. Suzuki, M. Fujii, H. Takahashi, and S. Abe. Increased airway vascularity in newly diagnosed asthma using a high-magnification bronchovideoscope. *Am J Respir Crit Care Med*, 168(12):1495–1499, Dec 2003.

[Terc05] M. Tercelj, H. Zeng, M. Petek, T. Rott, and B. Palcic. Acquisition of fluorescence and reflectance spectra during routine bronchoscopy examinations using the clearvu elite(tm) device: Pilot study. *Lung Cancer*, 50(1):35–42, 2005.

[Thib07] L. Thiberville, S. Moreno-Swirc, T. Vercauteren, E. Peltier, C. Cavé, and G. B. Heckly. In vivo imaging of the bronchial wall microstructure using fibered confocal fluorescence microscopy. *Am J Respir Crit Care Med*, 175(1):22–31, Jan 2007.

[Thib09a] L. Thiberville, M. Salaün, S. Lachkar, S. Dominique, S. Moreno-Swirc, C. Vever-Bizet, and G. Bourg-Heckly. Human in vivo fluorescence microimaging of the alveolar ducts and sacs during bronchoscopy. *Eur Respir J*, 33(5):974–985, May 2009.

[Thib09b] L. Thiberville, M. Salaün, S. Lachkar, S. Dominique, S. Moreno-Swirc, C. Vever-Bizet, and G. Bourg-Heckly. Confocal fluorescence endomicroscopy of the human airways. *Proc Am Thorac Soc*, 6(5):444–449, Aug 2009.

[Thon07] P. S.-P. Thong, M. Olivo, K.-W. Kho, W. Zheng, K. Mancer, M. Harris, and K.-C. Soo. Laser confocal endomicroscopy as a novel technique for fluorescence diagnostic imaging of the oral cavity. *J Biomed Opt*, 12(1):014007, 2007.

[Uehl09] P. Uehlinger, T. Gabrecht, T. Glanzmann, J.-P. Ballini, A. Radu, S. Andrejevic, P. Monnier, and G. Wagnieres. In vivo time-resolved spectroscopy of the human bronchial early cancer autofluorescence. *Journal of Biomedical Optics*, 14(2):024011, 2009.

[Utzi01] U. Utzinger, M. Brewer, E. Silva, D. Gershenson, R. C. Blast, M. Follen, and R. Richards-Kortum. Reflectance spectroscopy for in vivo characterization of ovarian tissue. *Lasers Surg Med*, 28(1):56–66, 2001.

[Verc08] T. Vercauteren. *Image Registration and Mosaicing for Dynamic In Vivo Fibered Confocal Microscopy.* PhD thesis, Ecole des Mines, 2008.

[Voeg66] R. Voegeli. Schiller's iodine test in the diagnosis of esophageal diseases. preliminary report. *Pract Otorhinolaryngol (Basel)*, 28(3):230–239, 1966.

[Wagn98a] G. Wagnières, C. Hadjur, P. Grosjean, D. Braichotte, J. F. Savary, P. Monnier, and H. van den Bergh. Clinical evaluation of the cutaneous phototoxicity of 5,10,15,20-tetra(m-hydroxyphenyl)chlorin. *Photochem Photobiol*, 68(3):382–387, 1998.

[Wagn98b] G. A. Wagnières, W. M. Star, and B. C. Wilson. In vivo fluorescence spectroscopy and imaging for oncological applications. *Photochem Photobiol*, 68(5):603–632, 1998.

[Warn10] A. Warnecke, T. Averbeck, M. Leinung, B. Soudah, G. I. Wenzel, H.-H. Kreipe, T. Lenarz, and T. Stöver. Contact endoscopy for the evaluation of the pharyngeal and laryngeal mucosa. *Laryngoscope*, 120(2):253–258, Feb 2010.

[Wolf93] O. S. Wolfbeis. *Fluorescence Spectroscopy: New Methods and Applications.* Springer-Verlag, 1993.

[Wool89] G. M. Woolf, R. H. Riddell, E. J. Irvine, and R. H. Hunt. A study to examine agreement between endoscopy and histology for the diagnosis of columnar lined (barrett's) esophagus. *Gastrointest Endosc*, 35(6):541–544, 1989.

[Yama05] G. Yamada, H. Takahashi, N. Shijubo, T. Itoh, and S. Abe. Subepithelial microvasculature in large airways observed by high-magnification bronchovideoscope. *Chest*, 128(2):876–880, 2005.

[Yama06] G. Yamada, M. Otsuka, T. Itoh, A. Watanabe, and H. Takahashi. Mucosal thickness influence on microvessel images of large airways observed by high magnification bronchovideoscopy. *Journal of Bronchology*, 13(4):181–183, 2006.

[Yama07] G. Yamada, N. Shijubo, J. Kitada, M. Takahashi, M. Otsuka, M. Fujii, S.-I. Inomata, and H. Takahashi. Narrow band imaging yields clear images of subepithelial microvessels in large airways in combination with high magnification bronchovideoscopy. *Journal of Bronchology*, 14(2):75–78, 2007.

[Zaak02] D. Zaak, H. Stepp, R. Baumgartner, P. Schneede, R. Waidelich, D. Frimberger, A. Hartmann, R. Künchel, A. Hofstetter, and A. Hohla. Ultraviolet-excited (308 nm) autofluorescence for bladder cancer detection. *Urology*, 60(6):1029–1033, Dec 2002.

[Zell01a] M. Zellweger, D. Goujon, R. Conde, M. Forrer, H. van den Bergh, and G. Wagnières. Absolute autofluorescence spectra of human healthy, metaplastic, and early cancerous bronchial tissue in vivo. *Appl Opt*, 40(22):3784–3791, Aug 2001.

[Zell01b] M. Zellweger, P. Grosjean, D. Goujon, P. Monnier, H. van den Bergh, and G. Wagnières. In vivo autofluorescence spectroscopy of human bronchial tissue to optimize the detection and imaging of early cancers. *J Biomed Opt*, 6(1):41–51, Jan 2001.

[Zhen03] K. Zheng, S. Z. Zhang, Y. M. Wang, and L. Heng. The relationship between microvessel density derived from transitional cell carcinonma of bladder tissues and its biological behavior and prognosis. *Chinese Journal of Clinical Rehabilitation*, 7(26):3586–3587, 2003.

Part I

Bladder cancer

Chapter 3

Introduction to Bladder Cancer

In this chapter, we will first introduce some facts and statistics about bladder cancer (BC) (Section 3.1), in order to show that BC is an important health burden. Then, we will present the anatomy of urinary system (Section 3.2) and histology of bladder cancer (Section 3.3) with the classification systems, continuously updated by the medical community. We will also illustrate the different evolution pathways of BC, and link them to the clinical management of BC, and focus on screening (Section 3.4) and diagnostic procedures (Section 3.5). In Section 3.6, we will introduce the photodetection of bladder cancer based on ALA-derivatives, and conclude this chapter with a short review on angiogenesis related to BC (Section 3.7) to motivate the vascular imaging, described in Chapter 5.

3.1 Facts and statistics about bladder cancer

Cancer (often defined as equivalent to *malignant tumor*) is defined a class of diseases in which a group of cells display uncontrolled growth (division beyond the normal limits), invasion (intrusion on and destruction of adjacent tissues), and sometimes metastasis (spread to other locations in the body via lymph or blood). These three malignant properties of cancers differentiate them from benign tumors, which are self-limited, and do not invade or metastasize.

In the past years, cancer statistics have been established by governmental institutes. The most common cancers that were expected to occur in men and women in 2009 are depicted in Figure 3.1.

Figure 3.2 shows the 5-year survival rate for the two cancers of interest in this manuscript (namely in the tracheo-bronchial tree and in the urinary bladder). One can clearly identify that a diagnostic procedure that would detect cancer on a localized state (i.e. not distant) would be associated with a better survival. That is the purpose of fluorescence detection.

3.2 Anatomy of the urinary system

The *urinary bladder* is a hollow muscular organ in the lower abdomen (see Figure 3.3). It stores *urine*, the liquid waste produced by the *kidneys*. Urine passes from each kidney into the bladder through a tube called a *ureter*. An outer layer of muscle surrounds the inner lining of the bladder. When the bladder is full, the muscles in the bladder wall can tighten to allow

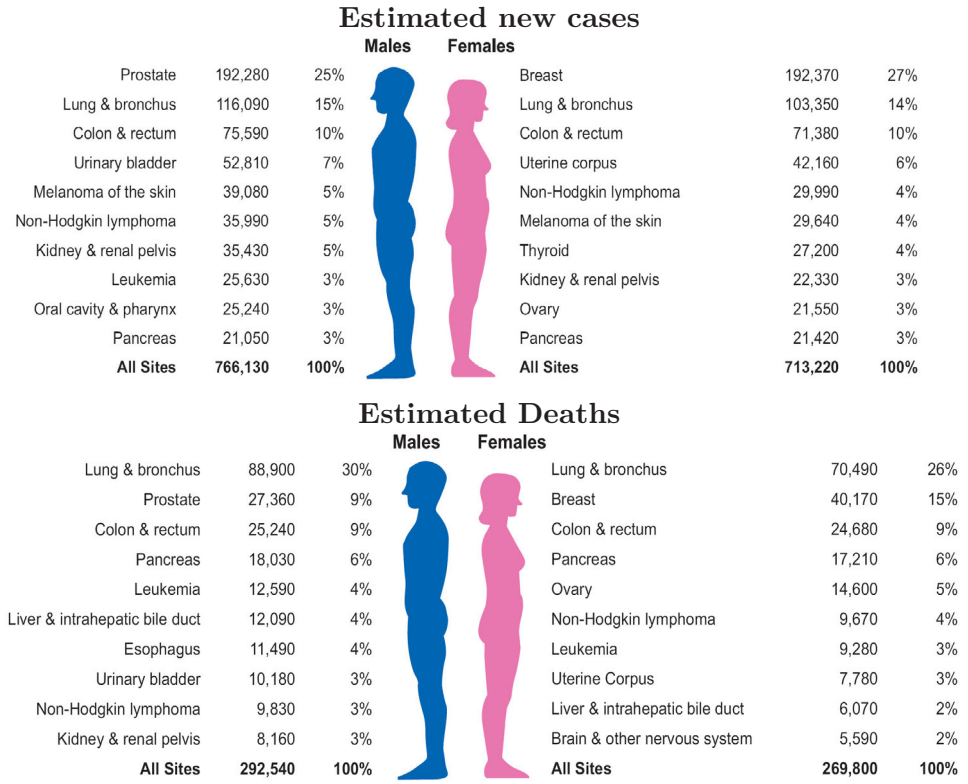

Figure 3.1: *Ten leading cancer types for estimated new cancer cases and deaths, by sex, United States, 2009 [Jema09].*

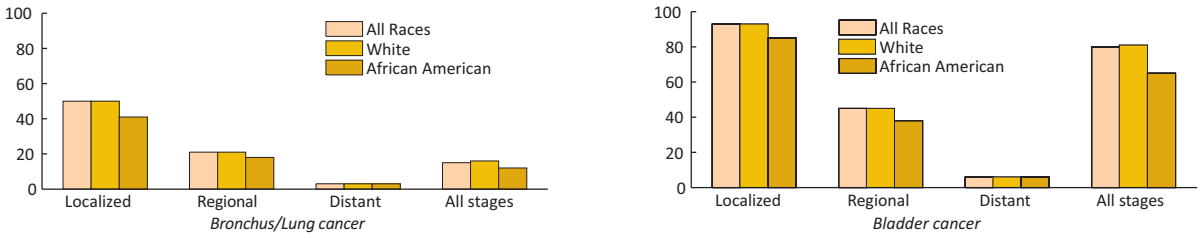

Figure 3.2: *Five-year Relative Survival Rates Among Patients Diagnosed with Selected Cancers by Race and Stage at Diagnosis,United States, 1996-2004.*

urination. Urine leaves the bladder through another tube, the *urethra*. The urinary bladder is a muscular sac lined with mucosa. Thus, it is highly distensible, with its volume varying typically from 30 cm^3 to 220 cm^3 [Wood86].

The urinary bladder is shaped roughly like a tetrahedron (see Figure 3.4) when empty and like a sphere when filled with urine. The posterior triangle of the tetrahedron forms the *base* of the bladder, the anterior the *apex*, the inferior angle leading to the urethra is called the *neck* and the two posterolateral angles admit the ureters. The smooth triangular area outlined by the ostia of the ureters and the internal orifice of the urethra is called the trigone.

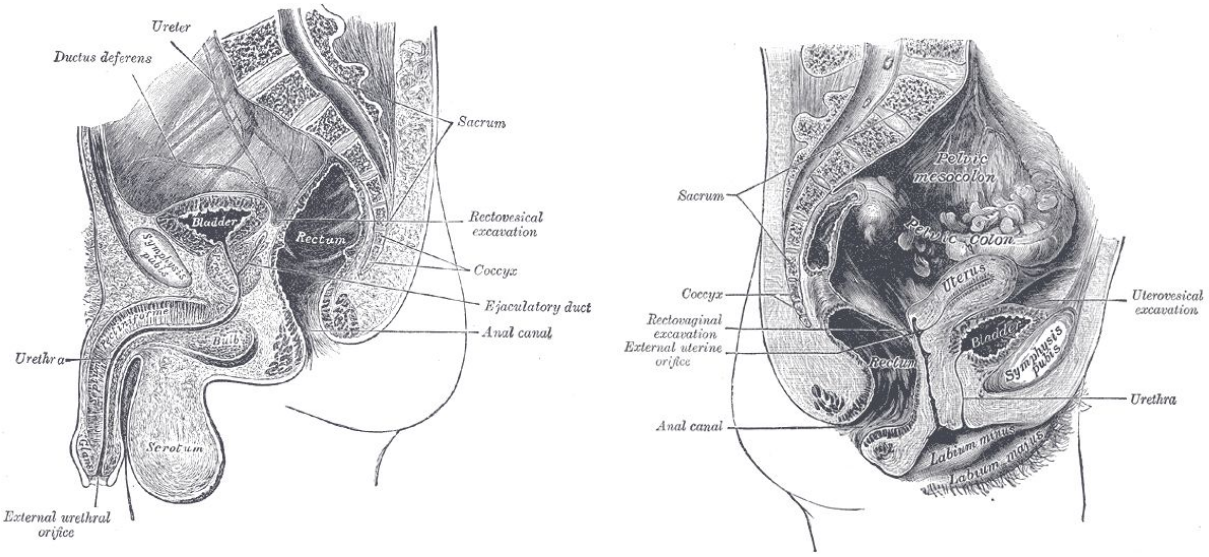

Figure 3.3: *Median sagittal section of male and female pelvis [Gray18].*

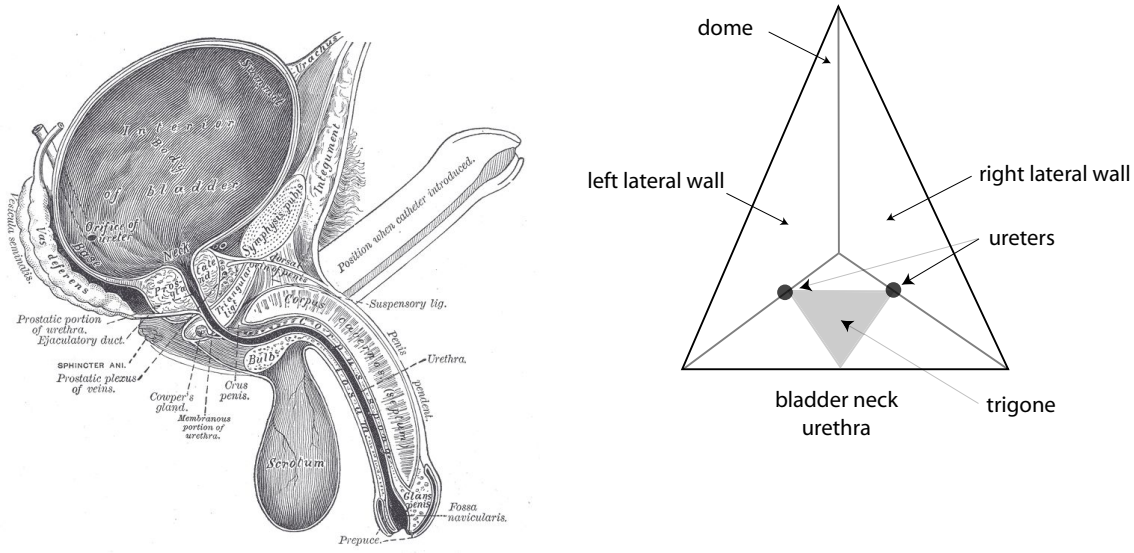

Figure 3.4: *Sagittal section and its corresponding tetrahedron representation of the empty bladder [Gray18].*

The bladder itself is made up of four layers (epithelium, lamina propria, muscularis propria, perivesical soft tissue) as shown in Figure 3.5. These layers are important landmarks in determining the depth of tumor invasion.

Epithelium lines the bladder and is in contact with the urine. It is referred as *transitional epithelium* or *urothelium*. Most bladder cancers originate from the cells of this transitional epithelium. The urethra, ureters and the pelvis of the kidney are also lined by this transitional epithelium, therefore, the same types of cancers seen in the bladder can also occur in these sites.

Lamina propria lies under the epithelium, as a layer of connective tissue and blood vessels. Within the lamina propria, there is a thin and often discontinuous layer of smooth muscle called the *muscularis mucosae*. This superficial layer of smooth muscle is not to be confused with the true muscular layer of the bladder called the *muscularis propria* or *detrusor muscle*.

Muscularis propria or detrusor muscle This deep muscle layer consists of thick smooth muscle bundles that form the wall of the bladder. For purposes of staging bladder cancer, the muscularis propria has been divided into a superficial (inner) half and a deep (outer) half.

Perivesical soft tissue This outermost layer consists of fat, fibrous tissue and blood vessels. When the tumor reaches this layer, it is considered out of the bladder.

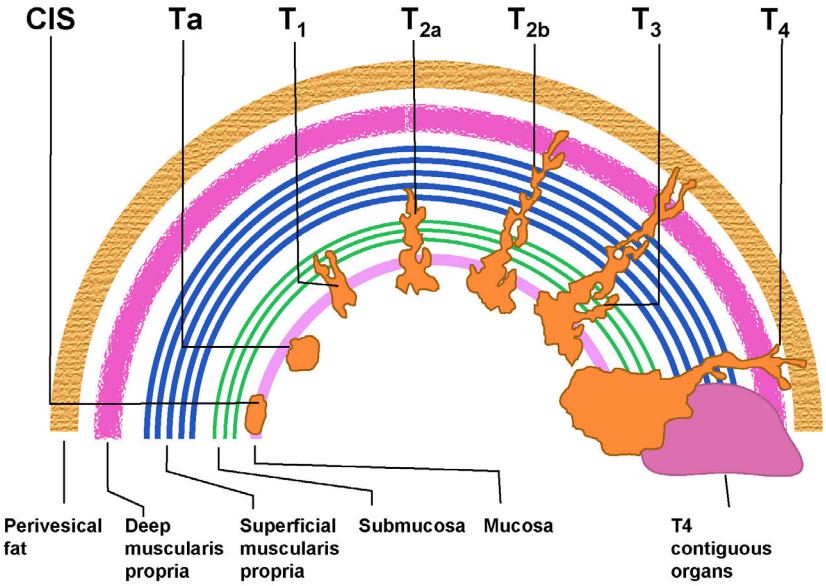

Figure 3.5: *Layered structure of the bladder wall*

The *urothelium* is the most specialized epithelium and plays important and conflicting roles: the urothelium must act as a permeability barrier – protecting underlying tissues against noxious urine components – while also stretching to accommodate urine pressures. Although the urothelium maintains a tight barrier to ion and solute flux, a number of local factors can modulate its barrier function (*e.g.* tissue pH, mechanical or chemical trauma, and bacterial infection) [Bird07].

Urothelium is a multilayered epithelium composed of at least three layers: a *basal cell layer* attached to a basement membrane, an *intermediate* layer, and a *superficial* or *apical* layer composed of large hexagonal cells (with diameters of 25-250 μm) known as *umbrella cells* [Drol05]. The umbrella cells are interconnected by tight junctions and are covered on their apical surface by crystalline proteins called *uroplakins* which assemble into hexagonal plaques [Apod04]. The thickness of the urothelium varies with the state of distension of the bladder (two to four cell layers when dilated and five to seven layers when contracted) [Mont08].

3.3 Histology of bladder cancer

Approximately 75-85% of patients with bladder cancer present with the disease confined to the mucosa (stage Ta,Tis) or submucosa (stage T1) [Babj08], but as many as 50-70% of those superficial tumors will recur and roughly 10-20% will progress to muscularis propria invasive disease (T2-4) [Rübb88]. A detailed description of this classification is to be found in Section 3.3.2.1.

Three types of bladder cancer begin in cells in the lining of the bladder. These cancers are named for the type of cells that become malignant (i.e. cancerous):

Transitional cell carcinoma begins in cells in the innermost tissue layer of the bladder (>90%). These cells are able to stretch when the bladder is full and shrink when it is emptied.

Squamous cell carcinoma begins in squamous cells, which are thin, flat cells that may form in the bladder after a long-term infection or irritation (∼6–8%).

Adenocarcinoma begins in glandular (secretory) cells that may form in the bladder after a long-term inflammation or irritation (2%).

3.3.1 Epidemiology and Risk factors

Cancer of the urinary bladder (in short *bladder cancer*) is frequent in the Western world. Bladder cancer is the 4th most common malignancy among men, the 8th most frequent among women [Joch05]. In 2009, an estimated of 70'980 cases were diagnosed in the United States with more than 14'330 dying from the disease [Jema09, N.-N09]. In Europe, more than 120'000 new cases of bladder cancer are diagnosed every year. The incidence of bladder cancer increases with age; the median age at diagnosis is 65-70 years [E.-O09].

Along with lung cancer, bladder cancer was one of the earliest cancers to undergo serious epidemiologic investigation [Zeeg04]. Aromatic amines were the first to be recognized as urothelial carcinogen [McCa97]. At-risk groups include workers in the following industries: printing, iron, and aluminium processing, industrial painting, gas and tar manufacturing. Another prominent risk factor is cigarette smoking, which triples the risk of developing bladder cancer and leads to its higher mortality [Babj08, Zeeg00, Stro08].

Kaufman *et al.* classified the bladder cancer associated risks factors into three subsets [Kauf09]:

- **genetic** (oncogenes, epidermal growth factor, tumor suppressor gene) and **molecular** (cell life regulatory proteins) abnormalities
- **chemical** (aromatic amine, aniline dyes, nitrites and nitrates, acrolein, coal, arsenic...) or **environmental** (cigarette smoking) exposures
- **others factors** such as chronic irritation, indwelling catheters, and pelvic irradiation.

Unfortunately, patients have often low overall knowledge regarding bladder cancer risk factors. For instance, most patients queried in the study of Nieder *et al.* had no idea regarding the relationship between bladder cancer and tobacco use regardless of smoking status [Nied06].

Zeegers *et al.* systematically reviewed the association between smoking, beverage consumption, diet and bladder cancer [Zeeg04]. Based on the results of previous epidemiologic studies and mechanistic evidence, they concluded that the most important risk factor for bladder cancer is cigarette smoking. In their opinion, prevention of cigarette smoking would result in a decrease of 50% of male bladder cancer cases and 23% of female bladder cancer cases. Alcohol consumption is the only other convincing risk factor for bladder cancer, although previous research suggests that the risk elevation for alcohol consumers is very small. Zeegers *et al.* stated that there is *probably* no association between coffee, tea, vitamin A and C intake and subsequent bladder cancer risk and a negative association with fruit consumption and selenium intake. Eventually, these authors stated that it is *possible* that cigar, pipe and passive smoking slightly increase bladder cancer risk, that total fluid consumption and folate intake are not associated with bladder cancer risk, and that vitamin E intake decreases bladder cancer risk. Further research is needed to confirm these latter conclusions.

3.3.2 Classification systems

The "gold standard" in endoscopy is still the histopathological analysis of biopsies. Over the years, the pathologists have defined a dedicated lexicon to *classify* the results. One often distinguishes between *staging* classification systems, which describe the *invasiveness* and *dissemination* of a tumor, and *grading* classification systems, which describes the *aggressiveness* of a tumor. In the following, one will present the 2002 TNM classification (staging) and the 1973 and 2004 WHO classification (grading).

3.3.2.1 TNM classification

The **TNM** classification is a cancer staging system that describes the extent of cancer in a patient's body. **T** describes the size of the tumor and whether it has invaded nearby tissue, **N** describes regional lymph nodes that are involved, and **M** describes distant metastasis (spread of cancer from one body part to another). The TNM staging system for all solid tumors was devised by Pierre Denoix between 1943 and 1952 [Deno46]. TNM is regularly updated by the *Union Internationale Contre le Cancer* (UICC) to achieve consensus on one globally recognized standard for classifying the extent of spread of cancer. Currently, clinicians use the 2002 TNM classification [Babj08, Rena02, MacL07]. Table 3.1 describe the categories.

The pathological classification (or *postsurgical histopathological classification*) is designated **pTNM**. This is based on the evidence acquired before treatment, supplemented or modified by the additional evidence acquired from surgery and from pathological examination [Witt03].

3.3.2.2 1973 Classification

The first widely accepted grading system for papillary urothelial neoplasms was the 1973 WHO classification system, which divided urothelial papillary tumors into four categories: papilloma, grade 1 carcinoma, grade 2 carcinoma and grade 3 carcinoma [Most73]. The 1973 WHO histological grading of bladder cancer is one of most successful grading systems among all organ sites and has been validated since its introduction three decades ago. An enormous amount of data has been accumulated using this system in studies of the morphological properties, clinical behavior, treatment and follow-up of urothelial tumors. Because of its relative simplicity

	T – Primary tumor
Tx	Primary tumor cannot be assessed
T0	No evidence of primary tumor
Ta	Non-invasive papillary carcinoma
Tis	Carcinoma in situ: *flat tumor*
T1	Tumor invades subepithelial connective tissue
T2	Tumor invades muscle
	T2a Tumor invades superficial muscle (inner half)
	T2b Tumor invades deep muscle (outer half)
T3	Tumor invades perivesical tissue:
	T3a Microscopically
	T3b Macroscopically (extravesical mass)
T4	Tumor invades any of the following: prostate, uterus, pelvic wall, abdominal wall
	T4a Tumor invades prostate, uterus, or vagina
	T4b Tumor invades pelvic wall or abdominal wall
	N – Lymph nodes
Nx	Regional lymph nodes cannot be assessed
N0	No regional lymph node metastasis
N1	Metastasis in a single lymph node $\leq$ 2 cm in greatest dimension
N2	Metastasis in a single lymph node $>$ 2 cm but $\leq$ 5 cm in greatest dimension, or multiple lymph nodes, each $\leq$ 5 cm in greatest dimension
N3	Metastasis in a lymph node $>$ 5 cm in greatest dimension
	M – Distant metastasis
Mx	Distant metastasis cannot be assessed
M0	No distant metastasis
M1	Distant metastasis

Table 3.1: *2002 TNM classification of urinary bladder cancer*

and its well-documented powerful predictive value, it has been well accepted by urologists and used globally for several decades in making clinical decisions for management of patients with urothelial cancer. However, in the early 1990s several factors emerged that resulted in the need to re-evaluate this approach and update the classification.

3.3.2.3 1998-2004 Classification

In October 1997, Dr. F. K. Mostofi assembled a group of individuals interested in bladder neoplasia at a meeting in Washington DC. The participants included urologic pathologists, urologists, urologic oncologists, and basic scientists with an interest in bladder neoplasia. The purpose of this meeting was to discuss bladder terminology and make recommendations to the World Health Organization (WHO) Committee on urothelial tumors [Epst98]. They eventually reached a consensus, that was presented one year later in Boston. This became known as the 1998 ISUP/WHO classification system. In 2004, this classification system was adopted in one of the WHO "blue books" for the classification of tumors [Saut04]. This is known as the 2004 WHO classification (see Table 3.2).

Normal
Normal
Hyperplasia (flat or papillary)
Flat lesions with atypia
Reactive (inflammatory) atypia
Atypia of unknown significance
Dysplasia (low-grade intraurothelial neoplasia)
Carcinoma in situ (high grade intraurothelial neoplasia)
Papillary neoplasms
Papilloma
Inverted papilloma
Papillary neoplasm of low malignant potential
Papillary carcinoma, low grade
Papillary carcinoma, high grade
Invasive neoplasms
Lamina propria invasion
Muscularis propria (detrusor muscle) invasion

Table 3.2: *2004 WHO/ISUP consensus classification*

According to its proponents, the 2004 WHO classification modified the 1973 WHO classification with the following key points :

1. the description of the categories has been expanded. One group (papillary urothelial neoplasm of low malignant potential, PUNLMP) is newly defined. The PUNLMP are lesions that do not have cytological features of malignancy but show normal urothelial cells in a papillary configuration. They have a negligible risk for progression, but still have a tendency to recur. Since they have particularly good prognosis for the patient, the PUNLMP do not carry the label of "cancer".

2. it avoids use of ambiguous grading such as grade 1/2 or 2/3. The intermediate grade (grade 2), which was the subject of controversy in the 1973 WHO classification, has been eliminated, such as it remains only *low* and *high* grade. The 1973 and the 2004 WHO grading systems are compared in Table 3.3.

1973 WHO Grading	2004 WHO Grading
Papilloma (benign)	Papilloma (benign)
Grade 1: well differentiated	Papillary urothelial neoplasm of low malignant potential (PUNLMP)
Grade 2: moderately differentiated	Low-grade papillary urothelial carcinoma
Grade 3: poorly differentiated	High-grade papillary urothelial carcinoma

Table 3.3: *WHO grading in 1973 and in 2004 adapted from [Babj08]*

Microphotographs showing the principal WHO classes of bladder cancer are depicted in Figure 3.6. The detailed morphological factors are listed in Table B.1 and Table B.2 (see Appendix B).

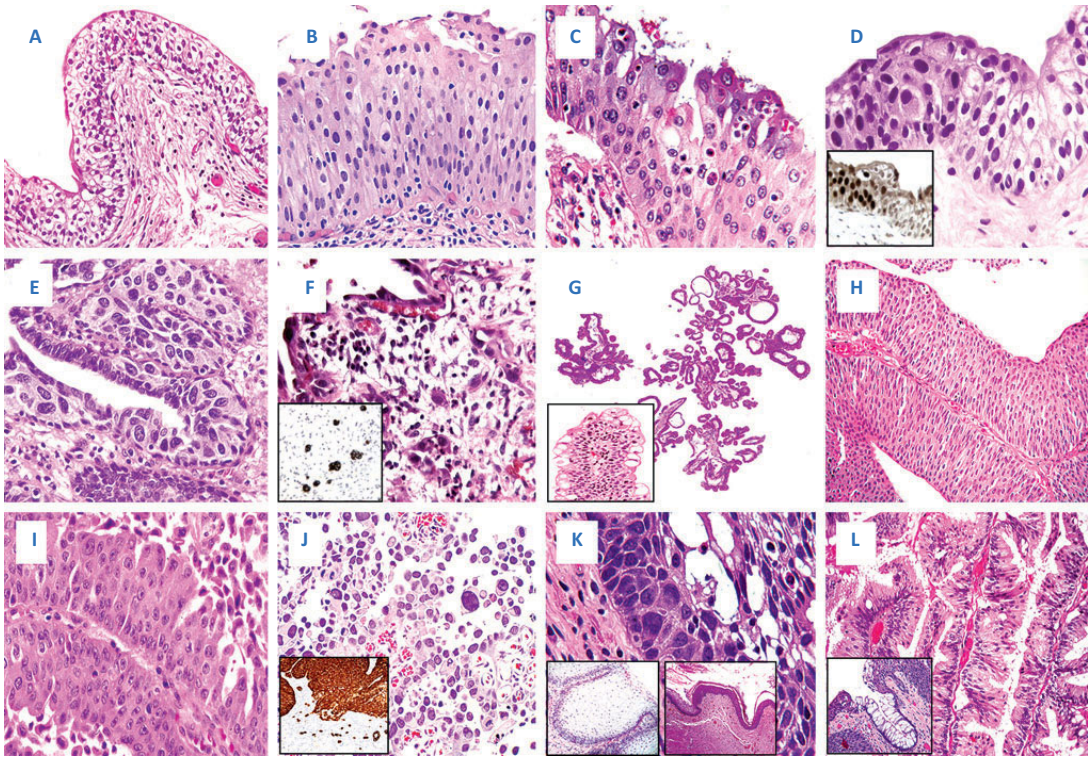

A normal urothelium. B flat urothelial hyperplasia. C reactive atypia.
D urothelial dysplasia (left part of the image) adjacent to normal urothelium (right) (insert:p53 expression in dysplasia).
E urothelial carcinoma in situ (CIS), pagetoid type.
F urothelial CIS with microinvasion (the invading cells are detected with antibody against AE1-AE3 cytokeratins).
G urothelial papilloma (insert: magnification of the lesion).
H papillary urothelial neoplasm with low malignant potential. I urothelial papillary carcinoma of low grade.
J urothelial papillary carcinoma of high grade (insert: microinvasion detected with antibody against AE1-AE3 cytokeratins).
K squamous cell CIS (insert 1: squamous cell metaplasia, vaginal type; insert 2: squamous cell metaplasia, keratinizing type).
L villous adenoma (insert: intestinal metaplasia).

Figure 3.6: *Classification of the bladder neoplasms with H&E staining (adapted from [Mont08]).*

3.3.3 Disease evolution & progression

The exact progression pathway to invasive cancer remains partly unknown. In patients with low grade Ta disease, it has been shown that the 15-year progression-free survival is 95% with no cancer specific mortality. Patients with high grade Ta tumors had a progression-free survival of

61% and a disease specific survival of 74%, whereas patients with T1 disease had a progression-free survival of 44% and a disease-specific survival of 62%, lending support to the view that invasion of the lamina propria is a prognostic indicator for risk of disease progression and reduced survival [Drol05].

Droller *et al.* updated the schematic depicting the multiplicity of pathways in bladder cancer development [Jone93, Drol05]. In Figure 3.7, the number of pathways and their likelihood of occurrence as represented by the size of the arrows accounts for the different types of bladder cancer that are seen. The majority of bladder tumors present with a papillary configuration and are generally confined to the mucosal layer. Resection of any visible lesion presumably restores a normal transitional cell epithelium, although conceivably there are changes elsewhere in the bladder not yet clinically detectable endoscopically. Although these generally low-grade tumors confined in the mucosa may recur, they generally do not follow a more aggressive, potentially life-threatening pathway. Rarely, additional genetic changes may induce development of a higher-grade papillary lesion. More commonly, however, high-grade lesions may develop directly through different genetic changes, suggesting a process termed *dysplasia*. Dysplasia may also lead to the production of high-grade cells that do not assume a papillary configuration but instead maintain growth along the flat plane of the urothelium, taking the form of *carcinoma in situ* (CIS,Tis). Although these lesions may proliferate to produce high-grade papillary tumors (rare), they are more often associated with a development of nodular tumors that become directly invasive without necessarily protruding into the lumen of the bladder until much later in their development. Solid tumors appear more commonly to be associated with lymphatic/vascular permeation and the development of distant metastases.

The genetic changes occurring in bladder cancer are not treated in this manuscript, but they are currently under research by many groups [Kiem09, Chen09b, Chen09a].

The classic way to categorize patients with TaT1 tumors is to divide them into risk groups based on prognostic factors derived from multivariate analysis. Based on the 2596 patients cohort using *European Organization for Research and Treatment of Cancer* (EORTC) risk tables, Sylvester *et al.* derived a simple scoring system was derived based on six clinical and pathological factors: number of tumors, tumor size, prior recurrence rate, T category, presence of carcinoma in situ, grade [Sylv06]. The scoring system is described in details in Table B.3 in Appendix B). The following endpoints were assessed: (1) time to first recurrence (disease-free interval) and (2) time to progression to muscle invasive disease. Depending on cancer stages, the probabilities of recurrence and progression at one year ranged from 15% to 61% and from less than 1% to 17%, respectively. At five years, the probabilities of recurrence and progression ranged from 31% to 78% and from less than 1% to 45%. Detailed results are listed in Table B.4 in Appendix B.

The most important prognostic factor in patients with T1G3 tumors is the presence of concomitant CIS. The probability of progression in T1G3 patients without CIS is 10% at one year and 29% at five years; in T1G3 patients with CIS, the corresponding figures are 29% and 74%, respectively. In such patients a cystectomy should be seriously considered very early in their treatment since progression in patients with a history of superficial bladder cancer is associated with a very poor prognosis [Schr04].

3.4 Screening method

The most common presenting symptom of bladder cancer is painless haematuria. Additionally, unexplained urinary frequency, urgency, or irritative voiding symptoms should alert the clinician to the possibility of bladder cancer.

The clinical necessity for a non-invasive test for bladder cancer is two-fold, including the early

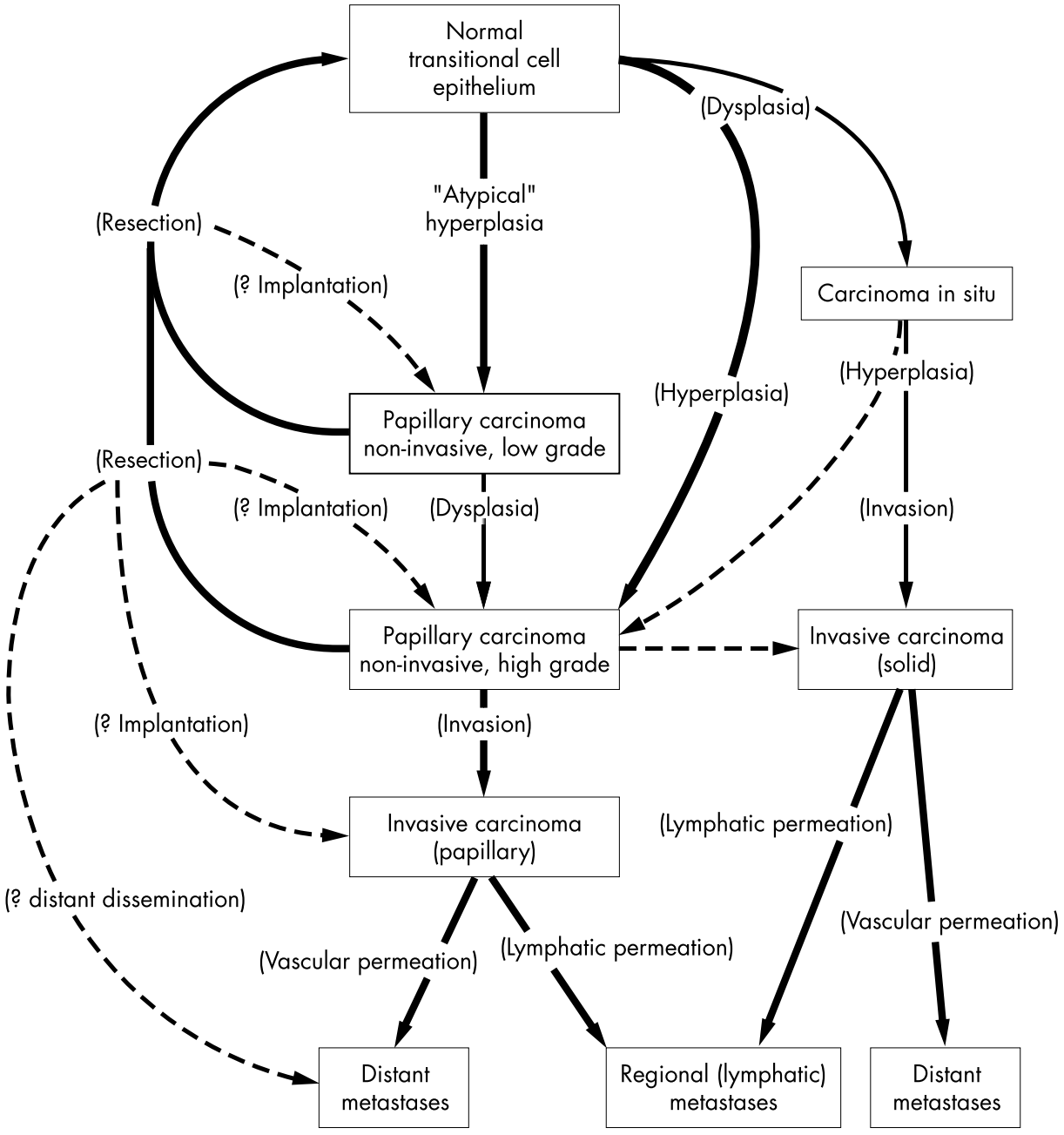

Figure 3.7: *Pathways in bladder cancer development [Jone93].*

detection of high grade bladder tumors before muscle invasion and monitoring tumor recurrence or new onset. An ideal noninvasive test should be sensitive, specific, rapid, technically simple and have low intra-assay and interassay variability [Loke01].

When a diagnosis of transitional cell carcinoma is suspected, the initial assessment consists of voided urine cytology, cystoscopy, and radiological investigation of the upper tracts.

3.4.1 State-of-the-art : cytology

Urine sample can be collected in a sterile container in the outpatient facility or during a cystoscopy. The urine sample is processed in a laboratory and examined under a microscope by a pathologist who looks for abnormal cells. This procedure is called *cytology*.

Urine cytology has high specificity but limited applicability due to its relatively low sensitivity and subjective nature. In a recent review, van Rhijn *et al.* stated that the overall specificity of urinary cytology has been high, with a range of 85%-100% for poorly differentiated tumors [van 05]. This has enabled the cytologist to distinguish differences between malignant and benign cells in the cytologic appearance of bladder wash specimens. In contrast, the overall sensitivity has been rather poor, especially for low-grade carcinoma, with a wide range of 13%-75% in reported in published studies.

3.4.2 New screening procedures

Therefore, several new screening tests have been developed based on biochemical markers found in sampled urine. Examples are listed in Table 3.4. Their value is yet to be established in larger clinical trials.

	Mechanism	**Sensitivity**	**Specificity**
Cytology	Tumors cells sloughed in urine	7-17% PUNMLP G1 53-90% high grade	90-98%
BTA Stat and TRAK	Detects urothelial basement membrane	50-80%	50-75%
NMP-22	Nuclear proteins released during apoptosis	50% in non-invasive disease 90% in invasive disease	85.7%
ImmunoCyt	Immunofluorescence 3 monoclonal antibodies	50-85%	62-73%
UroVysion	FISH with probes to Chr3,7,17,9p21	70-86%	66-93%

Abbreviations:
BTA=bladder tumor antigen.Stat=signal transducer and activator of transcription.
TRAK=total reference air karma.NMP-22=nuclear matrix protein-22.
FISH=fluorescence in-situ hybridisation.Chr=chromosome.

Table 3.4: *Non-invasive diagnostic tests for transitional cell carcinoma [van 09]*

3.5 Bladder cancer management

Up to 70% of newly diagnosed bladder tumors present as highly differentiated, superficial tumors, and can be readily treated with transurethral resection. Although up to 50% to 80% of patients may have recurrent tumors, at worst 10–20% ultimately progress to invasive disease [Kurt00]. In contrast, although it is also a superficial noninvasive lesion, CIS is a potentially aggressive tumor due to its unpredictable nature [Sylv06]. By definition, CIS of the bladder is a flat,

high grade intraurothelial neoplasm [Epst98]. It may occur as focal lesions, in diffuse form or concurrent with other high risk types of transitional cell carcinoma [Drol00]. Patients with bladder CIS are at significant risk for cancer progression and death from bladder carcinoma. Therefore, the detection of CIS has significant prognostic and therapeutic implications for the patient [Schm04, Loid05].

Early detection of bladder cancer is a key to better prognosis for the patient [Babj08, Oost02]. After a urothelial lesion is detected, the diagnosis and clinical stage is established by transurethral resection of the bladder (TURB) . This resection should include *muscularis propria*, especially if the *lamina propria* is affected or the tumor is high grade. When the transurethral resection shows lamina propria invasion but does not include sufficient muscularis propria in the specimen a repeat resection should be done to rule out muscularis propria invasion.

TaT1 tumors recur frequently and progress to muscle-invasive disease in a limited number of cases. It is therefore necessary to consider adjuvant therapy in all patients after TURB. It can be Bacillus Calmette-Guérin (BCG) or chemotherapeutic agents (*e.g.* mytomicin or farmorubicin) [Babj08, Drag10].

The high rate of recurrence is the feature of bladder cancer that makes follow-up a crucial component in effective management. After TURB of the tumor, early re-resection at 4-6 weeks should be considered to minimize the risk of staging error and to ensure complete resection. Moreover, patients should have cystoscopy and voided urine cytology every 3 months for 2 years, then 6-monthly for 2 years, and then once yearly indefinitely [Kauf09].

3.5.1 TURB Procedure

TURB remains the gold standard for management of bladder cancer, but there is evidence of a high rate of tumor recurrence after primary resection, and of variation between institutions [Thom08]. The aim of initial TURB is to remove all visible tumor and obtain tissue for histological diagnosis. The procedure is performed with the patient under general or locoregional anaesthesia to allow paralysis (if required by tumor location) and thereby minimize the risk of stimulating the obturator nerve and subsequent adduction of the thigh muscles, which can result in bladder perforation. Tumor resection occurs via a 26-28 Fr resectoscope with a 30-degree telescope and diathermy loop using glycine or water irrigation [Solo97]. Video-endoscopy is used routinely in most units and offers the advantages of ergonomic ease for the surgeon, better visibility, and more freedom of movement of the resectoscope, in addition to the teaching opportunities it affords. A continuous flow sheath provides a clear visual field while minimizing bladder overfilling, bladder perforation, stimulation of the obturator nerve, and obscuring carcinoma *in situ*.

The tumor is resected using precise movements of the loop. Once the tumor is resected, the base is either biopsied using cold-cup biopsy forceps or resected and sent for pathology in a separate, appropriately labeled pot. Any suspicious areas should also be biopsied and sent in separate, clearly labeled pots. Biopsy of normal mucosa is not routinely recommended unless there is positive cytology or the presence of multiple tumors or T1 stage tumor [Solo97]. Hemostasis is then obtained using a rollerball electrode to fulgurate the resected area and obtain biopsy.

After TURB alone, around 50-70% of patients develop recurrence due to incomplete TURB, tumor cell implantation, or aggressive tumor biology [Sylv06]. Over a century ago, it was postulated by Albarran and Imbert that bladder cancer recurrence was caused by implantation of floating tumor cells. Hence the standard TURB approach may explain the high recurrence rates for superficial bladder cancer [Parm89]; a theory supported by the common sites of recurrence –

90.6% of recurrent tumors occur in the dome, compared with 6.3% of primaries [Boyd74]. More recently, molecular studies have demonstrated that multifocal tumors are monoclonal, indicating a common origin [Hafn01].

Irrigation solution is used to distend the bladder, clear the surgical site, and remove blood and resected tissue. During transurethral resection of the prostate (TURP), the so-called TURP-syndrome was described. It is a real concern during electroresection, due to intravascular absorption of irrigating distilled water [Jens91]. Indeed, when excess fluid collects in the body, the concentration of sodium in the bloodstream is reduced, leading to the following common symptoms nausea, vomiting, fatigue, and confusion. That is similar in case of bladder resection, and that is why other irrigating solutions (*e.g.* distilled water, saline solution, and glycine solution) are used in the clinics. Indeed, this effect, which was incidentally discovered during prostate resection, is less marked with Glycine irrigation solution (due to its different osmotic pressure). During bipolar electroresection, saline (NaCl) solution is used, because it contains electrolytes to conduct the electrical current from one electrode to another.

3.5.2 Socio-economical concerns

The economic burden of bladder cancer is well-characterized in the literature. Bladder cancer (BC) has the highest lifetime treatment costs per patient (pp) of all cancers. Although most patients present with NMIBC, the high rate of recurrence and disease progression necessitates vigilant long-term monitoring for BC patients [Siev09]. Depending on the country, BC costs from diagnosis-to-death range between $89'287 and $202'203 pp [Bott03] and will likely increase as survival rates increase.

Sievert *et al.* reviewed several strategies for reducing BC's economic burden that have been proposed in the literature: (1) use of urine-based markers to identify incident or recurrent tumors earlier; (2) use of outpatient facilities for TURB reducing hospitalizations if surgical risks can be minimized; (3) improve efficacy of intravesical treatments; (4) the use of photodynamic diagnosis (PDD), instead of conventional white-light (WL) cystoscopy, to improve initial TURB efficacy and potentially reduce NMIBC's residual risk [Siev09]. This topic paper concludes that, while these new treatment options initially provoke higher costs after the initial diagnosis, long-term cost benefits can be achieved through reduced tumor recurrence and potentially reduced progression rates.

Daniltchenko *et al.* compared the cost-effectiveness of PDD vs. conventional WL cystoscopy [Dani05]. Fluorescence assisted TURB of superficial bladder cancer significantly improves visualization of all malignant lesions and, thus, the completeness of resection. This advantage of decreased tumor recurrence risk is maintained with statistical significance for at least 5 years, and effectively reduces patient morbidity and costs for repeat operations. Additionally, the cost-analysis presented in this study suggests a considerable economical advantage of fluorescence assisted TURB compared to the standard procedure.

3.6 Development of photodetection for bladder cancer

3.6.1 Historical perspective

Maximilian Carl-Friedrich Nitze (1848-1906) was a German urologist. In Dresden, he became inspired by the work of Julius Bruck, a dentist, who performed diaphanoscopy of the bladder by inserting a incandescent, water-cooled platinum wire in the rectum. The illumination of the bladder was insufficient, however, and the rectum was unfortunately burned in some cases.

Attempts to examine the interior of the bladder were not new, having been undertaken first by Bozzini in 1807 using a reflected candle light source, which had also proved to be an insufficient light source and was too painful for patients owing to the size of the instrument.

Dr. Nitze got the intuition that the field of view could be enlarged using an optical system, and that the light source should be placed at the tip of the instrument in the same way that "to light up a room, one must carry the lamp inside". Along with Viennese instrument maker Joseph Leiter (1830-1892), he is credited with the invention of the modern cystoscope. The Nitze-Leiter cystoscope was first publicly demonstrated in 1879 [Mout98]. Functionally, it used an electrically heated platinum wire for illumination, a cooling system of flowing ice-water, and telescopic lenses for visualization (see Figure 3.8). Invention of the incandescent light bulb by Thomas Edison allowed further improvements to the cystoscope; in 1887 Nitze constructed an apparatus that no longer needed a cooling-system. Nitze is also credited with producing the first endoscopic photographs.

Joaquin Albarrán (1860-1912) was a urologist who was born in Cuba. In 1878, he went to Paris, where he worked and studied under many renowned physicians. In 1906 he became director of the Clinic of Urology at the Hôpital Necker. He is credited with the invention of a device for adjustment of a cystoscope during the catheterization of the ureter. This device was to become known as the Albarrán lever. He was nominated in 1912 for a Nobel Prize in Medicine. He was one the first to enlighten the mechanism of recurrence of bladder cancer, due to cellular reimplantation in the bladder wall [Case06].

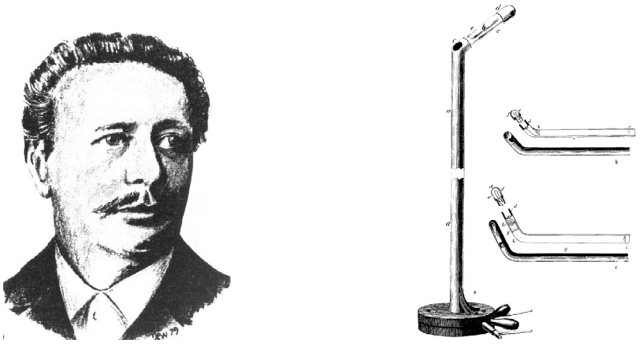

Figure 3.8: *Maximilian Nitze and his cystoscope from 1877.*

3.6.2 History of ALA-derivatives based photodetection

Porphyrins were identified in the mid-nineteenth century, but they were used in medicine until the early twentieth century. Hematoporphyrin was first produced by Scherer in 1841 during experiments investigating the nature of blood. Dried blood was heated with concentrated sulfuric acid, the precipitate was washed free of iron and then treated with alcohol [Sche41]. However, the fluorescent properties of hematoporphyrin were not described until 1867 and it was named hematoporphyrin in 1871 [Ackr01].

The first reports of attempts to localize human tumors with fluorescent porphyrins appeared in the early 1950s. In 1951, Manganiello and Figge studied the effects of hematoporphyrin in three patients with head and neck malignancies but fluorescence was not detected, very likely due to the lower doses of photosensitizer given to humans as compared with those in previous animal experiments [Mang51].

As shown in section 2.2.2.1, 5-aminolevulinic acid (ALA) is a precursor of many fluorescing porphyrins in the biosynthetic pathway for heme. In the following, we will simplify the

legibility by speaking only about the protoporphyrin IX (PpIX). Pioneering *in vitro* studies of ALA [Mali87] and the report of a successful ALA-based photodynamic treatment of skin tumors [Kenn90] opened the way to novel research. The first reports about fluorescence cystoscopy for the detection of bladder cancer were from the group of Munich in 1992 [Baum92, Krie94, Krie95].

Indeed, Baumgartner *et al.* easily observed ALA-induced fluorescence with the naked eye during cystoscopy under violet light illumination. All tumor lesions were sharply marked with brightly shining red fluorescence. Correlation of fluorescence and microscopic findings gave a sensitivity of 100% and a specificity of 68.5% [Baum92, Krie94].

Following these first tests, the group of Lausanne developed and optimized ALA-derivatives for the detection of non-muscle invasive bladder cancers. The main motivations behind this research were to increase the signal-to-background ratio (i.e. heighten the fluorescence intensity) and shorten the instillation interval to an acceptable time for clinical acceptance. Indeed, ALA used to be instilled between 2–4 hours prior to examination, which is not practical for ambulatory patients.

A collaboration between the Medical Photonics group (EPFL, Prof. van den Bergh), the Institute of Physiology (Faculty of Biology and Medicine, University of Lausanne, Prof. Kucera), and the Department of Urology (CHUV-University hospital, Lausanne, Profs. Leisinger and Jichlinski) led to the development of hexyl-ester aminolevulinic acid (HAL) for the detection of bladder cancer [Jich97]. The combined efforts of *in vitro*, preclinical and clinical studies in Lausanne eventually led to the phase II and III clinical trials undertaken together with Photocure ASA [Uehl00, Mart99, Lang99].

Clinical measurements of the PpIX fluorescence performed in human bladder cancers, with a optical fiber-based spectrofluorimeter confirmed a highly selective production of PpIX in the urothelium as compared to the detrusor muscle, as well as a high specificity for malignant urothelium. However, the PpIX fluorescence intensity was found to vary strongly between tumors [Chan96, Stei94, Forr95]. Consequently, the subsequent research program aimed at optimizing the conditions of PpIX accumulation and distribution within cancer tissue, by looking at different ways to improve the transfer of ALA (a hydrophilic molecule) through biological membranes. Various approaches were investigated, namely ALA-esterification, ALA combined with the administration of dimethylsulfoxyde (DMSO), iontophoresis, and addition of iron chelators like Desferal [Uehl00, Uehl06]. As clinical experience with iontophoresis was inconclusive [Sten96], various ALA esters administered at different concentrations were investigated.

The analysis of the PpIX accumulation kinetics and distribution across the photosensitized urothelium in the pig bladder model demonstrated the superiority of HAL administered at 4-8 mM, when compared to all other tested conditions [Mart99]. Following these preclinical studies, HAL was selected from the multitude of possible ALA-alkylesters because it represented a good compromise between water-urine solubility and sufficient PpIX formation capacity at low doses. Furthermore, HAL has been shown to lead to a homogenous distribution of PpIX-related fluorescence over the entire urothelium [Mart03]. The first clinical investigation indicated a significant increase (>2x) of PpIX fluorescence intensity could be observed with HAL using 20-fold lower concentrations as compared to ALA [Lang99]. Figure 3.9 shows some of the historical results from the *in vitro* tests, which led to the selection of the HAL for this urological application. Both figures describe the relationship of ALA-derivatives concentration and the measured fluorescence intensity on porcine mucosa and bladder cancer cells, respectively. It appears clearly on both samples (porcine mucosa and cell culture), that HAL reaches a higher level of fluorescence with a much lower concentration that ALA. Additionally, Marti *et al.* showed that instillation time required for HAL was much shorter than for ALA [Mart99]. Indeed, one

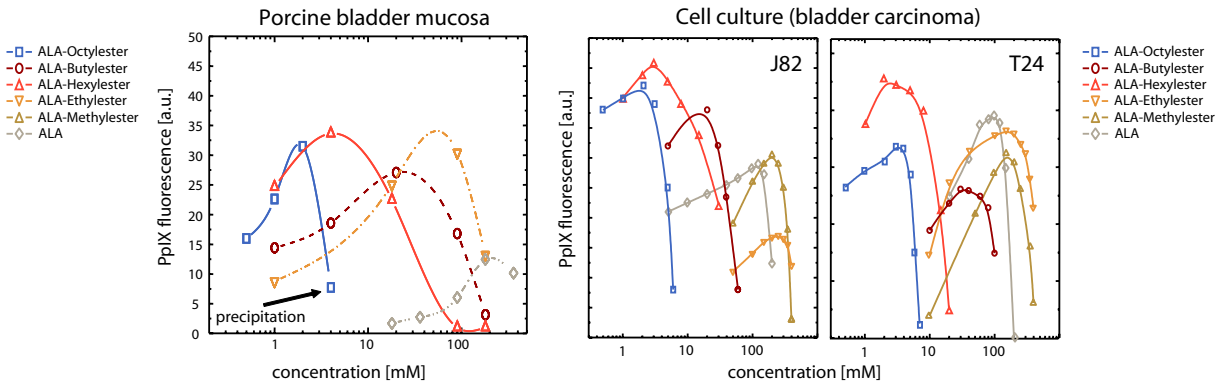

Figure 3.9: *Concentration dependence of PpIX accumulation for one culture of porcine bladder mucosa and two different cell lines with different precursors (methyl-, ethyl-, butyl-, hexyl-, and octyl-ester of ALA) [adapted from [Mart99, Uehl00]]*

hour instillation was shown to be sufficient to build-up enough PpIX in cancer cells with HAL to allow photodetection. This aspect was crucial in driving HAL as a standard method in clinical environment, as compared to ALA instillation time (2–4 hours).

This technology has been licensed to an industrial partner, PhotoCure ASA[1], leading to the approval of hexylaminolevulinate (Hexvix® as commercial name) in Europe in March 2005 for patients with known or suspected bladder cancer. Hexvix® is the first pharmaceutical product on the market that improves visual inspection of the bladder. The performance of this product is well recognized by the medical community since the European Association of Urology (EAU) officially recommended this procedure in 2005 [Babj05, Babj08]. GE Healthcare Inc.[2] licensed the global marketing and distribution rights for Hexvix® from Photocure in 2006. The benefit of Hexvix® is also supported by the fact that increased detection of non-invasive bladder tumors with Hexvix® leads to a reduced rate of recurrence of the tumors. The Food & Drug Administration (FDA) Advisory Committee agreed that Hexvix® as an adjunct to white light cystoscopy is a well-documented diagnostic procedure and has a favorable benefit/risk profile in the detection of non-muscular invasive bladder cancer. The Committee voted in favor of Hexvix® on FDAs question end of December 2009. The final approval for the new drug application (NDA) is effective since May 2010. Hexvix® will be sold on the USA-market under the name Cysview^{TM}, and must be used with a blue light cystoscopy system from Karl Storz GmbH.

3.6.3 False-positive predictors

The average specificity for PDD as reported by several groups is about 60% and ranges from 33 to 81%, mainly due to *false-positive* fluorescence areas (i.e. fluorescing lesions that are not cancer). These false-positive spots have been investigated by many groups, that reported several origins.

Dominicis *et al.* reported a learning curve for the procedure of about 15 patients [Domi01]. It will therefore not influence the sensitivity and specificity of the procedure in the large number of patients studied.

[1] `www.photocure.com`
[2] `www.gehealthcare.com` and `www.hexvix.com`

The degree of fluorescence in the tissue might vary according to the observation angle; the more tangent it is, the more the bladder mucosa may appear fluorescent, even if healthy. The use of a 30° or 70° lens is therefore recommended, and the mucosa should be observed as perpendicularly as possible to reduce the possibility of false-positive results. For these reasons false positive fluorescence may be noted during the observation of the prostatic urethra, bladder neck, and trigone [Grim03].

The fluorescence of tissue by excitation of induced PpIX is not only specific for cancer; fluorescence can also be detected in urothelial hyperplasia, squamous metaplasia, inflammatory or granulation tissue. Several factors — such as drug uptake, enzymatic activity — have been known to influence the production and conversion or depletion of PpIX after exogenous application of ALA-derivatives [Krie00]. Filbeck *et al.* also showed that inflammation or scar formation negatively influences the specificity of PDD within 6 weeks after transurethral resection [Filb99].

BCG is an important predictor for false positives in fluorescence cystoscopy. Indeed, the specificity of fluorescence cystoscopy is reduced by BCG immunotherapy up to 12 weeks after the last instillation, because it induces acute inflammatory reaction. In case of low and intermediate risk bladder tumors, it is recommended postponing PDD until 9-12 weeks after the last BCG instillation to optimally benefit from the procedure [Grim03, Drag09a, Drag09b, Drag10].

As a matter of fact, inflammation of the bladder mucosa also displays an enhanced metabolic activity, and accounts for most of the false-positive areas.

In about 90% of the cases, false positive fluorescent locations appear to be benign. Properly assessing false and true positive lesions should also incorporate genetic evaluation of false positive lesions. Zaak *et al.* have shown that some false positive lesions, histologically classified as normal urothelium, exhibit genetical changes identical to those of papillary tumors in the same patient [Zaak02].

3.6.4 Characterization of fluorescence positive-sites

Over the past years, new optical technologies have been integrated to the urological clinical environment to characterize false-positive sites: Raman spectroscopy (RS), optical coherence tomography (OCT) , and narrow-band imaging (NBI) [Caub09]. NBI was already described in Section 2.1.2. One provides here an overview of the technology and diagnostic of Raman spectroscopy and OCT, with a short explanation of the clinical significance.

3.6.4.1 Raman spectroscopy

Raman Spectroscopy (RS) enables measurement of molecular components of tissue in a qualitative and quantitative way. The principle of this optical technique is based on the Raman effect, discovered by Sir Chandrasekhara Venkata Raman in 1928 [Rao07].

Light that does not excite a molecule into one of the energy levels of the excited states (as with fluorescence) may still force it into a so-called virtual state (see Figure 3.10). This virtual state will be extremely short lived and the energy of the incident photon will be quickly reradiated, most likely as a photon with the same wavelength (*elastic scattering*). When nuclear motion (*e.g.* vibration) occurs during the lifetime of the virtual state, the molecule can relax to a higher vibrational level of the ground state while emitting a photon of longer wavelength. This process is called *Raman scattering*. Each molecule has unique vibrational energy levels, with their corresponding wavelength shifts. All of the shifted wavelengths from the different molecules in tissue, when combined, form the *Raman spectrum*, which is a function of the molecular composition of the tissue investigated.

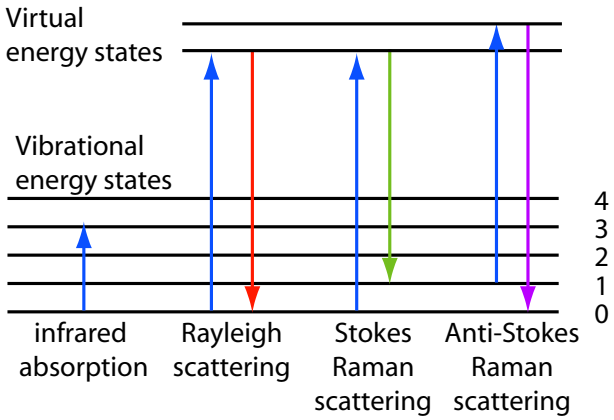

Figure 3.10: *Raman scattering, with vibrational and virtual energy states*

A change of the vibrational energy states results from the interactions of photons of the incident light interact with the tissue molecules. A new photon is emitted to account for the energy difference between the initial and the final states, resulting in a different wavelength of the scattered light. Each molecule has unique vibrational energy levels with their corresponding wavelength shifts. All of the shifted wavelengths from the different molecules in tissue combine to form the Raman spectrum, which is a function of the molecular composition of the tissue investigated. This molecular composition changes if pathologic transformations occur, and by this means RS can provide an objective prediction of pathologic diagnosis. To assist with interpretation of RS, a pseudocolor map of the tissue under examination can be created. Tissue areas with similar spectra, and therefore with similar molecular composition, are depicted in the same color, thus creating a picture comparable to histopathology.

Several groups have determined the diagnostic accuracy of RS by comparing *ex vivo* Raman measurements of bladder samples with histology. De Jong *et al.* showed that in 15 bladder tissue samples classification between tumor and non-tumor was possible with a sensitivity and specificity of 92% and 94%, respectively [deJ06]. Crow *et al.* demonstrated that differentiation between normal, inflammatory, and malignant tissue was feasible with a sensitivity of 90-95% and a specificity of 95-98% in 75 bladder tissue samples [Crow04].

3.6.4.2 Optical Coherence Tomography

Optical Coherence Tomography (OCT) produces high-resolution, cross-sectional images of tissue. The principle of this optical technique is analogous to B-mode ultrasonography except that infrared light is being used instead of sound.

The principle of optical time-domain reflectometry (OTDR) dates back in the 1980's. This method was developed for the diagnostics and optimization of fiber optic systems; in particular, the determination of fiber attenuation, splice quality, and the location of defects were of great interest. However, to investigate optical structures with dimensions in the submillimeter range, the resolution of a fiber optic OTDR system which lies in the centimeter to meter range was insufficient. In the late 1980's, an EPFL group led by René Salathé used an infrared subpicosecond pulse source in conjunction with balanced heterodyne detection, and showed experimental results demonstrating a sensitivity of more than 100 dB and a resolution of 60 μm in air. Taking advantage of the large tuning range of the laser system, it was even possible to improve the resolution to less than 10 μm [Beau89, Gilg89].

In parallel, the principle was transferred to the optical tissue characterization. First tests

of this new-called *femtosecond optical ranging* were performed in biological systems (the cornea in rabbit eyes *in vivo* and the epidermal structure of human skin *in vitro*) [Fuji86]. A first two-dimensional *in vivo* depiction of a human eye fundus along a horizontal meridian based on white light interferometric depth scans has been presented at the ICO-15 SAT conference in 1990 [Ferc90]. Cross sectional retinal imaging was also demonstrated in 1991 by a Massachusetts Institute of Technology (MIT) team headed by James G. Fujimoto [Huan91].

The working principle of an OCT system is based on a laser oscillator (*e.g.* Ti:sapphire, 800nm) coupled into the fiber-based Michelson-type interferometer. The light is split into a reference beam with variable path length and a probe beam, which is focused onto the sample. The light backscattered from the sample is recombined with the light reflected from the reference arm. The resulting interference between the recombined beams is detected as a function of the reference arm path length. An interference signal is only observed if the path difference of both arms is matched to within the coherence length of the light source, thus enabling depth resolved imaging. The demodulated interference pattern – representing a depth profile of the backscattered intensity – is transferred to a grayscale map for graphic representation. Adjacent A-scans are detected by scanning the laser beam across the sample resulting in a cross-sectional image (B-scan).

The main contrast mechanism is *elastic light scattering*. The amplitude of the scattered light, which is influenced by tissue type, is measured at different tissue depths. Adjacent depth profiles can be displayed in real time, resulting in an image comparable to histopathology, with resolutions down to 10 μm and at depths of around 1-3 mm [Zysk07]. Ultrahigh resolution systems even achieve an overall axial resolution of 3.6 μm in air (< 3 μm in tissue) [Herm08].

In non-diseased tissue, the three anatomic layers of the bladder wall can be well distinguished with OCT. This is feasible due to the different scattering properties of each distinct layer resulting in different intensities within an image [Tear97]. Figure 3.11 shows the three main layers (urothelium, lamina propria, muscularis mucosa). In bladder cancer tissue, these layers are usually no longer distinguishable [Herm08]. Furthermore, probably due to the higher nuclear-cytoplasm ratio, the OCT images can show different backscattering properties. A broadened urothelium is also seen in case of a papillary tumor. In contrast to ultrasonography, OCT does not require a conducting medium or direct contact during imaging, which makes it easily applicable in endourology [Many05].

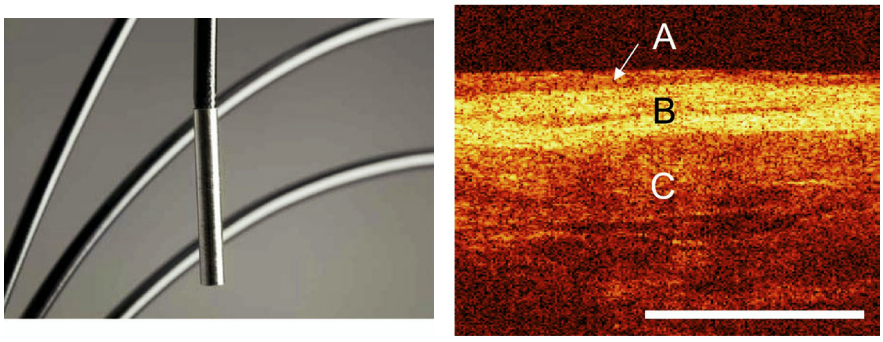

Figure 3.11: *Left: One of the current implementation of the optical fiber based OCT probe (diameter 2.7 mm). It easily passes through the working channel of standard cystoscopy equipment. Right: OCT image of normal urothelium: Mucosa is dark and thin (A). Lamina propria is bright and clearly defined (B). Muscularis layer is dark with striated appearance (C).*

Two recent clinical studies demonstrated the potential of OCT in a clinical context.

Schmidbauer *et al.* performed a single-center study with same-patient comparison, patients with suspected bladder cancer first received an intravesical instillation of HAL [Schm09]. Cystoscopy was performed in WL, followed by blue-light inspection and OCT scanning. In 66 patients studied, 232 lesions were detected and scanned by OCT, and were subsequently resected or biopsied. Additionally, 132 areas of normal-appearing urothelium were investigated by all three methods and biopsied. On a per-lesion basis, sensitivity and specificity were respectively 69.3% and 83.7% for WL, 97.5% and 78.6% for HAL, and 97.5% and 97.9% for HAL combined with OCT. Overall, bladder cancer was diagnosed in 58 patients (87.9%), with a per-patient sensitivity of 89.7% for WL and 100% for both HAL alone and HAL with targeted OCT. Per-patient specificity for HAL alone and targeted HAL was 62.5% and 87.5%, respectively.

Goh *et al.* obtained 94 images in 32 patients undergoing bladder biopsy or transurethral resection of bladder tumor [Goh08]. They correlated 38 suspicious areas with biopsy findings. OCT imaging correctly identified tumors confined to the mucosa with a sensitivity and specificity of 90% and 89%, respectively. Muscle-invasive tumors were detected in 7 of 7 lesions with 100% sensitivity, 90% specificity, and 92% accuracy.

3.6.4.3 Multiphoton endoscopy

Briefly, multiphoton microscopy (MPM) or multiphoton endoscopy (MPE) involve the illumination of tissue by near-infrared light from a femtosecond pulsed laser, which is used to excite fluorescence from the naturally occurring fluorophores residing at the focal volume. In addition to cellular autofluorescence, MPM allows the identification of non-centrosymmetric structures such as collagen by utilizing a higher order scattering phenomenon called *Second Harmonic Generation* (SHG). MPE enables visualization of cellular layers and intracellular organs with deep penetration depth (several hundred of microns), and can be used *in vivo* to directly observe molecular mechanisms of life without the need for removing tissue from the body (biopsy).

The human bladder is an ideal candidate for MPM imaging and MPE methodology, since it has a well-defined architecture, whose perturbation by cancer can be easily detected at cellular and tissue organization levels. MPM can identify the morphology of the umbrella cells very well, as well as the perturbation of the urothelial layer is visible by MPM. Indeed, the layer of connective tissue containing collagen and scattered smooth muscle cells, known as the lamina propria, can be well resolved with SHG.

Multiphoton endoscopes allow real time, non-invasive biopsies of the human bladder, as well as an up-close assessment of the resection margin. To demonstrate this principle, Mukherjee *et al.* used a bench-top multiphoton microscope to identify cancers in fresh, unfixed human bladder biopsies [Mukh09]. Multiphoton images were acquired in two channels: (1) broadband autofluorescence (420–530 nm) from cells, and (2) SHG (390±35 nm), mostly by tissue collagen. These images are then compared with gold standard hematoxylin/eosin (H&E) stained histopathology slides from the same specimen. These authors found excellent correlation between the multiphoton and histopathological diagnoses. These results are confirmed by Cicchi *et al.* [Cicc10]. Additionally, these latter authors showed that tumor cells appeared slightly different in shape and with a smaller cellular-to-nuclear dimension ratio with respect to corresponding normal cells. Further differences between the two tissue types were found in both spectral emission and fluorescence lifetime distribution by performing temporal- and spectral resolved analysis of fluorescence. This method may represent a promising tool to be used in a multi-photon endoscope for *in vivo* optical diagnosis of bladder cancer.

Several factors must be considered for the extension of MPM imaging technology from *ex*

vivo biopsies to endoscopic imaging in real patients. MPM has still a limited field of view and relatively slow image acquisition speeds, but can ideally combined with another high specificity primary detection technique. ALA-derivatives based fluorescence detection is a good candidate, but no study to date has shown that the porphyrin content in cells does not interfere with the autofluorescence signatures in MPM.

MPE has been implemented in several explorative fiber-based probes, but no commercial device has been developed up to now. For instance, Myaing *et al.* report on the development of a miniature, flexible, fiber-optic scanning endoscope for two-photon fluorescence imaging [Myai06]. The endoscope uses a tubular piezoelectric actuator for achieving two-dimensional beam scanning and a double-clad fiber for delivery of the excitation light and collection of two-photon fluorescence. Bao *et al.* developed an other approach for three-dimensional (3D) *in vivo* cellular imaging [Bao08]. Their device has a "large" field of view (475×475 μm^2), with 250 μm depth imaging capability. Its lateral and axial resolutions are better than 1 and 14.5 μm, respectively. This hand-held device can be easily adapted to an existing endoscopic imaging system. These authors had improved the acquisition speed by a factor 10 as compared to [Myai06], but it remains a important limitation for clinical use (0.4 mm^2/s vs. 0.04 mm^2/s).

Tang *et al.* developed a prototype based on a 1030 nm femto-second fiber laser, a two-axis microelectromechanical system (MEMS) mirror and double-cladding photonics crystal fiber [Tang09a, Tang09b]. The laser pulse duration is 150 fs, the average power is 200 mW, and the repetition rate is 40 MHz. They achieve an image rate of 0.25 Hz (128 × 128 pixels^2, with 3 μm resolution). They acquired sample images from rat tail tendon and human skin samples (SHG), and two-photon excited fluorescence from human skin tissues stained with exogenous fluorophore.

These multiphoton approach has shown great potential on bench-top microscopes regarding resolution and "non-invasive staining". However, the endoscopic approach is still under development, and needs tremendous progresses before being integrating in the clinical routine.

3.7 Angiogenesis related to bladder cancer

Once a tumor grows beyond approximately 100-200 μm in diameter, passive diffusion is no longer able to support malignant cell division, and neovascularization becomes essential [Carm00]. Charlesworth and Harris reviewed the mechanisms underlying urologic malignancies [Char06], including vessel sprouting and bridge formation. These processes depend on endothelial cell migration and proliferation.

In endoscopic imaging, we are interested to look at the new vessel formation and reorganization, because this vascular information is likely to be discriminant between true and false positive lesions in the bladder, and other organs.

3.7.1 General definitions

Angiogenesis is a physiological process involving the growth of new blood vessels from pre-existing vessels. Though there has been some debate over terminology, *vasculogenesis* is the term used for spontaneous blood-vessel formation, and *intussusception* is the term for new blood vessel formation by splitting off existing ones.

Angiogenic vessels show several differences from mature vessels. They have a disorganized and irregular structure. Angiogenic endothelial cells exhibit altered surface markers and cell adhesion molecules that reflect their increased proliferation, protein expression and secretion.

Angiogenesis related to bladder cancer may release proteins into the urine, that can be detected externally (see Section 3.4.2).

Angiogenesis is mostly hypoxia driven. Hypoxia promotes the formation of blood vessels, and is important for the formation of a vascular system. Indeed, hypoxia-inducible factors (HIFs) are transcription factors that respond to changes in available oxygen in the cellular environment, specifically, to decreases in oxygen. In particular, HIF-1, when stabilized by hypoxic conditions, upregulates several genes to promote survival in low-oxygen conditions, including *vascular endothelial growth factor* (VEGF) [Beni08]. Jain *et al.* highlighted that one specific type of VEGF (also referred to as VEGF-A) appears to be the most critical of all the known angiogenic molecules. VEGF promotes the survival and proliferation of endothelial cells, increases the display of adhesion molecules on these cells, and increases vascular permeability [Jain05].

Tumor blood vessels have different morphology than the normal vasculature. Angiogenesis in tumors causes excess recruitment of endothelial cells. However, VEGF over-expression leads to formation of additional micronetworks connected to higher order vessels, rather than insertion of individual capillaries into the existing vessels structure [Hein08]. In addition, tumor vessels are tortuous, dilated, and can have dead ends. They are not organized into definitive venules, arterioles and capillaries like their normal counterparts, but rather share chaotic features of all of them [Berg03].

The ideal imaging tool for angiogenesis would need to have a resolution high enough to demonstrate not only increased density of microvessels, but also to show the microscopic hallmarks of angiogenesis as mentioned before. In addition, characterization of the angiogenesis during the neoplastic process and monitoring of blood vessels, blood supply, and vessel architecture *in vivo* during ongoing therapy would be of interest. Within the last few years, certain developments have been achieved in endoscopic imaging with the potential to enable these objectives.

The first step was to enable magnifying endoscopy to get a deeper insight into tissue characteristics and vascularization. An irregular microvascular pattern appears to be capable of predicting the histologic characteristics of cancerous lesions in the GI tract [Yosh04, Curv08]. Meining *et al.* acquired images of blood vessels with the Cellvizio® fiber-based confocal probe (see Section 2.4). Here, again, an irregular vascular pattern with leakage of fluorescein was associated with neoplasia in the colon [Mein08]. In addition, this system can be combined with a "vessel viewer" application software, which seems to be very helpful to objectively measure vessel density and blood flow.

3.7.2 Microvessel density (MVD)

Tumor angiogenesis can be assessed on histopathological slides by using an antibody to endothelial cells, to identify tumor vasculature. Microvessel density (MVD) can then be measured either as an average of counts over a number of randomly selected areas, or quantified in the densest areas of neovascularization, termed *hotspots*. A variety of immunohistochemical techniques have been used to assess MVD, based on antibodies to CD31, CD34 or factor-VIII-related antigen [Char06]. The inconsistency between results from different investigators has often been partly blamed on variation in the methodology of measuring MVD.

High MVD was initially shown to be an independent predictor of survival [Dick94]. Increasing MVD has subsequently been shown to be associated with increasing incidence of tumor recurrence, stage progression, lymph-node metastases and the presence of vascular invasion [Boch95, Godd03].

There have been a number of reviews on MVD that summarize the growing body of evi-

dence supporting MVD as a method of assessing urologic malignancies, but that also show the pitfalls [Dick94, Kerb02, Fox04]. For instance, it was amply demonstrated in the study of Axelsson *et al.* , where after an initial training period with Weidner, no association between MVD and patient survival was observed [Axel95]. Hlatky *et al.* reviewed studies demonstrating the value of using tumor MVD as a prognostic indicator for a wide range of cancers. In this context, measurement of MVD facilitates assessments of disease stage and the likelihood of recurrence and helps guide treatment decisions [Hlat02]. Recently, however, it has been assumed by some investigators that measurements of MVD may also reveal the degree of angiogenic activity in a tumor. Based on this assumption, quantification of MVD is thought to constitute a surrogate marker for the efficacy of antiangiogenic agents as well as a mean by which to assess which patients are good candidates for antiangiogenic therapy prior to treatment. In the same review, Hlatky *et al.* showed that MVD is not by itself an indicator of therapeutic efficacy, nor should it be used to guide the stratification of patients for therapeutic trials.

3.7.3 Significance to bladder cancer

The vascular system of the urinary bladder wall effectively performs its function in spite of considerable spatial changes due to the filling/voiding cycle. However, only a few studies have dealt with the microvascular architecture of the bladder wall: a classical description of its histology including vascularization by von Möllendorff (1930) and a microangiographic study by Sarma (1981).

Miodonski *et al.* published two studies in which they described the microvasculature visualized by scanning electron microscopy (SEM) of vascular corrosion casts [Miod98, Miod99]. Postoperative bladder specimens obtained from patients with advanced bladder tumors were filled with small amount (80 ml) of saline and perfused via at least four largest arteries with anticoagulant-containing saline followed by paraformaldehyde/glutaraldehyde fixative and Mercox resin. After polymerization of the resin, the vascular casts were macerated with potassium hydroxide, cleaned with formic acid and water and freeze dried. Only regions of the bladder wall distant to the tumor were examined in light and scanning electron microscopes. They explained the adaptation of bladder mucosa to contraction of the muscularis by two mechanisms: 1) decrease in the epithelial surface by reorganization of the urothelium and 2) extensive folding of the mucosa. Miodonski *et al.* also highlighted two major vascular plexuses (adventitial/serosal and mucosal) and two distinct capillary networks (muscular and subepithelial) in the successive layers of the wall (see Figure 3.12).

Larger branches of main extra-vesical arteries and veins formed the adventitial/serosal plexus characterized by highly tortuous course of the vessels and numerous anastomoses. This plexus supplied and drained the capillary network of the muscularis and also sent long, perpendicular vessels, 100–300 μm in diameter, piercing the muscularis and communicating directly with the mucosal plexus. The perpendicular vessels were almost straight, wavy, tortuous or tightly coiled, depending on whether they joined the mucosal plexus near the top or near the base of the fold. The mucosal plexus consisted of some capillaries, thin arteries (50–100 μm) and more numerous, thicker veins (80–250 μm), showing a tortuous appearance and frequent interlacements; it formed a distinct vascular layer parallel to the inner surface of the bladder and following the profiles of mucosal folds [Miod98].

There is clear evidence that the features of angiogenesis (such as MVD) and expression of angiogenic factors (such as VEGF) are related to adverse outcomes in bladder cancer [Char06]. Goddard *et al.* showed that MVD in superficial bladder cancer is significantly higher in those cases that subsequently progress to muscle invasive disease [Godd03].

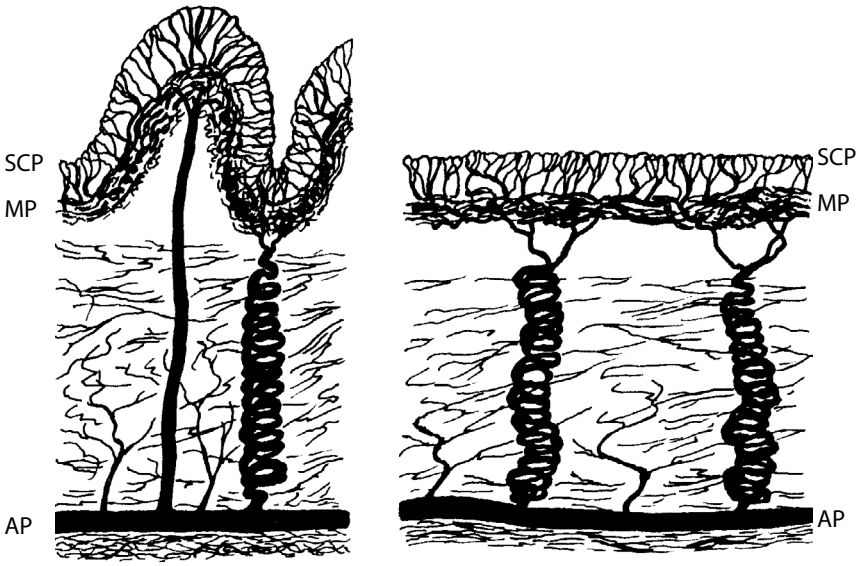

Figure 3.12: *Schematic representation of the vascular topography in the wall of empty (left) and filled (right) human urinary bladder. SCP, subepithelial capillary plexus; MP, mucosal plexus; AP, adventitial plexus ([Miod99]).*

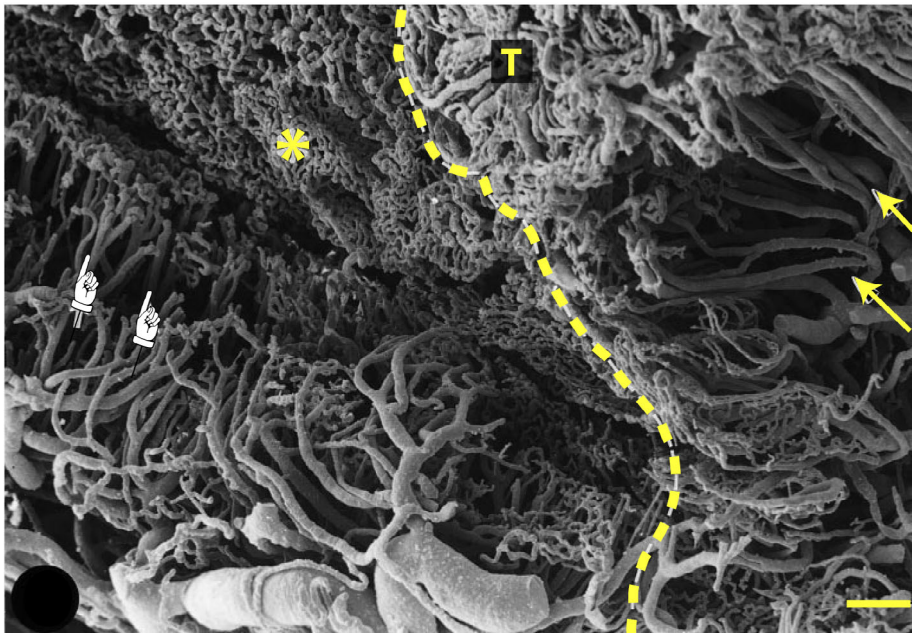

Figure 3.13: *Vascular architecture of mucosa adjacent to a tumor. The yellow dashed line separates the vasculature of the tumor (T). Note uneven surface of the subepithelial capillary network, with elevations and depressions (asterisk) and palisade-like array of its supplying and draining vessels (white hands, left) similar to that present in the tumor (yellow arrows, right). Bar 200µm(adapted from [Miod98])*

From a molecular point of view, thrombospondin-1 (TSP-1) is 430 kDa glycoprotein produced by normal urothelial cells that is strongly antiangiogenic. Campbell *et al.* showed that downregulation of TSP-1 secretion is a key event in the switch from an anti-angiogenic to an angiogenic phenotype, which occurs early in the development of bladder cancer [Camp98].

3.7.4 Imaging angiogenesis in the bladder

Zimmern *et al.* showed that fluorescein angiography reveals markedly increased uptake in papillary tumors and carcinoma in situ compared with normal urothelium [Zimm95]. Areas of papillary transitional cell tumor and carcinoma *in situ* developed a brilliant yellow-green fluorescence, indicating that neovascularity is acquired relatively early during bladder tumorigenesis. Adjacent normal urothelium was non-fluorescent and provided a contrasting dark background facilitating the detection of all lesions.

Several imaging techniques have been employed *in vivo* to analyze tumor vasculature, for instance before and after the administration of antiangiogenic and antivascular drugs, in order to assess (i) proof of principle, by demonstrating that a new drug has impacted on the tumor vasculature, and (ii) proof of concept, to confirm that the drug has achieved a clinically relevant end point.

The main techniques that have been employed to image angiogenesis in the clinic are MRI, CT and PET. Resection biopsy is the "gold standard" technique for the diagnosis and staging of bladder cancer. Prior to resection, conventional CT and MRI are performed, demonstrating equivalent high accuracy in staging of muscle-invasive (T2-T4) disease. However, their utility in distinguishing superficial (T1) from early muscle-invasive (T2) tumors is poor. Additionally, they are unable to detect flat lesions such as carcinoma *in situ*. Other techniques, such as contrast-enhanced ultrasonography (CEUS) and optical imaging, might play an important role in the future [Zee10]. CEUS allows imaging of vessels with diameters of 50-100 μm by combining the use of Doppler ultrasonography with contrast agents in the form of gas-encapsulated microbubbles under 10 μm in diameter [Nico08, Nico09].

Reiher *et al.* showed that the association of p53 status with microvessel density in their patient population was weak, whether assessed by staining for CD31 or CD34 [Reih02]. However, this study confirmed the strong association of p53 and microvessel density with the well established prognostic factors of grade and stage in superficial bladder cancer, supporting other evidence of an important role for p53 and angiogenesis in the tumor biology of this disease. Their data also suggested that p53 is not a primary regulator of angiogenesis in this patient population. This suggested that other genetic or environmental factors may contribute to the regulation of angiogenesis in superficial bladder cancer.

Korkolopoulou *et al.* stated that the studies based on microvessel density (MVD) as the only factor reflecting angiogenesis overlooked other parameters that might be significant as well, such as the complexity of the microvascular network, the size and shape of microvessels, and the immunostaining intensity of endothelial cells [Kork01]. These authors concluded that the prognostic significance of neovascularization is better assessed by area and shape-related morphometric characteristics, whereas MVD becomes influential only with regard to overall survival of patients with invasive tumors.

Summarily, all these studies tend to show that an *in situ* observation of the vascularization developing in early bladder cancer may give a useful information over tumor progression potential. Therefore, characterizing the vascularization underlying the fluorescence positive spots is of high interest. This thesis is an optical contribution to imaging angiogenesis in bladder cancer. That is the purpose of the study presented in Chapter 5.

Bibliography

[Ackr01] R. Ackroyd, C. Kelty, N. Brown, and M. Reed. The history of photodetection and photodynamic therapy. *Photochemistry and Photobiology*, 74(5):656–669, 2001.

[Apod04] G. Apodaca. The uroepithelium: not just a passive barrier. *Traffic*, 5(3):117–128, Mar 2004.

[Axel95] K. Axelsson, B. M. Ljung, D. H. Moore, A. D. Thor, K. L. Chew, S. M. Edgerton, H. S. Smith, and B. H. Mayall. Tumor angiogenesis as a prognostic assay for invasive ductal breast carcinoma. *J Natl Cancer Inst*, 87(13):997–1008, Jul 1995.

[Babj05] M. Babjuk, V. Soukup, R. Petrík, M. Jirsa, and J. Dvorácek. 5-aminolaevulinic acid-induced fluorescence cystoscopy during transurethral resection reduces the risk of recurrence in stage Ta/T1 bladder cancer. *BJU International*, 96(6):798–802, Oct 2005.

[Babj08] M. Babjuk, W. Oosterlinck, R. Sylvester, E. Kaasinen, A. Böhle, J. Palou-Redorta, and E. A. of Urology (EAU). EAU guidelines on non-muscle-invasive urothelial carcinoma of the bladder. *Eur Urol*, 54(2):303–314, Aug 2008.

[Bao08] H. Bao, J. Allen, R. Pattie, R. Vance, and M. Gu. Fast handheld two-photon fluorescence microendoscope with a 475 microm x 475 microm field of view for in vivo imaging. *Opt Lett*, 33(12):1333–1335, Jun 2008.

[Baum92] R. Baumgartner, M. Kriegmair, D. Jocham, A. G. Hofstetter, R. M. Huber, O. Karg, and K. Haeussinger. Photodynamic diagnosis of early stage malignancies: preliminary results in urology and pneumonology. In *Physiological Monitoring and Early Detection Diagnostic Methods*, volume 1641, pages 107–112, 1992.

[Beau89] P. Beaud, J. Schutz, W. Hodel, H. P. Weber, H. H. Gilgen, and R. P. Salathe. Optical reflectometry with micrometer resolution for the investigation of integrated optical devices. *Journal of Quantum Electronics*, 25(4):755–759, 1989.

[Beni08] E. Benizri, A. Ginouvès, and E. Berra. The magic of the hypoxia-signaling cascade. *Cell Mol Life Sci*, 65(7-8):1133–1149, Apr 2008.

[Berg03] G. Bergers and L. E. Benjamin. Tumorigenesis and the angiogenic switch. *Nat Rev Cancer*, 3(6):401–410, Jun 2003.

[Bird07] L. A. Birder and W. C. de Groat. Mechanisms of disease: involvement of the urothelium in bladder dysfunction. *Nat Clin Pract Urol*, 4(1):46–54, Jan 2007.

[Boch95] B. H. Bochner, R. J. Cote, N. Weidner, S. Groshen, S. C. Chen, D. G. Skinner, and P. W. Nichols. Angiogenesis in bladder cancer: relationship between microvessel density and tumor prognosis. *J Natl Cancer Inst*, 87(21):1603–1612, Nov 1995.

[Bott03] M. F. Botteman, C. L. Pashos, A. Redaelli, B. Laskin, and R. Hauser. The health economics of bladder cancer: a comprehensive review of the published literature. *Pharmacoeconomics*, 21(18):1315–1330, 2003.

[Boyd74] P. J. Boyd and K. G. Burnand. Site of bladder-tumour recurrence. *Lancet*, 2(7892):1290–1292, Nov 1974.

[Camp98] S. C. Campbell, O. V. Volpert, M. Ivanovich, and N. P. Bouck. Molecular mediators of angiogenesis in bladder cancer. *Cancer Res*, 58(6):1298–1304, Mar 1998.

[Carm00] P. Carmeliet and R. K. Jain. Angiogenesis in cancer and other diseases. *Nature*, 407(6801):249–257, Sep 2000.

[Case06] R. G. Casey and J. A. Thornhill. Joaquin Maria Albarran y Dominguez: microbiologist, histologist, and urologist–a lifetime from orphan in cuba to nobel nominee. *Int J Urol*, 13(9):1159–1161, Sep 2006.

[Caub09] E. C. C. Cauberg, D. M. de Bruin, D. J. Faber, T. G. van Leeuwen, J. J. M. C. H. de la Rosette, and T. M. de Reijke. A new generation of optical diagnostics for bladder cancer: technology, diagnostic accuracy, and future applications. *Eur Urol*, 56(2):287–296, Aug 2009.

[Chan96] S. C. Chang, A. J. MacRobert, and S. G. Bown. Biodistribution of protoporphyrin ix in rat urinary bladder after intravesical instillation of 5-aminolevulinic acid. *J Urol*, 155(5):1744–1748, May 1996.

[Char06] P. J. S. Charlesworth and A. L. Harris. Mechanisms of disease: Angiogenesis in urologic malignancies. *Nature Clinical Practice Urology*, 3(3):157–169, 2006.

[Chen09a] L. Cheng, R. Montironi, D. D. Davidson, and A. Lopez-Beltran. Staging and reporting of urothelial carcinoma of the urinary bladder. *Mod Pathol*, 22 Suppl 2:S70–S95, Jun 2009.

[Chen09b] L. Cheng, S. Zhang, D. D. Davidson, G. T. MacLennan, M. O. Koch, R. Montironi, and A. Lopez-Beltran. Molecular determinants of tumor recurrence in the urinary bladder. *Future Oncol*, 5(6):843–857, Aug 2009.

[Cicc10] R. Cicchi, A. Crisci, A. Cosci, G. Nesi, D. Kapsokalyvas, S. Giancane, M. Carini, and F. S. Pavone. Time- and spectral-resolved two-photon imaging of healthy bladder mucosa and carcinoma in situ. *Opt Express*, 18(4):3840–3849, Feb 2010.

[Crow04] P. Crow, J. S. Uff, J. A. Farmer, M. P. Wright, and N. Stone. The use of raman spectroscopy to identify and characterize transitional cell carcinoma in vitro. *BJU Int*, 93(9):1232–1236, Jun 2004.

[Curv08] W. L. Curvers, R. Kiesslich, and J. J. G. H. M. Bergman. Novel imaging modalities in the detection of oesophageal neoplasia. *Best Pract Res Clin Gastroenterol*, 22(4):687–720, 2008.

[Dani05] D. I. Daniltchenko, C. R. Riedl, M. D. Sachs, F. Koenig, K. L. Daha, H. Pflueger, S. A. Loening, and D. Schnorr. Long-term benefit of 5-aminolevulinic acid fluorescence assisted transurethral resection of superficial bladder cancer: 5-year results of a prospective randomized study. *J Urol*, 174(6):2129–33, discussion 2133, Dec 2005.

[deJ06] B. W. D. de Jong, T. C. B. Schut, K. Maquelin, T. van der Kwast, C. H. Bangma, D.-J. Kok, and G. J. Puppels. Discrimination between nontumor bladder tissue and tumor by raman spectroscopy. *Anal Chem*, 78(22):7761–7769, Nov 2006.

[Deno46] P. Denoix. Enquete permanent dans les centres anticancereaux. *Bull Inst Nat Hyg*, 1:70–5, 1946.

[Dick94] A. J. Dickinson, S. B. Fox, R. A. Persad, J. Hollyer, G. N. Sibley, and A. L. Harris. Quantification of angiogenesis as an independent predictor of prognosis in invasive bladder carcinomas. *Br J Urol*, 74(6):762–766, Dec 1994.

[Domi01] C. D. Dominicis, M. Liberti, G. Perugia, C. D. Nunzio, F. Sciobica, A. Zuccalà, A. Sarkozy, and F. Iori. Role of 5-aminolevulinic acid in the diagnosis and treatment of superficial bladder cancer: improvement in diagnostic sensitivity. *Urology*, 57(6):1059–1062, Jun 2001.

[Drag09a] R. O. P. Draga, M. C. M. Grimbergen, and J. L. H. R. Bosch. Noninvasive transitional cell carcinoma is associated with a high occurrence of false positives in photodynamic diagnosis. *Eur Urol*, Jul 2009.

[Drag09b] R. O. P. Draga, M. C. M. Grimbergen, E. T. Kok, T. N. Jonges, and J. L. H. R. Bosch. Predictors of false positives in 5-aminolevulinic acid-induced photodynamic diagnosis of bladder carcinoma: identification of patient groups that may benefit most from highly specific optical diagnostics. *Urology*, 74(4):851–856, Oct 2009.

[Drag10] R. O. P. Draga, M. C. M. Grimbergen, E. T. Kok, T. N. Jonges, C. F. P. van Swol, and J. L. H. R. Bosch. Photodynamic diagnosis (5-aminolevulinic acid) of transitional cell carcinoma after bacillus calmette-guérin immunotherapy and mitomycin c intravesical therapy. *Eur Urol*, 57(4):655–660, 2010.

[Drol00] M. J. Droller and P. U. Malmström. Premalignant lesions and carcinoma in situ in bladder neoplasia: introduction and overview. *Scand J Urol Nephrol Suppl*, 34(205):62–66, 2000.

[Drol05] M. J. Droller. Biological considerations in the assessment of urothelial cancer: a retrospective. *Urology*, 66(5 Suppl):66–75, Nov 2005.

[E.-O09] ECO-OEC. European cancer observatory, observatoire européen du cancer. international agency for research on cancer, lyon., 2009.

[Epst98] J. I. Epstein, M. B. Amin, V. R. Reuter, F. K. Mostofi, F. Algaba, W. C. Allsbrook, A. G. Ayala, M. J. Becich, A. L. Beltran, L. Boccon-Gibod, D. G. Bostwick, C. Busch, C. J. Davis, J. N. Eble, C. S. Foster, M. Furusato, D. J. Grignon, P. A. Humphrey, E. A. Ishak, S. L. Johansson, E. C. Jones, L. G. Koss, H. S. Levin, W. M. Murphy, R. O. Petersen, A. Renshaw, J. Y. Ro, J. R. Ross, I. A. Sesterhenn, J. R. Srigley, S. Suzigan, J. B. Tomaszewski, P. Troncoso, L. D. True, M. A. Weiss, T. M. Wheeler, and R. H. Young. The World Health Organization/International Society of Urological Pathology consensus classification of urothelial (transitional cell) neoplasms of the urinary bladder. *American Journal of Surgical Pathology*, 22(12):1435–1448, 1998.

[Ferc90] A. F. Fercher. Ophthalmic interferometry. In G. von Bally and S. Khanna, editors, *Proceedings of the International Conference on Optics in Life Sciences*, pages 221–228, 1990.

[Filb99] T. Filbeck, W. Roessler, R. Knuechel, M. Straub, H. J. Kiel, and W. F. Wieland. 5-aminolevulinic acid-induced fluorescence endoscopy applied at secondary transurethral resection after conventional resection of primary superficial bladder tumors. *Urology*, 53(1):77–81, Jan 1999.

[Forr95] M. Forrer, T. Glanzmann, J. Mizeret, D. Braichotte, G. Wagnieres, H. van den Bergh, P. Jichlinski, and H. Leisinger. Fluorescence excitation and emission spectra of ala-induced protoporphyrin ix in normal and tumoral tissue of the human bladder. In *Optical Biopsy and Fluorescence Spectroscopy and Imaging*, volume 2324, pages 84–88, 1995. cited By (since 1996) 7.

[Fox04] S. B. Fox and A. L. Harris. Histological quantitation of tumour angiogenesis. *APMIS*, 112(7-8):413–430, 2004.

[Fuji86] J. G. Fujimoto, S. D. Silvestri, E. P. Ippen, C. A. Puliafito, R. Margolis, and A. Oseroff. Femtosecond optical ranging in biological systems. *Opt Lett*, 11(3):150, Mar 1986.

[Gilg89] H. H. Gilgen, R. P. Novak, R. P. Salathe, W. Hodel, and P. Beaud. Submillimeter optical reflectometry. *Journal of Lightwave Technology*, 7(8):1225–1233, 1989.

[Godd03] J. C. Goddard, C. D. Sutton, P. N. Furness, K. J. O'Byrne, and R. C. Kockelbergh. Microvessel density at presentation predicts subsequent muscle invasion in superficial bladder cancer. *Clin Cancer Res*, 9(7):2583–2586, Jul 2003.

[Goh08] A. C. Goh, N. J. Tresser, S. S. Shen, and S. P. Lerner. Optical coherence tomography as an adjunct to white light cystoscopy for intravesical real-time imaging and staging of bladder cancer. *Urology*, 72(1):133–137, Jul 2008.

[Gray18] H. Gray. *Anatomy of the Human Body*. Lea & Febiger, Philadelphia, 1918.

[Grim03] M. C. M. Grimbergen, C. F. P. van Swol, T. G. N. Jonges, T. A. Boon, and R. J. A. van Moorselaar. Reduced specificity of 5-ala induced fluorescence in photodynamic diagnosis of transitional cell carcinoma after previous intravesical therapy. *Eur Urol*, 44(1):51–56, Jul 2003.

[Hafn01] C. Hafner, R. Knuechel, L. Zanardo, W. Dietmaier, H. Blaszyk, J. Cheville, F. Hofstaedter, and A. Hartmann. Evidence for oligoclonality and tumor spread by intraluminal seeding in multifocal urothelial carcinomas of the upper and lower urinary tract. *Oncogene*, 20(35):4910–4915, Aug 2001.

[Hein08] S. Heinzer, G. Kuhn, T. Krucker, E. Meyer, A. Ulmann-Schuler, M. Stampanoni, M. Gassmann, H. H. Marti, R. Müller, and J. Vogel. Novel three-dimensional analysis tool for vascular trees indicates complete micro-networks, not single capillaries, as the angiogenic endpoint in mice overexpressing human vegf(165) in the brain. *Neuroimage*, 39(4):1549–1558, Feb 2008.

[Herm08] B. Hermes, F. Spöler, A. Naami, J. Bornemann, M. Först, J. Grosse, G. Jakse, and R. Knüchel. Visualization of the basement membrane zone of the bladder by optical coherence tomography: feasibility of noninvasive evaluation of tumor invasion. *Urology*, 72(3):677–681, Sep 2008.

[Hlat02] L. Hlatky, P. Hahnfeldt, and J. Folkman. Clinical application of antiangiogenic therapy: microvessel density, what it does and doesn't tell us. *J Natl Cancer Inst*, 94(12):883–893, Jun 2002.

[Huan91] D. Huang, E. A. Swanson, C. P. Lin, J. S. Schuman, W. G. Stinson, W. Chang, M. R. Hee, T. Flotte, K. Gregory, and C. A. Puliafito. Optical coherence tomography. *Science*, 254(5035):1178–1181, Nov 1991.

[Jain05] R. K. Jain. Normalization of tumor vasculature: an emerging concept in antiangiogenic therapy. *Science*, 307(5706):58–62, Jan 2005.

[Jema09] A. Jemal, R. Siegel, E. Ward, Y. Hao, J. Xu, and M. J. Thun. Cancer statistics, 2009. *CA Cancer J Clin*, 59(4):225–249, 2009.

[Jens91] V. Jensen. The TURP syndrome. *Can J Anaesth*, 38(1):90–96, Jan 1991.

[Jich97] P. Jichlinski, M. Forrer, J. Mizeret, T. Glanzmann, D. Braichotte, G. Wagnières, G. Zimmer, L. Guillou, F. Schmidlin, P. Graber, H. D. Van Bergh, and H. J. Leisinger. Clinical evaluation of a method for detecting superficial transitional cell carcinoma of the bladder by light-induced fluorescence of protoporphyrin ix following topical application of 5-aminolevulinic acid: Preliminary results. *Lasers in Surgery and Medicine*, 20(4):402–408, 1997.

[Joch05] D. Jocham, F. Witjes, S. Wagner, B. Zeylemaker, J. Van Moorselaar, M. O. Grimm, R. Muschter, G. Popken, F. König, R. Knüchel, and K. H. Kurth. Improved detection and treatment of bladder cancer using hexaminolevulinate imaging: A prospective, phase iii multicenter study. *Journal of Urology*, 174(3):862–866, 2005.

[Jone93] P. A. Jones and M. J. Droller. Pathways of development and progression in bladder cancer: new correlations between clinical observations and molecular mechanisms. *Semin Urol*, 11(4):177–192, Nov 1993.

[Kauf09] D. S. Kaufman, W. U. Shipley, and A. S. Feldman. Bladder cancer. *Lancet*, 374(9685):239–249, Jul 2009.

[Kenn90] J. C. Kennedy, R. H. Pottier, and D. C. Pross. Photodynamic therapy with endogenous protoporphyrin ix: basic principles and present clinical experience. *J Photochem Photobiol B*, 6(1-2):143–148, Jun 1990.

[Kerb02] R. Kerbel and J. Folkman. Clinical translation of angiogenesis inhibitors. *Nat Rev Cancer*, 2(10):727–739, Oct 2002.

[Kiem09] L. A. Kiemeney, A. J. Grotenhuis, S. H. Vermeulen, and X. Wu. Genome-wide association studies in bladder cancer: first results and potential relevance. *Curr Opin Urol*, 19(5):540–546, Sep 2009.

[Kork01] P. Korkolopoulou, A. E. Konstantinidou, N. Kavantzas, E. Patsouris, P. M. Pavlopoulos, P. Christodoulou, E. Thomas-Tsagli, and P. Davaris. Morphometric microvascular characteristics predict prognosis in superficial and invasive bladder cancer. *Virchows Arch*, 438(6):603–611, Jun 2001.

[Krie94] M. Kriegmair, R. Baumgartner, R. Knuechel, P. Steinbach, A. Ehsan, W. Lumper, F. Hofstädter, and A. Hofstetter. Fluorescence photodetection of neoplastic urothelial lesions following intravesical instillation of 5-aminolevulinic acid. *Urology*, 44(6):836–841, Dec 1994.

[Krie95] M. Kriegmair, H. Stepp, P. Steinbach, W. Lumper, A. Ehsan, H. G. Stepp, K. Rick, R. Knüchel, R. Baumgartner, and A. Hofstetter. Fluorescence cystoscopy following intravesical instillation of 5-aminolevulinic acid: a new procedure with high sensitivity for detection of hardly visible urothelial neoplasias. *Urol Int*, 55(4):190–196, 1995.

[Krie00] R. C. Krieg, S. Fickweiler, O. S. Wolfbeis, and R. Knuechel. Cell-type specific protoporphyrin ix metabolism in human bladder cancer in vitro. *Photochem Photobiol*, 72(2):226–233, Aug 2000.

[Kurt00] K. H. Kurth, C. Bouffioux, R. Sylvester, A. P. van der Meijden, W. Oosterlinck, and M. Brausi. Treatment of superficial bladder tumors: achievements and needs. the eortc genitourinary group. *Eur Urol*, 37 Suppl 3:1–9, 2000.

[Lang99] N. Lange, P. Jichlinski, M. Zellweger, M. Forrer, A. Marti, L. Guillou, P. Kucera, G. Wagnières, and H. van den Bergh. Photodetection of early human bladder cancer based on the fluorescence of 5-aminolaevulinic acid hexylester-induced protoporphyrin ix: a pilot study. *Br J Cancer*, 80(1-2):185–193, Apr 1999.

[Loid05] W. Loidl, J. Schmidbauer, M. Susani, and M. Marberger. Flexible cystoscopy assisted by hexaminolevulinate induced fluorescence: a new approach for bladder cancer detection and surveillance? *Eur Urol*, 47(3):323–326, Mar 2005.

[Loke01] V. B. Lokeshwar and M. S. Soloway. Current bladder tumor tests: does their projected utility fulfill clinical necessity? *J Urol*, 165(4):1067–1077, Apr 2001.

[MacL07] G. T. MacLennan, Z. Kirkali, and L. Cheng. Histologic grading of noninvasive papillary urothelial neoplasms. *Eur Urol*, 51(4):889–98, Apr 2007.

[Mali87] Z. Malik and H. Lugaci. Destruction of erythroleukaemic cells by photoactivation of endogenous porphyrins. *British Journal of Cancer*, 56(5):589–595, 1987. Cited By (since 1996): 144.

[Mang51] L. O. J. Manganiello and F. H. J. Figge. Cancer detection and therapy ii. methods of preparation and biological effects of metalloporphyrins. *Bull. School Med., Univ. Maryland*, 36:3–7, 1951.

[Many05] M. J. Manyak, N. D. Gladkova, J. H. Makari, A. M. Schwartz, E. V. Zagaynova, L. Zolfaghari, J. M. Zara, R. Iksanov, and F. I. Feldchtein. Evaluation of superficial bladder transitional-cell carcinoma by optical coherence tomography. *J Endourol*, 19(5):570–574, Jun 2005.

[Mart99] A. Marti, N. Lange, H. van den Bergh, D. Sedmera, P. Jichlinski, and P. Kucera. Optimisation of the formation and distribution of protoporphyrin ix in the urothelium: an in vitro approach. *J Urol*, 162(2):546–552, Aug 1999.

[Mart03] A. Marti, P. Jichlinski, N. Lange, J. P. Ballini, L. Guillou, H. J. Leisinger, and P. Kucera. Comparison of aminolevulinic acid and hexylester aminolevulinate induced protoporphyrin ix distribution in human bladder cancer. *J Urol*, 170(2 Pt 1):428–32, 2003.

[McCa97] P. J. McCahy, C. A. Harris, and D. E. Neal. The accuracy of recording of occupational history in patients with bladder cancer. *Br J Urol*, 79(1):91–93, Jan 1997.

[Mein08] A. Meining and M. B. Wallace. Endoscopic imaging of angiogenesis in vivo. *Gastroenterology*, 134(4):915–918, Apr 2008.

[Miod98] A. J. Miodonski, A. Bugajski, J. A. Litwin, and Z. Piasecki. Vascular architecture of human urinary bladder carcinoma: a SEM study of corrosion casts. *Virchows Arch*, 433(2):145–151, Aug 1998.

[Miod99] A. J. Miodonski and J. A. Litwin. Microvascular architecture of the human urinary bladder wall: a corrosion casting study. *Anat Rec*, 254(3):375–381, Mar 1999.

[Mont08] R. Montironi, A. Lopez-Beltran, M. Scarpelli, R. Mazzucchelli, and L. Cheng. Morphological classification and definition of benign, preneoplastic and non-invasive neoplastic lesions of the urinary bladder. *Histopathology*, 53(6):621–633, Dec 2008.

[Most73] F. K. Mostofi, L. H. Sobin, and H. Torloni. *Histological Typing of Urinary Bladder Tumors, International Histological Classification of Tumors*. World Heath Organisation, WHO, Geneva, 1973.

[Mout98] W. G. Mouton, J. R. Bessell, and G. J. Maddern. Looking back to the advent of modern endoscopy: 150th birthday of Maximilian Nitze. *World J Surg*, 22(12):1256–1258, Dec 1998.

[Mukh09] S. Mukherjee, J. S. Wysock, C. K. Ng, M. Akhtar, S. Perner, M.-M. Lee, M. A. Rubin, F. R. Maxfield, W. W. Webb, and D. S. Scherr. Human bladder cancer diagnosis using multiphoton microscopy. *Proc Soc Photo Opt Instrum Eng*, 7161:nihpa96839, 2009.

[Myai06] M. T. Myaing, D. J. MacDonald, and X. Li. Fiber-optic scanning two-photon fluorescence endoscope. *Opt Lett*, 31(8):1076–1078, Apr 2006.

[N.-N09] NCI-NIH. National Cancer Institute of the National Institutes of Health. PDQ(r) NCI's comprehensive cancer database: bladder cancer, 2009.

[Nico08] C. Nicolau, L. Bunesch, and S. R. Contrast-enhanced ultrasound accuracy in the detection of bladder tumor in patients with hematuria. In *RSNA 94th scientific assembly and annual meeting*, page 575, 2008.

[Nico09] C. Nicolau, L. Bunesch, C. Sebastia, and R. Salvador. Diagnosis of bladder cancer: contrast-enhanced ultrasound. *Abdom Imaging*, May 2009.

[Nied06] A. M. Nieder, S. John, C. R. Messina, I. A. Granek, and H. L. Adler. Are patients aware of the association between smoking and bladder cancer? *J Urol*, 176(6 Pt 1):2405–8; discussion 2408, Dec 2006.

[Oost02] W. Oosterlinck, B. Lobel, G. Jakse, P.-U. Malmström, M. Stöckle, C. Sternberg, and E. A. of Urology (EAU) Working Group on Oncological Urology. Guidelines on bladder cancer. *Eur Urol*, 41(2):105–112, Feb 2002.

[Parm89] M. K. Parmar, L. S. Freedman, T. B. Hargreave, and D. A. Tolley. Prognostic factors for recurrence and followup policies in the treatment of superficial bladder cancer: report from the british medical research council subgroup on superficial bladder cancer (urological cancer working party). *J Urol*, 142(2 Pt 1):284–288, Aug 1989.

[Rao07] A. R. Rao, V. Hanchanale, P. Javle, O. Karim, and H. Motiwala. Spectroscopic view of life and work of the nobel laureate sir c.v. raman. *J Endourol*, 21(1):8–11, Jan 2007.

[Rübb88] H. Rübben, W. Lutzeyer, N. Fischer, F. Deutz, W. Lagrange, and G. Giani. Natural history and treatment of low and high risk superficial bladder tumors. *J Urol*, 139(2):283–285, Feb 1988.

[Reih02] F. Reiher, O. Ozer, M. Pins, B. D. Jovanovic, S. Eggener, and S. C. Campbell. p53 and microvessel density in primary resection specimens of superficial bladder cancer. *J Urol*, 167(3):1469–74, 2002.

[Rena02] K. Renaudin, A. Moreau, and F. Buzelin. Pathologic anatomy of infiltrating epithelial tumors of the bladder. *Prog Urol*, 12(5):787–802, Nov 2002.

[Saut04] G. Sauter, F. Algaba, and A. M. et al. *World Health Organization classification of tumours: pathology and genetics of tumours of the urinary system and male genital organ.*, chapter Non-invasive urothelial tumours, pages 110–123. IARC Press, 2004.

[Sche41] H. Scherer. Chemisch-physiologische Untersuchungen. *Ann. Chem. Pharm.*, 40:1, 1841.

[Schm04] J. Schmidbauer, F. Witjes, N. Schmeller, R. Donat, M. Susani, M. Marberger, and H. P. S. Group. Improved detection of urothelial carcinoma in situ with hexaminolevulinate fluorescence cystoscopy. *J Urol*, 171(1):135–138, Jan 2004.

[Schm09] J. Schmidbauer, M. Remzi, T. Klatte, M. Waldert, J. Mauermann, M. Susani, and M. Marberger. Fluorescence cystoscopy with high-resolution optical coherence tomography imaging as an adjunct reduces false-positive findings in the diagnosis of urothelial carcinoma of the bladder. *Eur Urol*, 56:914–919, Aug 2009.

[Schr04] B. P. Schrier, M. P. Hollander, B. W. G. van Rhijn, L. A. L. M. Kiemeney, and J. A. Witjes. Prognosis of muscle-invasive bladder cancer: difference between primary and progressive tumours and implications for therapy. *Eur Urol*, 45(3):292–296, Mar 2004.

[Siev09] K. D. Sievert, B. Amend, U. Nagele, D. Schilling, J. Bedke, M. Horstmann, J. Hennenlotter, S. Kruck, and A. Stenzl. Economic aspects of bladder cancer: what are the benefits and costs? *World J Urol*, 27(3):295–300, Jun 2009.

[Solo97] M. Soloway. *Optimal transurethral resection of bladder tumours.*, chapter Optimal therapy for patients with high risk superficial bladder cancer - controversy and consensus., pages 31–5. Oxford Medicine Publishing, 1997.

[Stei94] P. Steinbach, M. Kriegmair, R. Baumgartner, F. Hofstädter, and R. Knüchel. Intravesical instillation of 5-aminolevulinic acid: the fluorescent metabolite is limited to urothelial cells. *Urology*, 44(5):676–681, Nov 1994.

[Sten96] A. Stenzl, I. Eder, H. Kostron, H. Klocker, and G. Bartsch. Electromotive diffusion (emd) and photodynamic therapy with delta-aminolaevulinic acid (delta-ala) for superficial bladder cancer. *J Photochem Photobiol B*, 36(2):233–236, Nov 1996.

[Stro08] S. A. Strope and J. E. Montie. The causal role of cigarette smoking in bladder cancer initiation and progression, and the role of urologists in smoking cessation. *J Urol*, 180(1):31–7; discussion 37, Jul 2008.

[Sylv06] R. J. Sylvester, A. P. M. van der Meijden, W. Oosterlinck, J. A. Witjes, C. Bouffioux, L. Denis, D. W. W. Newling, and K. Kurth. Predicting recurrence and progression in individual patients with stage Ta T1 bladder cancer using EORTC risk tables: a combined analysis of 2596 patients from seven EORTC trials. *Eur Urol*, 49(3):466–5, Mar 2006.

[Tang09a] S. Tang, W. Jung, D. McCormick, T. Xie, J. Su, Y.-C. Ahn, B. J. Tromberg, and Z. Chen. Design and implementation of fiber-based multiphoton endoscopy with microelectromechanical systems scanning. *J Biomed Opt*, 14(3):034005, 2009.

[Tang09b] S. Tang, J. Liu, T. B. Krasieva, Z. Chen, and B. J. Tromberg. Developing compact multiphoton systems using femtosecond fiber lasers. *J Biomed Opt*, 14(3):030508, 2009.

[Tear97] G. J. Tearney, M. E. Brezinski, J. F. Southern, B. E. Bouma, S. A. Boppart, and J. G. Fujimoto. Optical biopsy in human urologic tissue using optical coherence tomography. *J Urol*, 157(5):1915–1919, May 1997.

[Thom08] K. Thomas and T. O'Brien. Improving transurethral resection of bladder tumour: The gold standard for diagnosis and treatment of bladder tumours. *European Urology Supplements*, 7(7):524 – 528, 2008. An Overview of Non-invasive Bladder Cancer: Epidemiology, Diagnosis, Treatment and Economics.

[Uehl00] P. Uehlinger, M. Zellweger, G. Wagnières, L. Juillerat-Jeanneret, H. van den Bergh, and N. Lange. 5-aminolevulinic acid and its derivatives: physical chemical properties and protoporphyrin ix formation in cultured cells. *J Photochem Photobiol B*, 54(1):72–80, Jan 2000.

[Uehl06] P. Uehlinger, J.-P. Ballini, H. van den Bergh, and G. Wagnières. On the role of iron and one of its chelating agents in the production of protoporphyrin ix generated by 5-aminolevulinic acid and its hexyl ester derivative tested on an epidermal equivalent of human skin. *Photochem Photobiol*, 82(4):1069–1076, 2006.

[van 05] B. W. G. van Rhijn, H. G. van der Poel, and T. H. van der Kwast. Urine markers for bladder cancer surveillance: a systematic review. *Eur Urol*, 47(6):736–748, Jun 2005.

[van 09] B. W. van Rhijn, H. G. van der Poel, and T. H. van der Kwast. Cytology and urinary markers for the diagnosis of bladder cancer. *European Urology Supplements*, 8(7):536 – 541, 2009. Incorporating the EAU-EBU Update Series.

[Witt03] C. Wittekind, F. Greene, R. V. P. Hutter, L. H. Sobin, and D. E. Henson, editors. *TNM Supplement: A Commentary on Uniform Use (UICC)*. Wiley, 3 edition, 9 2003.

[Wood86] H. Q. Woodard and D. R. White. The composition of body tissues. *Br J Radiol*, 59(708):1209–1218, Dec 1986.

[Yosh04] T. Yoshida, H. Inoue, S. Usui, H. Satodate, N. Fukami, and S. ei Kudo. Narrow-band imaging system with magnifying endoscopy for superficial esophageal lesions. *Gastrointest Endosc*, 59(2):288–295, Feb 2004.

[Zaak02] D. Zaak, H. Stepp, R. Baumgartner, P. Schneede, R. Waidelich, D. Frimberger, A. Hartmann, R. Künchel, A. Hofstetter, and A. Hohla. Ultraviolet-excited (308 nm) autofluorescence for bladder cancer detection. *Urology*, 60(6):1029–1033, Dec 2002.

[Zee10] Y.-K. Zee, J. P. B. O'Connor, G. J. M. Parker, A. Jackson, A. R. Clamp, M. B. Taylor, N. W. Clarke, and G. C. Jayson. Imaging angiogenesis of genitourinary tumors. *Nat Rev Urol*, 7(2):69–82, Feb 2010.

[Zeeg00] M. P. Zeegers, F. E. Tan, E. Dorant, and P. A. van Den Brandt. The impact of characteristics of cigarette smoking on urinary tract cancer risk: a meta-analysis of epidemiologic studies. *Cancer*, 89(3):630–639, Aug 2000.

[Zeeg04] M. P. A. Zeegers, E. Kellen, F. Buntinx, and P. A. van den Brandt. The association between smoking, beverage consumption, diet and bladder cancer: a systematic literature review. *World J Urol*, 21(6):392–401, Feb 2004.

[Zimm95] P. E. Zimmern, D. Laub, and G. E. Leach. Fluorescein angiography of the bladder: technique and relevance to bladder cancer and interstitial cystitis patients. *J Urol*, 154(1):62–65, Jul 1995.

[Zysk07] A. M. Zysk, F. T. Nguyen, A. L. Oldenburg, D. L. Marks, and S. A. Boppart. Optical coherence tomography: a review of clinical development from bench to bedside. *J Biomed Opt*, 12(5):051403, 2007.

Chapter 4

Optimization of the spectral design for fluorescence cystoscopy

4.1 Fluorescing metabolites present in urine

This study originates from the clinical observation that the images are somehow "blurred" by a greenish screen between endoscope tip and bladder mucosa during fluorescence cystoscopy, especially with the PDD setup from Richard Wolf. This effect is enhanced by the urine production. Indeed, when the bladder is not flushed regularly, greenish flows coming out of the ureters can easily be observed. For this reason, it is supposed that some fluorophores contained in the urine are excited by the photodetection excitation light, and appear greenish on the screen. This effect may impair the visualization of the bladder mucosa, and thus cancerous lesions, and lowers sensitivity of the fluorescence cystoscopy.

Surprisingly, the fluorescence of urine has not received particular attention in the past, although various attempts have been made to isolate and identify fluorescent substances. Several historical papers reported about metabolites present in urine, that may fluoresce under certain conditions [Bert01, Chas88, Hege93, Mans01].

Urine has frequently been reported to display a characteristic blue-green fluorescence that can change in case of pathological urine [Danc64]. This blue-green fluorescence has been attributed to the presence of two main groups of fluorophores, most are metabolites of tryptophan as shown in Figure 4.1.

Generally, the spectral characterization of a mixture of fluorophores is not easy. Most urine fluorophores possess very similar fluorescence parameters and may affect each other in a mixture by changing their individual spectra. Leiner *et al.* measured the total fluorescence of human urine at various excitation and emission wavelengths and presented it in 3-dimensional form, the so-called excitation-emission matrices (EEMs). Despite the complexity of the composition of urine, 3–5 distinct fluorescence maxima could be observed. Effects of pH were studied and tentative assignments as to the species responsible for the peaks were evaluated. They are listed in Table 4.1. Most likely, however, the peaks observed do not result from a single fluorescent urinary metabolite, but rather from several species having similar spectral properties and being present in comparable concentrations.

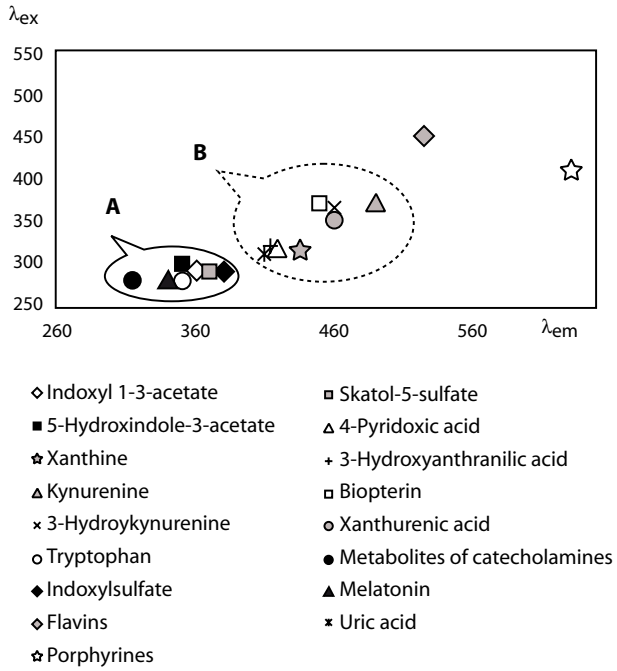

Figure 4.1: *Localization of urine fluorophores (A and B group) in the excitation-emission matrix (EEM). The group A of fluorophores represents the highest contribution to the whole urine fluorescence. The group B is characteristic with 4-6 times lower concentration than group A [Kusn05].*

Description	Excitation	Emission	Description of the Fluorophore-Chromophore
Peak 1	288.5±0.9	379±5.8	Indoxylsulphate
Peak 2	324.3±3.2	418.9±2.6	4-pyridoxic acid, very strong fluorescence
Shoulders	280	315	Species fluorescing at these wavelengths have been detected in the urine, but none of them could as such be assigned to this shoulder : (R-tryptophane,R1-acetic acid,tyrosine). Characteristic concentration changes were found in urine of cancer patients and newborn babies.
	370	455	3 kynurenines and 2 pterins (neo- and bio-) are known to fluoresce much more intensely than both folic acid and xanthurenic acid.
Peak 3-4	420,450,465	525	Riboflavin or one of its urinary metabolites or a combination thereof.
Shoulders	430 490	460 535	Sobel *et al.* reports that this peak is produced by an unknown substance, present in all urine specimens, sometimes in high concentration [Sobe74]
Peak 5	 405 400-405	 596, 619, 653 595,618, 652, 671	They are rather weak in intensity. It is assumed that they result from porphyrins which are known to be most strongly fluorescent in acidic solution. 3 emission maxima for uroporphyrin 4 emission maxima for coproporphyrin

Table 4.1: *Main fluorophores identified in urine as reviewed in [Lein87].*

Kusnir *et al.* showed that concentration of physiologically produced urine is very variable [Kusn05]. It is a result of such various effects as circadian rhythms, diet, amount of consumed water, physical activity of the person, ... Individual fluorophore concentrations differ by orders. Since fluorescence intensity is not a fully linear function of fluorophore concentration (auto-quenching effect, energy transfer, and other phenomena), each change in urine concentration (mixture of fluorophores) causes unpredictable changes in the shape and intensity of the whole spectrum.

Additionally, these authors studied the effect of dilution. Before fluorescent measurements, urine samples were centrifuged and supernatant was diluted via geometric progression. At the dilution 1:500, fluorophores of group A (as defined in Figure 4.1) dominate in EEM. Urine diluted by 1:30 is characterized by the quenching of group A and the rising fluorescence of group B. The EEM of urine diluted by 1:10 present only group B. The undiluted urine spectrum express only those fluorophores present in very low (trace) concentration because the fluorescence of both main fluorophore groups, A and B, disappears and is not manifested at all. The EEMs (not shown) clearly indicate principal concentration problem of multifluorophore system – fully different fluorescence spectra of the same material caused only by the dilution of the sample. Individual fluorophores in the mixture manifest themselves only in an appropriate concentration.

The dilution of the sample acquired during cystoscopy is depending on many factors: i) patient urine production varies strongly from one patient to an other; ii) patient's diet also have an influence on the metabolites present in the urine at the time of cystoscopy; iii) bladder flushing and/or rinsing is done when needed during the cystoscopy (so that the time interval between 2 flushes ranges from 10 seconds up 10 minutes).

In the following section, we will present spectrofluorimetric results acquired on samples relevant for cystoscopy (i.e. at different times during examination). Prior to the clinical samples, we measured each pure irrigation solution (NaCl, Aqua and Glycine). Figure 4.2 shows neither significant absorption peaks nor fluorescence peaks in the emission range 350–700nm. The shoulders observed around 400 nm, 600 nm, 635 nm, may be due to device-specific artifacts (*e.g.* UV-Visible lamp transition in the Cary spectrometer). The absolute value of the absorbance for these three liquid ranges between 0.1–0.17, at least 4-fold lower than hemoglobin absorption.

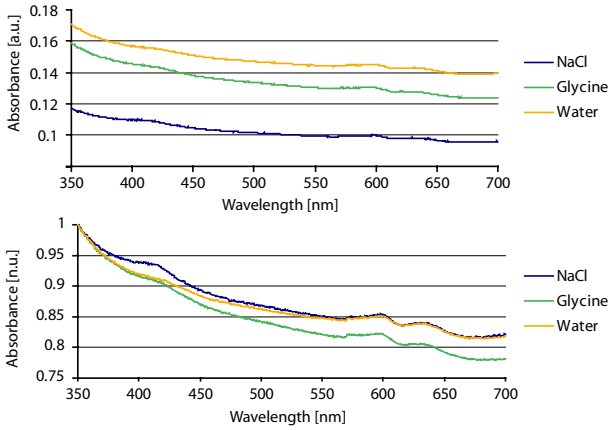

Figure 4.2: *Absorption spectra of the 3 solutions filling the bladder (Aqua, NaCl, Glycine) with (i) the original values and (ii) normalized at their maximum.*

4.2 SPIE proceeding

Fluorescence of the bladder washout fluid following cystoscopy: a preliminary study

Blaise Lovisa[a], Anna Maria Novello[a], Patrice Jichlinski[b], Hubert van den Bergh[a], and Georges Wagnières[a]

[a] Medical Photonics Group, EPFL, Batiment CH, Station 6, CH-1015 Lausanne, Switzerland
[b] Department of Urology, CHUV University Hospital, CH-1011 Lausanne, Switzerland

Published in *Proceeding of SPIE* No. 7548, San Francisco, 2010 [Lovi10]

Abstract: During fluorescence cystoscopy, it is observed that the acquired images are sometimes blurred by a greenish background originating from the bladder washout fluid. Several fluorophores are involved in this overall liquid fluorescence, and their exact origin and relative contributions remain unknown. In this study, the bladder washout fluid is sampled at different times during fluorescence cystoscopy examinations. In total, 32 samples from 12 patients are analyzed with a spectrofluorimeter (excitation range: 350-445 nm, emission range 380-700 nm). This study shows clearly that the position of the fluorescence peaks (excitation/emission wavelengths: 450/525 nm, 405/625 nm) and shoulder (440/525 nm) is reproducible between different patients. It also suggests that an excitation at wavelengths higher than 400 nm helps to suppress this solution background fluorescence. Additionally, the pH of the solution seems to influence the position of the fluorescence peaks, and this suggests that changing the pH of the examination liquid could help in avoiding the greenish background.

4.2.1 Introduction

Bladder cancer is an important topic in oncology. In the western world, it is the fourth most common malignancy in men and the eight most common in women [Kirk05]. White light cystoscopy has been established as a standard procedure for both detection and removal of bladder cancer. However, it has a limited sensitivity in particular for flat lesions [Jich05, Lovi09]. Fluorescence cystoscopy has been developed to enhance the detection of early bladder cancer. This technique is performed using blue-violet light to induce the fluorescence of photoactive porphyrins (PaPs) , mostly protoporphyrin IX (PpIX). PaPs are selectively produced in early lesions [Witj07] after an instillation into the bladder of a precursor solution, typically 2 hours prior the examination. The resulting fluorescence image has a blue-green color if the tissue is healthy while the cancer appears in red.

The main purpose of this study is to analyze the fluorescence characteristics of the bladder washout fluid and thus to identify the fluorophores and absorbers responsible for this environmental fluorescence.

4.2.2 Materials & Methods

Samples (typically 15 ml) of the bladder washout fluid were collected during the drainage of the bladder of 12 patients undergoing a transurethral resection of the bladder (TURB) under fluorescence cystoscopy. The mean operation (detection and resection) du-

ration was 45 minutes.

In order to reflect the alteration of the fluorescence properties over the course of examination and how different irrigation fluids and concentration influence fluorescence spectra, the content of the bladder was collected at four different points in time:

Just before the examination start – *PaPs-Urine sample* In order to perform fluorescence cystoscopy, a 50 ml precursor solution is instilled into the bladder 2 hours prior the examination. With an average urine production of 1-2 ml/min, the resulting precursor solution concentration in the bladder fluid after 2 hours instillation is 25-50%. In this phase, the washout fluid contains the remaining precursor (not fluorescing), PaPs, and the urine secreted in this interval. Measuring this type of sample was of interest because it corresponds to the initial conditions of the procedure with the highest urine concentration.

After the bladder wash – *NaCl-Urine sample* For cytological diagnosis, the bladder is rinsed with a 500 ml NaCl solution (NaCl 0.9%, B. Braun, Germany) to collect urothelial cells. This solution remains only for a very short time in the bladder (typically 5-10 seconds), and urine concentration is very low (i.e. diluted).

During the fluorescence cystoscopy – *Aqua-Urine sample* During the regular photodetection procedure, the bladder is irrigated with a water solution (Aqua, B. Braun, Germany) to ensure good visualization of the bladder mucosa. Therefore, urine concentration in these samples depends on the elapsed time after last flushing.

During the resection phase – *Glycine-Urine sample* During electro-resections, the bladder is irrigated with a glycine solution (Glycine 1.5% solution, Baxter, USA) to avoid water intoxication due to irrigation fluid entering the bloodstream, the so-called TURP syndrome. For short resection time, this risk is minimal and the water irrigation solution can still be used. In these samples, some blood was present due to the on-going resection procedure. This sample was of particular relevance since the greenish flows were often visible during this phase.

The number of samples of each type was not the same due to clinical reasons (*e.g.* no cytology requested, limited resection time without glycine). Consequently, 10 PaPs-Urine, 5 NaCl-Urine, 10 Aqua-Urine, and 7 Glycine-Urine were collected. Samples were stored at low temperature (T = 4°C) between collection and measurement. Typical time interval between collection and measurement was 2 hours.

The 32 samples were analyzed with a spectrofluorimeter (LS-50B, Perkin Elmer, USA) and the results are presented as assembled in an excitation-emission matrix (EEM), as well as fluorescence-emission spectra with excitation wavelengths ranging from 350 nm to 445 nm (5 nm step) and emission wavelengths ranging from 380 nm to 700 nm (see Figure 4.4). Fluorescence was collected with an angle of 90 degrees.

To identify possible sources of absorption, an absorption spectrum between 350 nm and 700 nm was also acquired for each sample with a spectrophotometer (Cary 500 UV/VIS/NIR, Varian, USA). For all measurements, samples were analyzed in a 1 cm thick quartz cuvette (OS, Hellma, Germany) with improved transmission in the near UV.

4.2.3 Results

We measured each pure irrigation solution (NaCl, Aqua and Glycine) and observed neither significant absorption peaks nor fluorescence peaks in the emission range 350-700nm (see Figure 4.2).

During the resection phase, the excitation light is much absorbed by the bladder washout fluid due to the variable blood content, impairing the PaPs fluorescence excitation, and thus, lowering the contrast between lesions and

healthy mucosa. Figure 4.3 shows a typical absorption spectrum of Glycine-Urine samples, where oxyhemoglobin strong absorption peaks can be clearly identified.

In the following, typical fluorescence spectra of the various samples are shown and described. The scales on Figure 4.4 [a-h] are comparable, because the samples were measured in the same conditions, but the color bars were adjusted to help visualization. Great variations in fluorescence intensities were observed between patients. Numbers indicated in brackets for each type of sample are the mean fluorescence intensity, the standard deviation and the observed range.

PaPs-Urine samples – Figure 4.4 [a-b] (290±95, range 160-420). Two main fluorescence peaks are visible at excitation/emission wavelengths of 360-380/450 nm (Peak 1) and of 405/635 nm (Peak 2). A shoulder of a third peak is also visible around 440/520 nm.

NaCl-Urine samples – Figure 4.4 [c-d] (181±88, range 47-260). The NaCl bladder wash has fluorescence intensity well above the NaCl background signal (1:30-1:50). In this case, only one peak is present (excitation wavelength < 350 nm and emission at 450 nm). The excitation peak is shifted towards shorter wavelengths. The second peak and the shoulder do almost disappear.

Aqua-Urine samples – Figure 4.4 [e-f] (471±174, range 220-720). For these samples, a small shift of the excitation maxima (related to Peak 1, from 365 to 340 nm) towards shorter wavelengths is observed as compared to PaPs-Urine samples, but the shift is smaller than in NaCl. The other peak and shoulder are still present but no variation in the excitation/emission is observed.

Glycine-Urine samples – Figure 4.4 [g-h] (120±69, range 32-220). The glycine background is also measured separately (data not shown) and it is verified that intensities are lower than the signal itself (1:30, 1:50), giving a good signal to noise ratio. As in NaCl, only one peak is clearly visible and its excitation is shifted respect to that of Peak 1 in PaPs-Urine sample.

4.2.4 Discussion

Many different molecules may play a role in the urine fluorescence, and it is not straightforward to identify all of them [Lein87]. These authors classified peaks and shoulders that are matching to our measurements. It is important to underline that among the manifold substances occurring in urine, only those having high values for the product $\varepsilon \cdot c \cdot \phi$ will significantly contribute to the total fluorescence, where ε is the molar extinction coefficient of the substance at the relevant excitation wavelength, c is its concentration, and ϕ is its fluorescence quantum yield. This means that variation in the EEM can be observed when we consider different dilutions of the urine sample [Kusn05], because the different fluorochromes have a spectral dependence to the concentration.

The interaction of the fluorochromes with the different physicochemical environment of the solvent can also influence the fluorescence properties of the sample. In particular, the pH of the solution seems to be important. The pH of normal urine is generally in the range 4.6–8, a typical average being around 6. Most of the variations are due to diet. For example, high protein diet results in more acidic urine, but vegetarian diet generally results in more alkaline urine. Many fluorophores present in the urine exhibit strong pH dependence [Sare51, Sato58]. Indeed, their fluorescence yield appears to be strongly related to the pH [Dros02, Buen04].

Pyridoxic acid has been recognized as one of the major fluorescent metabolites in urine with a maxima at 324/419 nm [Lein87, Sare51, Greg79]. In our measurements, it probably gives a large contribution to Peak 1. However, it should be noted that other substances

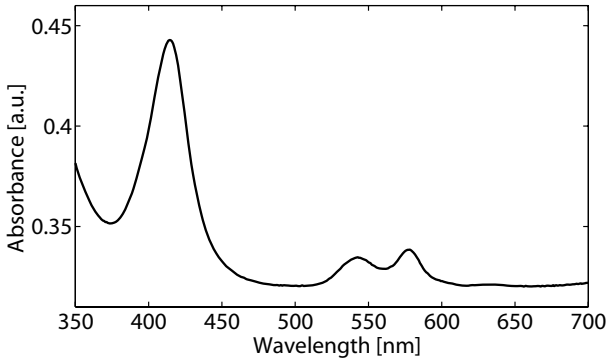

Figure 4.3: *Absorption of a Glycine-Urine sample. Three peaks can be identified at 414.7 nm, 542.7 nm, and 578 nm, which correspond to the main absorption peaks of hemoglobin (HbO_2: 414 nm, 542 nm, 578 nm; Hb: 434 nm, 556 nm) in good agreement with* `http://omlc.ogi.edu/`

interfere at these wavelengths. In particular, when the sample is undiluted, it seems that also kynurenine and xanthurenic acid play an important role in the total fluorescence [Kusn05, Lein87]. A shift towards shorter wavelengths of kynuretic acid fluorescence is observed when the solvent is less acidic [Sato58]. A similar shift is also observed in our emission spectra passing from PaPs-Urine sample (more acidic due to the precursor) to the other samples.

Comparing our measurements with the literature [Kusn05, Lein87], Peak 2 is attributed to porphyrins that are often present in urine as a degradation product of bilirubin or urobilin [Lein87]. Cancerous cells loaded with PaPs or free PaPs released to the bladder (also fluorescing at these wavelengths) are also likely to be present in the liquid. The shoulder is attributed to riboflavins, which have a peak at about 440/520 nm [Lein87].

For NaCl-Urine, Aqua-Urine, and Glycine-Urine, the shift in the excitation wavelength of Peak 1 and the almost total disappearance of Peak 2 and its shoulder is probably due to the fact that urine is more diluted than in PaPs-Urine sample. Some of them, with high fluorescence quantum yield, could be present in low concentration and probably almost disappear when urine is more diluted [Kusn05]. Another possible explanation is that there is a quenching of some fluorochromes due to the solvent.

In the case of NaCl-Urine samples, the fact that NaCl stays in the bladder for a short time (typically less than 5 seconds) has also to be considered. In fact, this could not allow a sufficient porphyrin accumulation in the bladder, resulting in Peak 2 disappearance.

Hemoglobin absorption can influence fluorescence measurements. Hence, it probably contributes in defining the shape of the peaks, particularly in Glycine-Urine samples. For the same reason, the presence of hemoglobin in the washout fluid can also impair the cancer detection, since it lowers the intensity of the light illuminating the bladder surface, and alters the spectroscopy of the fluorescence collected by the cystoscope.

Finally, although the exact influence of the alimentation over the urine composition (and thus fluorescence) remains unknown, it is pretty obvious that the whole body metabolism is affected by the patient diet. In this study, the patients are fasting over the night preceding the examination, and the inter-patient variations remain limited.

4.2.5 Conclusions

In this study, the total fluorescence of different liquids filling the bladder of patient subject to fluorescence cystoscopy is analyzed. Two main factors influence our measurements: dilution

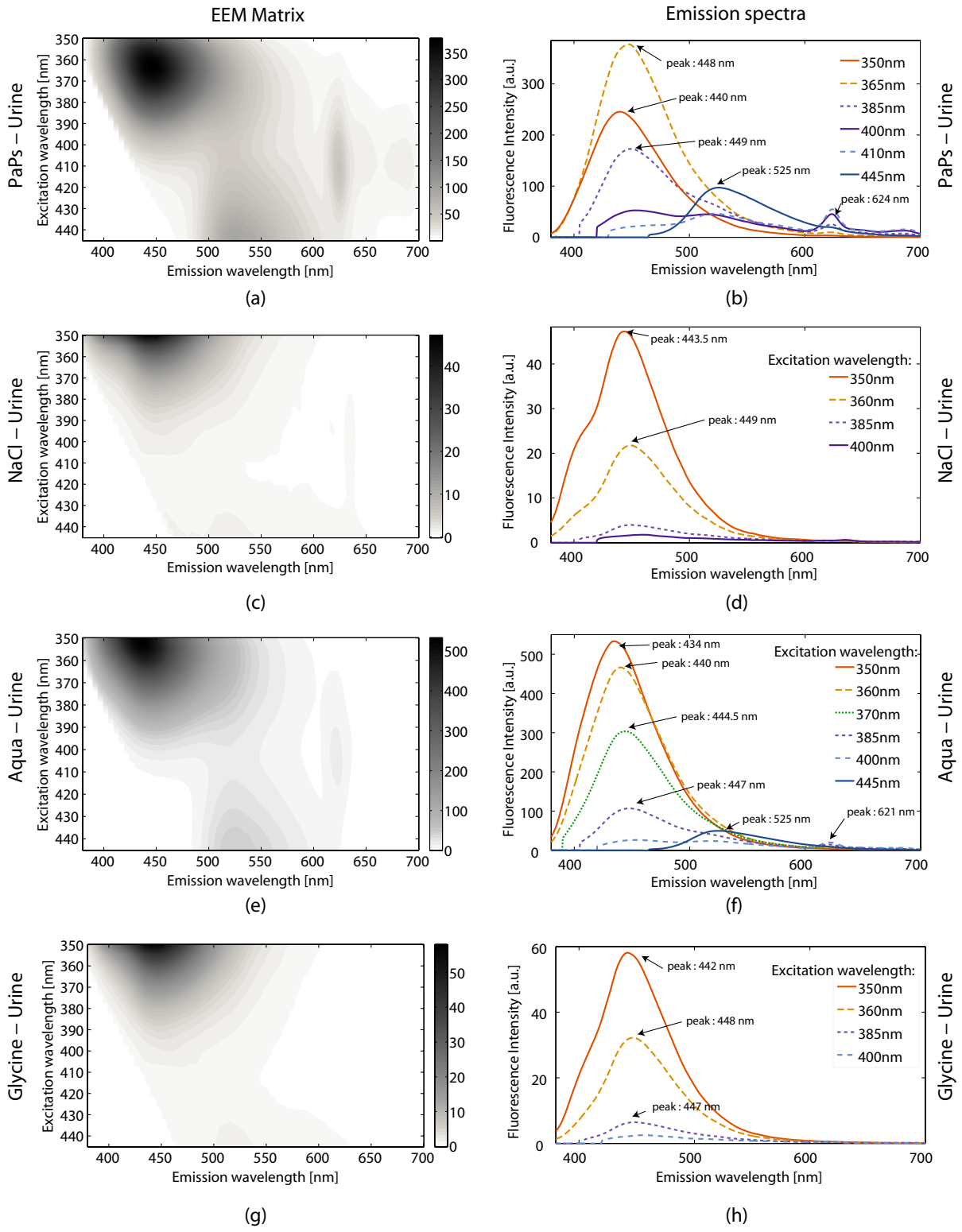

Figure 4.4: *Example of fluorescence measurements of different samples taken from the same patient: PaPs-Urine (a, b), NaCl-Urine (c, d), Aqua-Urine (e, f), and Glycine-Urine (g, h). EEMs are reported on the left, while emission spectra are reported on the right.*

and pH. A determination of the exact role of these factors, in particular of the pH, in the measurements can suggest the formulation of a new washout solution, in order to avoid the greenish background during fluorescence cystoscopy.

For the moment, what we can deduce from our measurements is that excitation wavelengths below 390 nm should be avoided in order to reduce the excitation of the main fluorophores of the urine. Additionally, in order to suppress the secondary peak attributed to riboflavins in the green spectral region (ex440/em520nm), one should avoid excitation below 450 nm, which is questionable, since we would like to excite PpIX in the violet spectral region.

Bibliography

[Bert01] A. Bertazzo, E. Ragazzi, M. Biasiolo, C. V. Costa, and G. Allegri. Enzyme activities involved in tryptophan metabolism along the kynurenine pathway in rabbits. *Biochim Biophys Acta*, 1527(3):167–175, Aug 2001.

[Buen04] C. Bueno and M. V. Guerrero, J. andand Encinas. Spectroscopic properties of 4-pyridoxic acid as a function of pH and solvent. *Helvetica Chimica Acta*, 87:940–948, 2004.

[Chas88] J. Chastain and D. Mccormick. Characterization of a new flavin metabolite from human urine. *Biochim. Biophys. Acta*, 967(1):131–134, 1988.

[Danc64] P. W. Danckwortt and J. Eisenbrand. *Luminescenz-Analyse im filtrierten ultravioletten Licht.* Akad. Verlags-Ges, Leipzig, 1964.

[Dros02] P. Drossler, W. Holzer, A. Penzkofer, and P. Hegemann. pH dependence of the absorption and emission behavior of riboflavin in aqueous solution. *Chem. Phys.*, 282:429–439, 2002.

[Greg79] J. F. Gregory and J. R. Kirk. Determination of urinary 4-pyridoxic acid using high performance liquid chromatography. *The American Journal of Clinical Nutrition*, 32:879–883, 1979.

[Hege93] Z. L. Hegedus and U. Nayak. Renal excretion of plasma soluble melanins by healthy human adults. *Arch Int Physiol Biochim Biophys*, 101(6):417–423, 1993.

[Jich05] P. Jichlinski and H.-J. Leisinger. Fluorescence cystoscopy in the management of bladder cancer: a help for the urologist! *Urol Int*, 74(2):97–101, 2005.

[Kirk05] Z. Kirkali, T. Chan, M. Manoharan, F. Algaba, C. Busch, L. Cheng, L. Kiemeney, M. Kriegmair, R. Montironi, W. M. Murphy, I. A. Sesterhenn, M. Tachibana, and J. Weider. Bladder cancer: Epidemiology, staging and grading, and diagnosis. *Urology*, 66(6 Suppl 1):4–34, 2005.

[Kusn05] J. Kusnir, K. Dubayova, L. Leskova, and M. Lajtar. Concentration matrices-solution for fluorescence definition of urine. *Analytical Letters*, 38:1559–1567, 2005.

[Lein87] M. Leiner, R. Hubmann, and O. Wolfbeis. The total fluorescence of human urine. *Analytica Chimica Acta*, 198:13–23, 1987.

[Lovi09] B. Lovisa, P. Jichlinski, D. Aymon, B.-C. Weber, H. van den Bergh, and G. Wagnieres. Bladder cancer detection by fluorescence imaging with hexvix(r): optimization of the excitation light during high magnification cystoscopy. In I. Georgakoudi, J. Popp, and K. Svanberg, editors, *Clinical and Biomedical Spectroscopy*, volume 7368, page 73681I. SPIE, 2009.

[Lovi10] B. Lovisa, A. M. Novello, P. Jichlinski, H. van den Bergh, and G. Wagnieres. Fluorescence of the bladder washout fluid following cystoscopy: a preliminary study. In N. Kollias, B. Choi, H. Zeng, R. S. Malek, B. J. Wong, J. F. R. Ilgner, K. W. Gregory, G. J. Tearney, L. Marcu, H. Hirschberg, S. J. Madsen, A. Mandelis, A. Mahadevan-Jansen, and E. D. Jansen, editors, *Photonic Therapeutics and Diagnostics VI*, volume 7548, page 75481J. SPIE, 2010.

[Mans01] A. Mansilla, I. Meras, and F. Salinas. Analysis of pteridines and creatinine in urine by hplc with serial fluorometric and photometric detectors. *Chromatographia*, 53:510–514, 2001.

[Sare51] H. P. Sarett. A study of the measurement of 4-pyridoxic acid in urine. *J. Biol. Chem.*, 189:769–777, 1951.

[Sato58] K. Satoh and J. M. Price. Fluorometric determination of kynurenic acid and xanthurenic acid in human urine. *J Biol Chem*, 230(2):781–789, Feb 1958.

[Sobe74] C. Sobel, C. Cano, and R. E. Thiers. Separation and quantitation of coproporphyrin and uroporphyrin in urine. *Clinical Chemistry*, 20(11):1397–1402, 1974.

[Witj07] J. A. Witjes and J. Douglass. The role of hexaminolevulinate fluorescence cystoscopy in bladder cancer. *Nature Clinical Practice Urology*, 4(10):542–549, 2007.

Chapter 5

High magnification reflectance imaging in the bladder

5.1 Introduction to HM cystoscopy

Fluorescence cystoscopy with Hexvix® represents one of the major recent advances in urologic oncology in the recent years (as described in details in Section 3.6). Hexvix® allows to detect early lesions with a very high sensitivity. Moreover, many clinical studies reported a very high detection rate of flat lesions (*e.g.* CIS, 92–95%) [Jich03a, Witj07], and a better identification of lesions that were overlooked with standard WL cystoscopy alone [Frad07, Gros07]. In addition, the precise staining and mapping obtained on the bladder mucosa give a direct visual appreciation of the disease extension. Therefore, random biopsies of the mucosa become useless, thus reducing the risk of unnecessary mucosal injury, one critical factor in bladder tumor recurrence [Theo03]. A secondary end-point that was demonstrated is the improved resection under fluorescence, contributing to the lower recurrence rate [Denz08].

However, tissue abnormalities such as inflammations, hyperplasia, metaplasia and scars may sometimes induce false-positive results. Although most of these false positives can easily be rejected under white light observation (see Section 3.6.3), inflammations are much more difficult to identify, resulting in supplementary biopsies. Therefore, the purpose of this research project is to develop novel, fast, and convenient method to characterize fluorescence positive spots *in situ* during fluorescence cystoscopy, thus reducing the false-positive rate and the cost of supplementary biopsies. The developed instrumentation should be kept compatible with the current PDD instrumentation in order to minimize the impact on the clinical routine.

As shown in Section 3.7, angiogenesis plays an important role in bladder cancer progression, as it is a prerequisite for growth and metastasis [Char06]. In this project, we will use the magnification and/or high-resolution cystoscopy to characterize the vascularization underlying flat lesions appearing as positive during fluorescence cystoscopy. We will particularly focus on the capillary/vessels patterns and the microvascular architecture. The objectives of this project were: i) to identify the smallest value of the magnification, ii) to identify the optimal features of these images (vessel or cellular structure) to characterize the lesions, and iii) to optimize the spectral design of the imaging system to better visualize the identified patterns.

Over the last years, high resolution and high magnification endoscopic observations were applied to many different organs. These technologies enhance the detection of the following features: modification of the vocal cords histology [Andr95a, Andr95b], cervical cancer onset with contact micro-colpohysteroscopy [Mats05], diagnostic improvement of Barrett's esophagus [Fort06], pit pattern classification of the colon [Kudo96], characterization of small and diminutive colonic polyps (pit pattern and vascular pattern intensity) [East08], observation of the looped capillary vessels inside the papillae in the oesophagus [Inou97], subepithelial vascular patterns in the bronchi, including increased vessel growth and complex networks of tortuous vessels [Shib02, Shib03, Shib10], microvascular architecture of the surface epithelium like vessel arborescence and interconnection in the upper gastro-intestinal tract [Kuma06]. In addition, endocytoscopy systems (together with vital staining) allowed the microscopic observation at the cellular level, including cellular density, pattern of the cellular arrangement, deformity and enlargement of the nuclei, nuclear-cytoplasmic ratio [Sasa06]. In this manuscript, we always bear in mind, that the magnification of our cystoscope should be kept into reasonable bounds (30–150×) in order not to transform it into a microscope, incompatible with the conventional surgical tools. In the following pages, to improve the legibility, we will call the range 80–120× *high magnification* not to be confused with the high magnification necessary to acquire images at the cellular level (>500×).

Since we were interested in transferring this magnification concept in urology, a dedicated rigid cystoscope was adapted in collaboration with Richard Wolf GmbH. This cystoscope equipped with a knob allowing to change the magnification *in situ* in both white light and fluorescence mode. The section 5.2 describes the optical properties of this cystoscope. A clinical study was designed to assess the feasibility of characterizing the vascularization *in situ*. In a first phase, an image atlas was created to register the vascular patterns of interest. In a second phase, 60 patients who were subject to "routine" fluorescence cystoscopies were recruited at the University Hospital in Lausanne, and their endoscopic finding were classified following the atlas. Section 5.3 summarizes the clinical results. We then analyzed whether the vessel classification information was fully contained in the image skeletons in the section 5.4. Since our method for the quantification of blood vessels involved some elements of subjectivity, Section 5.5 defines some algorithms to segment blood vessels and investigate the influence of color presentation. In Appendix E, the spectral design of our setup is modified to enhance the contrast between the tissue and the vessels.

5.2 Optical characterization of the HM cystoscope

The adapted rigid cystoscope is based on a Microview cystoscope (Richard Wolf GmbH, Knittlingen, Germany) with a viewing direction of 25°. It has a diameter of 4 mm, a working length of 30 cm, and can be inserted into a dedicated 17.5 Fr sheath, equipped with an endoscope bridge. This sheath is equipped with 2 fixed stop cocks to allow permanent irrigation of the bladder. The cystoscope itself is equipped with a knob allowing to change the magnification *in situ*. Figure 5.1 depicts the proximal part of the HM cystoscope. This rigid cystoscope was thought to be a measurement device rather than a final product. The results of the studies presented in this chapter will allow to define the "input design" of a new flexible cystoscope with integrated magnification.

In a quantitative approach, the main problem with a variable zooming instrumentation is to determine the size of the observed patterns. In addition, operating the knob on the rigid cystoscope results in a modification of the field of view (FOV), depth of field (DOF) and magnification. At the present time, the distance between the endoscope and the tissue cannot

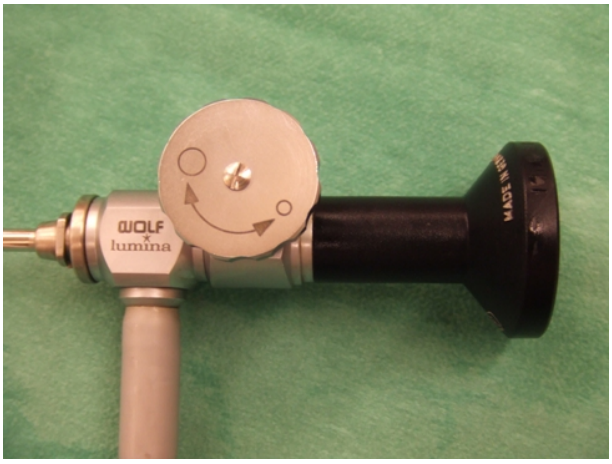

Figure 5.1: ***High magnification cystoscope.*** *The magnification can be adjusted with a knob on the optical device (range 30-650×).*

be measured *in vivo* (except of course when in contact with the tissue). In the next section, we will describe the calibration procedure with the help of a standardized target.

5.2.1 Useful definitions in geometrical optics

The *field of view* (FOV) is defined as the (angular or areal) extent of the real world being observed by the cystoscope. The size of the field of view and the size of the image detector directly affect the image resolution.

The *depth of field* (DOF) is the portion of a scene that appears acceptably sharp in the image. Although a lens can precisely focus at only one distance s, the decrease in sharpness is gradual on each side of the focused distance, so that within the DOF, the unsharpness is imperceptible due to the limited resolution of the detector (resp. display system). One usually define the DOF with a short distance L_1 and a long distance L_2, the closest and farthest sharp points, respectively (see Figure 5.2). The DOF calculation is not trivial, but many authors describe it in details [Merk93].

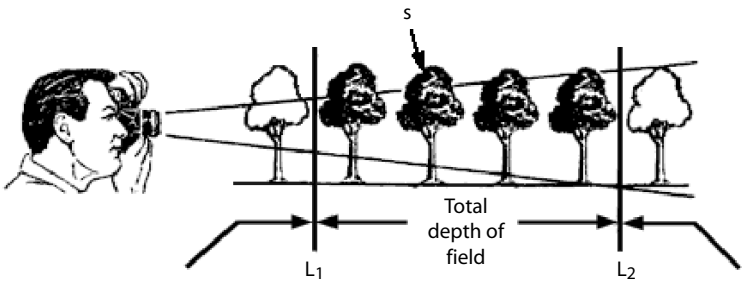

Figure 5.2: *Definition of the DOF with parameters L_1, L_2, and s*

In order to calculate the DOF, we need the following definitions:

The *circle of confusion* (CoC) is an optical spot caused by a cone of light rays from a lens not coming to a perfect focus when imaging a point source. Thus, it is usual to define the DOF as the region where the CoC is less than the resolution of the detector.

The *f-number* ($f/\#$) of an optical system expresses the diameter of the entrance pupil in terms of the focal length of the lens; in simpler terms, the f-number is the focal length divided by the "effective" aperture diameter. The f-number (often also notated as N) is given by

$$f/\# = N = \frac{f}{D} \text{ with } D \text{ the diameter of the entrance pupil and } f \text{ the focal length}$$

The *hyperfocal distance* H is the distance beyond which all objects are acceptably sharp for a lens focused at infinity, and is given by

$$H \approxeq \frac{f^2}{Nc} \approxeq \frac{fD}{c} \text{ with } c \text{ is the diameter of the CoC for a given image format.}$$

Let s be the distance at which the camera is focused (the "subject distance"). When s is large in comparison with the lens focal length, the distance L_1 from the camera to the near limit of DOF and the distance L_2 from the camera to the far limit of DOF are

$$L_1 \approx \frac{Hs}{H+s} \text{ and } L_2 \approxeq \frac{Hs}{H-s} \text{ for } s < H$$

When the subject distance is the hyperfocal distance (i.e. $s = H$),

$$L_2 = \infty \text{ and } L_1 = \frac{H}{2}$$

In general, the depth of field $L_2 - L_1$ is

$$\text{DOF} \approxeq \frac{2Hs^2}{H^2 - s^2} \text{ for } s < H$$

For $s \geq H$, the far limit of DOF is at infinity and the DOF is infinite; of course, only objects at or beyond the near limit of DOF will be recorded with acceptable sharpness.
Substituting for H and rearranging, DOF can be expressed as

$$\text{DOF} \approxeq \frac{2Ncf^2s^2}{f^4 - N^2c^2s^2}$$

Thus, for a given image format, depth of field is determined by three factors: the focal length of the lens, the f-number of the lens opening (the aperture), and the camera-to-subject distance.

5.2.2 Determination of the HM cystoscope resolution

A good way to determine resolution of an optical setup is to look at a pattern of known size and see whether it is resolved or not. The USAF-1951 test target (abbrev. *USAF-target*) was developed for this purpose. It contains patterns that get continuously smaller in order to measure the actual resolution of an imaging system. The structure of the USAF-target and the size of each element are standardized according to an American military standard [USAi51].

The USAF-target consists of a series of patterns decreasing in size, with a range depending on the applications. It consists on several *groups* that are serially numbered with -2,-1,...,6,7. Each group consists of six *elements*, which are progressively smaller. An element on the test target consists on 3 horizontal and 3 vertical lines (see Figure 5.3). Each of the lines are 5 times longer than wide; the distance between two lines is exactly equivalent to the width of a line. The combination of a black and a white line is called a *line-pair (lp)*.

For a defined group G, the element E has the following properties:

Resolution [lp/mm]	$x = 2^{G+\frac{E-1}{6}}$
Line length [mm]	$L = 2.5/x$
Line width [mm]	$l = L/5 = 0.5/x = 1/2x$

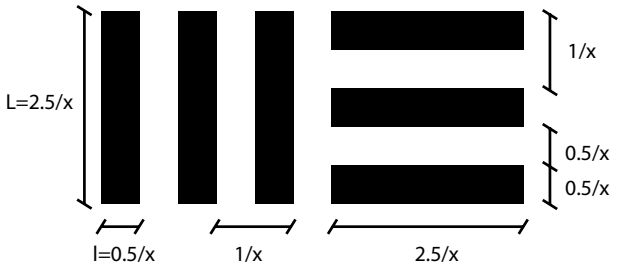

Figure 5.3: *Size of the elements on the USAF target*

In Table 5.1, the resolution is stated in line pairs per millimeter (lp/mm). From element to element(in a column downwards), the resolution increases by a factor 1.12. From group to group (in a line to the right), the resolution doubles.

	Group									
Element	-2	-1	0	1	2	3	4	5	6	7
1	0.25	0.50	1.00	2.00	4.00	8.00	16.00	32.00	64.00	128.00
2	0.28	0.56	1.12	2.24	4.49	8.98	17.96	35.92	71.84	143.68
3	0.31	0.63	1.26	2.52	5.04	10.08	20.16	40.32	80.63	161.27
4	0.35	0.71	1.41	2.83	5.66	11.31	22.63	45.25	90.51	181.02
5	0.40	0.79	1.59	3.17	6.35	12.70	25.40	50.80	101.59	203.19
6	0.45	0.89	1.78	3.56	7.13	14.25	28.51	57.02	114.04	228.07

Table 5.1: *Resolution in lp/mm rounded to 2 decimals of the USAF-1951 test target*

The endoscopic setup adapted for the HM study in the bladder (HM cystoscope coupled to the PDD camera) is able to resolve patterns down to the element 5 of the group 7, corresponding to a line width of 2.46 μm (see Figure 5.4).

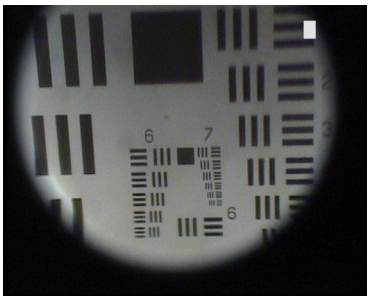

Figure 5.4: *Image of the USAF target acquired with the HM rigid cystoscope*

5.2.3 Calibration of the magnification

We performed calibration measurement for the HM rigid cystoscopes, with different settings and instrumentation :

- two HM cystoscopes (HM1 and HM2) built with the same architecture. Due to the sterilization process that last more than 12 hours at CHUV, we needed two cystoscopes to acquire images in two different patients on the same day.
- two endoscopic cameras : filtered (F) and non-filtered (NF). Filter was removed in one PDD camera to acquire blue-backscattered images to target hemoglobin absorption peak (see Appendix E).
- focusing position of the camera, controlled by a small handle on the camera side : extreme counter-clockwise (CCW) , infinite (inf), extreme clockwise (CW). While rotating the cystoscope knob, it is possible to acquire sharp images regardless if the camera is in CW or CCW position.
- the same test were done with different illumination light (WL, PDD blue light, green light). Since the results were similar, we present only the results acquired in WL.

For that purpose, we translated the cystoscope in a plane perpendicular to the USAF target plane, the cystoscope being tilted to compensate the viewing angle (25°). Images of the USAF target were then acquired at different distances (i.e. different magnification). The translation of lens groups (inside the cystoscope ocular) is such that for each distance endoscope-target ($\approx s$), this cystoscope model features two different magnification that yield a sharp image while rotating the knob : (i) "moderate"-magnification ($< 400\times$); (ii) "high"-magnification (400–650×).

In "moderate"-magnification, we can track the diameter of the endoscopic circular mask (i.e. field of view), which is varying with the knob position (Figure 5.5) and link it to the magnification since we can identify patterns of known size on the USAF target (Figure 5.6).

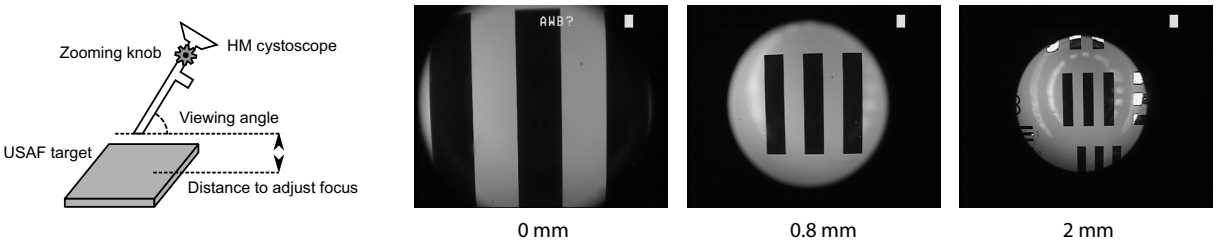

Figure 5.5: *Images of the same USAF element acquired at different distances. As one has to rotate the knob to stay in focus, one can observe the varying size of the circular mask around the image.*

Figure 5.6 plot the magnification vs. diameter of the endoscopic circular mask, which was measured in pixels, assuming that the whole image is extracted from a full PAL frame (720×576 pixels^2). The linear fitting parameters ($y = a \cdot x + b$) plotted in Figure 5.6 are summarized in Table 5.2 for each measurement configuration.

We observe first that the camera model has little influence over the a_i coefficients, whereas a small offset appears in the b_i coefficients. The offset can result from small differences in the measurement setup (position of the camera, angulation, etc.). Second, the infinite focusing lies between the two extreme position CW and CCW (except for HM1 NF), which means in the clinical environment that the camera should be focused at infinity *before* being clipped to the HM cystoscope. Even if the two HM cystoscopes are built with the same architecture, we observe variations when the camera is focused at infinity. This may result from optical imprecisions in

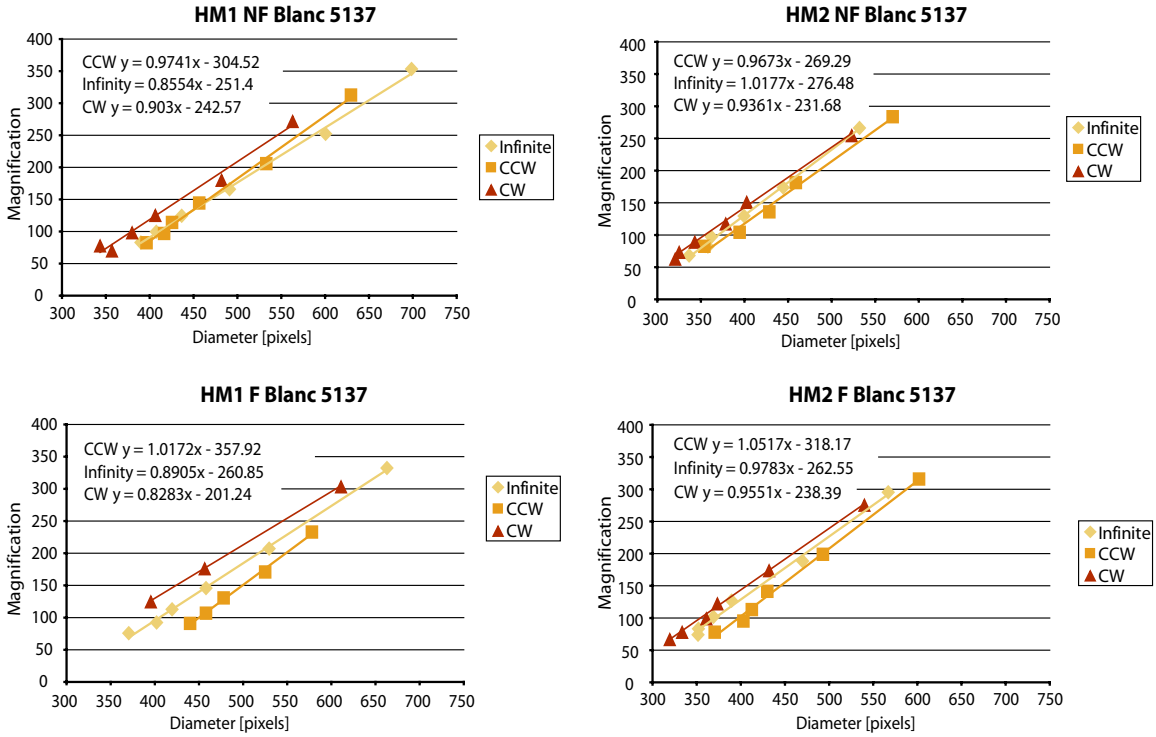

Figure 5.6: *Magnification vs. diameter of the endoscopic circular mask for the "moderate"-magnification regime.*

the manufacturing process. Even if the standard deviations are acceptable in this context, the measurements variations may result from the following imprecisions: (i) circle size measurement (circle edges were not clear steps, but rather diffuse borders); (ii) since the DOF is not equal to zero, errors may occur in finding the minimal distance at which the USAF target is sharp.

	CCW $a_1x + b_1$		Infinite $a_2x + b_2$		CW $a_3x + b_3$			
	a_1	b_1	a_2	b_2	a_3	b_3	a_i $(\mu \pm \sigma)$	b_i $(\mu \pm \sigma)$
HM1 NF	0.97	-304.52	0.86	-251.40	0.90	-242.57	*0.91±0.06*	*-266.16±33.51*
HM1 F	1.02	-357.92	0.89	-260.85	0.83	-201.24	*0.95±0.06*	*-295.82±53.92*
HM2 NF	0.97	-269.29	1.02	-276.48	0.94	-231.68	*0.96±0.05*	*-249.92±23.53*
HM2 F	1.05	-318.17	0.98	-262.55	0.96	-238.39	*1.00±0.05*	*-273.04±40.91*
mean	*0.99*	*-305.55*	*0.94*	*-262.82*	*0.94*	*-245.33*		
std dev	*0.05*	*48.28*	*0.08*	*10.34*	*0.02*	*16.21*		

Table 5.2: *Summary of the linear fitting coefficients for the relationship magnification vs. diameter*

In the "high"-magnification regime, the diameter is not changing significantly, and we thus tracked the knob position with the help of a graduation. Figure 5.7 shows the relationship between the knob position and the magnification. The quadratic fitting has been added for visual support. One unit corresponds to a rotation of $360°/14 \simeq 26°$.

5.2.4 Flexible HM endoscopes : optical specifications

Based on the results of the explorative study (see Section 5.3) which enabled us to define the optimal magnification (ranging 80–100 ×), our industrial partner decided to integrate the high magnification feature into the tip of a flexible endoscope. At this point, it should be noted that a

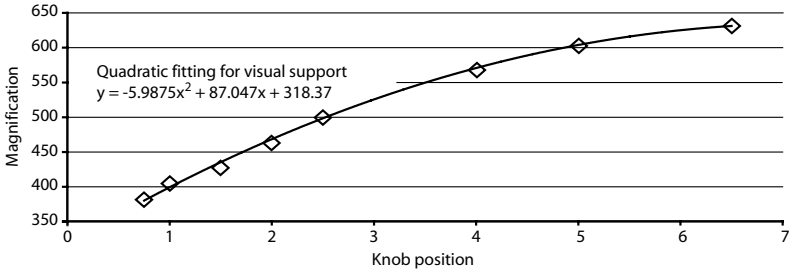

Figure 5.7: *Magnification vs. knob position for the "high"-magnification regime for the HM1 cystoscope with the filtered camera at infinite position.*

similar approach was conducted in bronchoscopy to characterize the false-positive lesions resulting from autofluorescence bronchoscopy (see Chapter 11). The first prototypes were designed with a fixed focal length, so that the only way to perform magnification cystoscopy/bronchoscopy was to get closer to the mucosa within the DOF.

The developed prototypes (broncho and cysto) are built following the same architecture. Only the CCDs and color settings are modified to account for the different fluorescence modes (AF vs. PDD).

Figure 5.8 plots the relationship between distance to the mucosa and magnification. The HM flexible scopes were compared to the non-modified flexible scopes for both broncho- and cystoscope. The dashed lines (located at 2 mm and 4 mm, respectively) represent the shortest theoretical limit of sharpness; the points measured below this limit are irrelevant, because the patterns of interest were not well resolved at these distances/magnifications. The exponential fits are presented for visual support. Interestingly, we can observe the same optical characteristics for the two non-modified scopes, as well for the HM scopes.

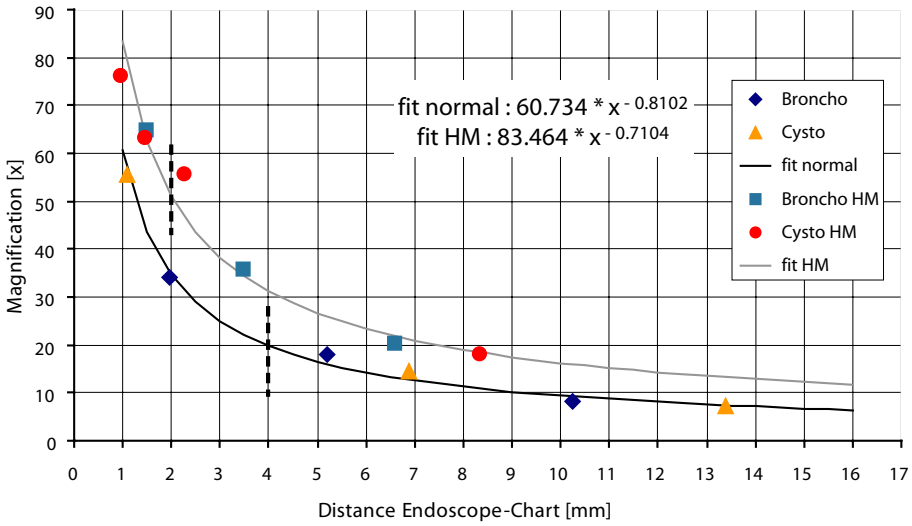

Figure 5.8: *Magnification on a 19 inches monitor of the flexible broncho- and cystoscopes*

In the bladder, we were able to show that the last flexible prototype developed for HM cystoscopy has a limit of sharpness, which prevents the imaging of the vessel of interests. Indeed, when comparing the performances of the HM rigid cystoscope (which served for the clinical study present in Section 5.3) and the flexible HM cystoscope, we observe a decrease in resolution. The flexible HM cystoscope can not focus on objects closer than 2 mm, resulting in a blurring of

the vessels even if the magnification would be sufficient to identify them. Figure 5.9 shows the direct comparison of the rigid and flexible HM cystoscopes, illuminated with green light (see Appendix E). We observe a similar field of view, but the resolution is higher with the rigid cystoscope. The white arrows shows the small capillaries that help to discriminate FP from TP on flat lesions, but they remain undetectable with the flexible HM scope.

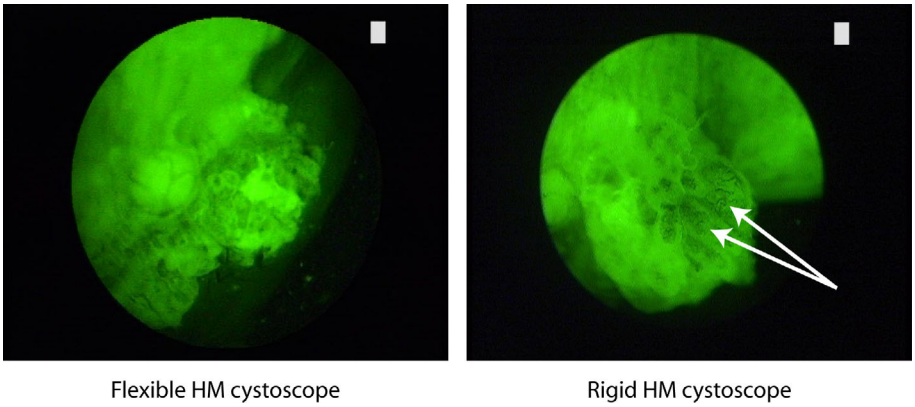

Figure 5.9: ***Comparison of the flexible and rigid HM cystoscopes.*** *The white arrows shows the capillary vessels that help to discriminate FP from TP on flat lesions.*

5.3 JBO Publication

High magnification vascular imaging to reject false-positive sites *in situ* during Hexvix® fluorescence cystoscopy

Blaise Lovisa[a], Patrice Jichlinski[b], Bernd-Claus Weber[c], Daniela Aymon[b], Hubert van den Bergh[a], and Georges Wagnières[a]

[a] Medical Photonics Group, EPFL, Batiment CH, Station 6, CH-1015 Lausanne, Switzerland
[b] Department of Urology, CHUV University Hospital, CH-1011 Lausanne, Switzerland
[c] Richard Wolf GmbH, Pforzheimerstr. 32, 75438 Knittlingen. Germany

Will be published in September/October 2010 issue of *Journal of Biomedical Optics*

Abstract: Fluorescence imaging for detection of non-muscle invasive bladder cancer is based on the selective production and accumulation of fluorescing porphyrins, mainly protoporphyrin IX (PpIX), in cancerous tissues after the instillation of Hexvix®. Although the sensitivity of this procedure is very good, its specificity is somewhat limited due to fluorescence false positive sites. Consequently, magnification cystoscopy has been investigated in order to discriminate false from true fluorescence positive findings. Both white light and fluorescence modes are possible with the magnification cystoscope, allowing observation of the bladder wall with magnification ranging between 30× for standard observation, and 650×. The optical zooming setup allows adjusting the magnification continuously *in situ*. In the high magnification regime, the smallest diameter of the field of view is 600 microns and the resolution is 2.5 microns, when in contact with the bladder wall. With this cystoscope, we characterized the superficial vascularization of the fluorescing sites in order to discriminate cancerous from non-cancerous tissues. This procedure allowed us to establish a classification based on observed vascular patterns. 72 patients subject to Hexvix® fluorescence cystoscopy were included in the study. Comparison of HM cystoscopy classification with histopathology results confirmed 32/33 (97%) cancerous biopsies, and rejected 17/20 (85%) non-cancerous lesions.

Abbreviations: ALA aminolevulinic acid, HAL hexyl ester of aminolevulinic acid, PpIX protoporphyrin IX, WL white light, HM high magnification, TP true positive, FP false positive, TN true negative, FN false negative

Keywords: non-muscle invasive bladder cancer, fluorescence cystoscopy, PDD, high magnification, Hexvix®, vessel patterns, vasculogenesis, angiogenesis

5.3.1 Introduction

Bladder cancer is the fourth most common cancer among men and the eighth most common malignancy in women in the Western world [Kirk05]. Urothelial cell carcinoma comprises 90% to 95% of all bladder cancers, with about 70% found initially as non-muscle-invasive bladder cancer and the remainder as invasive cancer [Oost01]. Flat lesions, such as high grade dysplasia or carcinoma in situ, are associated with a high risk of invasive progres-

sion, and an even higher recurrence rate (50-85%) [Drol05]. Therefore, there is a need for a reliable early detection method.

Over the past decades, white light (WL) cystoscopy was established as the standard diagnostic procedure to detect early bladder cancer. However, WL may lead to missing lesions, that are difficult or impossible to visualize [Joch05]. To overcome this limitation, fluorescence cystoscopy based on aminolevulinic acid (5-ALA) and its derivatives has now been well established. The fluorescence cystoscopy is performed using blue-violet light that excites the red fluorescence of the porphyrins, mainly protoporphyrin IX (PpIX) [Kenn90, Kenn92]. In the biosynthesis of heme, endogenous 5-ALA is a natural precursor of the fluorescing PpIX [Uehl00]. The subsequent conversion of PpIX into heme is relatively slow. The application of exogenous ALA-derivatives, including Hexvix®, can thus lead to accumulation of significant concentrations of fluorescing porphyrins. The latter are selectively produced and accumulated in these early lesions upon the instillation of the bladder with a solution of Hexvix® during about one hour [Jich03b, Jich08]. With this method, the sensitivity of cystoscopy for flat lesions that are overlooked in white light is improved to nearly 100% [Jich03b, Jich08, Schm04]. Thus, fluorescence cystoscopy will reveal areas in the bladder that are suspicious for flat lesions (dysplasia, pTis) or small papillary tumor (pTa, pT1) that can not always easily be seen with WL cystoscopy [Gros07, Frad07]. Furthermore, it has been shown that fluorescence cystoscopy reduces the tumor recurrence rate, probably due to a more complete resection [Dani05, Witj07, Denz07, Babj05].

Fluorescence cystoscopy has a high sensitivity, but still yields a relatively high percentage of fluorescence false positive lesions, typically 39% [Gros07, Frad07]. Histopathological diagnosis of the false positives showed that false fluorescence mostly occurred in tissues with a high cell turnover such as metaplasia, hyperplasia, and chronic inflammation [Jich03b]. In 2005, the European Association of Urology (EAU) has approved the fluorescence cystoscopy as standard method for the detection of non-muscle invasive bladder cancer [van 05]. The FDA positively reviewed this method as a new drug application for Hexvix® in 2009.

There is clear evidence that the features of angiogenesis (such as microvessel density) and expression of angiogenic factors are related to adverse outcomes in bladder cancer [Char06]. Reiher *et al.* et al. confirmed the strong association of microvessel density with the well established prognostic factors of grade and stage in non-muscle invasive bladder cancer [Reih02].

It is likely that developing new imaging capabilities for vascular imaging will also facilitate discriminating mucosal changes in the bladder. Vascular patterns, like tortuous vessels and vessel loops, are used to identify neoplasia in several organs including the bronchi, and the upper and lower gastrointestinal tract [East08, Kuma06, Shib02, Shib03]. In bronchoscopic studies, Shibuya *et al.* state that conventional white light bronchoscopes observe only increased redness and local swelling, whereas high magnification bronchoscopes enable the vascular network to be visualized in the bronchial mucosa [Shib02, Shib03]. Morphological features such as vessel growth and complex networks of tortuous vessels help these authors to identify this cancerization process [Shib03]. Indeed, they were able to distinguish between inflammatory tissue and neoplastic lesion in the bronchi by observing the complex neo-vascular structure and tortuosity. Different group showed that a zooming observation allows to observe changes in the intrapapillary capillary loops in the esophagus, including dilatation, weaving, changes in caliber and differences in shape [Kuma06, Inou97]. They also observed that the tumor vessels were rearranged at the surface of the tumor. Similarly, East el al. defined the vascular pattern intensity, which is directly related to the microvessel density, in combination with the Kudo pit pattern classification, to assess the malignancy of small colonic polyps [East08].

With the development of high magnification (HM) cystoscopy presented in this

manuscript, it is possible to visualize alterations of the vascular organization at the surface of the bladder mucosa. Thanks to its optical zoom, our cystoscope allows to adjust the magnification continuously between the low and high magnification regimes by turning a knob and changing the distance between the cystoscope tip and the mucosa. As compared to cellular imaging systems, the operator is able to first localize the area of interest with the help of fluorescence cystoscopy, and then to zoom in, to characterize the superficial vascularization, using one and the same device. Therefore, HM examination fits easily into the clinical routine, as it doesn't require much extra time and instrumentation.

The present study evaluates this vascular imaging technology on patients that were subject to routine fluorescence cystoscopy. To our knowledge, this is the first time that vascularization patterns are used as a discrimination criterion on fluorescence positive spots in the bladder. A flexible videoendoscope will be designed based on the results of this study in order to allow an observation of the whole bladder in both low and high magnification regimes.

5.3.2 Materials & Methods

High magnification setup

The bladder was first inspected with a conventional fluorescence cystoscope to localize the fluorescence positive sites under blue-violet light. The accessible fluorescing sites were then observed with the rigid magnification cystoscope (Lumina Microview 25°, Richard Wolf GmbH, Germany). This cystoscope (see Figure 5.1) was first operated in a "low-magnification" regime to identify the fluorescence positive lesions in fluorescence mode, and then in a HM regime to characterize the vascularization under white light reflectance mode. This approach is quite convenient, since it enables to observe the bladder wall with magnification ranging continuously between 30× and 650× under fluorescence or white light observation, without changing the cystoscope.

The HM cystoscope has an external diameter of 4 mm and is equipped with a knob allowing alteration of the magnification in situ. This continuous range is achieved by simultaneously adjusting the device's focal length and the cystoscope-tissue distance. The magnification is defined here as the ratio between the sizes of the object on the image displayed on a 19 inches monitor and the corresponding real object, given that our conventional cystoscope yields a 30x magnification. The present device is able to resolve patterns down to the element 5 of the group 7 on the USAF target 1951 (line width: 2.5μm, corresponding to 200 lp/mm, Figure 5.4).

Endoscopic image classification

The whole procedure was recorded on a DV recorder (DVCAM DSR 20MDP, Sony Corporation, Japan) and digitized using the IEEE1394 connection between the DV recorder and a portable PC. In an explorative preliminary study (data not shown), individual frames were extracted from the video sequences, and image classification was performed offline based on visual quantification of the vessel patterns. Images were classified in five categories: A) "linear", i.e. "normal", vascularization B) edema and/or vessel thickening C) tortuous vessels and/or vessel loops D) dense mesh and/or disorganized network E) no vascularization visualized while probing the lesion. In the latter, the images were excluded from the statistics. Typical HM images on flat fluorescence positive sites are shown in Figure 5.10 according to the classification.

In the study presented here, the vascularization patterns were classified intraoperatively based on the categories (A to E). DV recording was only used for documentation purposes.

Patient population

78 patients (54 men, 24 women; mean age 67; range 18-85) with suspected or verified blad-

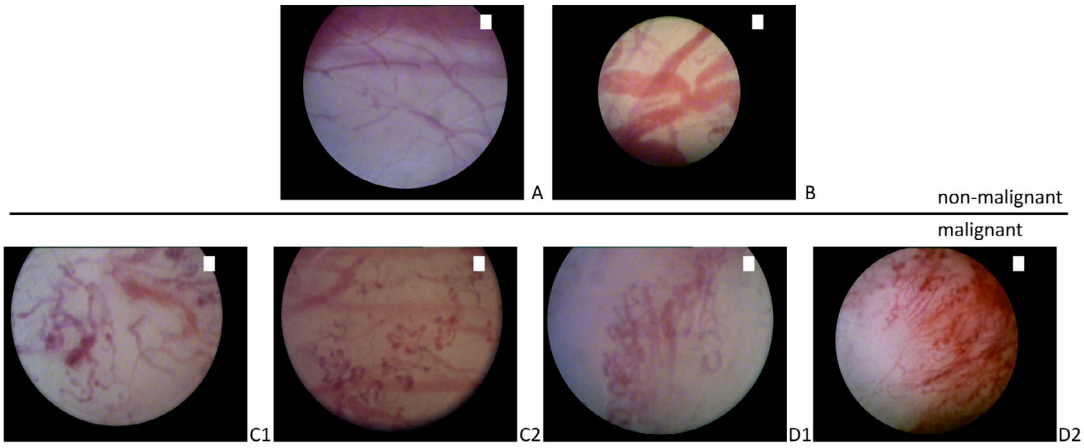

Figure 5.10: *High magnification endoscopic images acquired under white light.*
Non-malignant: A) normal vessels B) edema and vessel thickening
Malignant: C1) tortuous vessels C2) vessel loops D1) dense mesh D2) disorganized network

der cancer (by means of positive urinary cytology, prior cystoscopy or a history of urothelial cancer) were enrolled between September 2007 and August 2009. They underwent fluorescence cystoscopy with Hexvix® at the CHUV University Hospital (Lausanne, Switzerland), under loco-regional or general anesthesia. Patients were informed about the benefits and risks of the fluorescence procedure and the study was acknowledged by the local ethics committee.

Endoscopic procedure

Hexvix® (GE Healthcare, USA) was prepared by reconstitution of 100 mg of hexaminolevulinate (HAL) hydrochloride powder, equivalent to 85 mg of HAL, in 50 ml phosphate buffered saline. Following hospitalization, patients received an intravesical instillation of 50ml (8mM) solution of Hexvix® through a standard catheter for about one hour. After emptying of the bladder, inspection and mapping of all lesions and suspicious areas was done by an urologist with experience in this method.

Imaging system

The endoscopic fluorescence imaging system basically consists of a filtered light source and a filtered endoscopic camera, as shown schematically in Figure 5.11. Fluorescence cystoscopy was performed using a commercial system (Richard Wolf GmbH, Knittlingen, Germany), which allowed bladder wall inspection with both white light reflectance and blue-violet light excited fluorescence. The endoscopic light source is based on an IR filtered 300 W Xenon lamp (Richard Wolf GmbH, Germany) equipped with a flip-flop filter holder containing a light-attenuation grid for conventional white light illumination and a blue-violet interference filter (390-440 nm) to excite the fluorescence of the porphyrins, mainly PpIX. The camera collects the red fluorescence and the tissue autofluorescence through a long-pass filter (cut-on wavelength 450 nm). A foot switch allows rapid changing between white light illumination and blue-violet fluorescence excitation. The source light is delivered to the cystoscope optics by a liquid light guide.

Histopathological analysis

Each fluorescing positive site was cold-biopsied and/or resected. Tissue samples were fixed in formalin and examined by an experienced pathologist who was blinded to the high-magnification description of the vascularization. Urothelial carcinomas were graded according to the World Health Organization (WHO) 1973 classification [Most73] and to the

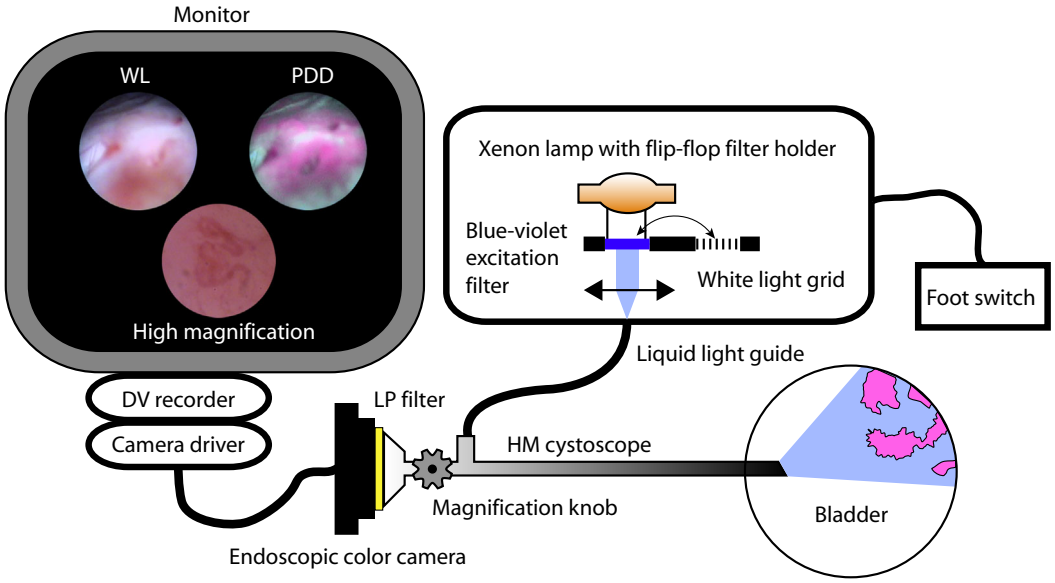

Figure 5.11: *Fluorescence cystoscopy setup.*

consensus WHO/International Society of Urological Pathology (ISUP) 1998 [Epst98]. Fluorescence positive biopsies were then grouped into two classes: non-malignant (normal, metaplasia, hyperplasia, chronical inflammation), malignant (dysplasia, pTa, pT1, pT2, pTis).

5.3.3 Results

Histopathology

A total of 179 biopsies taken on fluorescence positive (HAL+) spots were biopsied. They were macroscopically classified as being 111 flat, 51 exophytic, 17 scar tissues. In this study, we retained the macroscopic description, i.e. flat vs. exophytic, given by the operator intraoperatively, even if it differs from the pathological description. 10 pTa and 4 pT1 appeared flat, whereas 3 pTis and 1 dysplasia appeared exophytic.

The regions of interest that initially tested as fluorescence positive (HAL+) or white light positive (WL+) but upon pathological analysis were described as non-cancerous biopsies were characterized as false positives (HAL/FP and WL/FP, respectively). Similarly, HAL+ and WL+ regions of interest that demonstrated cancerous biopsies were characterized as true positives (HAL/TP and WL/TP, respectively).

Table 5.3 shows the histopathological analysis of the 179 HAL+ biopsies, detected by Hexvix® and WL cystoscopy, respectively. The additional columns list how many biopsies contained inflammatory tissue. Table 5.4 shows the same data for flat lesions only.

We can observe that fluorescence cystoscopy is much more sensitive to early lesions than WL cystoscopy (see Table 5.3), even in this case of a very experienced WL endoscopist. Indeed, 39 additional lesions were discovered with the help of Hexvix® cystoscopy. Table 5.3 shows that inflammation is present in 41/68 (61%) of the HAL/FP, whereas it is only the case in 17/111 (15%) of the HAL/TP. Table 5.4 shows that the same observation is valid for flat lesions; inflammatory tissue is present in 29/53 (55%) of the HAL/FP, whereas it is only the case in 12/58 (21%) of the HAL/TP. 35 additional flat lesions were discovered with the help of Hexvix® cystoscopy. It is interesting to note that no inflammatory tissue was found in the pT1 and pT2 cancers.

	No. detected on HAL+ sites					
	HAL+	with inflam.		WL+	with inflam.	
dysplasia	18	7	111 HAL/TP	8	5	72 WL/TP
pTa (G1-G3)	43	3		33	1	
pT1 (G1-G2)	12	0		11	0	
pT2	4	0		4	0	
pTis	34	7		15	4	
non-malignant	68	41	68 HAL/FP	27	17	27 WL/FP
Total	179	58		99	27	

Table 5.3: *Histopathological analysis of the 179 fluorescence positive (HAL+) lesions*

	No. detected on HAL+ sites					
	HAL+	with inflam.		WL+	with inflam.	
dysplasia	15	5	58 HAL/TP	5	3	23 WL/FP
pTa (G1-G3)	10	1		5	0	
pT1 (G1-G2)	4	0		3	0	
pT2	0	0		0	0	
pTis	29	6		10	3	
non-malignant	53	29	53 HAL/FP	16	8	16 WL/FP
Total	111	58		99	27	

Table 5.4: *Histopathological analysis of the 111 flat fluorescence positive (HAL+) lesions*

High magnification descriptive analysis

Among the 179 biopsies, 58 HAL+ sites from which 45 flat lesions were observed with high magnification in order to try to decrease the number of FP, and thus the number of biopsies taken. The HM clinically observed blood vessels were classified into four categories, including: A) normal or linear vascularization; B) edema and vessel thickening; C) tortuous vessels / vessel loops; D) dense mesh / disorganized network. Biopsies that were classified as cancerous and could be attributed with either HM classifications A and B are referred to as HM false-negative (HM/FN), while HM classifications C and D are referred to as HM true-positive (HM/TP). Conversely, biopsies that were classified as non-cancerous and could be attributed with either HM classifications A and B are referred to as HM true-negative (HM/TN), while HM classifications C and D are referred to as HM false-positive (HM/FP).

Table 5.5 summarizes the result of the classification analysis of the 58 HAL+ lesions observed with HM: 36 true positive (HAL/TP) and 22 false positive (HAL/FP). With the help of HM cystoscopy, 32/33 (97%) HAL/TP lesions with clinical in situ visualized vascularization could be confirmed and 17/20 (85%) HAL/FP lesions with a visible vascularization could be rejected. The cancerous lesion that was not confirmed by our HM method (HAL/TP–HM/FN) was infiltrated by a sarcomatoid carcinoma. Conversely, the 3 lesions with vascular irregularities that were described as non-cancerous by the histopathologist (HAL/FP-HM/FP) had the following histology: granulomatous inflammation, von Brunn nests that mimic urothelial carcinoma and lymphoid infiltration, respectively.

Table 5.6 summarizes the result of the visual classification of the 45 flat HAL+ lesions observed with high magnification: 24 true positive (HAL/TP) and 21 false positive (HAL/FP). With the help of HM cystoscopy, 22/22 (100%) HAL/TP flat lesions with visualized vascularization could be confirmed and 17/19 (89.5%) HAL/FP lesions with a visible vascularization could be rejected.

HM descriptive analysis		36 HAL/TP		22 HAL/FP	
non-malignant	(A) linear vascularization	0	1 HM/FN	15	17 HM/TN
	(B) edema and vessel thickening	1		2	
non-malignant	(C) tortuous vessels / vessel loops	22	32 HM/TP	2	3 HM/FP
	(D) dense mesh / disorganized network	10		1	
	Total	33		20	
discarded	(E) no visualized vascularization	3		2	

Table 5.5: *Visual classification of the 58 fluorescence positive lesions observed with high magnification: 36 true positive (HAL/TP) and 22 false positive (HAL/FP).*

HM descriptive analysis of the flat lesions		24 HAL/TP		21 HAL/FP	
non-malignant	(A) linear vascularization	0	0 HM/FN	15	17 HM/TN
	(B) edema and vessel thickening	0		2	
non-malignant	(C) tortuous vessels / vessel loops	12	22 HM/TP	2	2 HM/FP
	(D) dense mesh / disorganized network	10		0	
	Total	22		19	
discarded	(E) no visualized vascularization	2		2	

Table 5.6: *Visual classification of the 45 flat fluorescence positive lesions observed with high magnification: 24 true positive (HAL/TP) and 21 false positive (HAL/FP).*

5.3.4 Discussion

Over the last years, fluorescence cystoscopy has been established as standard method for early bladder cancer detection in the European Union [Witj07, Hall07]. Fluorescence cystoscopy is particularly useful at improving the detection of flat lesions, such as pTis and pTa [Jich03b]. However, this technique has been related to a relative high-number of false-positive sites. Areas with a higher cellular turnover like metaplasia, hyperplasia, and residual inflammation also accumulate PpIX and in that sense fluoresce similarly to malignant tissue [Witj07]. Grimbergen *et al.* showed that several factors including drug uptake, and enzymatic activity have been known to influence the production and conversion or depletion of PpIX after exogenous application of the ALA or ALA-esters [Grim03]. Jichlinski *et al.* speculated that false positives can arise, in certain specific cases, from oblique illumination of the mucosa if the distal end of the endoscope is too close to the bladder wall [Jich97]. Indeed, when the tissue is illuminated tangentially, it may produce a high level of fluorescence on the normal mucosa, particularly at the bladder neck and the trigone [Zaak08]. Additionally, bladder mucosa exposed to intravesical therapy in the weeks prior to fluorescence cystoscopy could also exhibit a higher rate of false-positive lesions [Grim03, Drag10]. Draga *et al.* also showed that the false-positive rate decreases during the first 12 weeks after the latest resection [Drag09].

In this study, we aimed to differentiate vascular patterns between non-malignant, false-positive, and malignant, true-positive changes in the bladder. Several groups have previously developed systems able to acquire images at the cellular level in the gastro-intestinal tract [Wang07], even in the bladder [Sonn09], but it appears that this approach has several limitations, particularly the microscopic field of view and the need for additional contrast dyes [Sonn09]. Scanning of the whole organ is thus not realistic in a clinical environment. Therefore, we have focused our research on the characterization of vascular patterns on suspicious sites already localized by Hexvix® fluorescence cystoscopy. In this configuration, a fluorescent site can easily be characterized with

high magnification by turning the knob, adjusting the distance and switching to the appropriate illumination light. This approach is very convenient since it allows visualization of the bladder using fluorescence and white light, both in the low and high magnification regime without changing the cystoscope.

Bladder cancer is often multi-focal in nature. In this study, due the bladder ovoid geometry, this rigid cystoscope prototype with small viewing angle (25°) doesn't allow instrumental access to all parts of the bladder. In particular, the anterior wall and dome could not be imaged easily. Thus, in the statistics, the number of sites that are observed with the HM cystoscope is much smaller that the total number of fluorescence positive sites observed. We reviewed both flat and papillary fluorescence positive sites. In each papillary tumor, we have observed the so-called intrapapillary loops, where the capillaries appear like small rings of about 50μm in diameter close to the surface. The shape of the vessels was in good agreement with those observed in other organs [Shib02].

All cystoscopy results can be more or less affected by the urologist learning curve. In particular, the rejection of false-positives highly depends on the physician's experience. The non-perfect specificity of the well-established drug Hexvix® has also been observed in larger HAL phase III studies [Gros07, Frad07]. Our false-positive rate 68/178 (38%) is in fact in good agreement to what has been obtained in the latter (39%). In the present study, HAL cystoscopy detects 57% (107/68) more non-muscle invasive lesions such including dysplasia, pTa, pT1, and pTis. Although there is an increase in the number of false-positive lesions, this clearly indicates a major advantage of HAL cystoscopy vs. conventional WL cystoscopy, because it will allow a more complete resection [Babj05].

The three HM/FP (see Table 5.5) that are not cancerous lesions are tissues of identified types that may also induce modulation of the superficial vascularization that presumably supports cellular changes at the surface of the urothelium [Roma03]. Conversely, no vascular alteration could be observed with our setup on the HM/FN lesion, even if it was protruding out of the bladder wall, probably because this pathology was not originated in the bladder mucosa.

Our results were based on the urologist subjective appreciation, whereas an image analysis method for quantifying blood vessels could be helpful to aim at greater objectivity. Experiments on small blood vessels in the chorioallantoic membrane (CAM) model have led to the development of a multistep mathematical procedure to obtain a skeleton representation of the vessels and capillaries [N.-S10]. Similarly, software analysis of retinal vasculature images highlighted the potential of defining site-based parameters, such as local vessel diameter, fractal dimension, and tortuosity [Vick09]. We are currently working at the integration of these quantification algorithms in our procedure. This may be of interest to assess the status of sites appearing positive during fluorescence cystoscopy. The next generation of prototypes with a better image quality may help algorithms to run with fewer artifacts.

Table 5.5 & 5.6 illustrates that HM image acquisition may be impaired by missing some vascular patterns while looking at the fluorescence positive sites (5 for all lesions, 4 for flat lesions). Recent studies have targeted the hemoglobin absorption peaks using the narrow-band imaging technology [Herr08]. At present, we are investigating the potential use of selected excitation wavelengths (data not shown) to improve the contrast between the vessels and the surrounding mucosa. This may help to point out the optimal vessels (depth and size) to discriminate FP from TP fluorescence positive sites. Furthermore, an increase in the cystoscope contact pressure may lead to a decrease in the superficial blood flow, and thus a decrease in reflectance light absorption, and hence the vessels close to the surface may disappear from the field of view. A spacer may be added to the cystoscope in the future to avoid this effect.

The observations made on exophytic le-

sions reveal a distinct pattern of vascularization, with loops sprouting along the papillary. In conjunction with a histochemical analysis of the biopsies, this approach may serve as a visual method for staging and grading of the exophytic bladder carcinomas.

The rigid cystoscope used in the present study prevents the visualization of the proximal part of the bladder wall, and has evident drawbacks regarding bladder accessibility. However, this cystoscope prototype helped us to demonstrate the proof-of-principle of this vessel characterization technique to identify false-positive lesions. This HM cystoscope approach can also be used for the characterization of sites suspicious under white light, or detected by other diagnostic techniques, including hypericin fluorescence cystoscopy [Bhuv10].

In summary, we claim that this "detect-and-characterize" procedure based on a high-magnification cystoscope is very convenient since no change of endoscope is required to switch between the fluorescence detection and tissue vascular characterization modes. Therefore, with a rejection rate (97%) of FP lesions, HM is likely to be a non-invasive, simple and convenient approach to reduce the number of biopsies and improve patient management.

5.3.5 Acknowledgments

This study was supported by Swiss National Science Foundation grant # 205320-116556/1. We would like also to thank Dr. Julia Jacobi for generous financial support. We thank physicians at CHUV university hospital for their contribution and advices (Drs. Valentin Praz, Cédric Treuthardt, Yves Chollet, Yassine Zarkik, Arnaud Doerfler, Laurent Vaucher, Thomas Tawadros, Cécile Tawadros, Matieu Uffer).

5.4 Evaluation of the vascular skeletonisation

The study of section 5.3 describes the classification of vascular patterns based on high magnification cystoscopy. As such, we acknowledge that the specificity and sensitivity depends on the operator, as it is the case in many diagnostic methods routinely used in the clinics. However, during this study, we observed that most of the vascular patterns could be correctly classified after only a short learning period (2–3 HM cystoscopies).

This section estimated whether the whole information that allows the observer to classify the vessel patterns in Section 5.3 is fully contained in the skeleton or not. Indeed, before spending a lot of time in implementing various image processing algorithms to extract the vessels from the background, it was worthwhile to see if the end result would contain the relevant information. In addition, this preliminary study aimed to identifying the critical features that should be used to discriminate the false-positive from the true-positive fluorescence areas.

We present here an offline classification study, in which 11 first-time observers were asked to classify 27 endoscopic images and to choose the most appropriate description for the vascular patterns they observed in the presented 27 HM pictures: linear, thickening, tortuous, dense network or loops (see Figures 5.14 & 5.15). These 27 images were acquired on areas, that were subsequently biopsied (11 non-cancerous, 16 cancerous). With these 27 images, the observers (blinded to the histopathological results) were told to define two image sets with 11 False-Positive (linear, thickening) and 16 True-Positive (Tortuous/Dense Network/Loops). This classification is the same one as that used in the publication (see Section 5.3.2). All images were acquired with WL illumination, except images No. 5, 10, 21, 25 that were acquired with green light illumination (derived from the spectral optimization described in Appendix E). The great variations in color appearance is due to the different tissue backscattering properties.

In a second step, we manually segmented the 27 images of interests. With the pen/bucket tool in ImageJ/Photoshop (NIH and Adobe Inc.), we divided the RGB image into two pixel classes : (i) vessel (ii) tissue. It resulted in black&white (BW) images, that are also depicted in Figures 5.14 & 5.15. The same 11 observers were asked to classify the 27 skeletons with the same criteria.

The percentage of false classification (PFC) is computed as the number of wrong answers over the total number of answers. For each image couple in Figure 5.14&5.15, the numbers in red indicate the PFC either for the original image or its skeleton (if $\neq 0$).

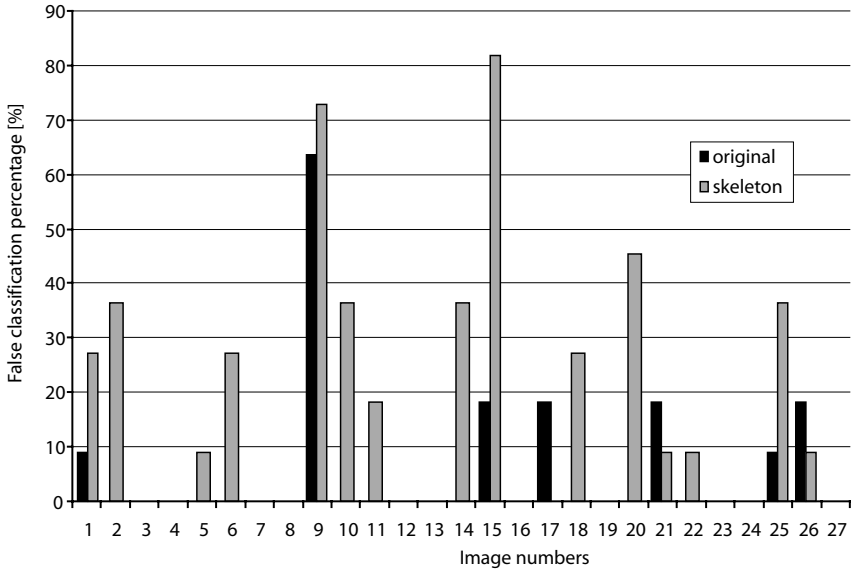

Figure 5.12: *Percentage of false classification of the 27 HM images (original & skeleton)*

Figure 5.12 shows the PFC for each image couple (original & skeleton). This small observer population ($n = 11$) reached an accuracy of 94% for original endoscopic images, which shows that a correct classification is likely not to be observer-dependent.

The skeletons are more difficult to classify than the original images (see Figure 5.12). Hence, such a visual classification based on the skeletons only would lead to a higher PFC. Indeed, the average error was higher for the skeletons (17.8%) than for the original images (5.7%). This may be explained by at least four factors :

- the depth information is lost in skeletons. Indeed, on conventional images, it is fairly easy to evaluate if a vessel is coming to the surface and entering at an other spot. In others words, if the vessel is fully contained in a plane parallel to the surface, or connected to other with vertical bridges.
- the layered structure of the urothelial vasculature is also lost. Indeed, when acquiring images *in vivo*, it is fairly easy to identify the different vasculature layers, due to the fact that some are altered when touching the surface with the endoscope (superficial vessels), whereas some remains unaffected (deeper vessels). In a skeletonized image, one perceives only the 2D network without any information about how the layered architecture of the vasculature.
- in the skeleton, the vessels appear as a uniform black tube, whereas in the original image, the vessels do not have a uniform cross-section and their profile can also contain information for the operator.

- in the skeleton, only the vessel tree is visible. All other structures (bubbles, mucosa irregularities, ...) are erased by the segmentation procedure. This gives a hint that extra-vascular patterns may also contain relevant information for the classification.

In Figure 5.10, we observe three classes of images : i) 0% PFC (3, 4, 7, 8, 12, 13, 16, 19, 23, 24, 27) ; ii) misclassification of original and/or skeleton (1, 9, 15, 17, 21, 25, 26); iii) only skeleton misclassification (2, 5, 6, 10, 11, 14, 18, 20, 22). Images with low density of vessels (7, 9, 12, 19, 23, 27) were classified mostly as TP (which is correct except for 9). This may be explain by the fact that small capillary loops appear as sparse vessel patterns. Images with large thickened vessels (5, 8, 13, 26) were mostly classified as FP. Vessel edema were often found on inflammatory mucosa.

Table 5.7 shows the statistics for the classification of the images (27 images for 11 observers correspond to a total of 297 occurrences).

a) Classification for original images

		Histopathology	
		Cancer	No cancer
Classification	Positive	173	14
	Negative	3	107

b) Classification for skeleton images

		Histopathology	
		Cancer	No cancer
Classification	Positive	142	19
	Negative	34	102

Table 5.7: *Classification vs. Histopathology for both original and skeleton images.*

Table 5.8 shows the compared values for sensitivity, specificity, positive and negative predictive value, likelihood ratio positive and negative. These terms are defined in Table 2.6. It appears clearly that the classification with the original image is more sensitive and more specific. It also displays a higher PPV and higher NPV.

	Sensitivity	Specificity	PPV	NPV	LR +	LR−
Original images	0.983	0.884	0.925	0.973	8.496	0.019
Skeleton images	0.814	0.843	0.887	0.75	5.185	0.22

Table 5.8: *Summary of the statistical values for the classification procedure.*

Figure 5.13 shows the post-test probability for both original and skeleton images. The larger the area between the blue and orange curves, the better the classification method, meaning that the classification based on the original images has better prediction capabilities.

Interestingly, the images acquired with green backscattered (GBS) light yield a higher PFC for the skeletons than the conventional images. Since, the small vessels are better resolved with GBS, the skeletons are appearing with a higher density of vessel, sometimes leading the observers to classify them as "dense mesh".

The "hand-made" segmentation procedure may suffer from some limitations, although it is often regarded as the "gold standard" for each vessel segmentation algorithms [M.-P07b, Sale10]. Since skeletons are more convenient to process with an automated image characterization procedure (vessel branching, areas, fractal dimension, ...), we also implemented an automated version of the skeletonisation process (see Section 5.5.1).

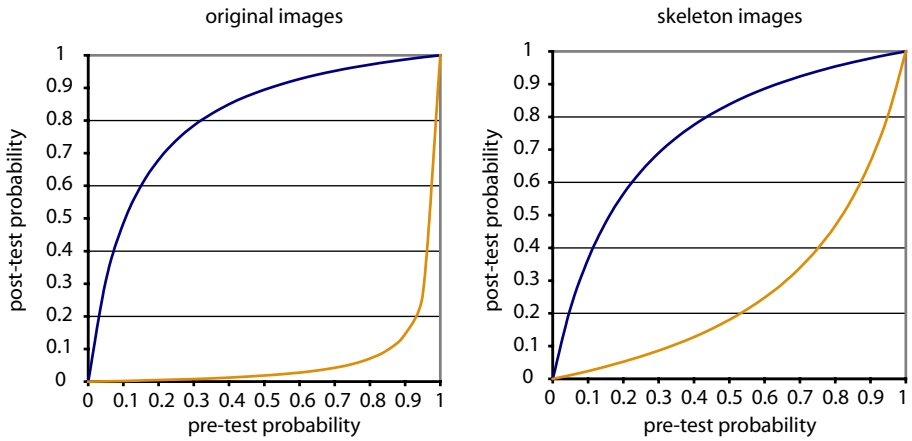

Figure 5.13: *Plot of the post-test probability for both original and skeleton images.*

In conclusion, based on the results of the visual classification, we can say that some visual information is lost after image skeletonisation. However, skeletonisation yields a binary image, that is best suited for image morphologic analysis. The latter analysis yields some non-visual parameters (number of branches, vessel mean length, fractal dimension) that can also be discriminant on fluorescence positive lesions.

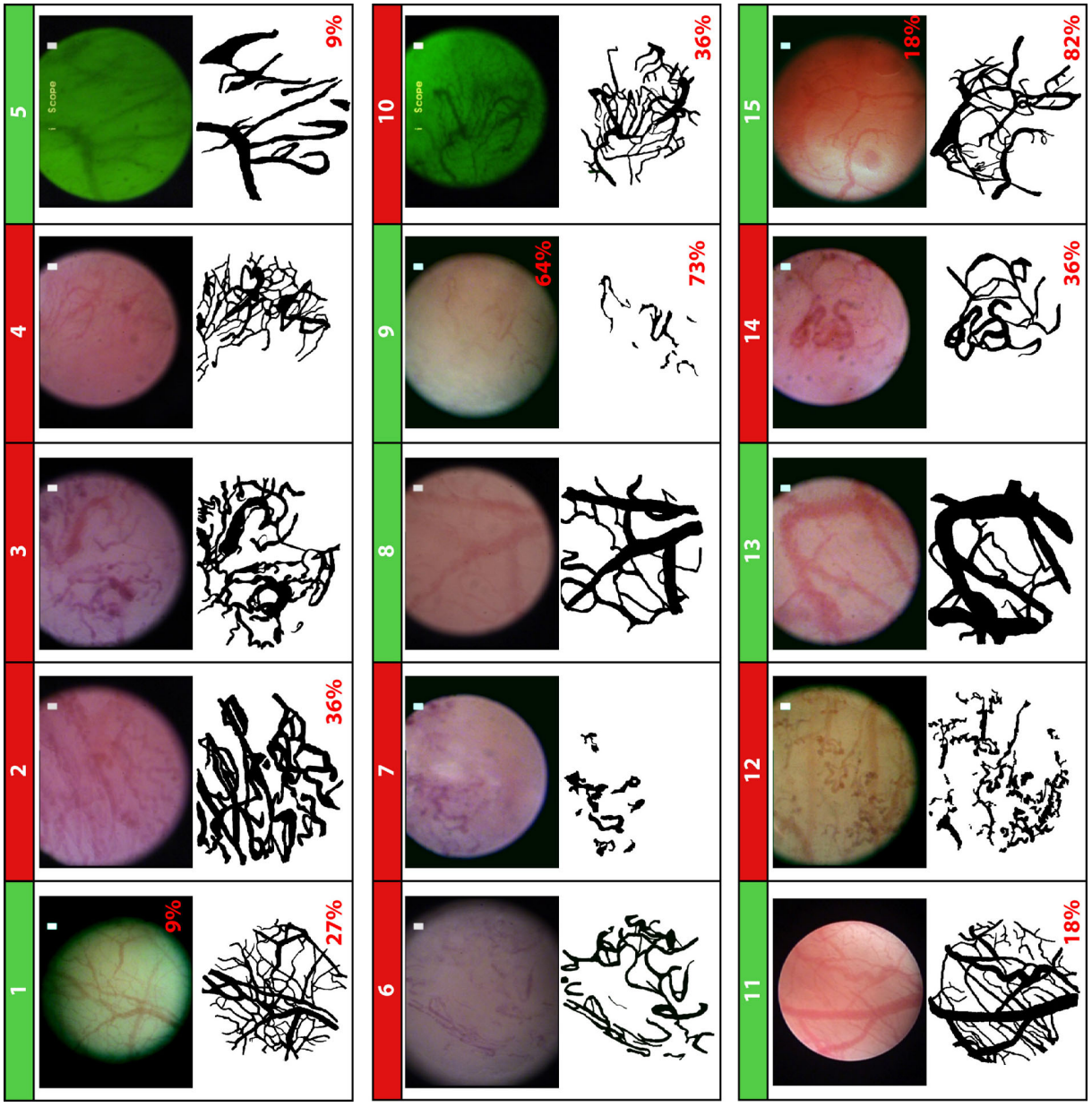

Figure 5.14: *Atlas of HM images (original images and corresponding skeletons)*

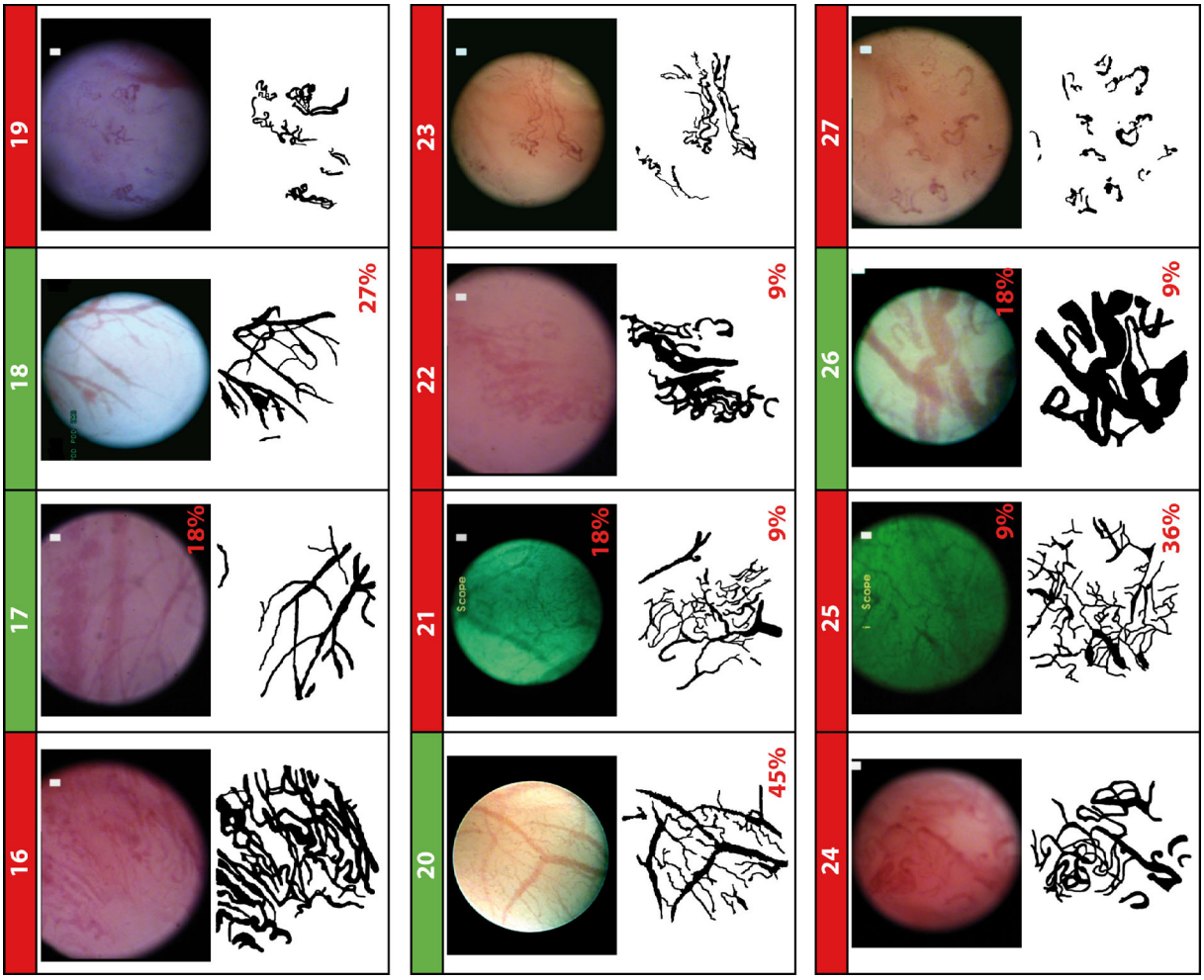

Figure 5.15: *Atlas of HM images (original images and corresponding skeletons)*

5.5 Image processing and analysis

We have shown in the clinical study (presented in Section 5.3) that the classification of vessel architecture may lead to a very good rejection of the false-positive lesions. However, it still relies on the physician learning curve, since it is only a qualitative description. In order to make this discrimination method even more robust, we made several attempts to implement a reliable and quantitative method of vessel description, that would be valuable for the early detection and characterization of morphological changes. This will allow the identification of the discrimination features.

In this section, we will present two methods. First, we will implement vessel segmentation algorithm to extract the vessel information from the background (see Section 5.5.1), and then we will try to extract global image information without the tedious extraction of each individual vessel (see Section 5.5.2).

5.5.1 Vessel segmentation

Over the last years, vessel architecture has been studied over time to diagnose some disease (*e.g.* in the eye). Retinal blood vessels have been shown to change in diameter, branching angles or tortuosity, as a result of a disease, such as hypertension [Stan95, Wong05a], onset of diabetes or diabetic renal disease [Wong05b]. Because of its diverse roles in key physiological and pathological processes, angiogenesis is an important area of medical research, with a considerable number of angiogenic and anti-angiogenic drugs currently undergoing clinical trials. Santos *et al.* developed an integrated angiogenesis screening system, with vessel segmentation as part of the work flow [Sant08].

In this section, we present a method to automatically segment blood vessels based upon multi-scale feature extraction. The input images are conventional endoscopic images converted to grayscale (intensity images). This method overcomes the problem of variations in contrast inherent in the endoscopic images by using the first and second spatial derivatives of the intensity image that gives information about vessel topology. Thus, this approach also enables the detection of blood vessels of different widths, lengths and orientations.

This algorithm is a multiple pass *region growing* procedure, limited by the gradient information and the maximum principal curvature. It progressively segments the blood vessels using feature information together with spatial information about the eight-neighboring pixels, obtaining in this way a segmented binary image. This method was adapted from a retinal image processing algorithms, known as *multi-scale analysis*, developed by Martinez *et al.* [M.-P07b, M.-P07a].

5.5.1.1 Feature extraction

Since the blood vessels present in the bladder have different sizes, it is convenient to introduce a measure that varies within a certain range of scales. Multi-scale techniques have been developed to provide a way to isolate information about objects in an image by looking for geometric features at different scales. Under this framework representing information at different scales is defined by convolving the original image $I(x, y)$ with a Gaussian kernel $G(x, y; s)$ of variance s^2:

$$I_s(x, y; s) = I(x, y) \otimes G(x, y; s) \text{ where } G(x, y; s) = \frac{1}{2\pi s^2} e^{-\frac{x^2+y^2}{s^2}} \text{ and } s \text{ is a length scale factor}$$

The effect of convolving an image with a Gaussian kernel is to suppress most of the structures in the image with a characteristic length less than s. The use of Gaussian kernels to generate

multiscale information ensures that the image analysis is invariant with respect to translation, rotation and size [Koen84].

To extract geometric features from an image, a framework based on differentiation is used. Derivatives of an image can be numerically approximated by a linear convolution of the image with scale-normalized derivatives of the Gaussian kernel.

$\partial^n I_s(x, y; s) = I(x, y) \otimes s^n \partial^n G(x, y; s)$ where n indicates the order of the derivative.

The normalization by scale makes the derivatives dimensionless which means that the derivatives will have the proper behavior under spatial rescaling of the original image and that structures at different scales will be treated in a similar manner.

Detection of tube-like structures using multiscale approach has been carried out by other researchers [Sato97, Lore97]. The main purpose of these works was to develop a line-enhancement filter based on the eigenvalue analysis of the Hessian matrix. To make a proper feature extraction, we will use these algorithms in combination with a gradient information to segment blood vessels rather than to enhance them.

The first directional derivatives describe the variation of image intensity in the neighborhood of a point. The magnitude of the *gradient* represents the slope of the image intensity for a particular value of the scale length factor s and is defined as

$$|\nabla I_s| = \sqrt{(\partial_x I_s)^2 + (\partial_y I_s)^2}$$

The second derivative information is derived from the Hessian of the intensity image $I(x, y)$:

$$H = \begin{pmatrix} \partial_{xx} I_s & \partial_{xy} I_s \\ \partial_{yx} I_s & \partial_{yy} I_s \end{pmatrix}$$

Since $\partial_{xy} I_s = \partial_{yx} I_s$, the Hessian matrix is symmetrical with real eigenvalues and orthogonal eigenvectors which are rotation invariant. The eigenvalues, λ_+ and λ_- (assuming $\lambda_+ \geq \lambda_-$) measure the convexity and concavity in the corresponding eigendirections. For an image with white vessels over a dark background, $\lambda_+ \approx 0$ and $\lambda_- \ll 0$. Conversely, for an image with black vessels over a light background, $\lambda_+ \gg 0$ and $\lambda_- \approx 0$ [M.-P07b]. For the sake of simplification, we define here :

$$\lambda_1 = min(|\lambda_+|, |\lambda_-|) \text{ and } \lambda_2 = max(|\lambda_+|, |\lambda_-|)$$

The maximum eigenvalue λ_2 corresponds to the maximum principal curvature of the Hessian tensor, which we will refer to as *maximum principal curvature*.

To illustrate the algorithm, we will use the same image throughout the text. Figure 5.16 depicts the original image, which shows the regular vascularization present in the bladder acquired with 80× magnification.

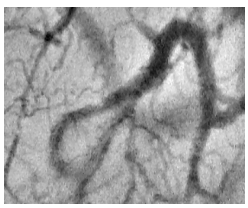

Figure 5.16: *Original image converted to grayscale.*

We calculated the features for all integer values of s, assuming $s_{min} \leq s \leq s_{max}$, where s_{min} and s_{max} are fixed according to the approximate sizes of the smallest and largest vessel radius

to be detected in the image. These two parameters have to be known *a priori* and will depend on the pixel resolution of the original image as well as on the field of view of the endoscopic camera. Figure 5.17 shows the maximum principal curvature and magnitude of the gradient at different scales. For our endoscopic images, we chose $s_1 = 1$ and $s_2 = 10$. It clearly illustrate that the size of the detected vessels is depending on s. Indeed, increasing s results in observation of larger vessel structure.

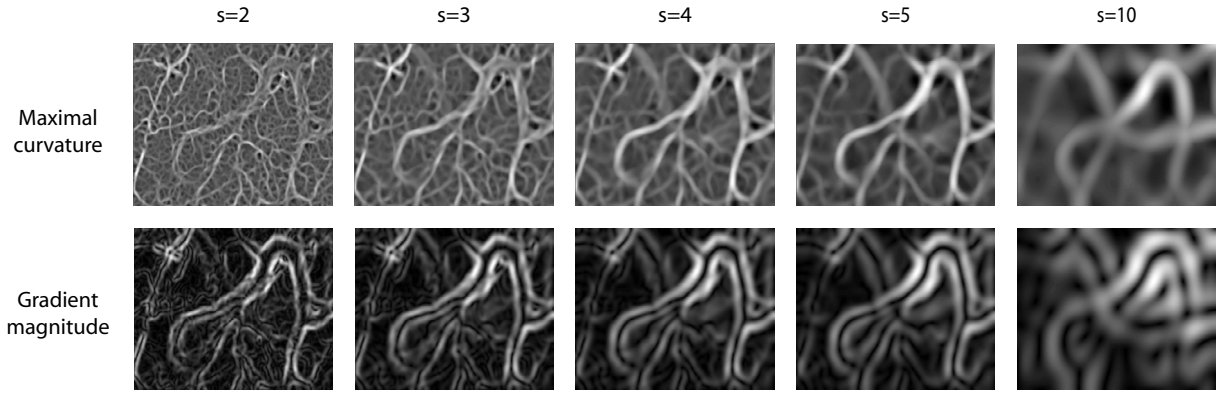

Figure 5.17: *Maximum principal curvature λ_2 and magnitude of the gradient at different scales for $s = 2, 3, 4, 5,$ and 10.*

At this point, we have to take into account that absorption properties of the large vessels may differ from small vessels due to the different amount of red blood cells, and thus varying hemoglobin concentration. Hence, we have to equalize our two parameters with a diameter-dependent factor. Since our best approximation of vessel radius at this stage of the algorithm is the scale factor s, we used this in our equalization. Thus, since vessels with diameter $d \approxeq 2s$ are most strongly detected when the scale factor is s, we normalized each feature along scales by d and then kept the local maxima over scales:

$$\gamma = \max_s \left[\frac{|\nabla I_s(s)|}{d} \right] \text{ and } \kappa = \max_s \left[\frac{\lambda_2(s)}{d} \right]$$

Therefore, the local maxima of the equalized gradient magnitude γ and the local maxima of the equalized maximum principal curvature κ are the two features used to classify pixels in the image into two region classes, *background* and *vessel*, using a multiple pass *region growing* procedure. Figure 5.18 depicts the local maxima responses over the scales.

5.5.1.2 Region growing procedure

The region growing algorithm we use is based on an iterative relaxation technique. For each image, all the parameters used in this algorithm are automatically calculated from the histograms of the extracted features (see Figure 5.19). The classification of pixels as *vessel* or *background* is based primarily upon the maximum principal curvature κ, from which the criteria for determining seeds are defined. Using spatial information from the classification of the eight-neighboring pixels, classes grow initially in regions with low gradient magnitude, γ, allowing a relatively broad and fast classification while suppressing classification in the edge regions where the gradients are large. In a second stage, the classification constraint is relaxed and classes grow based solely upon κ to allow the definition of borders between regions.

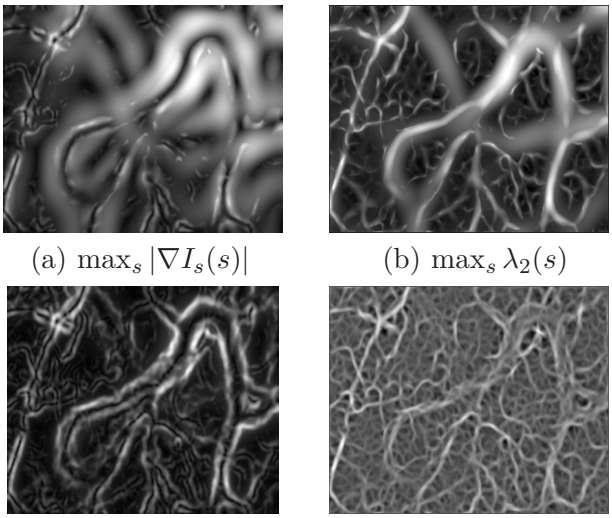

(a) $\max_s |\nabla I_s(s)|$ (b) $\max_s \lambda_2(s)$

(c) γ (d) κ

Figure 5.18: *Local maxima response over the scales for: (a) gradient magnitude $|\nabla I_s(s)|$, (b) maximum principal curvature λ_2, (c) diameter-dependent equalized gradient magnitude γ, and (d) diameter-dependent equalized maximum principal curvature κ*

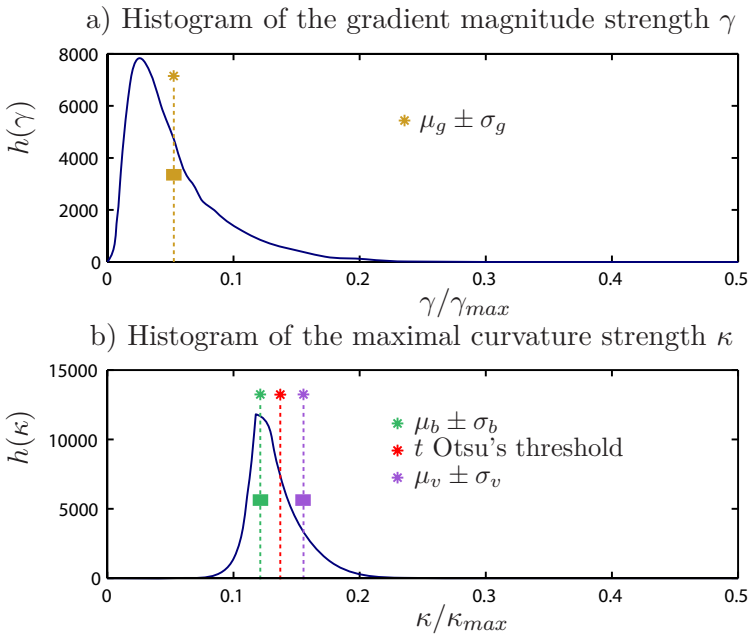

Figure 5.19: *Parameters used in the region growing algorithm. (a) Histogram of the local maxima of the gradient magnitude strength, γ. One class: low gradient, $\gamma < \mu_g + \sigma_g$. (b) Histogram of the local maxima of the maximum principal curvature strength κ where t is the threshold. Two classes:* background $\kappa/\kappa_{max} \in [0, t]$ *and* vessel, $\kappa/\kappa_{max} \in (t, 1]$

The histograms of both features $h(\gamma)$ and $h(\kappa)$ are calculated. For $h(\gamma)$, only one class is used: *low gradient*, which is defined as $\gamma < \mu_g + \sigma_g$ for the complete histogram, where μ_g is the mean and σ_g is the standard deviation.

$h(\kappa)$ is automatically divided into two classes using the Otsu's threshold algorithm [Otsu79], in which an optimal threshold is selected by discriminant criteria, where the separability between the resulted classes in gray levels is maximized. It uses the zero and first order cumulative moments of the gray level histogram. The means and standard deviations of $h(\kappa)$ for each class are calculated: *background*, for $\kappa/\kappa_{max} \in [0, t]$ with mean μ_b and standard deviation σ_b; and vessel, for $\kappa/\kappa_{max} \in (t, 1]$ with mean μ_v and standard deviation σ_v, where t is the threshold. The size of the interval for each class varies depending on the value of a parameter a, which changes during the iteration process. Intervals for each class are defined as: $\mu \pm a\sigma$.

The algorithm begins by planting seeds for each region: *background seeds* are pixels for which $\kappa \leq \mu_b$, whereas *vessel seeds* are defined as $\gamma \geq \mu_v$. Figure 5.20 shows an example of the planting stage where vessel seeds are shown in black, background seeds in white and unknown pixels in gray. These conditions ensure that only those pixels in the inner areas of each region, with a very high probability of belonging to the region, are labeled as seeds.

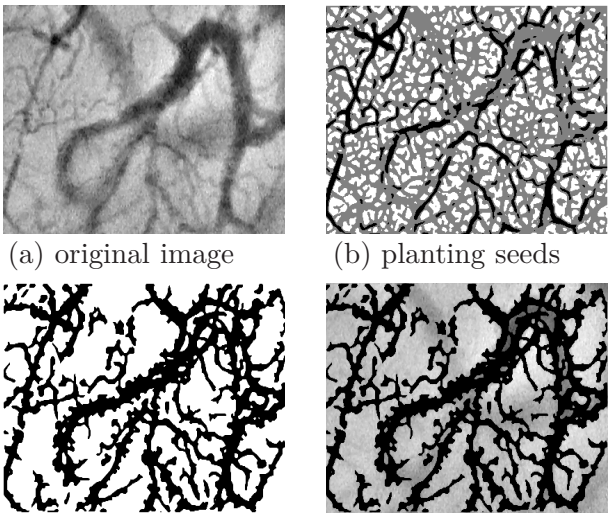

(a) original image (b) planting seeds

(c) final segmentation (d) overlay image

Figure 5.20: ***Region growing algorithm.*** *(a) Original image converted to 32-bits grayscale image (b) Planting seeds: black,* vessel *seeds; white,* background *seeds and gray,* unknown *pixels; (c) Final segmented image (d) Overlay image.*

Region growing is an iterative process: an unlabeled pixel is classified as belonging to class j if it has at least one neighbor of class j already classified and if it fulfils a specific condition with initial parameters $a_i = 1$. a_i will specify the size of the class interval for the iteration i. Figure 5.21 shows a case where the value of the pixel falls within the current interval for class 2 and will be classified as 2 since it also has nearest neighbors already classified as 2.

A gray value which may belong to two different classes is assigned to the one to which most of its neighbors belong. Growing is repeated from left to right and top to bottom until no more pixels are classified. The constraints are relaxed by incrementing the parameters a_i in steps of 0.5 and the growing is repeated. After the seeds are planted, the conditions for growing are defined as follows: in the first stage, the growing for both classes is restricted to regions with low gradients allowing rapid growth of regions outside of the boundaries, and allowing vessels to grow where the values of j lie within a wide interval.

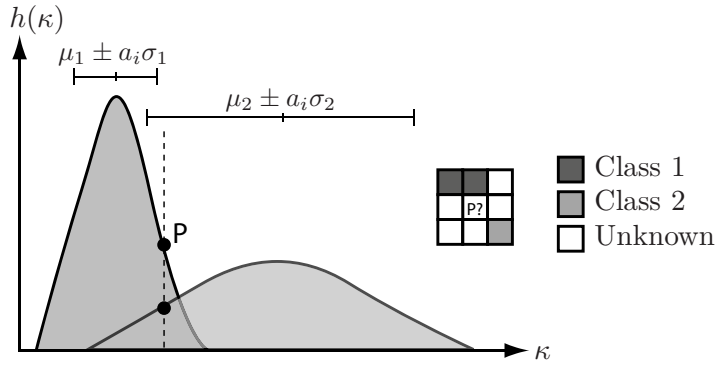

Figure 5.21: *From the histogram of κ, intervals for each class j are defined as: $\mu_j \pm a_i\sigma_j$, where a_i will specify the size of the class interval for the iteration i. An unlabeled pixel P is classified as belonging to class j if it lies inside the interval j and if it has at least one neighbor of class j already classified*

The condition for class *vessel* is :

$$(\mu_v - a_v\sigma_v) \leqslant \kappa \text{ AND } \gamma \leqslant (\mu_g + a_g\sigma_g) \text{ AND } N_v \geqslant 1$$

and for class *background*:

$$\kappa \leqslant (\mu_b + a_b\sigma_b) \text{ AND } \gamma \leqslant \mu_g \text{ AND } N_b \geqslant 1$$

where N_j is the number of neighbors already labeled as class j.
After alternating these two steps until no further classifications are found, the final stage of the algorithm grows vessel and background classes simultaneously without the gradient restriction. Now the condition for class j is:

$$(\mu_j - a\sigma_j) \leqslant \kappa \leqslant (\mu_j + a\sigma_j) \text{ AND } N_j \geqslant 1$$

and again the condition is relaxed by increasing a from $a = 1$ by steps of 0.5 until all pixels are classified. With this final stage, borders between classes are defined. Figure 5.20 shows the result of the growing after this second stage. Interestingly, the non-relevant "deep" vessels were ignored by this algorithm.

5.5.1.3 Limitations of the multi-scale algorithm

In order to yield good performance, the presented multi-scale algorithm needs input images with good intrinsic contrast (i.e. a clear intensity variations between vessels and background), because noise can be very disturbing in the gradient and maximal curvature measurement.

Indeed, noise impairs the detection of large vessels, because gradient variations are wrongly detected in the middle of the vessel where the gradient should be flat. It results a non-uniform detection of large vessels (as to be seen in Figure 5.20d). Noise can also impair the detection of small vessel. For instance, small intensity variations can be dissolved in the overall noise induced by video compression algorithm.

With standard WL illumination, we reached a signal-to-noise (S/N) ratio close to 1.2 (when converted to grayscale intensity) on endoscopic images. Figure 5.22 shows an example of vascular patterns underlying a carcinoma *in situ* in the bladder. If one looks only at the image on the left, one can distinguish the vessel network, whereas the gray level intensity plot on the right doesn't show a huge contrast out of the noise. A vessel displays only a 15-counts drop as compared

to the background (when measured peak-to-peak, even less when measured at 50% intensity). Interestingly, the human eye is able to accommodate for such small intensity variations and can easily recognize the vessel structure (see Section 5.3), whereas the variations of gray level intensities yields a poor numerical contrast.

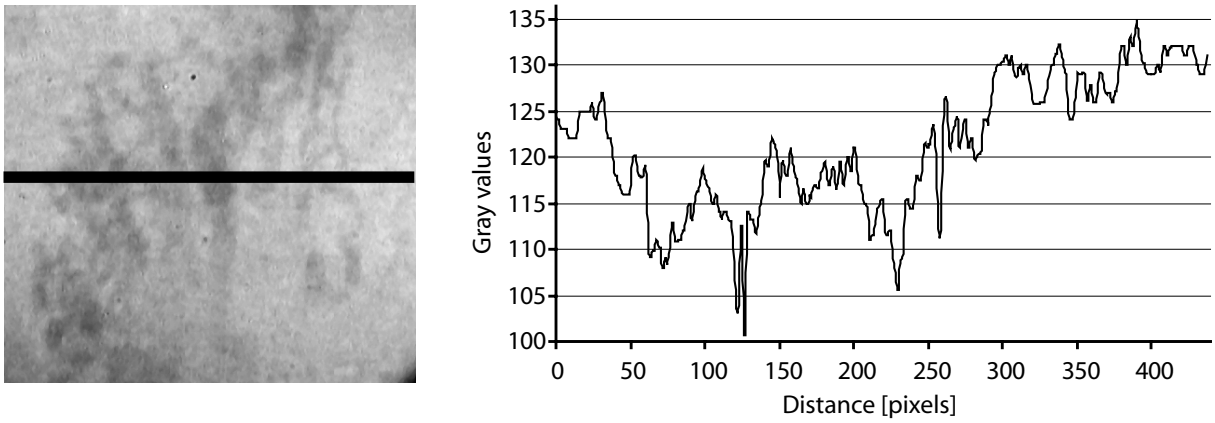

Figure 5.22: *(a) left: vascularization underlying a bladder carcinoma* in situ *with the profile drawn as a black line; (b) right: intensity profile of the image*

Additionally, the non-uniform illumination of the endoscopic site may also result in wrong behavior of this algorithm, even if it is more robust than standard thresholding methods. A pre-processing routine (*e.g.* subtracting the image low frequencies) can be added to the algorithm presented here in order to mimic a pseudo-uniform illumination patterns, similar to what is available in microscopic studies.

In order to maximize this vessel-background contrast, we implemented some contrast maximization schemes (such as spectral optimization) described in details in Appendix E.

5.5.2 Global information extraction

As described in the section 5.4, the skeletonized image does not contain the full information to allow discrimination of the true and false positive. In order to overcome this limitation, we describe here a method to extract the global features of the images without extracting each individual vessel.

For that purpose, we developed an algorithm to quantify the amount of variations in the image spatial frequencies, and investigate whether it could serve as a discrimination basis between the observed vascular patterns. This framework was implemented as a simple software prototype in ImageJ (National Institute of Science, NIH, Bethesda, MD).

The flow chart of the algorithm is summarized in Figure 5.23. First, still images were digitized using the IEEE1394 connection between the DV recorder (DVCAM DSR 20MDP, Sony Corporation, Japan) and a portable PC. We first convert the image from 24-bits RGB color space to 32-bits grayscale intensity with a contrast maximizing method (developed at BIG lab at EPFL). Then, to avoid artifact due to the endoscopic circular mask (i.e. variations of the diameter of the FOV), whose size depends on the knob's position (see Section 5.2), we defined a region-of-interest (ROI) (340x380 pixels^2). The ROI was then blurred by a Gaussian filtering with a variance of 20, and subtracted to the original ROI in order to create a pseudo-uniform illumination pattern.

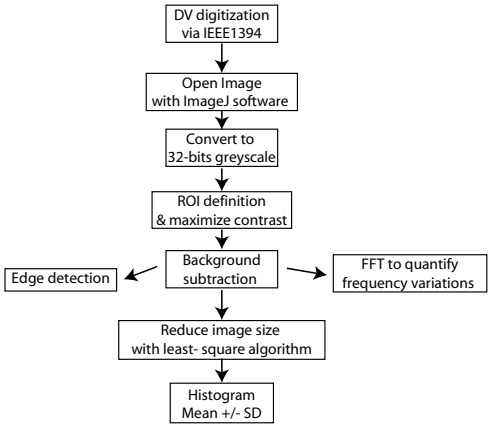

Figure 5.23: *Image analysis flow chart that describes ImageJ procedure*

Fast-Fourier Transformation (FFT) was applied on the background-subtracted image following the well-known transformation formula:

$$F(u,v) = \frac{1}{N^2} \sum_{x=0}^{N-1} \sum_{y=0}^{N-1} f(x,y) e^{-2\pi j \frac{ux+vy}{N}}$$

In the Fourier domain image, each point represents a particular frequency contained in the spatial domain image. The basis functions are sine and cosine waves with increasing frequencies. $F(0,0)$ represents the DC-component of the image which corresponds to the average brightness and $F(N–1, N–1)$ represents the highest frequency. The low frequencies of the image are located in the center of the power spectrum. As they should help to discriminate between linear and tortuous vessels, we extracted this information by shrinking the size of the image down to 20x22 pixels^2 with least-square method and cubic splines. We computed mean and standard deviation of this new pixel distribution, and visualized it with the help of a histogram.

Figure 5.24 depicts the different steps of this image analysis procedure. In this preliminary study, the FFT yielded some interesting results. In Figure 5.24, we can clearly observe a variation in the pixel distribution of the low frequencies (i.e. in the center of the image). The frequency distribution around the center is larger for the carcinoma *in situ* than on the normal tissue, suggesting that we will have to focus in low frequencies spectrum for the next experiments. Indeed, the pixels in the reduced image has the potential to be a good indicator of the image complexity. This could help to discriminate modified vascular structure from linear architecture, thus between true and false positive lesions.

Moreover, this global approach is simpler to implement than a vessel segmentation procedure, and could be complementary to the method presented in Section 5.5.1. A summary of this approach has been published in [Lovi09].

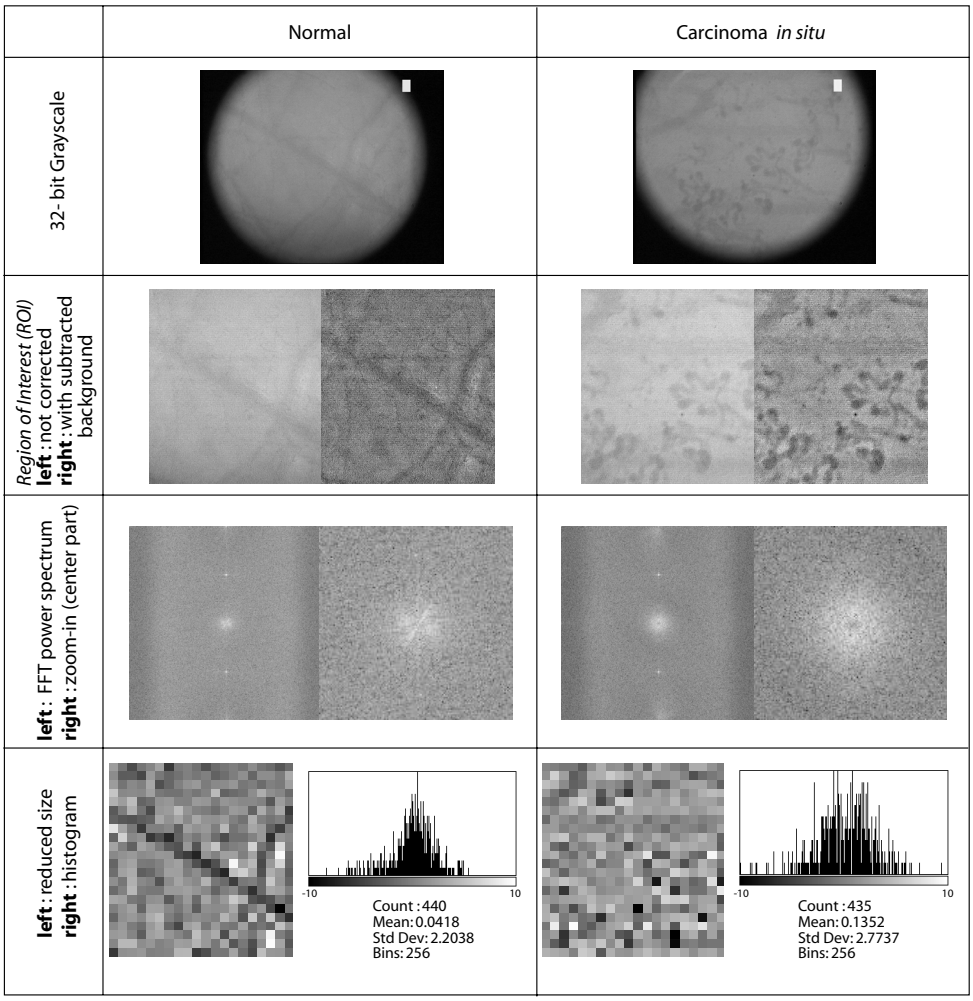

Figure 5.24: *Image analysis results (background substraction, FFT, histogram plot)*

Bibliography

[Andr95a] M. Andrea, O. Dias, and A. Santos. Contact endoscopy during microlaryngeal surgery: a new technique for endoscopic examination of the larynx. *Ann Otol Rhinol Laryngol*, 104(5):333–339, May 1995.

[Andr95b] M. Andrea, O. Dias, and A. Santos. Contact endoscopy of the vocal cord: normal and pathological patterns. *Acta Otolaryngol*, 115(2):314–316, Mar 1995.

[Babj05] M. Babjuk, V. Soukup, R. Petrík, M. Jirsa, and J. Dvorácek. 5-aminolaevulinic acid-induced fluorescence cystoscopy during transurethral resection reduces the risk of recurrence in stage Ta/T1 bladder cancer. *BJU International*, 96(6):798–802, Oct 2005.

[Bhuv10] R. Bhuvaneswari, P. S. P. Thong, Y.-Y. Gan, K. Soo, and M. Olivo. Evaluation of hypericin-mediated photodynamic therapy in combination with angiogenesis inhibitor bevacizumab using in vivo fluorescence confocal endomicroscopy. *J Biomed Opt*, 15(1):011114, 2010.

[Char06] P. J. S. Charlesworth and A. L. Harris. Mechanisms of disease: Angiogenesis in urologic malignancies. *Nature Clinical Practice Urology*, 3(3):157–169, 2006.

[Dani05] D. I. Daniltchenko, C. R. Riedl, M. D. Sachs, F. Koenig, K. L. Daha, H. Pflueger, S. A. Loening, and D. Schnorr. Long-term benefit of 5-aminolevulinic acid fluorescence assisted transurethral resection of superficial bladder cancer: 5-year results of a prospective randomized study. *J Urol*, 174(6):2129–33, discussion 2133, Dec 2005.

[Denz07] S. Denzinger, M. Burger, B. Walter, R. Knuechel, W. Roessler, W. F. Wieland, and T. Filbeck. Clinically relevant reduction in risk of recurrence of superficial bladder cancer using 5-aminolevulinic acid-induced fluorescence diagnosis: 8-year results of prospective randomized study. *Urology*, 69(4):675–679, Apr 2007.

[Denz08] S. Denzinger, W. F. Wieland, W. Otto, T. Filbeck, R. Knuechel, and M. Burger. Does photodynamic transurethral resection of bladder tumour improve the outcome of initial t1 high-grade bladder cancer? a long-term follow-up of a randomized study. *BJU Int*, 101(5):566–569, Mar 2008.

[Drag09] R. O. P. Draga, M. C. M. Grimbergen, E. T. Kok, T. N. Jonges, and J. L. H. R. Bosch. Predictors of false positives in 5-aminolevulinic acid-induced photodynamic diagnosis of bladder carcinoma: identification of patient groups that may benefit most from highly specific optical diagnostics. *Urology*, 74(4):851–856, Oct 2009.

[Drag10] R. O. P. Draga, M. C. M. Grimbergen, E. T. Kok, T. N. Jonges, C. F. P. van Swol, and J. L. H. R. Bosch. Photodynamic diagnosis (5-aminolevulinic acid) of transitional cell carcinoma after bacillus calmette-guérin immunotherapy and mitomycin c intravesical therapy. *Eur Urol*, 57(4):655–660, 2010.

[Drol05] M. J. Droller. Biological considerations in the assessment of urothelial cancer: a retrospective. *Urology*, 66(5 Suppl):66–75, Nov 2005.

[East08] J. E. East, N. Suzuki, P. Bassett, M. Stavrinidis, H. J. Thomas, T. Guenther, P. P. Tekkis, and B. P. Saunders. Narrow band imaging with magnification for the characterization of small and diminutive colonic polyps: pit pattern and vascular pattern intensity. *Endoscopy*, 40(10):811–817, Oct 2008.

[Epst98] J. I. Epstein, M. B. Amin, V. R. Reuter, F. K. Mostofi, F. Algaba, W. C. Allsbrook, A. G. Ayala, M. J. Becich, A. L. Beltran, L. Boccon-Gibod, D. G. Bostwick, C. Busch, C. J. Davis, J. N. Eble, C. S. Foster, M. Furusato, D. J. Grignon, P. A. Humphrey, E. A. Ishak, S. L. Johansson, E. C. Jones, L. G. Koss, H. S. Levin, W. M. Murphy, R. O. Petersen, A. Renshaw, J. Y. Ro, J. R. Ross, I. A. Sesterhenn, J. R. Srigley, S. Suzigan, J. B. Tomaszewski, P. Troncoso, L. D. True, M. A. Weiss, T. M. Wheeler, and R. H. Young. The World Health Organization/International Society of Urological Pathology consensus classification of urothelial (transitional cell) neoplasms of the urinary bladder. *American Journal of Surgical Pathology*, 22(12):1435–1448, 1998.

[Fort06] P. J. Fortun, G. K. Anagnostopoulos, P. Kaye, M. James, S. Foley, S. Samuel, A. Shonde, R. Badreldin, E. Campbell, C. J. Hawkey, and K. Ragunath. Acetic acid-enhanced magnification endoscopy in the diagnosis of specialized intestinal metaplasia, dysplasia and early cancer in barrett's oesophagus. *Alimentary Pharmacology and Therapeutics*, 23(6):735–742, 2006.

[Frad07] Y. Fradet, H. B. Grossman, L. Gomella, S. Lerner, M. Cookson, D. Albala, M. J. Droller, and P. B. S. Group. A comparison of hexaminolevulinate fluorescence cystoscopy and white light cystoscopy for the detection of carcinoma in situ in patients with bladder cancer: a phase iii, multicenter study. *Journal of Urology*, 178(1):68–73; discussion 73, 2007.

[Grim03] M. C. M. Grimbergen, C. F. P. van Swol, T. G. N. Jonges, T. A. Boon, and R. J. A. van Moorselaar. Reduced specificity of 5-ala induced fluorescence in photodynamic diagnosis of transitional cell carcinoma after previous intravesical therapy. *Eur Urol*, 44(1):51–56, Jul 2003.

[Gros07] H. B. Grossman, L. Gomella, Y. Fradet, A. Morales, J. Presti, C. Ritenour, U. Nseyo, and M. J. Droller. A phase iii, multicenter comparison of hexaminolevulinate fluorescence cystoscopy and white light cystoscopy for the detection of superficial papillary lesions in patients with bladder cancer. *Journal of Urology*, 178(1):62–67, 2007.

[Hall07] M. C. Hall, S. S. Chang, G. Dalbagni, R. S. Pruthi, J. D. Seigne, E. C. Skinner, J. S. Wolf, and P. F. Schellhammer. Guideline for the management of nonmuscle invasive bladder cancer (stages ta, t1, and tis): 2007 update. *J Urol*, 178(6):2314–2330, Dec 2007.

[Herr08] H. W. Herr and S. M. Donat. A comparison of white-light cystoscopy and narrow-band imaging cystoscopy to detect bladder tumour recurrences. *BJU Int*, 102(9):1111–1114, Nov 2008.

[Inou97] H. Inoue, T. Honda, K. Nagai, T. Kawano, K. Yoshino, K. Takeshita, and M. Endo. Ultra-high magnification endoscopic observation of carcinoma in situ of the esophagus. *Digestive Endoscopy*, 9(1):16–18, 1997. cited By (since 1996) 52.

[Jich97] P. Jichlinski, M. Forrer, J. Mizeret, T. Glanzmann, D. Braichotte, G. Wagnières, G. Zimmer, L. Guillou, F. Schmidlin, P. Graber, H. D. Van Bergh, and H. J. Leisinger. Clinical evaluation of a method for detecting superficial transitional cell carcinoma of the bladder by light-induced fluorescence of protoporphyrin ix following topical application of 5-aminolevulinic acid: Preliminary results. *Lasers in Surgery and Medicine*, 20(4):402–408, 1997.

[Jich03a] P. Jichlinski. New diagnostic strategies in the detection and staging of bladder cancer. *Curr Opin Urol*, 13(5):351–5, 2003.

[Jich03b] P. Jichlinski, L. Guillou, S. J. Karlsen, P. U. Malmstrom, D. Jocham, B. Brennhovd, E. Johansson, T. Gartner, N. Lange, H. van den Bergh, and H. J. Leisinger. Hexyl aminolevulinate fluorescence cystoscopy: new diagnostic tool for photodiagnosis of superficial bladder cancer–a multicenter study. *J Urol*, 170(1):226–9, 2003.

[Jich08] P. Jichlinski and D. Jacqmin. Photodynamic diagnosis in non-muscle-invasive bladder cancer. *European Urology, Supplements*, 7(7):529–535, 2008.

[Joch05] D. Jocham, F. Witjes, S. Wagner, B. Zeylemaker, J. Van Moorselaar, M. O. Grimm, R. Muschter, G. Popken, F. König, R. Knüchel, and K. H. Kurth. Improved detection and treatment of bladder cancer using hexaminolevulinate imaging: A prospective, phase iii multicenter study. *Journal of Urology*, 174(3):862–866, 2005.

[Kenn90] J. C. Kennedy, R. H. Pottier, and D. C. Pross. Photodynamic therapy with endogenous protoporphyrin ix: basic principles and present clinical experience. *J Photochem Photobiol B*, 6(1-2):143–148, Jun 1990.

[Kenn92] J. C. Kennedy and R. H. Pottier. Endogenous protoporphyrin ix, a clinically useful photosensitizer for photodynamic therapy. *J Photochem Photobiol B*, 14(4):275–292, Jul 1992.

[Kirk05] Z. Kirkali, T. Chan, M. Manoharan, F. Algaba, C. Busch, L. Cheng, L. Kiemeney, M. Kriegmair, R. Montironi, W. M. Murphy, I. A. Sesterhenn, M. Tachibana, and J. Weider. Bladder cancer: Epidemiology, staging and grading, and diagnosis. *Urology*, 66(6 Suppl 1):4–34, 2005.

[Koen84] J. J. Koenderink. The structure of images. *Biol Cybern*, 50(5):363–370, 1984.

[Kudo96] S. Kudo, S. Tamura, T. Nakajima, H. Yamano, H. Kusaka, and H. Watanabe. Diagnosis of colorectal tumorous lesions by magnifying endoscopy. *Gastrointest Endosc*, 44(1):8–14, Jul 1996.

[Kuma06] Y. Kumagai, M. Iida, and S. Yamazaki. Magnifying endoscopic observation of the upper gastrointestinal tract. *Digestive Endoscopy*, 18(3):165–172, 2006.

[Lore97] C. Lorenz, I. Carlsen, T. Buzug, C. Fassnacht, and J. Weese. Multiscale line segmentation with automatic estimation of width, contrast and tangential direction in 2d and 3d medical images. In J. Troccaz, E. Grimson, and R. Mösges, editors, *Proceedings of the CVTMed-MRCAS'97, Lecture Notes in Computer Science*, pages 233–242, 1997.

[Lovi09] B. Lovisa, P. Jichlinski, D. Aymon, B.-C. Weber, H. van den Bergh, and G. Wagnieres. Bladder cancer detection by fluorescence imaging with hexvix(r): analysis and processing of images obtained during high magnification cystoscopy. In D. H. Kessel, editor, *Photodynamic Therapy: Back to the Future*, volume 7380, page 738047. SPIE, 2009.

[M.-P07a] M. Martinez-Perez, A. D. Hughes, S. A. Thom, and K. H. Parker. Improvement of a retinal blood vessel segmentation method using the insight segmentation and registration toolkit (itk). *Conf Proc IEEE Eng Med Biol Soc*, 2007:892–895, 2007.

[M.-P07b] M. E. Martinez-Perez, A. D. Hughes, S. A. Thom, A. A. Bharath, and K. H. Parker. Segmentation of blood vessels from red-free and fluorescein retinal images. *Med Image Anal*, 11(1):47–61, Feb 2007.

[Mats05] M. Matsuda, G. Watanabe, and M. Hashimoto. Contact endoscopy during cholecystectomy: A new technique for staging laparoscopy in gallbladder cancers. *Digestive Endoscopy*, 17(2):138–142, 2005.

[Merk93] H. M. Merklinger. *Focusing the View Camera : A Scientific Way to Focus the View Camera and Estimate Depth of Field*. MacNab Print, 1993.

[Most73] F. K. Mostofi, L. H. Sobin, and H. Torloni. *Histological Typing of Urinary Bladder Tumors, International Histological Classification of Tumors*. World Heath Organisation, WHO, Geneva, 1973.

[N.-S10] P. Nowak-Sliwinska, J.-P. Ballini, G. Wagnières, and H. van den Bergh. Processing of fluorescence angiograms for the quantification of vascular effects induced by anti-angiogenic agents in the cam model. *Microvasc Res*, 79(1):21–28, 2010.

[Oost01] W. Oosterlinck, A. V. Bono, D. Mack, R. Hall, R. Sylvester, C. De Balincourt, and M. Brausi. Frequency of positive biopsies after visual disappearance of superficial bladder cancer marker lesions. *European Urology*, 40(5):515–517, 2001.

[Otsu79] N. Otsu. A threshold selection method from gray-level histograms. *IEEE Trans. Syst. Man Cybern.*, 9:62–66, 1979.

[Reih02] F. Reiher, O. Ozer, M. Pins, B. D. Jovanovic, S. Eggener, and S. C. Campbell. p53 and microvessel density in primary resection specimens of superficial bladder cancer. *J Urol*, 167(3):1469–74, 2002.

[Roma03] A. Romanenko, K. Morimura, H. Wanibuchi, M. Wei, W. Zaparin, W. Vinnichenko, A. Kinoshita, A. Vozianov, and S. Fukushima. Urinary bladder lesions induced by persistent chronic low-dose ionizing radiation. *Cancer Sci*, 94(4):328–333, Apr 2003.

[Sale10] M. D. Saleh, C. Eswaran, and A. Mueen. An automated blood vessel segmentation algorithm using histogram equalization and automatic threshold selection. *J Digit Imaging*, online:1–9, Jun 2010.

[Sant08] A. F. Santos, A. B. Zaltsman, R. C. Martin, A. Kuzmin, Y. Alexandrov, E. P. Roquemore, R. A. Jessop, M. G. M. van Erck, and J. H. Verheijen. Angiogenesis: an improved in vitro biological system and automated image-based workflow to aid identification and characterization of angiogenesis and angiogenic modulators. *Assay Drug Dev Technol*, 6(5):693–710, Oct 2008.

[Sasa06] K. Sasajima, S. e. Kudo, H. Inoue, T. Takeuchi, H. Kashida, E. Hidaka, H. Kawachi, M. Sakashita, J. Tanaka, and A. Shiokawa. Real-time in vivo virtual histology of colorectal lesions when using the endocytoscopy system. *Gastrointestinal Endoscopy*, 63(7):1010–1017, 2006.

[Sato97] Y. Sato, S. Nakajima, H. Atsumi, T. Koller, G. Gerig, S. Yoshida, and R. Kikinis. 3d multi-scale line filter for segmentation and visualization of curvilinear structures in medical images. In J. Troccaz, E. Grimson, and R. Mösges, editors, *Proceedings of the CVTMed-MRCAS'97, Lecture Notes in Computer Science*, pages 213–222, 1997.

[Schm04] J. Schmidbauer, F. Witjes, N. Schmeller, R. Donat, M. Susani, M. Marberger, and H. P. S. Group. Improved detection of urothelial carcinoma in situ with hexaminolevulinate fluorescence cystoscopy. *J Urol*, 171(1):135–138, Jan 2004.

[Shib02] K. Shibuya, H. Hoshino, M. Chiyo, K. Yasufuku, T. Iizasa, Y. Saitoh, M. Baba, K. Hiroshima, H. Ohwada, and T. Fujisawa. Subepithelial vascular patterns in bronchial dysplasias using a high magnification bronchovideoscope. *Thorax*, 57(10):902–7, 2002.

[Shib03] K. Shibuya, H. Hoshino, M. Chiyo, A. Iyoda, S. Yoshida, Y. Sekine, T. Iizasa, Y. Saitoh, M. Baba, K. Hiroshima, H. Ohwada, and T. Fujisawa. High magnification bronchovideoscopy combined with narrow band imaging could detect capillary looops of angiogenic squamous dysplasia in heavy smokers at high risk for lung cancer. *Thorax*, 58(11):989–995, 2003.

[Shib10] K. Shibuya, T. Nakajima, T. Fujiwara, M. Chiyo, H. Hoshino, Y. Moriya, M. Suzuki, K. Hiroshima, Y. Nakatani, and I. Yoshino. Narrow band imaging with high-resolution bronchovideoscopy: A new approach for visualizing angiogenesis in squamous cell carcinoma of the lung. *Lung Cancer*, in press:NA, Jun 2010.

[Sonn09] G. A. Sonn, S.-N. E. Jones, T. V. Tarin, C. B. Du, K. E. Mach, K. C. Jensen, and J. C. Liao. Optical biopsy of human bladder neoplasia with in vivo confocal laser endomicroscopy. *J Urol*, 182(4):1299–1305, Oct 2009.

[Stan95] A. V. Stanton, B. Wasan, A. Cerutti, S. Ford, R. Marsh, P. P. Sever, S. A. Thom, and A. D. Hughes. Vascular network changes in the retina with age and hypertension. *J Hypertens*, 13(12 Pt 2):1724–1728, Dec 1995.

[Theo03] D. Theodorescu. Molecular pathogenesis of urothelial bladder cancer. *Histol Histopathol*, 18(1):259–274, Jan 2003.

[Uehl00] P. Uehlinger, M. Zellweger, G. Wagnières, L. Juillerat-Jeanneret, H. van den Bergh, and N. Lange. 5-aminolevulinic acid and its derivatives: physical chemical properties and protoporphyrin ix formation in cultured cells. *J Photochem Photobiol B*, 54(1):72–80, Jan 2000.

[USAi51] USAirForce. MIL-STD-150A. *U.S. Military Standards*, 1951.

[van 05] A. P. M. van der Meijden, R. Sylvester, W. Oosterlinck, E. Solsona, A. Boehle, B. Lobel, E. Rintala, and for the EAU Working Party on Non Muscle Invasive Bladder Cancer. Eau guidelines on the diagnosis and treatment of urothelial carcinoma in situ. *Eur Urol*, 48(3):363–371, Sep 2005.

[Vick09] M. B. Vickerman, P. A. Keith, T. L. McKay, D. J. Gedeon, M. Watanabe, M. Montano, G. Karunamuni, P. K. Kaiser, J. E. Sears, Q. Ebrahem, D. Ribita, A. G. Hylton, and P. Parsons-Wingerter. Vesgen 2d: automated, user-interactive software for quantification and mapping of angiogenic and lymphangiogenic trees and networks. *Anat Rec (Hoboken)*, 292(3):320–332, Mar 2009.

[Wang07] T. D. Wang, S. Friedland, P. Sahbaie, R. Soetikno, P.-L. Hsiung, J. T. C. Liu, J. M. Crawford, and C. H. Contag. Functional imaging of colonic mucosa with a fibered confocal microscope for real-time in vivo pathology. *Clin Gastroenterol Hepatol*, 5(11):1300–1305, Nov 2007.

[Witj07] J. A. Witjes and J. Douglass. The role of hexaminolevulinate fluorescence cystoscopy in bladder cancer. *Nature Clinical Practice Urology*, 4(10):542–549, 2007.

[Wong05a] T. Y. Wong and R. McIntosh. Hypertensive retinopathy signs as risk indicators of cardiovascular morbidity and mortality. *Br Med Bull*, 73-74:57–70, 2005.

[Wong05b] T. Y. Wong and R. McIntosh. Systemic associations of retinal microvascular signs: a review of recent population-based studies. *Ophthalmic Physiol Opt*, 25(3):195–204, May 2005.

[Zaak08] D. Zaak, W. F. Wieland, C. G. Stief, and M. Burger. Routine use of photodynamic diagnosis of bladder cancer: Practical and economic issues. *European Urology, Supplements*, 7(7):536–541, 2008.

Chapter 6

Conclusions and future prospects in urology

The main aims of the part of this manuscript dedicated to research performed in urology were to optimize the photodetection instrumentation of bladder cancer, and to find an efficient method to reduce the false-positive rate associated with fluorescence cystoscopy. Several clinical and *ex vivo* imaging and spectrofluorimetric studies were performed to gain insight on the optical characterization of bladder carcinoma, defining further possibilities to increase the sensitivity and specificity of photodetection. These studies identified vascular patterns, whose shape and organization were characteristics to differentiate false and true positive lesions.

Violet LEDs positioned at the distal end of the endoscopes will be used in the future as excitation light source for endoscopic fluorescence imaging. Since the spectral emission of these LEDs will be narrower than the emission of light sources used at the present time for fluorescence cystoscopy, we have now the opportunity to improve the spectroscopy of this excitation light by selecting relatively precisely the wavelength producing the best Tumor/Normal tissues (T/N) contrasts and brightness. This concept is of particular relevance in the bladder where the sharp fluorescence excitation peak of PpIX interferes with the very strong and sharp absorption peak of hemoglobin contained in the tissues and in the liquid filling the bladder. Therefore, the determination of the wavelength corresponding to the optimal trade-off resulting from the partial overlap between these PpIX excitation and hemoglobin absorption peaks is not trivial.

To address this issue, we have compared the endoscopic images resulting from a Krypton laser (407, 413 nm) with a conventional filtered light source (370–430 nm). With this very preliminary study, we were able to show a possible increase of the tumor-to-background contrast using a narrow excitation centered on the PpIX excitation peak. More detailed results are presented in Appendix C.

Similarly, the value of the optimal excitation wavelength also depends on the spectroscopy of the endogenous fluorophores and/or absorbers that are present in the liquid used to fill the bladder. These liquid are producing a greenish background signal degrading the T/N contrast. This effect is particularly important with the Wolf system that detects the green tissue autofluorescence to generate the background image. Therefore, the comprehensive determination of the spectroscopy of this liquid will enable to identify the optimal excitation and, possibly, detection wavelengths to be used to generate a minimal background and, consequently, an optimal contrast.

In Chapter 4, the main metabolites present in the urine mixture were identified, but their exact interplay still needs to be investigated. In a second study, we showed that the fluorescence of the bladder washout fluid collected during the examination is strongly related to urine production. We were able to identify the main metabolites that fluoresce when excited with blue-violet light. High variations were observed between samples and patients. We could show that some spectral range have to be avoided in order to suppress the greenish appearance of the flows coming out of the ureters.

Not only the excitation but also the wavelengths to be detected need a specific optimization. More precisely, it is still not known if the decrease in the green autofluorescence — observed between small papillary lesions and their normal surrounding tissues — is also present on flat carcinoma *in situ* (CIS). Since detecting CIS as early as possible is crucial in terms of patient management, we can investigate this problematic in the future.

Even if the fluorescence cystoscopy is a well established method for the detection of flat bladder carcinoma, the dedicated PDD instrumentation has still to be tested for its reliability over time. Several parameters such as illumination light power, excitation spectrum, overall transmission and integrity of the detection system are subject to variations over time. In the clinics, a regular check of these parameters is necessary. It helps to prevent misinterpretation of the obtained endoscopic images and avoid under/over diagnosis leading to an evident reduction of patient benefit. In the framework of this thesis, we designed some reference validation samples to evaluate the system performances. They are described in Appendix D.

Since fluorescence cystoscopy still suffers from limited specificity, we investigated in Chapter 5 the use of high magnification cystoscopy to characterize fluorescence positive lesions in the bladder. This method is convenient, since it fits perfectly into the current clinical routine. We were able to show in a clinical study that comparison of HM cystoscopy classification with histopathology results confirmed 32/33 (97%) cancerous biopsies, and rejected 17/20 (85%) non-cancerous lesions. In the future, we will have to transfer this magnification technology on a flexible platform to overcome the geometric limitations. At this point, it is to be noted that most of the surgical tools are nowadays available for the rigid platform only (*e.g.* electro-resection and cautery for TURB). A trade-off has to be found between the existing platform and the promising HM characterization of false positive sites.

Since the HM classification was based on subjective criteria in the clinical study, we wanted to quantify the observed vascularization with more robust criteria. In Section 5.4, we evaluated the pertinence of extracting vascular skeleton out of the endoscopic image. It resulted a clear loss of visual information, when converting an original image into a skeleton. In Section 5.5, we implemented an image processing algorithm to automatically extract the vessel information based on a region-growing procedure. In the future, two approaches may be combined : 1) a quantitative analysis of the image skeleton, so that *non-visual* parameters (*e.g.* branching, fractal dimensions, concavity) can be evaluated with respect to their discrimination capability of true vs. false positive spots; 2) an improvement of the *visual* classification parameters as to be observed with conventional endoscopic images. As final stage, we analyzed global image features (such as low frequencies spatial distribution) without extracting each individual vessel. This approach also showed some potential to discriminate vascularization.

In order to better visualize the vessels, we may improve their contrast with respect to the background. Since hemoglobin is a very strong absorber of green and blue light, it can be used as an intrinsic marker of the vessel, because it is contained almost exclusively in the red blood cells. Consequently, we moved towards a spectral optimization of our endoscopic observation system. The first preliminary results are presented in Appendix E, where we showed that images acquired with a restricted excitation bandwidth targeting the hemoglobin absorption peaks yielded much

more contrasted vascularization pictures.

It is now clearly established that the chromatic presentation of the images on the TV monitor observed by the endoscopist has an important impact on the visualization/detectability of lesions during endoscopic fluorescence imaging. In Appendix F, we reviewed the parameters that influence the tumor detectability with respect to chromatic presentation of the contrast. Indeed, foreground-to-background contrast (*e.g.* tumor-to-healthy) can be enhanced by giving specific hue values to the relevant areas. Our preliminary tests showed that complementary color presentation is likely to improve the tumor detectability. Nevertheless, the inter-observer variations regarding optimal color presentation are very poorly documented. In the future, we will quantify the impact of false-color allocation on lesion detectability.

In this manuscript, we have shown the great potential of high magnification vascular imaging to reject false-positive lesions. We also showed that imaging of backscattered wavelengths has a great potential to improve the vessel-to-background contrast. However, the combination of reflectance and fluorescence imaging in the same device remains a great challenge. Several attempts have been made up to now (*e.g.* virtual filtering, dual-CCD endoscope), but the optimal device has still to be developed.

This high magnification procedure could be applied to virtually all hollow organs accessible with endoscopy, as long as vascular characterization is relevant to discriminate false from true positive lesions. Very preliminary tests were made on vocal cords to assess feasibility of this observation in the larynx. We showed that this approach could be a useful tool to characterize early lesions, as an adjuvant to the existing combined procedure that involves autofluorescence, endoluminal ultrasound and OCT.

In the bladder, only few groups are working on characterizing the false-positive lesions. Schmidbauer *et al.* postulated that OCT is able to resolve the layered structure of the urothelium. Recently, this group published a study characterizing the positive lesions detected by HAL fluorescence cystoscopy. They reported an increase specificity from 78.6% to 97.9% for HAL with targeted OCT as compared to HAL alone. Sensitivity was not modified since they only target HAL+ lesions. With a depth of penetration of 1-2 mm, this devices enables urothelium, lamina propria, and muscularis propria to be distinguished. Current system has however only a limited resolution (30 μm lateral resolution). Since urothelium does not exhibit the same layer definition as the retina, the operator may need a special training before using this tool to reduce discrepancies in interpretation of OCT images. After a dedicated training, these authors claims to be able to reject 36/42 (86%) of the false-positive. Their 2.3 mm probe is also fully compatible with the clinical routine since it can be inserted into standard surgical instruments.

Nowadays, several groups aimed to perform an *in vivo* "optical biopsy" to virtually replace the histopathological analysis. For instance, Cicchi *et al.* used multiphoton endoscopes [Cicc10]. These authors showed that tumor cells appeared slightly different in shape and with a smaller cellular-to-nuclear dimension ratio with respect to corresponding normal cells. Further differences between the two tissue types were found in both spectral emission and fluorescence lifetime distribution by performing temporal- and spectral resolved analysis of fluorescence. Sonn *et al.* used confocal laser endomicroscopy. This imaging technique requires the intravesical/intravenous use of fluorescein. These authors could highlight clear differences in the cellular between normal mucosa, and low and high grade tumors.

Since it is not timely possible to scan the whole bladder with such a small field of view, both methods are promising only as characterization method. However, no combination of endomicroscopy and/or multiphoton endoscopy with fluorescence cystoscopy has been reported up to now.

A new design trend that was reported recently in endoscopy is the "wireless" endoscope, with

radio-communication from the CCD to the monitor, and LED-based integrated illumination. An extreme example of this would be the technology called *capsule endoscopy*, where patients swallow a vitamin-size camera that will acquire images throughout the GI tract (stomach, small bowel and colon) and send them to the doctor for review (Pillcam from Given Imaging Inc., EndoCapsule from Olympus Inc.). With 6 LEDs built-in for illumination, these devices achieve compactness (11 mm $\times$ 26 mm) with a wide field of view (145°) and enhanced depth of field (0–20 mm), but they still suffer from battery lifetime limitations. The power supply will remain a crucial technical issue in the development of wireless endoscopy.

Since the cost of miniaturization are still decreasing, novel zooming setup (*e.g.* Optotune AG) to perform high magnification endoscopy can now be integrated at the distal end of the endoscope, in the same manner than confocal endoscopy was integrated as MEMS [Cham07].

Bibliography

[Cham07] S. R. Chamot and C. Depeursinge. Mems for enhanced optical diagnostics in endoscopy. *Minim Invasive Ther Allied Technol*, 16(2):101–108, 2007.

[Cicc10] R. Cicchi, A. Crisci, A. Cosci, G. Nesi, D. Kapsokalyvas, S. Giancane, M. Carini, and F. S. Pavone. Time- and spectral-resolved two-photon imaging of healthy bladder mucosa and carcinoma in situ. *Opt Express*, 18(4):3840–3849, Feb 2010.

Part II

Bronchial cancer

Chapter 7

Introduction to Bronchial cancer

7.1 Bronchial Anatomy and Histology

External respiration (i.e. the gas exchange between air and blood) takes place in the lungs, where the venous blood is oxygenized and sent back to the body blood circulation via the arteries. The blood carbon dioxide (CO_2) resulting from the body's oxygen consumption is released to the external environment and replaced by oxygen (O_2). The human thorax holds two lungs (right and left) that are subdivided into a total number of 5 lobes. Three lobes are in the right lung, and two in the left lung. Indeed, the left lung's architecture is slightly different due to the heart's volume in the left part of the thorax (see Figure 7.1).

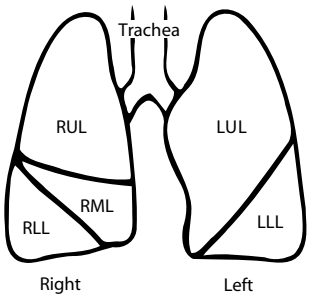

Figure 7.1: *Lobar structure of the lung. The right lung consists of 3 lobes, namely the right upper lobe (RUL), the middle lobe (RML) and the right lower lobe (RLL). The left lung consists of the left upper lobe (LUL) and the left lower lobe (LLL).*

The human respiratory system may be subdivided into two parts: (i) the *conducting portion* is a continuum of air passageways that conduct air from the environment into respiratory spaces (and back out); (ii) the *respiratory portion* (gas exchange) consists of many interconnected air-filled spaces with very thin linings which allow rapid gas exchange. The air flows down the so-called "tracheo-bronchial tree", a tubular system dividing in bronchi, bronchioles, and alveoli (see Figure 7.2). It starts with the trachea, which divides into the two primary or *extra-lobar* bronchi. These primary bronchi further divide into the secondary or *intra-lobar* bronchi which on their part divide into bronchi of decreasing size (segmental bronchi). The small bronchi

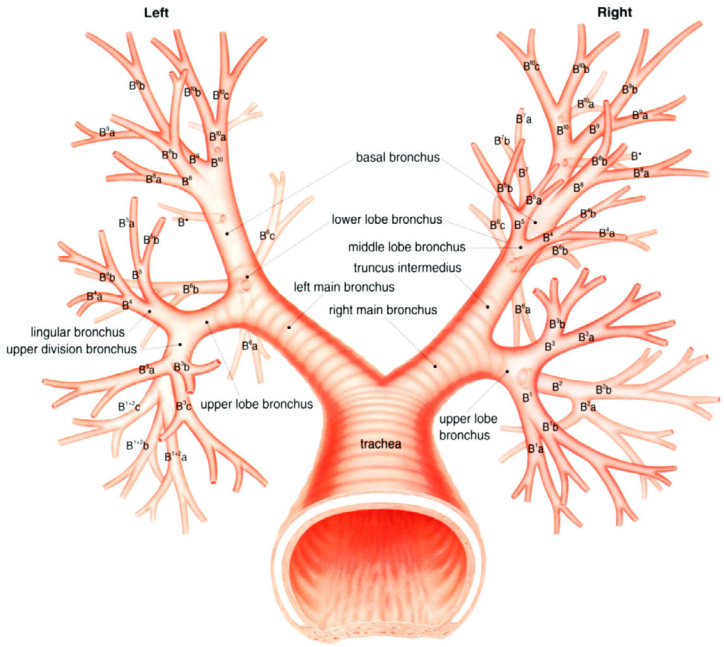

Figure 7.2: *The tracheo-bronchial tree viewed from the trachea. The trachea divides into a right and a left main bronchus which further subdivide into the higher generation bronchi and bronchioli. The "B-numbers" give the official nomenclature of the bronchi (adapted from Pentax documentation).*

subdivide into terminal and respiratory bronchioles and form the alveoli. Essentially all gas exchange between air and blood occurs across the walls of alveoli.

The diameter of the trachea is typically 20 mm in adults. This diameter decreases to about 16 mm for the extra-lobar bronchi, 11 mm for the intra-lobar bronchi, and is less than 8 mm for the segmental bronchi. The bronchioli have diameters smaller than 0.6 mm. The terminal alveoli are less than 0.3 mm in diameter [Yeh80]. Due to the decreasing size of the bronchial diameter, only the primary and secondary bronchi are accessible with conventional bronchoscopes. The histology of the tracheo-bronchial tree is not uniform, and undergoes significant changes from the trachea to the alveoli.

The function of the conducting portion of the tracheo-bronchial tree, i.e. from the trachea down to the terminal bronchioles, is to modify the incoming air by heating, increasing its relative humidity, and purification from particles. Indeed, the proximity of the rich vascularization of the airway walls heats the incoming air before reaching the respiratory portion. Humidification and purification are achieved by the so-called "mucociliary escalator" which results from the interaction of the mucous and serous layers, and the cilia overlaying the epithelium. The *serous layer* is in immediate contact with the epithelium and mostly contains water and proteins. A viscous *mucous layer* sitting on the serous layer humidifies the air and traps particles. The cilia of the respiratory epithelium beat in concert, and moved the secreted mucous towards the pharynx, for either expectoration or swallowing to the stomach where the acidic pH helps to neutralize foreign material and micro-organisms. In smokers, the number of ciliated cells in the epithelium is significantly reduced. Thus, the efficiency of the mucociliary escalator is reduced, resulting in irritations of the mucosa and an increased coughing reflex[1].

[1]Department of Physiology and Biophysics, Suny Stony Brook University, *The respiratory system*, `http://www.pnb.sunysb.edu/hby531/chap11%20respiratory.pdf`

The principal histologic features of the trachea and the accessible bronchi are given in the following section.

7.1.1 The trachea

The trachea is supported by 15 to 20 hyaline cartilaginous structures (C-shaped, open dorsally), which are replaced by smooth muscle bundles in the posterior wall. The inner lining of the trachea consists of 4 layers : the mucosa, the lamina propria (or tunica propria), the submucosa, and hyaline cartilage, as depicted in the photomicrograph in Figure 7.3[2]. The tracheal mucosa forms a ciliated pseudo-stratified columnar epithelium. A very prominent basement membrane separates the epithelium from the lamina propria. In contrast to the avascular epithelium, the lamina propria is highly vascularized and contains numerous elastic fibers and fine, densely packed collagen fibers. The elastic fibers are arranged in bundles that run along the longitudinal axis of the bronchial wall giving it a stripe-like morphology. The thin layer of the lamina propria separates the epithelium from the submucosa. It contains less elastic fibers and only loosely packed collagen fibers. The secretory portions of exocrine glands are located in the upper part of the submucosa.

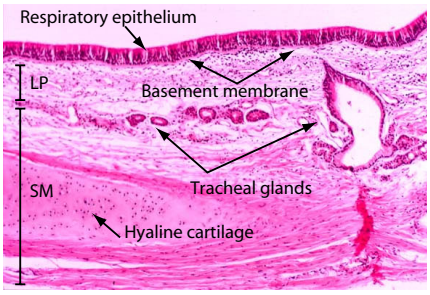

Figure 7.3: ***Histology of the trachea.*** *The ciliated pseudo-stratified columnar epithelium (respiratory epithelium) is separated from the lamina propria (LP) by the basement membrane. A portion of a cartilage ring is visible in the submucosa (SM).*

7.1.2 The bronchi

The histological appearance of the extra-lobar, intra-lobar, and segmental bronchi is similar to that of the trachea. A photomicrograph of healthy bronchial wall tissue is shown in Figure 7.4[3].

The most superficial layer of the bronchi is formed by a ciliated pseudo-stratified columnar epithelium that lays on the lamina propria. The two tissues are separated by the thin basement membrane. In the extra-lobar and first segmentary bronchi, the epithelial thickness is $\approx$ 40–60 μm. However, the epithelial thickness with successive branching, becoming a simple ciliated epithelium close to the bronchioles. The lamina propria contains elastin and collagen fibers as well as blood vessels. The extra-lobar bronchi, and the trachea alike, contain smooth muscles only on their posterior wall, whereas they are found right below the lamina propria in the intra-lobar bronchi. They are arranged helically in crisscrossing bundles around the bronchi, and become more prominent as one approaches the bronchioles. The cartilage arrangement and shape change significantly with successive branching. In particular, the cartilage rings found in the trachea and the extra-lobar bronchi make room for isolated plates (islands) of cartilage in

[2]Indiana University School of Medicine [PERL] : `http://pathology.iupui.edu/`
[3]Institut für Pathologie der Universität Basel : `http://alf3.urz.unibas.ch/pathopic`

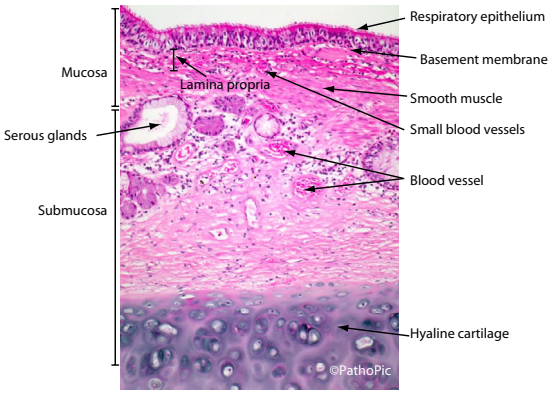

Figure 7.4: ***Normal bronchial histology.*** *The mucosa (M) consists of the ciliated respiratory epithelium and the lamina propria (LP). Smooth muscle fibers and small blood vessels are visible in the LP. The submucosa (SM) contains serous glands and blood vessels. A portion of the hyaline cartilage is visible in the lower part of the image*

the intra-lobar and segmentary bronchi. A gradual transition is observed between the histologic characteristics of successive branching.

7.2 Facts about bronchial cancer

Lung cancer is the deadliest cancer in the world with the highest incidence rates occurring in North America and Europe[4] (see Figure 3.1). However, over the past few years, lung cancer incidence has dramatically increased in developing countries [Youl08]. Still, a clear demarcation line is visible between the developed and the less developed countries[5] (see Figure 7.5). The mortality rate for lung cancer in Europe exceeds that of all other most common cancers, including prostate, colorectal, stomach, bladder, and head and neck cancer, by a factor more than 2. In European women, only breast cancer is associated with a higher mortality rate [Levi04]. In 2009, it was estimated that about 219'440 new lung cancer cases would occur in 2009 and about 159'390 lung cancer patients would die of their disease in the USA [Jema09].

Malignant and non-malignant tumors in the lung can develop from all tissues in the bronchi and lung parenchyma. However, bronchial carcinoma represents about 90% to 95% of all malignant lung tumors [Schu94]. About 60–70% of these lesions are centrally located, i.e. accessible by bronchoscopic procedures [Auer91, Pari03b], and only 20–30% are peripheral. The central bronchial lesions occur 25.6% in the RUL, 13.3% in the RML, 15.4% in the RLL, 30% in the LUL, and 15.7% in the LLL [Schu94]. However, over the last decades, changes in patterns of lung cancer were observed [Auer91] with an increasing incidence of peripheral and adenocarcinoma [Gazd97, Thun97] principally due to modification in the smoking behavior of individuals and cigarette design (filters, light tobacco cigarettes, profound inhalation) [Fran99].

Among all central lesions, the *squamous cell carcinoma* (SCC) is the most frequent carcinoma type; its prevalence ranging between 29% to 43% [Auer91, Kenn00]. Other types of bronchial carcinoma are adenocarcinoma, large cell lung carcinoma, and small cell lung carcinoma (SCLC). This thesis work will focus on the detection and characterization of squamous cell carcinoma and its non-invasive stages.

The most important risk behavior for lung cancer is tobacco smoking, being responsible for

[4]SEER Cancer Statistics Review: 1975-2005. `http://seer.cancer.gov/csr/1975_2005/`
[5]GLOBOCAN 2008 `http://globocan.iarc.fr/`

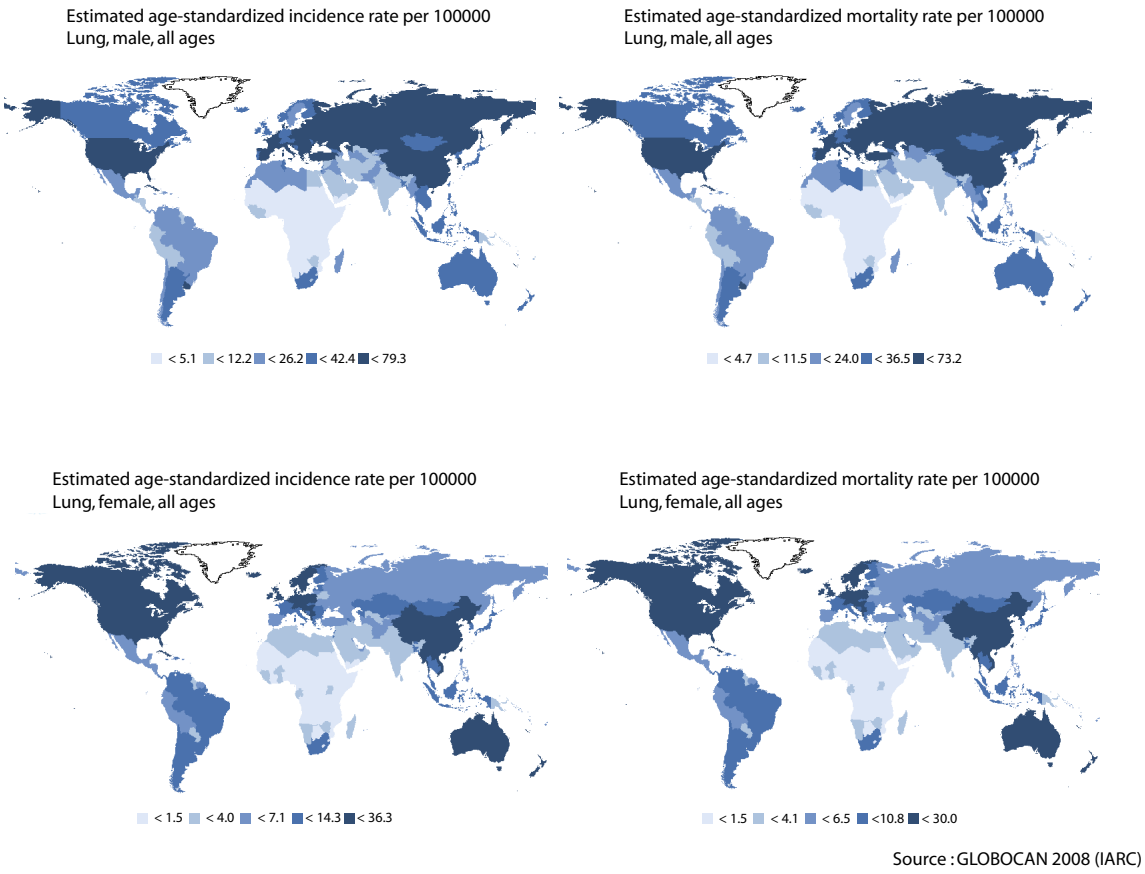

Figure 7.5: *Age-standardized incidence and mortality rate for men and women in 2009 [Ferl10].*

85–90% of all bronchial carcinoma [Tycz03]. In 2005, it was estimated that around 1.25 billion adults throughout the world were smokers (1 billion men and 250 million women) [Mack06]. This represented approximately 35% of men and 22% of women in more developed countries, compared with 50% of men and 9% of women in less developed countries.

The relationship between smoking and lung cancer is one of the most thoroughly investigated issues in biomedical research [Albe03], and compelling evidence has built up since the middle of the twentieth century to indicate that smoking is the predominant causal factor for lung cancer [Thun02, Sasc04]. Epidemiological studies show a clear dose-response relationship between lung cancer risk and the number of cigarettes smoked per day, the degree of inhalation, and the age at initiation of smoking [Enge96, Agud00]. Odds Ratios (OR) of lung cancer are estimated at 23.9 (19.7–29) for male current smokers *vs.* never smokers, and at 7.5 (6.2–9.1) for male former smokers *vs.* never smokers [Simo01]. In other words, smokers have a 15- to 30-fold increased risk of developing lung cancer compared with nonsmokers [Sasc04]. This excess risk of lung cancer is lower in women, with an estimated OR of 8.7 (7.4–10.3) for female current smokers *vs.* nonsmokers and 2.0 (1.6–2.4) for female former smokers *vs.* never smokers [Agud00].

Clinical characteristics and risk factors of nonsmoker patients with lung cancer are still debated. To evaluate the consequences of exposure to second-hand smoke (commonly known as "passive smoking"), more than 1600 key articles were reviewed in 2007 by the Surgeon General office[6]. They concluded that exposure to second-hand smoke can also cause lung cancer, correlated by other authors [Wake07]. In a recent meta-analysis [Khud01], all histological types were found to be associated with tobacco smoking, the relationship being stronger for squamous cell carcinoma (OR: 25.4 [18.4–35.1]) and small cell carcinoma (OR: 42.0 [21.7–81.2]) than for adenocarcinoma (OR: 6.18 [4.59–8.32]). In two recent studies, Clément-Duchêne and Paris demonstrated that some risk factors, such as duration of smoking and certain occupational exposures but not gender or age, have a more important influence on the incidence of lung adenocarcinomas than on other histologic types [C.-D10, Pari10]. However, they also showed that neither occupational nor exposures suffice to explain the occurrence of such disease in never smokers. Their findings suggest that a sizeable fraction of lung cancer cases, both in male and female never smokers, may share common characteristics, and possibly underlying biological mechanisms, as recently suggested by Toyooka *et al.* [Toyo07].

Other factors are occupational exposure to carcinogens like asbestos, some metals (e.g. chromate, nickel, arsenic, cadmium), radon, and ionizing radiation [Albe07]. However, these factors account for less than 9% of bronchial carcinoma [Stee96, Dris05]. This is also true for environmental factors, principally air-pollution, which is estimated to be responsible for less than 5% of the cases [Schu94]. However, occupational factors seem to be only secondary to the formation of bronchial cancer in smokers. A clinical AF bronchoscopy study on high risk patients by Paris *et al.* showed that definite occupational respiratory exposure to carcinogens and active smoking were independently associated with the presence of high grade bronchial pre-neoplastic lesions [Pari03a]. In this study, 9% of all patients showed high grade dysplasia, whereas low grade dysplasia were detected in 45%. Similar data have been reported by Lam *et al.* [Lam93, Hawk99].

7.2.1 Carcinogenesis and staging of bronchial cancer

Bronchial carcinogenesis is a multi-step process, that usually begins with alterations of the squamous epithelium under the effect of inhaled harmful components. The individual steps were classified by the World Health Organization (WHO) and the International Association for the

[6] `http://www.surgeongeneral.gov/library/smokeexposure/index.html`

Study of Lung Cancer (IASLC) in the WHO/IASLC histological classification of pulmonary and pleural tumors that was revised in 1999 [Trav99, Bram01, Nich01]. This updated classification was developed with the aim to adhere to the principles of reproducibility, clinical significance, and simplicity in order to minimize the number of unclassifiable lesions as compared to the previous one [Worl81], including *e.g.* the addition of two pre-invasive lesions to squamous dysplasia and carcinoma *in situ*.

The staging of squamous cell carcinoma is described by the International System for staging of lung cancer. In this classification system, lung cancer stages are grouped according to their TNM (**T** – primary tumor, **N** – regional lymph nodes, and **M** – metastasis) anatomical subsets (similar to bladder cancer classification, see Section 3.3.2.1). Table 7.1 & 7.2 show an overview of the TNM descriptors and the stage grouping (adapted from [Moun00]).

	T – Primary tumor
Tx	Primary tumor cannot be assessed
T0	No evidence of primary tumor
Ta	Non-invasive papillary carcinoma
Tis	Carcinoma in situ: *flat tumor*
T1	Tumor $\leq$ 3 cm in greatest dimension, no invasion more proximal than the lobar bronchus
T2	Tumor with any of the following features: $>$ 3cm in greatest dimension; $\geq$ 2 cm distal to the carina; invading pleura; associated with atelectasis or local obstructive pneumonitis
T3	Tumor of any size directly invading any of the following: chest wall, diaphragm, mediastinal pleura, parietal pericardium; or $<$ 2 cm distal to the carina; or atelectasis or obstructive pneumonitis of entire lung.
T4	Tumor of any size with invasion of mediastinal organs (e.g., heart, trachea, oesophagus, mediastinum) or vertebral body
	N – Lymph nodes
Nx	Regional lymph nodes cannot be assessed
N0	No regional lymph node metastasis
N1	Ipsilateral peribronchial and/or ipsilateral hilar lymph node meatastasis
N2	Ipsilateral mediastinal and/or subcarinal lymph node metastasis
N3	Metastasis to contralateral mediastinal, contralateral hilar, ipsilateral or contralateral scalene, or supraclavicular lymph nodes
	M – Distant metastasis
Mx	Distant metastasis cannot be assessed
M0	No distant metastasis
M1	Distant metastasis

Table 7.1: *The international TNM descriptor system for the staging of lung cancer (1997 revision).*

The steps of early carcinogenesis in the epithelium are defined as (1) reactive changes (include basal cell or goblet cell hyperplasia, and squamous metaplasia); (2) *low-grade* squamous dysplasia (LGD); (3) *high-grade* squamous dysplasia (HGD); (4) microinvasive carcinoma and (5) invasive carcinoma. Microphotographs showing the 5 principal WHO classes are shown in Figure 7.6, that depicts hematoxylin and eosin (H&E) stained slides.

Hyperplasia is characterized by increased proliferation of basal or goblet cells, increasing the number of cell layers in the epithelium to 3-10 [F.-E98, Chha05]. In *squamous metaplasia*, the ciliated pseudo-stratified normal epithelium is replaced by a stratified cell structure of variable thickness [F.-E98]. Reactive changes frequently show spontaneous regression and are not consid-

Stage	TNM subset		
0	Carcinoma *in situ*		
IA	T1	N0	M0
IB	T2	N0	M0
IIA	T1	N1	M0
IIB	T2	N1	M0
	T3	N0	M0
IIIA	T3	N1	M0
	T1-3	N2	M0
IIIB	T4	N0-3	M0
	T1-3	N3	M0
IV	any T	any N	M1

Table 7.2: ***Stage Grouping.*** *International definition of the TNM subsets for lung cancer staging.*

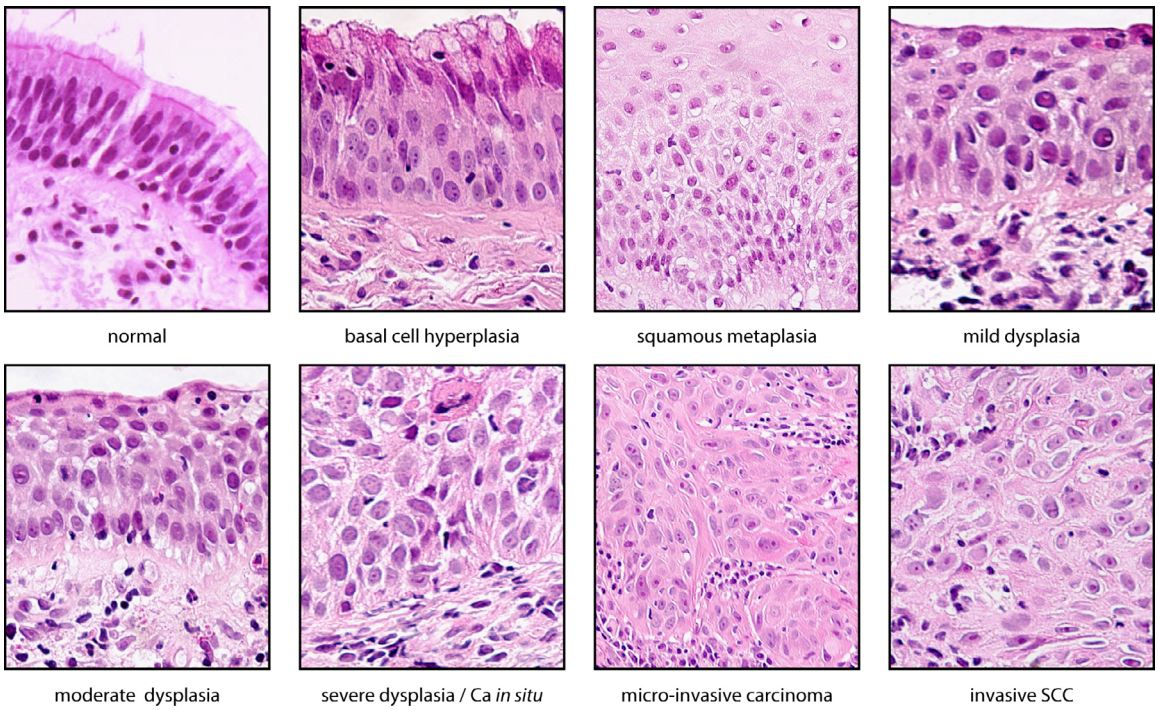

Figure 7.6: *H&E stained photomicrographs of the principal WHO classes: basal cell hyperplasia, metaplasia, mild dysplasia, moderate dysplasia, severe dysplasia, carcinoma* in situ *(CIS), microinvasive carcinoma and invasive squamous cell carcinoma (courtesy from S. Andrejevic-Blant, Institute form Pathology, CHUV University Hospital, CH-Lausanne)*

ered as pre-neoplasia, but they can occasionally turn into low-grade squamous dysplasia (mild and moderate dysplasia). In *mild dysplasia*, the microscopic architectural and cytological disturbance of the epithelium is minimal. The epithelial cells exhibit a mild increased in size and show pleomorphism. A continuous progression of maturation from the base to the luminal surface and variations in nuclei-cytoplasma (N/C) ratio are observed. *Moderate dysplasia* is characterized by a moderate increase of the epithelial thickness with a superficial flattening of the cells. The N/C ratio is higher than in the mild dysplasia and mitosis can be detected in the lower third of the epithelium. The changes in the N/C ratios and mitosis are even more marked in *high-grade dysplasia*, where cells are markedly increased in size and show strong pleomorphism. High-grade dysplasia includes severe dysplasia and carcinoma *in situ* (CIS), considered as equivalent by several authors. Low and high grade dysplasia are referred to as *pre-neoplasia*. They are limited to the epithelium and do not break through or infiltrate the basement membrane. If the epithelial changes extend over the basement membrane and invade the subepithelial layers, they are referred to as *neoplasia*. If the infiltration into the subepithelial layers is less than 3 mm, the lesion is considered a *microinvasive* carcinoma. Neoplasia that penetrate into deeper tissue layers are referred to as *invasive* carcinoma. More details on the microscopic features of squamous cell dysplasia and higher grade epithelial neoplasia are listed in Table 7.3.

Reactive, pre-neoplastic and neoplastic changes of the epithelium are often associated with inflammatory reactions in the bronchial mucosa and submucosa. Eosinophils are often considered as inflammation flag in H&E images. They do stain as characteristic black dots well demarcated in the micrographs.

The exact prevalence of severe dysplasia and CIS in the bronchial tree is unknown. In a review of fluorescence bronchoscopy data in a selected population of smokers and former smokers with sputum atypia, prevalence rates of 6% and 1.6% were reported for severe dysplasia and CIS, respectively [Lam00].

7.3 Management of bronchial cancer: an overview

Lung cancer survival depends of the disease stage at presentation [Pari03b]. The extremely high mortality rate of lung cancer is strongly attributed to the general late detection and diagnosis of the disease. Indeed, stage I and II are often asymptomatic and consequently, less than 25% of lung cancer patients will present with an early stage cancer [Pari03b]. On the other hand, the yield of curative therapy for advanced stage (III - IV) is still low [Bepl03]. Indeed, the overall 5-year survival rate for lung cancer is only 14%. This rate is about 25–1% for stage III and IV, but can reach 25–67% when the lung cancer is detected at an early stage (I or II) [Moun97]. Thus, efficient detection of early stage bronchial carcinoma is crucial for a successful therapeutic outcome and survival. This is particularly true for the detection of flat, small pre-neoplastic lesions such as dysplasia and CIS, because those lesions have a high probability for growing into invasive lesions within a short period of time [Bota01, Venm00, Lam98].

Clinical studies have shown that approximately 10% of moderate dysplasia and 19% to 83% of severe dysplasia will progress to invasive lesions [Venm01, Shes00]. Monitoring the progression of pre-neoplasia to neoplasia is especially important in the context of the management and follow-up (interval between control bronchoscopies, chemoprevention) of patients diagnosed with a primary cancer in the bronchi and/or in any ear-nose-throat (ENT) localization, because these patients are at particularly high risk for secondary or second primary bronchial neoplasia [Mart95, Anta95, Jone95, John98, Levi99, Stoe01].

The incidence of second primary bronchial neoplasia for lung cancer patients ranges from 0.5% to 10% [Anta95]. Sixty percent (60%) of all second primary bronchial cancers are *meta-*

Abnormality	Epithelial Thickness	Cell size	Maturation/Orientation	Nuclei
Mild dysplasia	Mildly increased	Mildly increased; Mild anisocytosis, pleomorphism	Continuous progression of maturation from base to luminal surface; basilar zone expanded with cellular crowding in the lower third of the epithelium; superficial flattening of epithelial cells	Mild increase of N/C ratio; inconspicuous or absent nucleoli; lower third of epithelium: nuclei vertically orientated; rare or absent mitosis
Moderate dysplasia	Moderately increased	Mild increase; cells often small; pleomorphism	Partial progression of maturation from base to luminal surface; expanded basilar zone; cellular crowding in 2 lower thirds of epithelium; superficial flattening of epithelial cells	Moderate increase of N/C ratio; inconspicuous or absent nucleoli; nuclei vertically orientated in lower two thirds; signs of mitosis in lower third
Severe dysplasia	Markedly increased	Markedly increased; pleomorphism	Low progression from base to luminal surface; expanded basilar zone; cellular crowding into upper third; superficial flattening of epithelial cells; intermediate zone greatly attenuated	High and variable N/C ratio; frequent and conspicuous nucleoli; vertically orientated nuclei in lower 2 thirds; mitosis present in lower 2 thirds
Carcinoma *in situ*	+/− increased	may be markedly increased; pleomorphism	maturation: no progression of maturation from base to luminal surface; epithelium could be inverted with little change in appearance; expanded basilar zone with cellular crowding throughout epithelium; flattening only of the most superficial cells	High and variable N/C ratio; inconspicuous nucleoli; no consistent orientation of nuclei relative to epithelial surface; mitosis visible throughout full thickness of epithelium

Table 7.3: ***The revised WHO/IASLC grading system.*** *The table lists the microscopic features of squamous dysplasia and carcinoma* in situ *(adapted from [Nich01])*

chronous (i.e. developing at different times), and 40% are *synchronous* (i.e. at the same time). The prevalence of second primary bronchial neoplasia in head and neck (H&N) cancer patients has been reported to be 7–32% [Dele97, León99]. In a clinical autofluorescence (AF) bronchoscopy study, Venmans *et al.* found pre-neoplastic central bronchial lesions in 25% of patients with a history of H&N SCC [Venm01]. Long-term studies on patients with secondary or second primary lung cancers showed that resection of early metachronous lesions improved the long-term survival rate [Anta95, Asap00]. However, most patients (68%) are asymptomatic at the time of diagnosis of the second primary cancer [Asap00], which is frequently detected only "by accident" during a follow-up examination. Since secondary and second primary bronchial cancers may occur several years after the first cancer diagnosis [Anta95], patients surviving treatment of a first primary carcinoma (bronchi or H&N) require lifelong screening of second primary bronchial lesions [Dodd01]. Further high-risk populations that should be considered for screening for bronchial cancer include long-term survivors of small cell lung cancer, occupationally exposed groups, and subgroups of smokers (heavy smoker, lung cancer history in the family) [Batt95].

7.3.1 Screening and detection of bronchial cancer

The most common detection methods for lung cancer are sputum cytology, chest X-ray (CXR), computed tomography (CT), low-dose spiral CT, positron emission tomography (PET), magnetic resonance imaging (MRI) and bronchoscopy (white light or AF).

Sputum analysis is currently a widely used screening tool in high risk populations [Thun03]. It involves microscopic examination of the cells that are either coughed up from the lungs, or collected through a bronchoscope. It has a high specificity especially for bronchial SCC, but only a limited sensitivity of 65% [Thun03, Depp04]. This percentage is likely to be much smaller for dysplasia and squamous cell carcinoma. DNA analysis, automated quantitative cytometry and methylation of the sputum samples have shown promising results to improve sensitivity [McWi03]. Sputum analysis is the least invasive and least costly of the detection methods mentioned so far, and can easily be used in wide range screening programmes. However, it does not allow localization of the lesion within the tracheo-bronchial tree. Indeed, bronchoscopy is the only established method that allows detection and localization of central bronchial lesions and parallel tissue sampling for histological diagnosis.

Chest x-ray is a projection radiograph of the chest and is a very common procedure of diagnostic. It helps physicians to diagnose pneumonia, emphysema, and lung tumors of important size. Unfortunately has only a limited resolution and thus, has only poor sensitivity for the detection of early bronchial lesions.

Low-dose CT scan is a computerized x-ray procedure that produces cross-sectional images of the body. This procedure is widely used for screening of high-risk patients, because it is non-invasive and brief. Several studies showed that multi-detector spiral CT has a higher sensitivity to early and small sized lung cancer than CXR [Bepl03, McWi03]. Its detection rate is about 3-fold higher than with CXR attributed to better resolution and volume rendering capability. Indeed, spiral CT can detect lesions as small as 2-3mm in size [Kenn00], but at the price of a low specificity [Hens99, Hens03]. Moreover, CT is not sensitive to superficial, pre- or microinvasive central lung cancers [McWi03].

PET is a nuclear medicine imaging technique which produces a three-dimensional image or picture of functional processes in the body with the help of a radio-active sugar. With this technology, cancer areas with increased metabolism can be highlighted. In lung cancer management, PET with 18-fluorodeoxyglucose has to be considered as a diagnostic and staging

tool, rather than a screening tool [vanZ02, Port02]. Pastorino *et al.* demonstrated that the combined use of low-dose spiral CT and PET improves the specificity of early stage lung cancer detection [Past03].

Several attempts were made in the last years to establish *breath test* as a valid tool for lung cancer screening, since it is non-invasive and totally painless. It was pioneered by Dr. Michael Phillips *et al.* in 1999 [Phil99], an Autralian physician located in New York. These tests were refined by several groups. For instance, Peng *et al.* showed with gas chromatography/mass spectrometry studies that several volatile organic compounds (VOC) , which normally appear at levels of 1-20 ppb in healthy human breath, are elevated to levels between 10 and 100 ppb in lung cancer patients. In this study, 42 volatile organic compounds that represent lung cancer biomarkers were indentified [Peng09]. Bajtarevic *et al.* assessed the performance of two methods : proton transfer reaction mass spectrometry (PTR-MS) vs. solid phase microextraction with subsequent gas chromatography mass spectrometry (SPME-GCMS) [Bajt09]. These authors showed that isoprene, acetone and methanol are compounds appearing in everybody's exhaled breath, whereas potential marker compounds are alcohols, aldehydes, ketones and hydrocarbons. They also claimed that PTR-MS gives much more reliable quantitative results then GCMS-SPME, since it does not need pre-concentration. Sensitivity for detection of lung cancer patients based on presence of (one of) 4 different compounds not arising in exhaled breath of healthy volunteers was 52% with a specificity of 100%. Using 15 (or 21) different compounds for distinction, sensitivity was 71% (80%) with a specificity of 100%. These approaches have often 2 classes of patients : healthy and cancer-bearing. In this studies, no description is available about the stages of the cancer, and it is difficult to figure out whether their conclusion are also valid for early non-invasive cancers.

Finally, bronchoscopy is a technique of visualizing the inside of the airways. The first bronchoscopy was performed in 1897 by a German, Gustav Killian. For this examination, an instrument bronchoscope is inserted into the airways, usually through the nose or mouth, or occasionally through a tracheostomy. This allows the practitioner to examine the patient's airways for abnormalities such as foreign bodies, bleeding, tumors, or inflammation. Specimens may be taken from inside the lungs: biopsies, fluid (known as broncho-alveolar lavage), or endobronchial brushing. The practitioner may use either a rigid bronchoscope or flexible bronchoscope. A *rigid* bronchoscope is a straight, hollow, metal tube. Doctors perform rigid bronchoscopy less often today, but it remains the procedure of choice for removing foreign materials, as its increased thickness allows instruments to be more easily inserted through it. Rigid bronchoscopy also becomes useful when bleeding interferes with viewing the examining area, and allows for more interventions, such as cautery to stop the bleeding. A *flexible* bronchoscope is a long thin tube that contains small clear optical fibers that transmit light images as the tube bends. Its flexibility allows this instrument to reach further into the airway. The procedure can be performed easily and safely under local anesthesia. Nowadays flexible videobronchoscopes are introduced on the market. The optical fibers inside the tube are replaced by a CCD-detector placed at the distal tip of the endoscope. Drawbacks related to the fibers (e.g. loss of transmission, breakage) are voided.

Conventional white light bronchoscopy has a high sensitivity and specificity for early stage, invasive, central bronchial cancer, but is limited in the detection of small pre-neoplastic lesions. Indeed, in the central airways, less than 40% of high grade dysplasia is detectable by conventional white light bronchoscopy [Lam00, Wagn03]. Autofluorescence bronchoscopy (AFB) has been introduced as a tool for the detection of flat pre-neoplastic central bronchial lesions. Its sensitivity for pre-invasive squamous lesions is about twice that of conventional white light bronchoscopy [Lam98, Gouj03]. AFB will be discussed in Chapter 7.5 of this thesis in more detail.

Some trials involving *virtual bronchoscopy* have been carried out. Data set acquired with CT scan can be process with computer-generated, three-dimensional reconstruction techniques. It can render surfaces or endoluminal images. These approaches could be added to the conventional imaging technique to enhance visualization.

7.3.2 Treatment of bronchial cancer

Surgery is the preferred curative therapy of localized non-small cell lung cancer (NSCLC) at stage III and below. Depending on the stage and the extent of the lesion, surgery is performed as pneumectomy (surgical removal of a lung), or lobectomy (surgical removal of a lobe). The overall 5-year survival rate for complete surgical resection of stage I and II NSCLC is about 40% [Dien01]. Limited resection such as segmentectomy or wedge resection reduce mortality and morbidity, but are associated with a 3 times higher local recurrence rate and a decrease in 5-year survival [Dien01].

Post-operative radiotherapy and (neo-)adjuvant chemotherapy can improve survival [PORT98, Stew00]. However, about 30% of all patients with localized NSCLC don't undergo surgery due to presentation at an advanced stage, unresectability of the carcinoma, medical comorbidities, or advanced age [Baum01]. In these cases, radiotherapy (alone or in combination with chemotherapy) offers the only curative possibility. However, the mean 5-year survival rates for those treatments are below 27% for stage I–II lung cancer [Zimm03] and around 10% for stage III–IV disease [Souh98].

For localized pre-neoplasia, i.e. squamous dysplasia and CIS, (micro-)invasive carcinoma, and early stage bronchial carcinoma, minimal-invasive bronchoscopic therapies provide alternative treatment options [Shes00, Hert05]. Most common therapies include PDT [Mach95], endobronchial brachytherapy (EB) [Mach95, Nag01], cryotherapy [Deyg01], argon plasma coagulation (APC) [Cros01], laser therapy with Nd:YAG laser and electrocautery [vanB01]. The endoscopic treatment of early-stage bronchial cancer has been reviewed by Sheski [Shes00] and Herth [Hert05]. PDT for the treatment of early stage bronchial cancer and pre-neoplastic endobronchial lesions has been widely investigated. Clinical studies have shown that the response rate of PDT is highest for CIS and microinvasive SCC sized < 1 cm. 5-year survival rates in patients treated with PDT for early stage bronchial carcinoma or bronchial pre-neoplasia vary between 43% and 72% [Mazi04]. The most common photosensitizer used for bronchial PDT is Photofrin® [Monn90, Kato98], but clinical studies using m-THPC [Sava97] and mono-L aspartyl chlorin e6 [Kato03] have also been reported.

In a 3-year follow up study, Monnier *et al.* [Monn90] and Savary *et al.* [Sava97] reported a local recurrence rate after PDT for dysplasia and CIS inferior to 15%. However, the use of bronchoscopic therapies for the treatment of bronchial cancer demands accurate delineation and staging of the lesion, especially the determination of the lesion's infiltration into the bronchial mucosal layers and the exclusion of nodal extension [Sute01].

7.4 Angiogenesis

Carcinogenesis in the bronchial wall is associated with an increased growth of new blood vessels, called *angiogenesis*, as reported by Fisseler-Eckhoff *et al.* [F.-E96, F.-E98] and Fontanini *et al.* [Font99]. These groups investigated the *micro-vessel density* (MVD) in the tunica propria of normal, metaplastic, dysplastic and early cancerous human bronchial tissue. The morphometric findings reported by the two groups are summarized in Table 7.4. Both groups reported an increase in the MVD with increasing degrees of tissue degeneration. High grade dysplasia and

CIS were found to have a 3 to 4 times higher MVD than normal tissue. In samples with advanced dysplasia, increased angiogenesis was found in the vicinity of the basement membrane. In a more recent work, Keith *et al.* observed the presence of capillary blood vessels closely juxtaposed to and projecting into dysplastic squamous epithelium of bronchial biopsy specimens [Keit00]. The MVD in this so-called *angiogenic squamous dysplasia* (ASD) was increased in comparison with normal mucosa, but comparable to the MVD in other forms of dysplasia. Figure 7.7 illustrates the angiogenic squamous dysplasia and angiogenesis in bronchial neoplasia (adapted form [Keit00]). Shibuya *et al.* also reported an increase in MVD and the presence of ASD in bronchial pre-neoplasia and early cancerous lesions in a clinical in vivo study using a high magnification bronchoscope [Shib02, Shib03]. Shijubo *et al.* reviewed tumor angiogenesis of non-small cell lung cancer, showing recent evidence suggesting that angiogenesis is related to poor prognosis in many solid tumors [Shij03]. All aforementioned changes in the vascularization of pre-neoplastic tissue are associated with an increased blood (thus, haemoglobin) concentration in this type of tissue relative to normal tissue.

	Fisseler-Eckhoff *et al.* 0.4 mm below the basement membrane in the lamina propria		Fontanini *et al.* in the lamina propria (depth not specified)
Measured Value	**Microvessel Density** [mm^{-2}]	**Vessel Cross section** [10^{-4} mm^2]	**Microvessel Density** [mm^{-2}]
Healthy Bronchial Wall	33	9.04	12
Chronic Inflammation	55	14.4	-
Acute Inflammation	43	11.3	-
Hyperplasia	40	5.38	11 ± 5
Squamous cell Metaplasia	55	15.3	11 ± 5
Mild Dysplasia	83	2.95	13.5
Moderate Dysplasia	-	-	28 ± 20
Severe Dysplasia/ CIS	101	9.08	56 ± 14
Invasive SCC	105	7.61	77 ± 10

Table 7.4: *Morphometric data for vascularization of healthy and neoplastic bronchial mucosa, derived from Fisseler-Eckhoff [F.-E96, F.-E98] and Fontanini [Font99]. Though the absolute values for the vessel density in the subepithelial layers of the bronchial wall are different, both reports show an increase in the vessel density with increasing grade of pre-neoplasia and neoplasia.*

As already stated in Section 2.2.1.1, Gabrecht *et al.* recently showed that hemoglobin content in the tissue is likely to be responsible for the AF chromatic contrast [Gabr07a]. These observations were the rationale that allows us to observe the vascularization that lies "under" the early lesions with a dedicated high magnification bronchoscope. Preliminary results are shown in Chapter 11.

7.5 Autofluorescence bronchoscopy development

Conventional diagnostic procedures have a low sensitivity for intra-epithelial lesions. This may be attributed to several factors. First, the small size of these lesions (usually only a few mm in diameter, with an extension over only a few cell layers) [Lam00]. As a result, they cannot always be distinguished from surrounding healthy tissue by their form; in other words by their size and elevation. Second, differentiation based on color reflectance is very restricted or even impossible for early lesions. As a result, only approximately 30% of existing carcinomas *in situ* could previously be made visible [Kenn01].

Autofluorescence (AF) endoscopy was a great improvement in the detection and localization

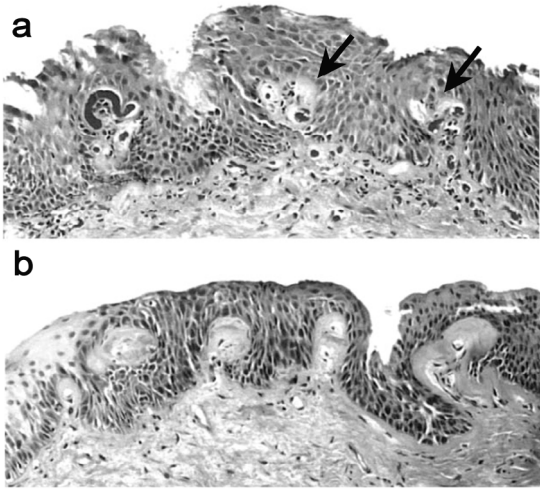

Figure 7.7: ***Photomicrographs of ASD****. a) capillary tufts (arrows) are projecting into the dysplastic squamous epithelium of the bronchial wall. The epithelium is thickened. b) Thickening of the basement membrane is frequently observed in ASD lesions.*

of intraepithelial lesions as compared to white light bronchoscopy [Horv99, vanR01, Gouj03]. By exciting bronchial tissue by exposing it to violet and blue light at a defined wavelength, autofluorescence light is induced in the endogenous fluorophores of the bronchial wall (see Section 2.2.1.1).

Several advantages of AF bronchoscopy vs. WL bronchoscopy were acknowledged over the last years : (i) bronchial carcinoma can be visualized and treated at a stage at which the chances of healing are still very good; (ii) margins of the tumor can be clearly demarcated; (iii) and the extent of a tumor is much easier to recognize than under white light allowing more accurate staging; (iv) in contrast to PDD (photodynamic diagnosis), no medication is required to produce the fluorescence. This avoids a number of potential problems such as the approvals for the medication (known as photosensitizers), the method of administering the medication and the dose, toxicity, bleaching of the tumor marker, etc. (iv) the change over between conventional white light and AF endoscopy is simple and fast by pressing a foot switch. No bronchoscope changes is required.

Autofluorescence bronchoscopy (AFB) was introduced by Stephen Lam's group, in Vancouver, and was first reported in the early 1990's [Hung91, Lam93]. Several endoscopic AF imaging systems have been developed and are commercially available [Wagn03]. Instruments from the following companies are currently on the market: the LIFE system by Novadaq (ancient Xillix Technologies, Vancouver, BC, Canada), the SAFE system by Pentax (Tokyo, Japan), the D-Light system by Karl Storz GmbH (Tuttlingen, Germany), the DAFE system by Richard Wolf GmbH (Knittlingen, Germany), and the Evis Lucera Spectrum by Olympus Inc. (Tokyo, Japan) (see Table 7.5).

Over the last years, several photodetection system have been developed at EPFL (in collaboration with Richard Wolf GmbH) in the framework of different PhD thesis (see Figure 7.8 [Wagn92, Zell00, Step02, Uehl05, Gabr06]). In 2002, the first generation of DAFE (Diagnostic AutoFluorescence Endoscopy) was commercialized by Wolf. Since then, the device has been updated with the addition of backscattered light (blue and red) following the prospective work of Gabrecht *et al.* [Gabr07b, Gabr08]. The color presentation (lesion vs. background) was adapted with the different system generations (red vs. green, red vs. pinkish, blue vs. gray).

Manufacturer	Excitation	Emission &Image presentation
Xillix I	Helium-Cadmium laser (442 nm) & separate WL source	2 spectral regions : 500–575 nm (green) and 615–630 nm (red). Lesions as reddish brown zones on a greenish background [Lam90, Lam93]
Xillix Oncolife	Xenon light source for WL & AF	[Stri08, Edel09]
SAFE-3000, Pentax	408 nm laser diode	One green spectral domain (490–590 nm). Tissue background (light green), lesions (dark green) with simultaneous display of WL and AF [Lee07]
D-Light, Storz	Xe lamp WL & AF exc. (380–460 nm)	3-CCD camera [Häuß05]
DAFE, Richard Wolf	Xe lamp WL & AF exc. (370–430 nm)	1-CCD camera with LP filter at 455nm. Red lesions over pinkish background [Gouj03, Gabr07c]
DAFE II, Richard Wolf	Xe lamp WL & AF exc. (370–430 nm)	1-CCD camera with LP filter at 455nm. Blue lesions over grayish background after intelligent Color Balance[7].
Evis Lucera Spectrum, Olympus	Xe lamp WL & AF exc. (395–475 nm)	AF 490–625 nm, reflected light (550,610 nm). Normal mucosa (light green), tumor (pinkish), vessel (dark green) [Chiy05, Ueno07]

Table 7.5: *Development of the fluorescence detection setup over the last years.*

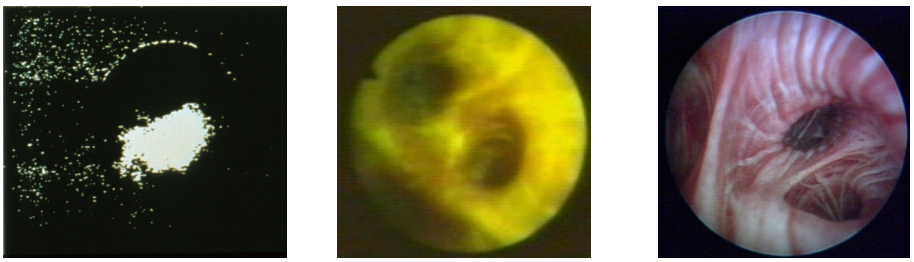

Figure 7.8: *Different generations of the endoscopic fluorescence imaging system developed at EPFL: Berta (1992), Anna (1998-99), DAFE I (2002)*

Bibliography

[Agud00] A. Agudo, W. Ahrens, E. Benhamou, S. Benhamou, P. Boffetta, S. Darby, F. Forastiere, C. Fortes, V. Gaborieau, C. Gonzalez, K.-H. Jockel, M. Kreuzer, F. Merletti, H. Pohlabeln, L. Richiardi, E. Whitley, H.-E. Wichmann, P. Zambon, and L. Simonato. Lung cancer and cigarette smoking in women: A multicenter case-control study in europe. *International Journal of Cancer*, 88(5):820–827, 2000.

[Albe03] A. J. Alberg and J. M. Samet. Epidemiology of lung cancer. *Chest*, 123(1 Suppl):21S–49S, Jan 2003.

[Albe07] A. J. Alberg, J. G. Ford, J. M. Samet, and A. C. of Chest Physicians. Epidemiology of lung cancer: Accp evidence-based clinical practice guidelines (2nd edition). *Chest*, 132(3 Suppl):29S–55S, Sep 2007.

[Anta95] T. Antakli, R. Schaefer, J. Rutherford, and R. Read. Second primary lung cancer. *Ann Thorac Surg*, 59:863–867, 1995.

[Asap00] J. Asaph, J. Keppel, J. Handy, E. Douville, A. Tsen, and G. Ott. Surgery for second lung cancers. *Chest*, 118:1621–1625, 2000.

[Auer91] O. Auerbach and L. Garfinkel. The changing pattern of lung carcinoma. *Cancer*, 68(1):1973–1977, 1991.

[Bajt09] A. Bajtarevic, C. Ager, M. Pienz, M. Klieber, K. Schwarz, M. Ligor, T. Ligor, W. Filipiak, H. Denz, M. Fiegl, W. Hilbe, W. Weiss, P. Lukas, H. Jamnig, M. Hackl, A. Haidenberger, B. Buszewski, W. Miekisch, J. Schubert, and A. Amann. Noninvasive detection of lung cancer by analysis of exhaled breath. *BMC Cancer*, 9:348, 2009.

[Batt95] J. F. Battey, P. H. Brown, E. R. Gritz, W. K. Hong, B. E. Johnson, D. D. Karp, J. L. Mulshine, G. L. Shaw, D. R. Shopland, M. E. Sunday, and E. Szabo. Primary and secondary prevention of lung cancer: an international association for the study of lung cancer workshop. *Lung Cancer*, 12(1-2):91–103, 1995.

[Baum01] M. Baumann, S. Appold, C. Petersen, D. Zips, and T. Herrmann. Dose and fractionation concepts in the primary radiotherapy of non-small cell lung cancer. *Lung Cancer*, 33(Supplement 1):S35–S45, 2001.

[Bepl03] G. Bepler, B. Djulbegovic, R. Clark, and M. Tockman. A systemic review and lessons learned from early lung cancer detection trial using low-dose computed tomography of the chest. *Cancer Control*, 10(4):306–324, 2003.

[Bota01] S. Bota, A. J-B., C. Paris, J. Métayer, R. Sesboüé, G. Nouvet, and L. Thiberville. Follow-up of bronochial precancerous lesions and carcinoma in situ using fluorescence endoscopy. *Am J Respir Crit Care Med*, 164:1688–1693, 2001.

[Bram01] E. Brambilla, W. D. Travis, T. V. Colby, B. Corrin, and Y. Shimosato. The new world health organization classification of lung tumours. *Eur Respir J*, 18(6):1059–68, 2001.

[C.-D10] C. Clément-Duchêne, J.-M. Vignaud, A. Stoufflet, O. Bertrand, A. Gislard, L. Thiberville, G. Grosdidier, Y. Martinet, J. Benichou, P. Hainaut, and C. Paris. Characteristics of never smoker lung cancer including environmental and occupational risk factors. *Lung Cancer*, 67(2):144–150, Feb 2010.

[Chha05] P. Chhajed, K. Shibuya, H. Hoshino, M. Chiyo, K. Yasufuku, K. Hiroshima, and T. Fujisawa. A comparison of video and autofluorescence bronchoscopy in patients at high risk of lung cancer. *European Respiratory Journal*, 25(6):951–955, 2005.

[Chiy05] M. Chiyo, K. Shibuya, H. Hoshino, K. Yasufuku, Y. Sekine, T. Iizasa, T. Fujisawa, and K. Hiroshima. Effective detection of bronchial preinvasive lesions by a new autofluorescence imaging bronchovideoscope system. *Lung Cancer*, 48(3):307–313, 2005.

[Cros01] C. Crosta, L. Spaggiari, A. D. Stefano, G. Fiori, D. Ravizza, and U. Pastorino. Endoscopic argon plasma coagulation for palliative treatment of malignant airway obstructions: early results in 47 cases. *Lung Cancer*, 33(1):75–80, 2001.

[Dele97] F.-B. Deleyiannis and D. Thomas. Risk of lung cancer among patients with head and neck cancer. *Otolaryngology - Head and Neck Surgery*, 116(6):630–636, 1997.

[Depp04] K.-M. Deppermann. Lung cancer screening - where we are in 2004 (take home messages). *Lung Cancer*, 2004.

[Deyg01] N. Deygas, M. Froudarakis, G. Ozenne, and J. M. Vergnon. Cryotherapy in early superficial bronchogenic carcinoma. *Chest*, 120(1):26–31, 2001.

[Dien01] H. Dienemann. Principles of surgical treatment in localized non-small cell lung cancer. *Lung Cancer*, 33(Supplement 1):S3–S8, 2001.

[Dodd01] C. Doddoli, P. Thomas, O. Ghez, R. Guidicelli, and P. Fuentes. Surgical management of metachronous bronchial carcinoma. *European Journal of Cardio-thoracic Surgery*, 19:899–903, 2001.

[Dris05] T. Driscoll, D. Nelson, M. Fingerhut, A. Prüss-Ustun, K. Steenland, J. Leigh, and M. Concha-Barrientos. The global burden of disease due to occupational carcinogens. *American Journal of Industrial Medicine*, 48(6):419–431, 2005.

[Edel09] E. Edell, S. Lam, H. Pass, Y. E. Miller, T. Sutedja, T. Kennedy, G. Loewen, R. L. Keith, and A. Gazdar. Detection and localization of intraepithelial neoplasia and invasive carcinoma using fluorescence-reflectance bronchoscopy: an international, multicenter clinical trial. *J Thorac Oncol*, 4(1):49–54, Jan 2009.

[Enge96] A. Engeland, T. Haldorsen, A. Andersen, and S. Tretli. The impact of smoking habits on lung cancer risk: 28 years' observation of 26,000 norwegian men and women. *Cancer Causes and Control*, 7(3):366–376, 1996.

[F.-E96] A. Fisseler-Eckhoff, D. Rothstein, and K. Müller. Neovascularization in hyperplastic, metaplastic and potentially preneoplastic lesions of the bronchial mucosa. *Virchows Arch*, 429(2-3):95–100, 1996.

[F.-E98] A. Fisseler-Eckhoff. *Stromareaktionen in bronchialen Präneoplasien und Lungentumoren.* Springer-Verlag GmbH, 1 edition, 1998.

[Ferl10] J. Ferlay, H. Shin, F. Bray, D. Forman, C. Mathers, and D. Parkin. Cancer incidence and mortality worldwide: Iarc cancerbase, 2010.

[Font99] G. Fontanini, A. Calcinai, L. Boldrini, M. Lucchi, M. Mussi, C. Angeletti, C. Cagno, M. Tognetti, and F. Basolo. Modulation of neoangiogenesis in bronchial preneoplastic lesions. *Oncol Rep*, 6(4):813–817, 1999.

[Fran99] S. Franceschi and E. Bidoli. The epidemiology of lung cancer. *Annals of Oncology*, 10(0):3–6, 1999.

[Gabr06] T. Gabrecht. *Clinical fluorescence spectroscopy and imaging for the detection of early carcinoma by autofluorescence bronchoscopy and the study of the protoporphyrin IX pharmacokinetics in the endometrium.* PhD thesis, EPFL No 3537, 2006.

[Gabr07a] T. Gabrecht, S. Andrejevic-Blant, and G. Wagnières. Blue-violet excited autofluorescence spectroscopy and imaging of normal and cancerous human bronchial tissue after formalin fixation. *Photochem Photobiol*, 83(2):450–458, 2007.

[Gabr07b] T. Gabrecht, T. Glanzmann, L. Freitag, B.-C. Weber, H. van den Bergh, and G. Wagnières. Optimized autofluorescence bronchoscopy using additional backscattered red light. *J Biomed Opt*, 12(6):064016, 2007.

[Gabr07c] T. Gabrecht, A. Radu, M. Zellweger, B. Lovisa, D. Goujon, P. Grosjean, H. van den Bergh, P. Monnier, and G. Wagnières. Autofluorescence bronchoscopy: Clinical experience with an optimized system in head and neck cancer patients. *Medical Laser Application*, 22:185–192, 2007.

[Gabr08] T. Gabrecht, A. Radu, P. Grosjean, B. Weber, G. Reichle, L. Freitag, P. Monnier, H. van den Bergh, and G. Wagnières. Improvement of the specificity of cancer detection by autofluorescence imaging in the tracheo-bronchial tree using backscattered violet light. *Photodiagnosis Photodyn Ther*, 5(1):2–9, Mar 2008.

[Gazd97] A. Gazdar and J. Minna. Cigarettes, sex, and lung adenocarcinoma. *Journal of the National Cancer Institute*, 89(21):1563–1565, 1997.

[Gouj03] D. Goujon, M. Zellweger, A. Radu, P. Grosjean, B.-C. Weber, H. van den Bergh, P. Monnier, and G. Wagnières. In vivo autofluorescence imaging of early cancers in the human tracheobronchial tree with a spectrally optimized system. *J Biomed Opt*, 8(1):17–25, Jan 2003.

[Hawk99] E. Hawk, G. Kelloff, A. F. Gazdar, S. Lam, J. C. LeRiche, Y. Zheng, A. Coldman, and C. MacAulay. Sex-related differences in bronchial epithelial changes associated with tobacco smoking. *Journal of the National Cancer Institute*, 91(8):691–696, 1999.

[Hens99] C. I. Henschke, D. I. McCauley, D. F. Yankelevitz, D. P. Naidich, G. McGuinness, O. S. Miettinen, D. M. Libby, M. W. Pasmantier, J. Koizumi, N. K. Altorki, and J. P. Smith. Early lung cancer action project: overall design and findings from baseline screening. *The Lancet*, 354(9173):99–105, 1999.

[Hens03] C. Henschke, J. Wisnivesky, D. Yankelevitz, and O. Miettinen. Small stage i cancers of the lung: genuineness and curability. *Lung Cancer*, 39:327–330, 2003.

[Hert05] F. J. F. Herth and L. Freitag. Interventionelle therapie. *Der Onkologe*, 11(7):759–767, 2005.

[Horv99] T. Horvath, M. Horvathova, F. Salajka, B. Habanec, L. Foretova, J. Kana, H. Koukalova, P. Pafko, F. Wurst, E. Novotna, J. Pecina, V. Vagunda, R. Vrbacky, R. Talac, H. Coupkova, and Z. Pacovsky. Detection of bronchial neoplasia in uranium miners by autofluorescence endoscopy (safe-1000). *Diagnostic and Therapeutic Endoscopy*, 5(2):91–98, 1999.

[Häuß05] K. Häußinger, F. Stanzel, M. Kohlhäufl, H. Becker, F. Herth, A. Kreuzer, B. Schmidt, J. Strausz, S. Cavaliere, K.-M. Müller, R.-M. Huber, U. Pichlmeier, and C. Bolliger. Autofluorescence bronchoscopy with white light bronchoscopy compared with white light bronchoscopy alone for the detection of precancerous lesions: A european randomised controlled multicentre trial. *Thorax*, 60(6):496–503, 2005.

[Hung91] J. Hung, S. Lam, J. C. LeRiche, and B. Palcic. Autofluorescence of normal and malignant bronchial tissue. *Lasers Surg Med*, 11(2):99–105, 1991.

[Jema09] A. Jemal, R. Siegel, E. Ward, Y. Hao, J. Xu, and M. J. Thun. Cancer statistics, 2009. *CA Cancer J Clin*, 59(4):225–249, 2009.

[John98] B. E. Johnson. Second lung cancers in patients after treatment for an initial lung cancer. *Journal of the National Cancer Institute*, 90(18):1335–1445, 1998.

[Jone95] A. S. Jones, P. Morar, D. E. Phillips, J. K. Field, D. Husband, and T. R. Helliwell. Second primary tumors in patients with head and neck squamous cell carcinoma. *Cancer*, 75(6):1343–1353, 1995.

[Kato98] H. Kato. Photodynamic therapy for lung cancer - a review of 19 years' experience. *Journal of Photochemistry and Photobiology B: Biology*, 42(2):96–99, 1998.

[Kato03] H. Kato, K. Furukawa, M. Sato, T. Okunaka, Y. Kusunoki, M. Kawahara, M. Fukuoka, T. Miyazawa, T. Yana, K. Matsui, T. Shiraishi, and H. Horinouchi. Phase ii clinical study of photodynamic therapy using mono-l-aspartyl chlorin e6 and diode laser for early superficial squamous cell carcinoma of the lung. *Lung Cancer*, 42(1):103–11, 2003.

[Keit00] R. Keith, Y. Miller, R. Gemmill, H. Drabkin, E. Dempsey, T. Kennesy, S. Prindiville, and W. Franklin. Angiogenic squamous dysplasia in bronchi of individuals at high risk for lung cancer. *Clinical Cancer Research*, 6(5):1616–1625, 2000.

[Kenn00] T. Kennedy, Y. Miller, and S. Prindiville. Screening for lung cancer revisited and the role of sputum cytology and fluorescence bronchoscopy in a high-risk group. *Chest*, 117(Suppl.):72S–79S, 2000.

[Kenn01] T. Kennedy, S. Lam, and F. Hirsch. Review of recent advances in fluorescence bronchoscopy in early localization of central airway lung cancer. *Oncologist*, 6(3):257–262, 2001.

[Khud01] S. A. Khuder. Effect of cigarette smoking on major histological types of lung cancer: a meta-analysis. *Lung Cancer*, 31(2-3):139–148, 2001.

[Lam90] S. Lam, B. Palcic, D. McLean, J. Hung, M. Korbelik, and A. E. Profio. Detection of early lung cancer using low dose photofrin ii. *Chest*, 97(2):333–7, 1990.

[Lam93] S. Lam, C. MacAulay, J. Hung, J. LeRiche, A. E. Profio, and B. Palcic. Detection of dysplasia and carcinoma in situ with a lung imaging fluorescence endoscope device. *Journal of Thoracic and Cardiovascular Surgery*, 105(6):1035–1040, 1993.

[Lam98] S. Lam, T. Kennedy, and M. Unger. Localization of bronchial intraepitheloial neoplastic lesions by fluorescence bronchoscopy. *Chest*, 113(3):696–702, 1998.

[Lam00] S. Lam, C. MacAulay, J. C. leRiche, and B. Palcic. Detection and localization of early lung cancer by fluorescence bronchoscopy. *Cancer Suppl.*, 89(11):2468–2473, 2000.

[Lee07] P. Lee, H. A. P. Brokx, P. E. Postmus, and T. G. Sutedja. Dual digital video-autofluorescence imaging for detection of pre-neoplastic lesions. *Lung Cancer*, 58(1):44–49, Oct 2007.

[León99] X. León, M. Quer, S. Diez, C. Orús, J. Burgués, and A. López-Pousa. Second neoplasm in patients with head and neck cancer. *Head and Neck*, 21(3):204–210, 1999.

[Levi99] F. Levi, L. Randimbison, V. C. Te, and C. La Vecchia. Second primary cancers in patients with lung carcinoma. *Cancer*, 86(1):186–190, 1999.

[Levi04] F. Levi, F. Lucchini, C. La Vecchia, E. Negri, and F. Levi. Trends in mortality from major cancers in the european union, including acceding countries, in 2004. *Cancer*, 101(1):2843–2850, 2004.

[Mach95] H. N. Macha, B. Wahlers, C. Reichle, and D. Von Zwehl. Endobronchial radiation therapy for obstructing malignancies: Ten years' experience with iridium-192 high-dose radiation brachytherapy afterloading technique in 365 patients. *Lung*, 173(5):271–280, 1995.

[Mack06] J. Mackay, M. Eriksen, and S. O. *The tobacco atlas.* American Cancer Society, 2nd ed edition, 2006.

[Mart95] N. Martini, M. S. Bains, M. E. Burt, M. F. Zakowski, P. McCormack, V. W. Rusch, R. J. Ginsberg, L. P. Faber, J. R. Benfield, and D. L. Morton. Incidence of local recurrence and second primary tumors in resected stage i lung cancer. *Journal of Thoracic and Cardiovascular Surgery*, 109(1):120–129, 1995.

[Mazi04] D. Maziak, B. Markman, J. MacKay, and W. Evans. Photodynamic therapy in nonsmall cell lung cancer: a systematic review [in process citation]. *Ann Thorac Surg*, 77(4):1484–91, 2004.

[McWi03] A. McWilliams, J. Mayo, S. MacDonald, J. leRiche, B. Palcic, E. Szabo, and S. Lam. Lung cancer screening. *Am J Respir Crit Care Med*, 168:1167–1173, 2003.

[Monn90] P. Monnier, M. Savary, C. Fontolliet, G. A. Wagnieres Chatelain, P. Cornaz, C. Depeursinge, and H. Van den Bergh. Photodetection and photodynamic therapy of 'early' squamous cell carcinomas of the pharynx, oesophagus and tracheo-bronchial tree. *Lasers in Medical Science*, 5(2):149–168, 1990.

[Moun97] C. Mountain. Revisions in the international system for staging lung cancer. *Chest*, 111(6):1710–1717, 1997.

[Moun00] C. F. Mountain. The international system for staging lung cancer. *Semin Surg Oncol*, 18(2):106–15, 2000.

[Nag01] S. Nag, J. F. Kelly, J. L. Horton, R. Komaki, and D. Nori. Brachytherapy for carcinoma of the lung. *ONCOLOGY*, 15(3):371–381, 2001.

[Nich01] A. Nicholson, L. Perry, P. Cury, P. Jackson, C. McCormick, B. Corrin, and A. Wells. Reproducibility of the who/iaslc grading system for pre-invasive squamous lesions of the bronchus: A study of inter-observer and intra-observer variation. *Histopathology*, pages 202–208, 2001.

[Pari03a] C. Paris, J. Benichou, S. Bota, S. Sagnier, J. Metayer, S. Eloy, J. B. Auliac, G. Nouvet, and L. Thiberville. Occupational and nonoccupational factors associated with high grade bronchial pre-invasive lesions. *Eur Respir J*, 21(2):332–341, Feb 2003.

[Pari03b] C. Paris, F. Saunier, J. Benichou, J. Metayer, P. Brochard, L. Thiberville, and G. Nouvet. Smoking status, occupational asbestos exposure and bronchial location of lung cancer. *Lung Cancer*, 40(1):17–24, 2003.

[Pari10] C. Paris, C. Clement-Duchene, J. M. Vignaud, A. Gislard, A. Stoufflet, O. Bertrand, L. Thiberville, G. Grosdidier, Y. Martinet, J. Benichou, and P. Hainaut. Relationships between lung adenocarcinoma and gender, age, smoking and occupational risk factors: A case-case study. *Lung Cancer*, 68(2):146–153, May 2010.

[Past03] U. Pastorino, M. Bellomi, C. Landoni, E. De Fiori, P. Arnaldi, M. Picchio, G. Pelosi, P. Boyle, and F. Fazio. Early lung-cancer detection with spiral ct and positron emission tomography in heavy smokers: 2-year results. *The Lancet*, 362(9384):593–597, 2003.

[Peng09] G. Peng, U. Tisch, O. Adams, M. Hakim, N. Shehada, Y. Y. Broza, S. Billan, R. Abdah-Bortnyak, A. Kuten, and H. Haick. Diagnosing lung cancer in exhaled breath using gold nanoparticles. *Nat Nanotechnol*, 4(10):669–673, Oct 2009.

[Phil99] M. Phillips, K. Gleeson, J. M. Hughes, J. Greenberg, R. N. Cataneo, L. Baker, and W. P. McVay. Volatile organic compounds in breath as markers of lung cancer: a cross-sectional study. *Lancet*, 353(9168):1930–1933, Jun 1999.

[PORT98] PORT Meta-analysis Trialists Group. Postoperative radiotherapy in non-small-cell lung cancer: systematic review and meta-analysis of individual patient data from nine randomised controlled trials. *The Lancet*, 352(9124):257–263, 1998.

[Port02] J. Port, M. Kent, and N. Altorki. Early lung cancer detection and treatment strategies. *Surg Oncol*, 11(4):191–9, 2002.

[Sasc04] A. J. Sasco, M. B. Secretan, and K. Straif. Tobacco smoking and cancer: a brief review of recent epidemiological evidence. *Lung Cancer*, 45 Suppl 2:S3–S9, Aug 2004.

[Sava97] J. F. Savary, P. Monnier, C. Fontolliet, J. Mizeret, G. Wagnières, D. Braichotte, and H. van den Bergh. Photodynamic therapy for early squamous cell carcinomas of the esophagus, bronchi, and mouth with m-tetra (hydroxyphenyl) chlorin. *Archives of Otolaryngology - Head and Neck Surgery*, 123(2):162–168, Feb 1997.

[Schu94] V. Schulz, D. Zeidler, J. Adolph, and K. Zum Winkel. *Bronchopulmonare Tumoren.* Georg Thieme Verlag, Stuttgart, 1 edition, 1994.

[Shes00] F. Sheski and P. Mathur. Endoscopic treatment of early stage lung cancer. *Cancer Control*, 7(1), 2000.

[Shib02] K. Shibuya, H. Hoshino, M. Chiyo, K. Yasufuku, T. Iizasa, Y. Saitoh, M. Baba, K. Hiroshima, H. Ohwada, and T. Fujisawa. Subepithelial vascular patterns in bronchial dysplasias using a high magnification bronchovideoscope. *Thorax*, 57(10):902–7, 2002.

[Shib03] K. Shibuya, H. Hoshino, M. Chiyo, A. Iyoda, S. Yoshida, Y. Sekine, T. Iizasa, Y. Saitoh, M. Baba, K. Hiroshima, H. Ohwada, and T. Fujisawa. High magnification bronchovideoscopy combined with narrow band imaging could detect capillary looops of angiogenic squamous dysplasia in heavy smokers at high risk for lung cancer. *Thorax*, 58(11):989–995, 2003.

[Shij03] N. Shijubo, H. Kojima, M. Nagata, T. Ohchi, A. Suzuki, S. Abe, and N. Sato. Tumor angiogenesis of non-small cell lung cancer. *Microsc Res Tech*, 60(2):186–198, Feb 2003.

[Simo01] L. Simonato, A. Agudo, W. Ahrens, E. Benhamou, S. Benhamou, P. Boffetta, P. Brennan, S. C. Darby, F. Forastiere, C. Fortes, V. Gaborieau, M. Gerken, C. A. Gonzales, K. H. Jöckel, M. Kreuzer, F. Merletti, F. Nyberg, G. Pershagen, H. Pohlabeln, F. Rösch, E. Whitley, H. E. Wichmann, and P. Zambon. Lung cancer and cigarette smoking in europe: an update of risk estimates and an assessment of inter-country heterogeneity. *Int J Cancer*, 91(6):876–887, Mar 2001.

[Souh98] R. Souhami and J. Tobias. *Cancer and its management*. Blackwell Science Ltd., Oxford, 3 edition, 1998.

[Stee96] K. Steenland, D. Loomis, C. Shy, and N. Simonsen. Review of occupational lung carcinogens. *American Journal of Industrial Medicine*, 29(5):474–490, 1996.

[Step02] T. Stepinac. *Caractérisation de tissus biologiques in vivo par imagerie de l'intensité ou du temps de vie de luminescence*. PhD thesis, EPFL no 2645, 2002.

[Stew00] L. Stewart. Chemotherapy for non-small cell lung cancer. non-small cell lung cancer collaborative group. *Cochrane Database Syst Rev*, 1(2):CD002139, 2000.

[Stoe01] S. J. Stoeckli, R. Zimmermann, and S. Schmid. Role of routine panendoscopy in cancer of the upper aerodiaestive tract. *Otolaryngology - Head and Neck Surgery*, 124(2):208–212, 2001.

[Stri08] M. R. Stringer, K. Moghissi, and K. Dixon. Autofluorescence bronchoscopy in volunteer asymptomatic smokers. *Photodiagnosis Photodyn Ther*, 5(2):148–152, Jun 2008.

[Sute01] G. Sutedja and P. Postmus. The role of photodynamic therapy in the management of stage I/II NSCLC. *Lung Cancer*, 34 Suppl 3:S35–8, 2001.

[Thun97] M. Thun, C. Lally, E. Calle, C. Heath Jr., J. Flannery, W. Flanders, and M. Thun. Cigarette smoking and changes in the histopathology of lung cancer. *Journal of the National Cancer Institute*, 89(21):1580–1586, 1997.

[Thun02] M. J. Thun, S. J. Henley, and E. E. Calle. Tobacco use and cancer: an epidemiologic perspective for geneticists. *Oncogene*, 21(48):7307–7325, Oct 2002.

[Thun03] F. B. J. M. Thunnissen. Sputum examination for early detection of lung cancer. *J Clin Pathol*, 56(11):805–810, 2003.

[Toyo07] S. Toyooka, K. Matsuo, H. Shigematsu, T. Kosaka, M. Tokumo, Y. Yatabe, S. Ichihara, M. Inukai, H. Suehisa, J. Soh, K. Kiura, K. M. Fong, H. Lee, I. I. Wistuba, A. F. Gazdar, T. Mitsudomi, and H. Date. The impact of sex and smoking status on the mutational spectrum of epidermal growth factor receptor gene in non small cell lung cancer. *Clin Cancer Res*, 13(19):5763–5768, Oct 2007.

[Trav99] W. Travis, T. V. Colby, B. Corrin, Y. Shimosato, E. Brambilla, L. In collaboration with Sobin, and P. from 14 Countries. *World Healthy Organization international histological classification of tumours. Histological typing of lung and pleural tumours*. Springer Verlag, 3rd edition, 1999.

[Tycz03] J. Tyczynski, F. Bray, and D. Parkin. Lung cancer in europe in 2000: epidemiology, prevention, and early detection. *Lancet Oncology*, 4(1):45–55, 2003.

[Uehl05] P. Uehlinger. *Optimalisation de la photothérapie dynamique et de la photodétection de cancers précoces par spectroscopie résolue en temps de luminophores endogènes et exogènes*. PhD thesis, EPFL No 3149, 2005.

[Ueno07] K. Ueno, Y. Kusunoki, F. Imamura, M. Yoshimura, S. Yamamoto, J. Uchida, and Y. Tsukamoto. Clinical experience with autofluorescence imaging system in patients with lung cancers and precancerous lesions. *Respiration*, 74(3):304–308, 2007.

[vanB01] A. van Boxem, J. Westerga, B. Venmans, P. Postmus, and G. Sutedja. Photodynamic therapy, nd-yag laser and electrocautery for treating early-stage intraluminal cancer: which to choose? *Lung Cancer*, 31(1):31–6, 2001.

[vanR01] M. van Rens, F. Schramel, J. Elbers, and J.-W. Lammers. The clinical value of lung imaging fluorescence endoscopy for detecting synchronous lung cancer. *Lung Cancer*, 32:13–18, 2001.

[vanZ02] N. van Zandwijk. New methods for early diagnosis of lung cancer. *Lung Cancer*, 38:S9–S11, 2002.

[Venm00] B. J. Venmans, T. J. van Boxem, E. F. Smit, P. E. Postmus, and T. G. Sutedja. Outcome of bronchial carcinoma in situ. *Chest*, 117(6):1572–6, 2000.

[Venm01] B. Venmans, T. Van Boxem, E. Smit, P. Postmus, and T. Sutedja. Bronchial intraepithelial neoplastic lesions in head and neck cancer patients: Results of autofluorescence bronchoscopy. *Annals of Otology, Rhinology and Laryngology*, 110(7 I):635–638, 2001.

[Wagn92] G. A. Wagnières. *Photochimiothérapie et photodétection du cancer à l'aide de photosensibilisateurs ou de colorants fluorescents.* PhD thesis, EPFL no 1024, 1992.

[Wagn03] G. Wagnières, A. McWilliams, and S. Lam. *Handbook of Biomedical Fluorescence.* CRC Press, 2003.

[Wake07] H. A. Wakelee, E. T. Chang, S. L. Gomez, T. H. Keegan, D. Feskanich, C. A. Clarke, L. Holmberg, L. C. Yong, L. N. Kolonel, M. K. Gould, and D. W. West. Lung cancer incidence in never smokers. *J Clin Oncol*, 25(5):472–478, Feb 2007.

[Worl81] World Health Organization, editor. *Histological Typing of Lung Tumours.* World Health Organization., 2nd edition edition, 1981.

[Yeh80] H. C. Yeh and G. M. Schum. Models of human lung airways and their application to inhaled particle deposition. *Bull Math Biol*, 42(3):461–80, 1980.

[Youl08] D. R. Youlden, S. M. Cramb, and P. D. Baade. The international epidemiology of lung cancer: geographical distribution and secular trends. *J Thorac Oncol*, 3(8):819–831, Aug 2008.

[Zell00] M. Zellweger, A. Radu, P. Monnier, H. van den Bergh, and G. Wagnières. Fluorescence pharmacokinetics of lutetium texaphyrin (pci-0123, lu-tex) in the skin and in healthy and tumoral hamster cheek-pouch mucosa. *J Photochem Photobiol B*, 55(1):56–62, Mar 2000.

[Zimm03] F. B. Zimmermann, M. Bamberg, M. Molls, and B. Jeremic. Radiation therapy alone in early stage non-small cell lung cancer. *Semin Surg Oncol*, 21(2):91–7, 2003.

Chapter 8

Narrow-band excitation in the bronchi

As already mentioned in Chapter 7, all commercially available AFB systems show high sensitivity, but only limited specificity for the detection of early cancerous and precancerous lesions in the bronchi.

A fundamental understanding of the origins of the mechanisms underlying the AF contrast is essential for a better differentiation between true and false positive results. It has been described elsewhere (Section 2.2.1.1) that the autofluorescence (AF) contrast between (pre-)neoplastic lesions and healthy tissues in the bronchi results from (i) an overall decrease in AF intensity ("intensity contrast") and (ii) a stronger decrease in the green (450–600 nm) relative to the red (600–800 nm) ("spectral contrast"), i.e. a distortion of the AF spectral shape. The purpose of the present chapter was to investigate the influence of the excitation *bandwidth* on the healthy-to-lesion AF contrasts in AFB.

In a spectrofluorometric study, Zellweger *et al.* demonstrated *in vivo* that the excitation wavelengths producing the highest healthy-to-lesion contrasts (intensity and spectral) are between 400 nm and 430 nm with a peak around 405 nm [Zell01]. The authors concluded that this wavelength range would be optimal to discriminate between healthy tissue and (pre-)neoplastic lesions. Since it corresponds to the absorption peak of hemoglobin, it is very likely that light absorption due to tissue hemoglobin is playing a major role in the build-up of AF contrasts. This is in good agreement with Bard *et al.* , who showed that bronchial tumors are characterized by a lower blood oxygen saturation and a higher blood content than normal mucosa. No differences were observed between normal and metaplastic/mild dysplastic mucosa [Bard05]. Since blue-violet light at wavelength around 405 nm does not penetrate deeply in bronchial tissue, these results also suggest that the contrast mechanisms are located in the superficial layers of the bronchial walls. This is confirmed by the data of Qu *et al.* , who showed that the main contribution of bronchial AF arises from the upper part of the sup-epithelial layer while no significant AF is observed form the superficial epithelium [Qu94, Qu95].

Nevertheless, we should stress at this point the influence of the measurement geometry. Indeed, point measurement is more sensitive to chromophores and absorbers present in the vicinity of the mucosa, whereas imaging covers a larger surface, and collects information from deeper layers. Thus, fiber-based measurements are very sensitive to epithelium thickening – from

about 40μm in normal tissue up to more than 100μm in CIS [Qu94, Häuß99]–, and displays often an intensity contrast between pre-cancerous lesions and healthy tissue [Qu94]. Autofluorescence imaging has been shown to be less sensitive to surface modification. Conversely, the fluorescence signal originating in the submucosa can be better collected with AFB, since epithelium in itself is not fluorescing (i.e. being almost transparent). Therefore, the chromatic contrast (green AF is much more lowered than red AF) has been almost exclusively demonstrated with imaging studies.

Gabrecht *et al.* reported previously on the addition of blue and red backscattered light to enhance the contrast [Gabr07, Gabr08]. In this chapter, we are comparing the contrast obtained with a narrow-band excitation around 410 nm from a laser light source (*superficial* excitation, $< 100\mu$m) and a broadband excitation around 430 nm (*deep* excitation, 100–300μm) from a filtered lamp.

Some optical tricks were investigated to achieve an homogenous illumination at the distal end of the endoscope, necessary for good endoscopic image quality. Problems occurred at the interface between the laser extension fiber and the liquid light guide that conveys light to the endoscope. Indeed, the fiber has a numerical aperture (NA) of 0.4 and a diameter of 400 μm and the guide had a NA of 0.53 and a diameter of 4 mm. We designed a coupler having a SMA plug on one side and custom made plug for the light guide on the other side, as shown in Figure 8.1. The part containing the SMA plug could be rotated in the x-y plane around a central axis in order to change the injection angle between the extension fiber and the light guide. Perpendicular injection resulted in a "forward peaked" light output (i.e. inhomogeneous illumination of the endoscopic site). A slight rotation of the SMA connector results in a bell-shaped light distribution which fits the angular distribution of the illumination with the broadband light source [Gabr06].

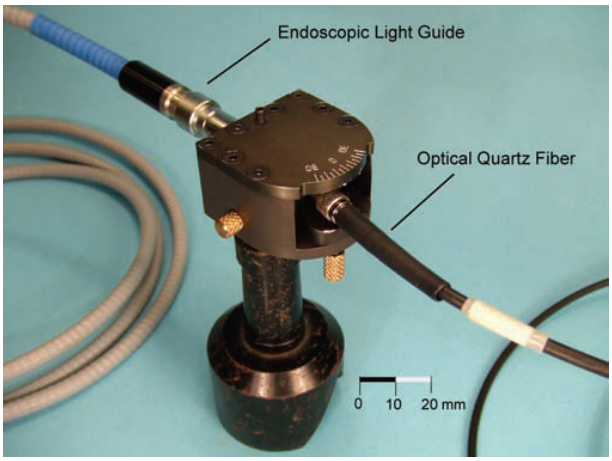

Figure 8.1: ***The custom-made light guide coupler.*** *The optical quartz fibre and the endoscopic light guide are plugged at opposite sites. The coupling angle can be adjusted by the screws at either side of the unit.*

In the article reproduced hereinafter [Lovi07], only the green channels of the relevant images were reproduced, because they contain the contrast information. Indeed, some red backscattered light was collected in the red color channel, so that the pure AF contrast could not be observed in this channel. Figure 8.2 displays the white light reflectance image, and both AF images, excited with DAFE and Kr^+, respectively.

A biopsy was taken on each suspicious site, and the analysis revealed the following histopathological status:

A 60-year old female patient. CIS located in the inferior bronchus. The lesion is clearly visible at the "11 o'clock" position on the cardiac wall of the bronchus. The intensity decrease on the lesion relative to the healthy surrounding is clearly enhanced with the narrow band Kr+ excitation.

B 59-year old patient. High grade squamous dysplasia on the division of the middle lobe. The spur exhibits strong red fluorescence in DAFE. The grayscale images reveal a strong intensity decrease of the green AF on the lesion.

C 70-year old patient. CIS in the left lower bronchus. Hardly suspect with WLB, the spur exhibited a dark red fluorescence with both DAFE and Kr+ excitation.

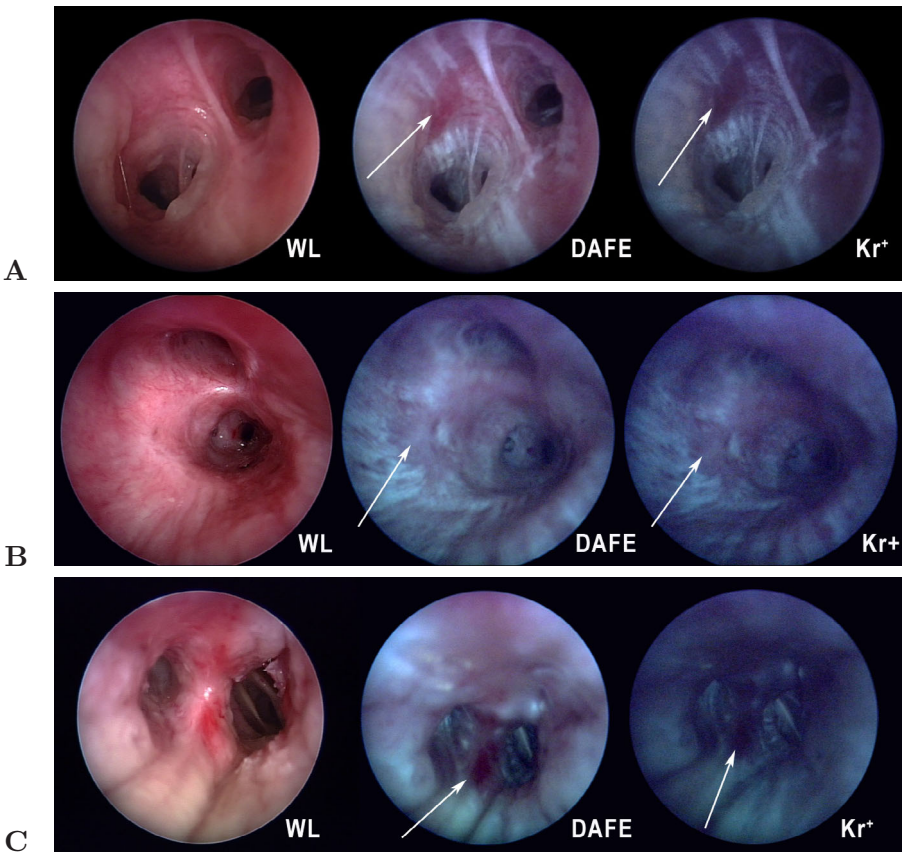

Figure 8.2: *White light, autofluorescence (DAFE) and Krypton (Kr^+) images from three patients.*
A *CIS located in the inferior bronchus.*
B *High grade squamous dysplasia on the division of the middle lobe.*
C *CIS in the left lower bronchus.*

In this study, we can conclude that narrow-band excitation improves the intensity contrast. Indeed, for each site, the healthy/tumor ratio in the green channel (G_h/G_t) for the narrowband excitation exceeds G_h/G_t for the broadband excitation, with a mean ratio equal to 1.43±0.20. As described in previous studies [Gabr05], the bandwidth of the excitation light has no detectable influence on the spectral contrast, i.e. the intensity ratio between the red and green channels. In this study, since no red fluorescence intensity can be measured due to the red backscattered light, no valid statement about spectral contrast can be made.

Bibliography

[Bard05] M. P. L. Bard, A. Amelink, V. N. Hegt, W. J. Graveland, H. J. C. M. Sterenborg, H. C. Hoogsteden, and J. G. J. V. Aerts. Measurement of hypoxia-related parameters in bronchial mucosa by use of optical spectroscopy. *Am J Respir Crit Care Med*, 171(10):1178–1184, May 2005.

[Gabr05] T. Gabrecht, P. Uehlinger, S. Andrejevic, P. Grosjean, A. Radu, P. Monnier, B.-C. Weber, H. van den Bergh, and G. Wagnieres. Influence of the excitation wavelength on the tumor-to-healthy contrast in autofluorescence bronchoscopy: a comprehensive study. In M.-A. Mycek, editor, *Proc. SPIE*, volume 5862, page 586207. SPIE, 2005.

[Gabr06] T. Gabrecht. Adaptation d'une fibre SMA à un guide de lumière endoscopique pour une illumination homogène du site endoscopique. private communication, 2006.

[Gabr07] T. Gabrecht, T. Glanzmann, L. Freitag, B.-C. Weber, H. van den Bergh, and G. Wagnières. Optimized autofluorescence bronchoscopy using additional backscattered red light. *J Biomed Opt*, 12(6):064016, 2007.

[Gabr08] T. Gabrecht, A. Radu, P. Grosjean, B. Weber, G. Reichle, L. Freitag, P. Monnier, H. van den Bergh, and G. Wagnières. Improvement of the specificity of cancer detection by autofluorescence imaging in the tracheo-bronchial tree using backscattered violet light. *Photodiagnosis Photodyn Ther*, 5(1):2–9, Mar 2008.

[Häuß99] K. Häußinger, F. Stanzel, R. Huber, J. Pichler, and S. H. Autofluorescence detection of bronchial tumors with the d-light/af. *Diagnostic and Therapeutic Endoscopy*, 5(2):105–112, 1999.

[Lovi07] B. Lovisa, T. Gabrecht, S. Andrejevic, P. Grosjean, A. Radu, P. Monnier, H. van den Bergh, and G. Wagnières. Improvement of the contrast in cancer detection by autofluorescence bronchoscopy using a narrowband spectral violet excitation: A preliminary study. *Biomedical Signal Processing and Control*, 2(3):234–238, 2007.

[Qu94] J. Qu, C. MacAulay, S. Lam, and B. Palcic. Optical properties of normal and carcinomatous bronchial tissue. *Applied Optics*, 33(31):7397–7405, 1994.

[Qu95] J. Qu, C. MacAulay, S. Lam, and B. Palcic. Laser-induced fluorescence spectroscopy at endoscopy: tissue optics, monte carlo modeling and in vivo measurements. *Optical Engineering*, 34(11):3334–3343, 1995.

[Zell01] M. Zellweger, D. Goujon, R. Conde, M. Forrer, H. van den Bergh, and G. Wagnières. Absolute autofluorescence spectra of human healthy, metaplastic, and early cancerous bronchial tissue in vivo. *Appl Opt*, 40(22):3784–3791, Aug 2001.

Available online at www.sciencedirect.com
ScienceDirect
Biomedical Signal Processing and Control 2 (2007) 234–238
Biomedical Signal Processing and Control
www.elsevier.com/locate/bspc

Improvement of the contrast in cancer detection by autofluorescence bronchoscopy using a narrowband spectral violet excitation: A preliminary study

Blaise Lovisa [a], Tanja Gabrecht [a], Snezana Andrejevic [b], Pierre Grosjean [b], Alexandre Radu [b], Philippe Monnier [b], Hubert van den Bergh [a], Georges Wagnières [a,*]

[a] *Swiss Federal Institute of Technology (EPFL), Laboratory of Photomedicine, Station 6, Building CH, 1015 Lausanne, Switzerland*
[b] *The CHUV University Hospital, ENT Department, 1011 Lausanne, Switzerland*

Received 28 February 2007; received in revised form 25 June 2007; accepted 4 July 2007
Available online 24 August 2007

Abstract

Autofluorescence (AF) bronchoscopy is a useful tool for early cancer detection. However, the mechanisms involved in this diagnosis procedure are poorly understood. We present a clinical autofluorescence imaging study to assess the depth of the principal contrast mechanisms within the bronchial tissue comparing a narrowband (superficial) and broadband (penetrating) violet excitation. Knowledge of this parameter is crucial for the optimization of the spectral and optical design of clinical diagnostic AF imaging devices. An intensity contrast improvement was observed with the narrowband excitation, suggesting that the heme absorption plays a key role in the AF contrast mechanism.

Keywords: Medical systems; Intensity contrast enhancement; Autofluorescence imaging; Bronchial cancer; Clinical study

1. Introduction

Bronchial carcinoma is the leading cause of cancer deaths in the world with the highest incidence rate in North America and Europe. Most of the lesions are diagnosed at an advanced stage, which explains the very small 5-years survival rate corresponding to this condition [1]. Thus, improved techniques for detection of early lesions are urgently needed. Bronchoscopy is the only established method that allows detection, localization and definitive histological diagnosis of endobronchial lesions.

Conventional white-light bronchoscopy (WLB) has nevertheless important diagnostic limitations; the most important being its small sensitivity for early cancerous and pre-cancerous lesions [2]. Therefore, one promising approach to overcome this limitation is based on the imaging of the tissue autofluorescence (AF) [3,4]. While WLB detects mostly minimal alterations of the tissues, autofluorescence bronchoscopy (AFB) exploits the spectral differences and intensity contrasts between normal and early cancerous tissues. More precisely, the spectral contrast in AFB is based on the decrease in the green spectral region of the tissue AF intensity of the spectrum for (pre-)cancerous lesions compared to healthy tissue under violet excitation [4–6]. Such contrasts can be visualized with the help of specific endoscopic imaging devices [7].

Numerous clinical studies have demonstrated that AFB is about twice more sensitive than WLB for the detection of bronchial carcinoma in situ (CIS) and dysplasia [3,4,8–11]. However, this high sensitivity comes along with a limited specificity [4]. Although the mechanisms underlying the tumor/healthy contrasts are poorly understood at the present time, it is likely that the increase of hemoglobin concentration in the submucosa plays a significant role. An extensive spectral study of the bronchial tissue AF [6] demonstrated that the best contrasts between healthy and (pre-)malignant tissues are observed with an excitation spectral domain much smaller (410 nm, FWHM 3 nm), than usually used in AFB (typically 430 nm, FWHM 80 nm). Therefore, the preliminary study described here aims to investigate the influence of the excitation spectrum bandwidth on the contrast obtained with AFB imaging. More precisely, we report the green contrast improvement between a broadband

* Corresponding author. Tel.: +41 21 6933120; fax: +41 21 6935110.
E-mail address: georges.wagnieres@epfl.ch (G. Wagnières).

1746-8094/$ – see front matter © 2007 Elsevier Ltd. All rights reserved.
doi:10.1016/j.bspc.2007.07.004

filtered light source and a narrowband (line shape) excitation from a Krypton laser.

2. Materials and methods

2.1. Imaging system

In this study, we compared AF images obtained with a broadband and a narrowband excitation light source, as illustrated schematically in Fig. 1. The illumination system basically consists of a filtered endoscopic light source and a camera driver unit. An IR filtered 300 W Xenon lamp was used as a broadband excitation source. It is equipped with a flip–flop filter holder, allowing the operator to switch easily between white and violet excitation light, this light being delivered to the bronchoscope optics via a liquid light guide (numerical aperture (NA) = 0.53, diameter 4 mm). The violet excitation filter has a central transmission wavelength at 430 nm with a FWHM of 80 nm.

Light from a Krypton (Kr^+) laser (Type 171, Spectra Physics, USA) was used as the narrowband excitation. The Kr^+ laser was used in the multi-line mode (407 nm, 413 nm) with a maximal output power of 2.5 W. This light was injected into a 400 μm optical quartz fiber (NA = 0.4) and coupled into the liquid light guide mentioned above using a custom-made fiber coupler. The latter was necessary to accommodate the mismatch of diameters and numerical apertures (NA) for best light transmission efficiency. The coupler itself had a SMA plug on one side and a custom-made plug for the light guide on the other side. The SMA plug could be rotated in the x–y plane around a central axis in order to change the injection angle into the light guide. A slight rotation of the SMA connector resulted in a more homogenous light distribution, mimicking the broadband light source angular distribution. Due to the limited coupling efficiency and transmission of the light guide, the power of the violet light at the endoscope distal tip was about 150 mW with both excitation sources.

The white-light and the AF images were detected in both setups by a 3 CCD endoscopic color camera (Panasonic Corp., USA) clipped to the endoscopic optics. The camera delivered images in real-time, with frame accumulation. A 475 nm cut-on long pass filter was sealed in a standard zoom objective, in order to reject all violet excitation light. A white balance was performed prior to beginning an examination. The system can be used with conventional rigid optics or flexible fibroscope.

2.2. Endoscopic procedure

All five patients participating in the study had known bronchial lesions which had been identified by AF bronchoscopy in a preliminary examination. In this study, the lesions were first examined under conventional white-light (WL) illumination, and then with the broadband excitation. Eventually, the broadband light source was replaced by the Krypton laser, and the same lesions were examined. Suspect sites under violet excitation were classified as autofluorescence positive (AF+), whereas unsuspicious sites were labeled autofluorescence negative (AF−). At the end of each site observation, one biopsy per site was taken to perform a histopathological analysis of the site. All the examinations were performed under total anesthesia using rigid optics. The whole procedure was captured by the endoscopic camera and tape-recorded on the DV recorder (DSR-11, Sony Corp., Japan).

2.3. Image analysis

Image analysis was performed offline in order to compute the green channel intensity ratio between the lesion and the surrounding healthy tissue. Still images from the DV recording were digitized via the IEEE1394 port of a portable PC. In the region of the later-taken biopsy, analysis zones were classified according to their visual appearance on the image. Selection criteria for a zone labeled "lesion" were an AF+ area and

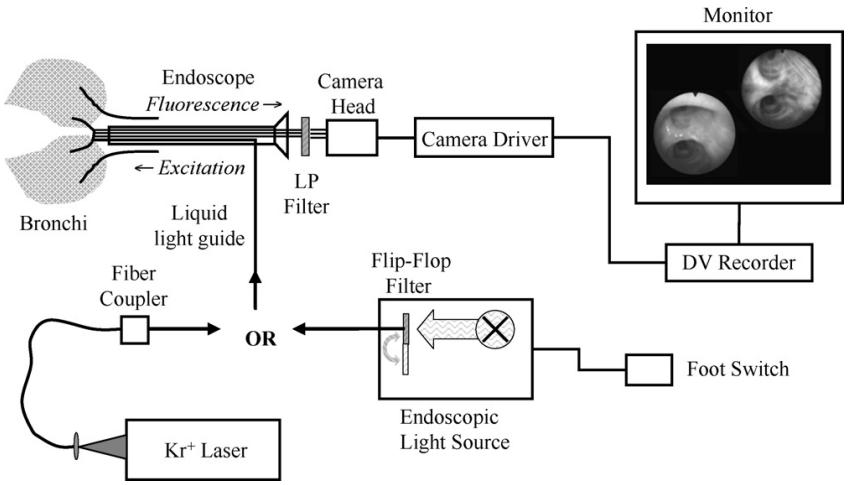

Fig. 1. Schema of the fluorescence imaging setup, consisting of a filtered endoscopic light source and a filtered endoscopic camera. Light from the Kr^+ laser can be coupled into the endoscope instead of the light from the endoscopic light source.

absence of blood spots, whereas a "healthy" zone had no suspect appearance (AF−). Typically six analysis zones (three of each type) were selected per site to accommodate the geometry artifacts resulting from different angles of view, distance between bronchoscope tip and tissue, and position of the endoscope within the bronchi. For each analysis zone, the mean pixel intensity value and its standard deviation were recorded. All the pixel intensity values were background-subtracted and corrected for the gamma factor of the camera. The resulting green-to-green ratio is given by $(G_h/G_t) = (G_{healthy})/(G_{tumor})$. Consequently, a high ratio is associated with a high contrast between a lesion and healthy tissue.

Image analysis of each image pair, including selection of areas of interest (one broad- and one narrowband excitation image per site), was performed by three independent observers to assess the inter-observer variability of the described image analysis method.

3. Results

Five patients undergoing pre-therapeutic or therapeutic bronchoscopy were included in the study. A total of six positive lesions were examined alternatively with the broadband and the narrowband excitation. Each lesion was AF+ in both excitation modes, but hardly visible under WL illumination. According to the new WHO classification of lung tumors [12], two lesions (1 and 3) were graded as CIS, three lesions (2, 4 and 5) as moderate to severe dysplasia, and lesion 6 was graded as invasive squamous cell carcinoma.

3.1. Visual results

Fig. 2 depicts the green channel images of the AF images obtained with the broadband and line-shape (Kr^+) excitation light. It shows two lesions on the spur and the inner wall of the intermediate bronchus (A), a CIS in the left lower bronchus (B), and CIS located in the inferior bronchus (C). A distinct intensity decrease (i.e. contrast) in the lesion areas compared to the normal surrounding tissues is clearly distinguishable. For each site, the intensity decrease of the green AF was more marked with the Kr^+ laser than with the broadband excitation.

3.2. Image analysis

Fig. 3 shows the mean G_h/G_t ratios obtained on the six suspect sites. The white bars show the mean G_h/G_t ratios per site obtained with the broadband excitation source, while the grey bars show ratios obtained with the line-shape (Kr^+) excitation source. All three observers calculated the ratios of the green channels on AF+ and AF− zones, and concluded that narrowband excitation was more favorable to obtain a higher G_h/G_t ratio, hence to yield a better contrast between healthy tissue and (pre-)neoplastic lesions. The error bars (±20%) represent the image analysis variability due to heterogeneity within the selected zones. The standard deviation of the improvement ratio between narrow- and broadband excitation was inferior to 15% between the three observers. Dividing the G_h/G_t ratio of the narrowband by that of the broadband excitation for the sites 1–6 yields a mean ratio of 1.43 ± 0.20.

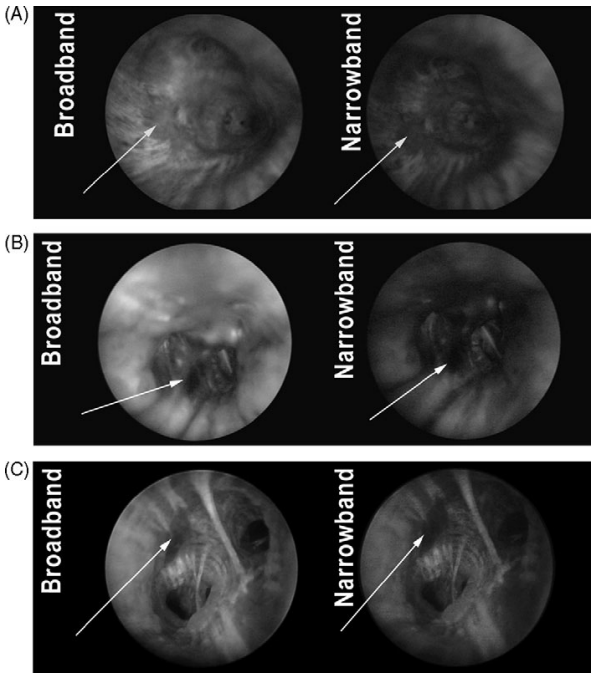

Fig. 2. Green color channel of an image showing the intermediate bronchus (A), a CIS in the left lower bronchus (B), and CIS located in the inferior bronchus (C) excited with the broadband and the narrowband (Kr^+) excitations. The white arrows show a pre-cancerous lesion with sharp intensity decrease.

4. Discussion

Over the past years, endoscopic autofluorescence imaging has been shown to be a powerful and highly sensitive tool for

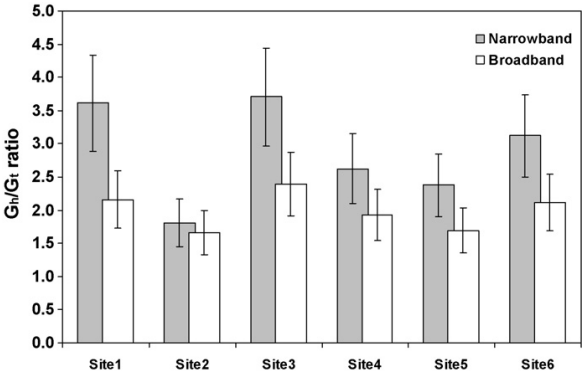

Fig. 3. Healthy vs. tumor tissue intensity contrast of the green autofluorescence excited with the broadband light source or Krypton (Kr^+) laser. The errors bars show the error resulting from the image analysis procedure (±20%).

the detection of early cancerous lesions in the bronchi. Nevertheless, the mechanisms underlying the contrasts remain poorly understood. Investigating and understanding the origin of the contrast between (pre-)neoplastic and healthy tissue will allow an optimization of the available devices.

It is to be noted that this preliminary study was conducted on a limited number of cases, due to the cumbersome instrumentation setup and the clinical procedure requirements. Inclusion criteria restricted this study to patients having known bronchial (pre-)neoplastic lesions, whereas their lesions were invisible with standard white-light illumination.

Spectrofluorometric in vivo studies [6,13–15] have shown a sharp intensity decrease in the green part of the AF spectrum on (pre-)neoplastic lesions relative to normal tissues. These results are also in good agreement with the G_h/G_t ratios computed in our study, which are larger than 1. As shown in Fig. 3, our preliminary study suggests that a better intensity contrast between healthy tissues and lesions is achieved with the narrowband excitation in the green channel. Indeed, for each site, G_h/G_t for the narrowband excitation exceeds G_h/G_t for the broadband excitation, with a mean ratio equal to 1.43 ± 0.20. This is in reasonable agreement with the mean ratio ($G_h/G_t = 1.63$) adapted from published spectrofluorometric data [6].

Since the ratio was only computed for the green channel in our study, we cannot assess whether the spectral contrast is modified by the bandwidth. However, as described in previous studies [16], the bandwidth of the excitation light has no detectable influence on the spectral contrast, i.e. the intensity ratio between the red and green channels.

Both scattering and absorption properties of tissue are altered with cancer progression. Scattering modifications are related to changes in tissue architecture and cellular changes [17]. Absorption modifications are mostly related to modifications of the concentration and distribution of light absorbers such as hemoglobin [18]. The better contrasts obtained with the narrowband excitation suggests that the concentration of blood in the tissue can be regarded as a key factor underlying these contrast mechanisms. Indeed, the Kr^+ laser light is centered on 410 nm, which corresponds to the absorption peak of hemoglobin. Previous morphometric studies [19,20] showed an increase in the microvessel density (MVD) in the (pre-)neoplastic bronchial tissues, the increase of MVD preferentially occurring in the vicinity of the basement membrane [21]. Hence, the blood concentration is higher in/under the abnormal tissue than in its healthy surrounding tissue. Previous spectrometric studies suggest that optical changes present in cancerous tissues are already detectable in the first 150–200 μm of the tumor surface, where precancerous changes develop [17]. Due to the light absorption properties of blood, the Kr^+ excitation light will be strongly absorbed by the tissue blood in the superior layers of the sub-mucosa. Moreover, the tissue blood in the sub-mucosa shields the AF from detection at the tissue surface. This shielding effect is more important in (pre-)neoplastic than in normal tissue and will consequently result in an additional amplification of the intensity contrast.

5. Conclusions

In conclusion, our results suggest that the tumor to healthy contrast in the green channel can be improved using an excitation wavelength corresponding to the hemoglobin absorption peak. In addition, these results support the conclusions derived by Zellweger et al. [6] and Gabrecht et al. [16] regarding the tumor to healthy intensity and spectral contrasts.

References

[1] A. Jemal, et al., Annual report to the nation on the status of cancer, 1975–2001, with a special feature regarding survival, Cancer 101 (1) (2004) 3–27.

[2] F.R. Hirsch, et al., Fluorescence versus white-light bronchoscopy for detection of preneoplastic lesions: a randomized study, J. Natl. Cancer Inst. 93 (18) (2001) 1385–1391.

[3] D. Goujon, et al., In vivo autofluorescence imaging of early cancers in the human tracheobronchial tree with a spectrally optimized system, J. Biomed. Opt. 8 (1) (2003) 17–25.

[4] G. Wagnières, A. McWilliams, S. Lam, Lung cancer imaging with fluorescence endoscopy, in: M.-A. Myceck, B.W. Pogue (Eds.), Handbook of Biomedical Fluorescence, Marcel Dekker, Inc., 2003 , pp. 361–396.

[5] J. Hung, S. Lam, J. LeRiche, B. Palcic, Autofluorescence of normal and malignant bronchial tissue, Lasers Surg. Med. 11 (1991) 99–105.

[6] M. Zellweger, P. Grosjean, D. Goujon, P. Monnier, H. van den Bergh, G. Wagnières, In vivo autofluorescence spectroscopy of human bronchial tissue to optimize the detection and imaging of early cancers, J. Biomed. Opt. 6 (1) (2001) 41–51.

[7] G. Wagnieres, W. Star, B. Wilson, In vivo fluorescence spectroscopy and imaging for oncological applications, Photochem. Photobiol. 68 (5) (1998) 603–632.

[8] S. Lam, T. Kennedy, M. Unger, Localization of bronchial intraepithelial neoplastic lesions by fluorescence bronchoscopy, Chest 113 (3) (1998) 696–702.

[9] P. Pierard, B. Martin, J.-M. Verdebout, J. Faber, M. Richez, J.-P. Sculier, V. Ninane, Fluorescence bronchoscopy in high-risk patients—a comparison of LIFE and Pentay systems, J. Bronchol. 8 (2001) 254–259.

[10] T.G. Sutedja, H. Condrigton, E.K. Risse, R.H. Breuer, J.C. van Mourik, R.P. Golding, P.E. Postmus, Autofluorescence bronchoscopy improves staging of radiographically occult lung cancer and has an impact on therapeutic strategy, Chest 120 (4) (2001) 1327–1332.

[11] K. Häußinger, et al., Autofluorescence bronchoscopy with white light bronchoscopy compared with white light bronchoscopy alone for the detection of precancerous lesions: a European randomised controlled multicentre trial, Thorax 60 (6) (2005) 496–503.

[12] E. Brambilla, W.D. Travis, T.V. Colby, B. Corrin, Y. Shimosato, The new World Health Organization classification of lung tumours, Eur. Respir. J. 18 (6) (2001) 1059–1068.

[13] J. Qu, C.E. MacAulay, S. Lam, B. Palcic, Laser-induced fluorescence spectroscopy at endoscopy: tissue optics, Monte Carlo modeling, and in vivo measurements, Opt. Eng. 34 (11) (1995) 3334–3343.

[14] M. Zellweger, D. Goujon, R. Conde, M. Forrer, H. Van den Bergh, G. Wagnières, Absolute autofluorescence spectra of human healthy, metaplastic, and early cancerous bronchial tissue in vivo, Appl. Opt. 40 (22) (2001) 3784–3791.

[15] R. Richards-Kortum, E. Sevick-Muraca, Quantitative optical spectroscopy for tissue diagnosis, Annu. Rev. Phys. Chem. 47 (1) (1996) 555–606.

[16] T. Gabrecht, et al., Influence of the excitation wavelength on the tumor-to-healthy contrast in autofluorescence bronchoscopy—a comprehensive study, in: Proceedings of SPIE—The International Society for Optical Engineering, 2005, pp. 1–6.

[17] M.P.L. Bard, et al., Optical spectroscopy for the classification of malignant lesions of the bronchial tree, Chest 129 (4) (2006) 995–1001.

[18] K. Sokolov, M. Follen, R. Richards-Kortum, Optical spectroscopy for detection of neoplasia, Curr. Opin. Chem. Biol. 6 (5) (2002) 651–658.
[19] A. Fisseler-Eckhoff, D. Rothstein, K.M. Müller, Neavascularization in hyperplastic, metaplastic and potentially preneoplastic lesions of the bronchial mucosa, Virchows Arch. 429 (2–3) (1996) 95–100.
[20] G. Fontanini, et al., Modulation of neoangiogenesis in bronchial preneoplastic lesions, Oncol. Rep. 6 (1999) 813–817.
[21] R.L. Keith, et al., Angiogenic squamous dysplasia in bronchi of individuals at high risk for lung cancer, Clin. Cancer Res. 6 (5) (2000) 1616–1625.

Chapter 9

Calibration and optimization of the AF imaging system

This chapter present two studies aiming to quantify the intra- and inter-patient variations in the AF intensities in order to optimize the spectral response and the settings of the DAFE imaging system (manufactured by Richard Wolf GmbH). These variations can negatively affect the image quality of AF bronchoscopy (AFB) and, thus, the learning curve of the clinician. Moreover, some knowledge about the magnitude of these variations can help to scale the dynamic range of future AFB systems.

Variations in the AF intensity have already been described in spectrometric study [Zell01a], as well as in imaging study [Hirs01, Kenn01, Gouj03], where bronchial AF is investigated, but to our knowledge, this is the first reported quantitative analysis of the inter-patient variations of AF intensity and reflectivity of endobronchial tissue. Zellweger *et al.* demonstrated that the intra-patient variations were significantly smaller than the inter-patient variations (approximately 50%) [Zell01b]. Compared to this value, the inter-patient variations found in our study were surprisingly small: approximately 25% on the healthy carina in the green part of the spectrum (490–580 nm) and only slightly higher (32%) in the red part of the spectrum. The depth-probing issue has to be taken into account when comparing imaging and spectroscopic studies, but it has been already addressed in the Introduction of the Chapter 8).

The quantification of the AF intensities with routinely used endoscopic imaging systems is not trivial. Indeed, these systems often feature camera gain control, frame integration, or shutter time adjustment to dynamically react to the varying imaging conditions during endoscopy (thoroughly described in [Gabr06]). Therefore, the quantification of the tissue AF requires the use of an optical reference allowing normalization of the intensity levels. We designed this reference so that it can be placed in the patient's bronchi during bronchoscopy. Having the reference and the bronchial mucosa in the same field of view (i.e. the same camera settings) allows us to normalize the images off-line.

In the first article (published in *Physics in Medicine and Biology* [Gabr07]), the design and characterization of a reference for AFB is presented. The second article (published in *Lasers in Medical Science* [Gabr09]) presents a preliminary clinical study aiming to quantify the inter-patient variations during AFB with the help of the developed reference. Both studies are reproduced in their published format.

The experiments were mainly realized in the framework of Tanja Gabrecht's PhD thesis [Gabr06]. The contributions of the author of this thesis manuscript were the following:

Design of an endoscopic reference I prepared the measurement set up and characterized the reference's optical properties (i) R_∞, the total diffuse reflectance, (ii) μ_{eff}, the effective attenuation coefficient (and calculation of μ_a and μ'_s), (iii) the fluorescence properties (emission spectrum) with an optical fiber-based spectrofluorimeter, and (iv) the photostability of the material.

Quantification of the inter-patient variations I performed image acquisitions in the clinical environment in order to enlarge the patient cohort, and obtain representative sampling. I was also involved in the off-line analysis of the images in order to compute the red/green ratios on the tissue and reference. This latter work was realized in parallel with Ms. Gabrecht, in order to lower bias due to the observer.

IOP PUBLISHING PHYSICS IN MEDICINE AND BIOLOGY

Phys. Med. Biol. **52** (2007) N163–N171 doi:10.1088/0031-9155/52/8/N02

NOTE

Design of an endoscopic optical reference to be used for autofluorescence bronchoscopy with a commercially available diagnostic autofluorescence endoscopy (DAFE) system

T Gabrecht, B Lovisa, F Borle and G Wagnières

Swiss Federal Institute of Technology (EPFL), Photomedicine Laboratory, Station 6, 1015 Lausanne, Switzerland

E-mail: georges.wagnieres@epfl.ch

Received 16 May 2006, in final form 1 February 2007
Published 26 March 2007
Online at stacks.iop.org/PMB/52/N163

Abstract

We present the design of a sterilizable optical reference to characterize and quantify the inter-patient variations in tissue autofluorescence during autofluorescence bronchoscopy with Richard Wolf's diagnostic autofluorescence endoscopy (DAFE) system. The reference was designed to have optical and spectral properties similar to those of the human bronchial wall in spectral conditions corresponding to autofluorescence bronchoscopy conducted with the DAFE system (fluorescence excitation at 390–470 nm and red backscattering light at 590–680 nm). The reference's effective attenuation coefficient and reflectance were measured at 675 nm. In addition, its fluorescence emission spectrum was determined under 430 nm wavelength excitation. The reference is photostable, reproducible, biocompatible and small enough to be easily inserted through the working channel of a conventional bronchofibrescope. This cylindrical (length: 2 mm; diameter: 2 mm) optical reference was validated in a clinical environment.

(Some figures in this article are in colour only in the electronic version)

1. Introduction

Autofluorescence bronchoscopy has proven to be a highly sensitive tool for the detection and localization of early bronchial cancers and pre-cancers (Goujon *et al* 2003, Häußinger *et al* 2005, Lam *et al* 2000). Several autofluorescence bronchoscopy imaging systems are commercially available (Wagnières *et al* 2003). All are based on the visualization of the spectral and intensity contrast of the tissue autofluorescence between healthy bronchial tissue and (pre-)neoplastic lesions when excited with light in the blue-violet wavelength

region. Early-neoplastic or (pre-)neoplastic bronchial lesions exhibit a significant decrease in autofluorescence intensity (Qu *et al* 1995, Hung *et al* 1991, Zellweger *et al* 2001b). The group in Lausanne reported a detailed spectral study demonstrating that this decrease is more distinct in the green part of the spectrum, i.e. between 490 nm and 600 nm (Zellweger *et al* 2001b). Using additional red backscattered light as a constant background instead of the red (600–800 nm) tissue autofluorescence can increase the contrast by a factor of 2 (Zellweger *et al* 2001b). Indeed, the autofluorescence bronchoscopy system used in Lausanne employs red backscattered light for contrast improvement. Spectrofluorometric point measurement studies in the human tracheo-bronchial tree revealed significant fluctuations >50% in the autofluorescence intensities of healthy bronchial mucosa among different individuals ('inter-patient fluctuations') (Zellweger *et al* 2001a). Clinical practice has shown that these fluctuations, in terms of brightness and colour aspect, are quite common between individuals in autofluorescence bronchoscopy (Wagnières *et al* 2003) and these inter-patient fluctuations can adversely affect the learning curve of autofluorescence bronchoscopists. Therefore, quantitative measurements of inter-patient fluctuations are an important consideration when designing future autofluorescence bronchoscopy systems. Quantification of the autofluorescence intensity using imaging techniques is based on a retrospective analysis of the digitized intensity levels detected by the cameras in different colour channels. It requires the use of an optical/fluorescence standard or reference that can be used in the bronchi during autofluorescence image acquisition. The reference, positioned so that it fills a small portion of the field of view, allows the user to correct and normalize the autofluorescence image for the settings of the autofluorescence bronchoscopy system at the time of recording and to compare the autofluorescence signals from different endoscopic sites with one another.

The fluorescence properties of such a reference should mimic the autofluoresecence properties of healthy bronchial mucosa in terms of spectroscopy and intensity. This latter feature is critical for preventing saturation of the camera. As our diagnostic autofluorescence imaging system (DAFE) detects backscattered red light around 680 nm, the reference's reflectance at this wavelength must necessarily be similar to that of the bronchial mucosa. The optical properties of the reference must be stable and the physical dimensions of the reference need to be small enough to be inserted through the working channel of the bronchoscopic optics. Moreover, the material must be biocompatible and endure decontamination procedures.

2. Materials and methods

2.1. Design of the endoscopic reference

We selected a white opaque polymethyl methacrylate (PMMA) acrylic glass (Perspex® Blanc Opal 1 × 20, Lucite Solutions, Southampton, UK) for the endoscopic reference. This material is easy to process and demonstrates resistance to conventional sterilization detergents used in the hospital. Its Rockwell hardness is 101, according to the manufacturer's specifications. Small cylinders 2 mm in diameter and 2 mm in length were machined and provided with a central longitudinal drilling of 0.5 mm diameter. The outer diameter of the cylinder was chosen according to the inner diameter of the working channel of most conventional bronchofibrescopes. The cylinder was beaded on a surgical steel guide wire (Unimed, Lausanne, Switzerland) with a diameter of 0.5 mm and a length of 2 m. A small bead, formed at the distal tip of the guide wire by thermal heating, prevents the cylinder from slipping off the wire. Biocompatible and non-fluorescing epoxy resin (Epo-Tek 301, Epoxy Technology, Billerica, USA, distributor: Polyscience AG, Cham, Switzerland) applied to the

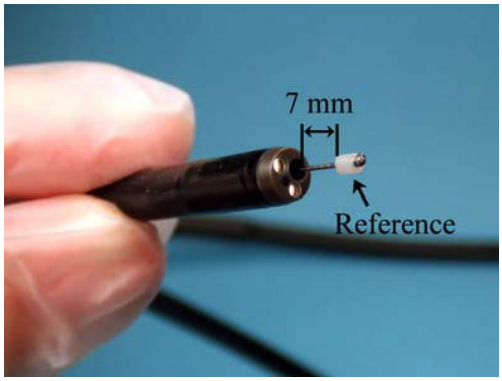

Figure 1. Close-up look at the endoscopic reference protruding out of the working channel of the autofluorescence bronchofibrescope.

distal tip of the guide wire keeps the PMMA cylinder in position and rounds off the tip to prevent damage to the patient's mucosa during measurement.

A mechanical adjustable marker set on the proximal end of the guide wire assures a constant distance of 7 mm between the bronchoscope tip and the reference during measurements. The position of the marker was adjusted prior to each bronchoscopy for the length of the bronchofibrescope to be used. An image of the endoscopic reference is shown in figure 1.

2.2. The imaging system

The DAFE system used in this study has been described in detail elsewhere (Gabrecht 2006). Briefly, it consists of a filtered endoscopic xenon light source and a filtered three CCD endoscopic colour camera. A flip-flop filter system in the light source allows for rapid changes between conventional white light illumination (white light mode) (390–680 nm) and blue-violet autofluorescence excitation (autofluorescence mode) (430 ± 40 nm). In the autofluorescence mode, a small variable amount of red light around 685 nm is added to the blue-violet excitation and detected in the backscattering mode. The light from the light source is delivered to the endoscopic site via a liquid light guide and the bronchoscope optics. The endoscopic images are captured by the endoscopic camera clipped to the optic's eyepiece. A 475 nm long pass filter in the camera objective eliminates all blue-violet autofluorescence excitation light. The spectral detection ranges for the three camera channels are 475–490 nm (blue), 490–580 nm (green) and 580–650 nm (red).

2.3. Characterization of the reference's optical properties

The diffuse reflectance R_∞ of the reference material was measured by means of an integrating sphere (LabSphere Inc., North Sutton, USA) according to a standard procedure described by Wagnières *et al* (1997). A thick sample ($d = 14$ mm) of the reference material was put to one port of the sphere. A collimated light beam from a 675 nm diode laser (FWHM 2 nm, Spectra Diode Labs, Inc., San Jose, USA) illuminated the sample from the opposite port. The reflectance signal $R_{\text{reference}}$ was detected by a photodiode located in the third port of the integrating sphere. Then the reference material was replaced by a white reflecting standard (LabSphere Inc., North Sutton, USA) with a 100% reflectivity. The total reflectance R_∞ of the reference material at 675 nm is derived from the ratio $R_\infty = R_{\text{reference}}/R_{100\%}$.

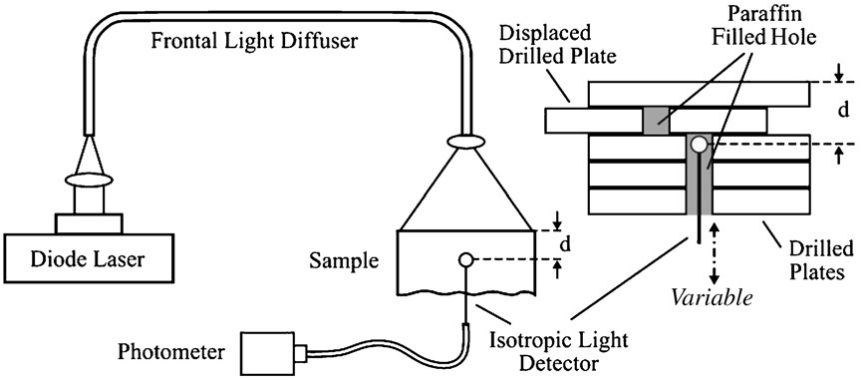

Figure 2. A block diagram of the experimental set-up used to measure the effective attenuation coefficient μ_{eff}.

For obtaining the measurements of the light penetration depth and the determination of the effective attenuation coefficient μ_{eff} (as depicted in figure 2), we used a 21 mm thick block sample consisting of individual plates 3 mm thick each with a square cross section 40 mm × 40 mm of the reference material. Each plate, except the top most one, had a central hole of 1 mm diameter drilled into it. Paraffin oil was used for index matching between the plates and inside the drilled hole. The non-drilled side of the sample was homogenously irradiated with light from the 675 nm diode laser mentioned above using a frontal light distributor (Type FD, Medlight SA, Ecublens, Switzerland) with a top hat emission profile. This perpendicular illumination gave a circular light spot with a diameter of 40 mm on the sample surface. An optical fibre based isotropic spherical light detector with a diameter of 850 μm (Type IP85, Medlight SA, Ecublens, Switzerland) was inserted into the drilled hole. The light detected by this detector was guided by an optical fibre (core diameter = 0.40 mm) and analysed by a photometer (Thorlabs Det210, Thorlabs, Newton, USA). The space irradiance I in the sample was measured for different surface–detector distances 'd' in 0.5 mm steps. During the pulling back of the detector, the plates located above the detector were displaced horizontally in order to close the drilled and to minimize the effect of the paraffin filled gap. Plotting ln(I) versus d now allows determination of the effective attenuation coefficient μ_{eff}. Indeed, μ_{eff} is the slope of the line representing the space irradiance decay curve of I versus d.

The fluorescence emission of the reference material was measured using an optical fibre based spectrofluorometer. The set-up is described in detail elsewhere (Zellweger *et al* 1999). The excitation wavelength was 430 ± 15 nm. The distal tip of the optical fibre was put in slight contact with a 3 mm thick sample of the reference material.

2.4. Photostability of the reference material

We assessed the photostability of the reference material by long-time exposure to a high intensity IR-filtered WL source (Light Projector 5137, Richard Wolf GmbH, Knittlingen, Germany). One half of the surface of a 40 mm × 40 mm plate of the reference material (thickness 3 mm) was covered with lightproof, black aluminium foil. The plate's whole surface was then exposed homogeneously to intensive white light (range 390–680 nm) from the light source. The irradiance on the plate's surface was 25 mW cm^{-2}. Irradiation was performed during a 7 h period, resulting in a total light dose of 630 J cm^{-2} on the plate's surface. After irradiation, the fluorescence and backscattering properties from the shielded

and the unshielded half of the plate were compared by imaging with the DAFE system. No difference of the fluorescence and backscattering signal between the exposed and unexposed areas was observed.

2.5. *Influence of the environmental green and red space irradiance in the bronchi*

The behaviour of the reference in a fluorescing and light scattering environment (the 'space irradiance modification') was investigated in seven cases undergoing diagnostic DAFE bronchofibroscopy. The bronchoscope was placed in the primary bronchus with the light source set in the autofluorescence mode. The reference was inserted into the bronchi via the biopsy channel of the bronchofibrescope and positioned close to the main carina. Then the bronchoscope was slowly redrawn towards the trachea, placing the reference in close contact to and at several different distances from the bronchial wall. Then the entire bronchoscope-reference unit was removed from the patient. The bronchoscope tip with the protruding reference was placed in a 40 cm $\times$ 50 cm non-fluorescing and non-reflecting black box with the same illumination and detection settings of the DAFE system. The entire procedure was recorded by a digital video (DV) recorder (Sony DSR-11, Sony Corp., Tokyo, Japan). Still images from different positions of the reference in the bronchi and in the black box were digitized. In each image the red (R) and green (G) intensity level values were computed from an area on the reference and an area on the neighbouring healthy bronchial wall. All intensity level values were corrected for the gamma factor of the camera (gamma = 0.62) and the image background. The intensity level values were computed from the reference as a function of the intensity level values of the tissue and the distance between reference and bronchial wall. Moreover, we computed the green (G_{ref}/G_{tis}) intensity ratios of the intensities measured on the reference (G_{ref}) and the main carina (G_{tis}). The mean value of this ratio was computed from three images per clinical case to determine the inter-patient variation in the tissue AF intensities.

3. Results

Figure 3 shows the endoscopic reference in the upper bronchial tree during bronchoscopy. The diffuse reflectance of the reference material at 675 nm was determined to be 73%.

The results from the measurements of the effective attenuation coefficient at the same wavelength are shown in figure 4. In this graphic, $\ln(I)$ is plotted against d. The effective attenuation coefficient was determined to be 0.14 mm^{-1} $\pm$ 0.02 mm^{-1}. Thus, the penetration depth $d = 1/\mu_{eff}$ is 7.1 mm for red light at 675 nm.

Knowing the diffuse reflectance and the effective attenuation coefficient, the absorption and reduced scattering coefficients can be deduced according to Wagnières *et al* (1997). For the reference material, the absorption coefficient was computed to be $\mu_a = 0.001$ mm^{-1} and the reduced scattering coefficient, $\mu_s' = 6$ mm^{-1}.

The reference fluorescence emission spectrum measured with the optical fibre based spectrofluorometer is shown in figure 5. For illustrative purposes, the same graphic shows a typical *in vivo* autofluorescence spectrum of healthy human mucosa.

The reference showed a high photostability since the long-term exposure to a white light dose of 630 J cm^{-2} did not affect the fluorescence and backscattering behaviour.

Imaging of the reference in the tracheo-bronchial tree showed no correlation between the autofluorescence intensity levels of the bronchial wall and that of the reference when it was not in direct contract with the wall. However, when the reference cylinder was put in direct contact with high fluorescing bronchial tissue areas, the red and green intensity levels

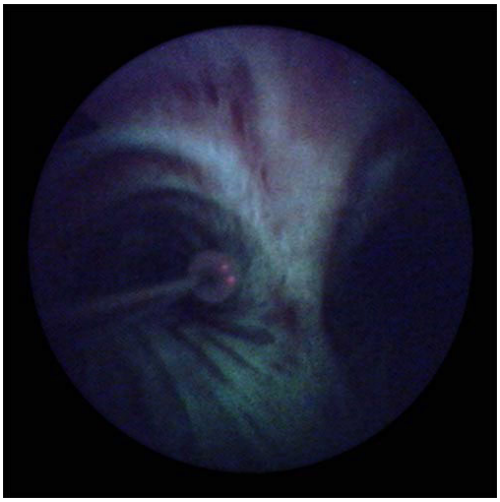

Figure 3. Endoscopic view of the reference close to the main carina. The cylinder's cross-section surface is facing the observer. The two red specular reflections observed on the right side of the reference are due to the reflection of the red light delivered by the DAFE light source through the two illumination fibre bundles of the bronchofibrescope.

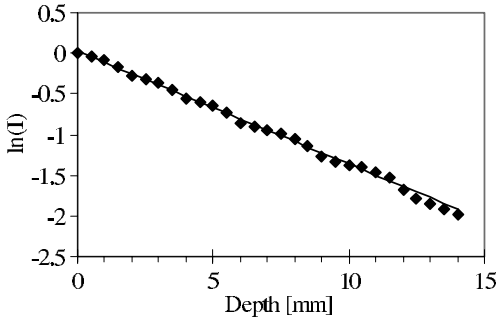

Figure 4. The graphic shows the decrease of the space irradiance versus the depth of the isotropic probe within the sample.

computed from the reference increased by a factor of 2 (data not shown). This is due to the coupling of the strong tissue AF light in the reference material.

Figure 6 shows the mean green intensity levels (figure 6(a)) and the (G_{ref}/G_{tis}) intensity ratios (figure 6(b)) computed from seven clinical cases. The error bars indicate the standard deviation deduced from three measurements each. The horizontal dashed lines represent the mean values over all cases. The straight lines depict the standard deviation. The standard deviation was 37% for the green intensity levels and 19% for the (G_{ref}/G_{tis}) intensity ratios.

4. Discussion

Due to its size, the endoscopic fluorescence and reflectance standard for autofluorescence bronchoscopy with the DAFE system presented in this work is compatible with most

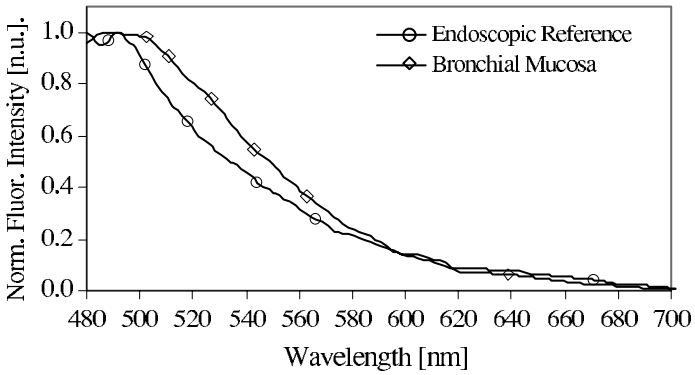

Figure 5. Fluorescence emission spectra of the reference material obtained at 430 nm excitation. A typical *in vivo* autofluorescence spectrum from healthy bronchial tissue (adapted from Zellweger *et al* (2001a)) measured with the same set-up is shown for comparison.

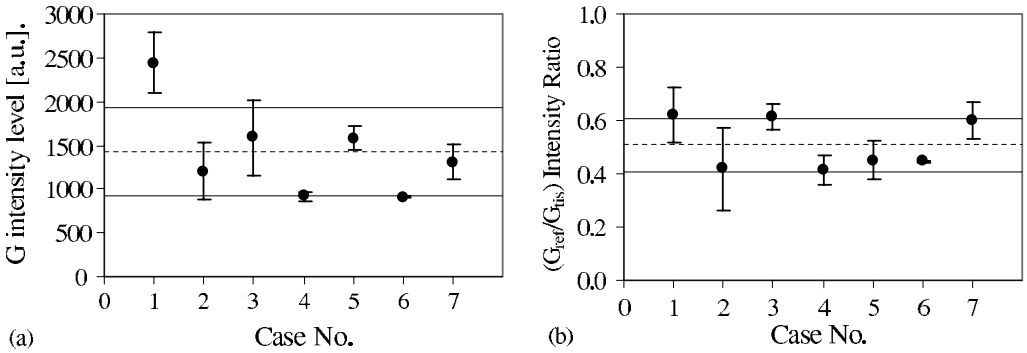

Figure 6. Green intensity levels (a) and (G_{ref}/G_{tis}) intensity ratios (b) computed from the clinical cases. The dotted line depicts the mean values over all cases with the standard variation (straight lines).

bronchofibrescopes and the more recent chip-on-tip videobronchoscopes equipped with a standard working channel.

Image acquisition and analysis is most reliable and reproducible when performed with the even, homogenous surfaces of the reference perpendicular to the optical axis. The cylinder cross cut-section, maintained perpendicularly to the optical axis of the bronchoscope, allows unbiased read-out of the intensity levels.

The shape of the Perspex's fluorescence spectrum is similar to the *in vivo* autofluorescence spectrum of human bronchial mucosa excited at 430 nm. However, it should be noted that the relative contribution of wavelength >590 nm, i.e. the ratio between the autofluorescence intensity at wavelengths >590 nm and the fluorescence intensity at wavelength <590 nm, is slightly higher in the reference fluorescence spectrum than in the *in vivo* spectrum. However, this difference does not adversely affect the material's functionality as an endoscopic reference since most (about 60%) of the red light coming from the reference during autofluorescence bronchoscopy originates from the red backscattered light.

The fluorescence intensity of the reference in the green spectral part was found to be about 50% of that of the tissue AF. The latter is in the order of 4.2 pW $(\mu W\ nm)^{-1}$ (Zellweger

et al 2001a). Since the DAFE camera uses automatic shutter and gain control functions based on central image measurements to optimize its image brightness during autofluorescence bronchoscopy, the lower fluorescence of the reference might be affected by a poor signal-to-noise ratio when used in a high fluorescing/backscattering environment. In addition, the low luminescence of the reference increases the distortion of the measurements by the space irradiance due to the autofluorescence of the bronchial wall. Indeed, as described above, the endoscopic measurements on the reference are modified in a high light emitting or backscattering surrounding. Using a material with a fluorescence intensity in the same order of magnitude as that of the tissue autofluorescence intensities will reduce the relative contribution of the space irradiance to the detected reference signal. The reference material has a relatively high (73%) reflectance at 675 nm. The diffuse reflectance of normal bronchial mucosa was measured by Tercelj *et al* (2005) to be about 75% at 675 nm wavelength. Thus the reflectance of the reference can be considered identical to that of the bronchial mucosa.

Unfortunately very little is known about the values of the effective absorption coefficient μ_{eff} of human bronchial mucosa *in vivo*. However, Bays *et al* (1996) reported a value of 0.24 mm^{-1} for μ_{eff} for the human esophageal mucosa at 630 nm. Since the reflectance of the bronchial mucosa is higher than that of the esophageal mucosa, the absorption and consequently μ_{eff} is likely to be smaller than the value given by Bays *et al*. Moreover, μ_{eff} decreases with increasing wavelengths in the wavelength range addressed in this study. Thus the effective absorption coefficient (0.14 mm^{-1}) of the reference is expected to be close to that of the human bronchial mucosa.

The preliminary clinical measurements show that the reference allows us to reduce the variations in the detected tissue autofluorescence related to changes in the system's performance by a factor 2. The mean normalized inter-patient variation (19%) was lower than the variations observed by Zellweger *et al* (2001a). However, the number of data is very small and does not yet allow us to draw final conclusions. Further clinical studies are necessary to assess the real inter-patient variations.

In conclusion, the reference presented in this work has optical and spectroscopic properties simulating that of the bronchial tissue *in vivo* for the spectral conditions corresponding to that of the DAFE system. Since the optical properties of this reference correspond to the fluorescence and red reflectance of the human bronchial mucosa, this probe can potentially be used with other endoscopic autofluorescence imaging systems based on similar spectral designs.

References

Bays R, Wagnières G, Robert D, Braichotte D, Van Den Bergh H, Savary J F and Monnier P 1996 Clinical determination of tissue optical properties by endoscopic spatially resolved reflectometry *Appl. Opt.* **35** 1756–66

Gabrecht T 2006 Clinical fluorescence spectroscopy and imaging for the detection of early carcinoma by autofluorescence bronchoscopy and the study of protoporphyrin IX pharmacokinetics in the endometrium *EPFL Thesis 3537* Swiss Federal Institute of Technology (EPFL), Lausanne, Faculty of Architecture, Civil and Environmental Engineering

Goujon D, Zellweger M, Radu A, Grosjean P, Weber B-C, van den Bergh H, Monnier P and Wagnières G 2003 *In vivo* autofluorescence imaging of early cancers in the human tracheobronchial tree with a spectrally optimized system *J. Biomed. Opt.* **8** 17–25

Häußinger K *et al* 2005 Autofluorescence bronchoscopy with white light bronchoscopy compared with white light bronchoscopy alone for the detection of precancerous lesions: a European randomised controlled multicentre trial *Thorax* **60** 496–503

Hung J, Lam S, LeRiche J and Palcic B 1991 Autofluorescence of normal and malignant bronchial tissue *Lasers Surg. Med.* **11** 99–105

Lam S, MacAulay C, leRiche J C and Palcic B 2000 Detection and localization of early lung cancer by fluorescence bronchoscopy *Cancer Suppl.* **89** 2468–73

Qu J, MacAulay C, Lam S and Palcic B 1995 Laser-induced fluorescence spectroscopy at endoscopy: tissue optics, Monte Carlo modeling and *in vivo* measurements *Opt. Eng.* **34** 3334–43

Tercelj M, Zeng H, Petek M, Rott T and Palcic B 2005 Acquisition of fluorescence and reflectance spectra during routine bronchoscopy examinations using the ClearVu Elite(TM) device: pilot study *Lung Cancer* **50** 35–42

Wagnières G, Cheng S, Zellweger M, Utke N, Braichotte D, Ballini J-P and van den Bergh H 1997 An optical phantom with tissue-like properties in the visible for use in PDT and fluorescence spectroscopy *Phys. Med. Biol.* **42** 1415–26

Wagnières G, McWilliams A and Lam S 2003 *Handbook of Biomedical Fluorescence* ed M-A Myceck and B W Pogue (New York: Dekker) pp 361–96

Zellweger M, Goujon D, Conde R, Forrer M, van den Bergh H and Wagnières G 2001a Absolute autofluorescence spectra of human healthy, metaplastic, and early cancerous bronchial tissue in vivo *Appl. Opt.* **40** 3784–91

Zellweger M, Grosjean P, Goujon D, Monnier P, van den Bergh H and Wagnières G 2001b *In vivo* autofluorescence spectroscopy of human bronchial tissue to optimize the detection and imaging of early cancers *J. Biomed. Opt.* **6** 41–51

Zellweger M, Grosjean P, Monnier P, van den Bergh H and Wagnieres G 1999 Stability of the fluorescence measurement of Foscan in the normal human oral cavity as an indicator of its content in early cancers of the esophagus and the bronchi *Photochem. Photobiol.* **69** 605–10

Lasers Med Sci
DOI 10.1007/s10103-007-0518-y

ORIGINAL ARTICLE

Autofluorescence bronchoscopy: quantification of inter-patient variations of fluorescence intensity

Tanja Gabrecht · Blaise Lovisa · Huber van den Bergh · Georges Wagnières

Received: 3 August 2007 / Accepted: 18 October 2007

Abstract Autofluorescence (AF) from bronchial tissue is increasingly used for the endoscopic detection of early bronchial neoplasia. Several imaging systems are commercially available, all detecting the absolute or relative AF intensity and/or spectral contrasts between normal tissue and early neoplastic lesions. These devices have a high sensitivity for flat neoplasia, but the specificity remains limited. Variations in the AF intensity between individuals (inter-patient variations) is considered one of the most limiting factors. In the clinical study presented here, we quantified those variations using a non-invasive optical reference positioned in situ during AF bronchoscopy. The inter-patient variations in intensity on the main carina were in the order of 25– 30%. The results of this study are quite useful for improving and defining the design of the optical features (dynamic range, physical sensitivity) of AF detection systems.

Keywords Autofluorescence bronchoscopy · Inter-patient variations · In vivo · Clinical · Imaging · Diagnostic autofluorescence endoscopy (DAFE) · Dynamic range

Introduction

Autofluorescence bronchoscopy (AFB) using blue–violet excitation light is a powerful tool for the detection and location of early cancers and pre-cancers in the tracheo-bronchial tract [1, 2]. Its sensitivity exceeds that of conventional white-light bronchoscopy (WLB) by a factor of 2 [3–6]. AFB is based on the visualisation of the intensity and spectral contrasts of the autofluorescence (AF) of healthy bronchial mucosa and neoplastic or early cancerous lesions. Several AFB imaging systems are commercially available [3]. These systems use filtered arc lamps [5, 7, 8] or laser sources [9] for the AF excitation, whereas AF imaging is performed with endoscopic colour cameras. One limitation of AFB that contributes to the limited specificity of this approach is due to the fluctuation of the AF intensity [5, 10, 11]. Spectrofluorometric in vivo studies have shown significant variations in the AF intensities of healthy bronchial mucosa among patients (inter-patient variations) [12]. Those inter-patient variations can adversely affect the image quality in AFB and the learning curve of bronchoscopists. The unique complex morphology and anatomy of the tracheo-bronchia tree makes AFB imaging highly sensitive to inter-patient and intra-patient variations. One example of the inter-patient variations affecting AFB is the regular striped structure on the bronchial wall that is mainly present on the dorsal wall of the primary and secondary bronchi. The size and structure of these stripes can vary between patients, depending on anatomical variations and bronchial abnormality, mainly chronic inflammation and bronchitis. In AFB with the Richard Wolf diagnostic autofluorescence endoscopy (DAFE) system used in this study, the structures appear as white stripes alternating with dark red stripes, running along the longitudinal axis of the bronchi. The white stripes are formed by longitudinal bundles of elastic fibres situated just below the epithelium in the lamina propria of the bronchial wall. These bundles are less pronounced on the red stripes. Disruption and mutation of this stripe structure is an important diagnostic criterion in AFB.

T. Gabrecht · B. Lovisa · H. van den Bergh · G. Wagnières (✉)
Photomedicine Laboratory,
Swiss Federal Institute of Technology (EPFL),
Station 6, Building CH,
1015 Lausanne, Switzerland
e-mail: georges.wagnieres@epfl.ch

Knowledge of the inter-patient variations of the bronchial AF intensity is extremely important for the design and development of improved future AF imaging systems. However, the determination of the inter-patient variations with imaging systems is not easy. Indeed, clinical AFB imaging systems generally employ features such as camera gain control, frame integration, or adjustment of the shutter time to react to the dynamic imaging conditions during endoscopy. This allows the brightness of the visualised images to be adjusted to an optimal value, independent of the object's signal intensity. More specifically, the intensities of signals from tissue with low autofluorescence are amplified, while those from tissue with high autofluorescence are reduced. These adjustments are performed automatically by the system and can generally not be tracked either in real time, or retrospectively. In addition, the automatic white balancing procedure performed prior to each bronchoscopy in the white-light mode frequently influences the camera settings for the AFB mode. Quantification of the optical properties of tissues by an AFB system therefore demands the use of an optical/ fluorescence standard or reference that can be used at the endoscopic site during AF image recording. Such a reference, placed where it fills a small portion of the field of view, allows one to correct the tissue AF image for the settings of the AFB system at the time of recording and to compare AF signals from different endoscopic sites. The design and the characterisation of an endoscopic reference for use with the Richard Wolf DAFE system has recently been reported by Gabrecht et al. [13]. In that report we describe the detailed optical and spectral characterisation of this reference sample.

In this article we present a quantitative analysis of the inter-patient variations of AF intensity and reflectivity of endobronchial tissue. To our best knowledge, no such data obtained in vivo have previously been reported.

Materials and methods

The imaging system

AF imaging was performed with the DAFE system commercialised by Richard Wolf Endoscopes GmbH, Germany. Very briefly, the system consisted of an infrared (IR) filtered endoscopic xenon arc lamp light source and a filtered 3 CCD endoscopic colour camera. A two-step flip-flop filter holder containing a grid and a colour band pass filter allowed rapid changes between (1) violet AF excitation at 430 nm±40 nm and (2) a conventional white light (WL) illumination (wavelength range 390 nm–680 nm). For AF detection, a variable amount of red light around 680 nm was added to the blue–violet AF excitation. This light was detected to create a background image [14]. In this study the system was used with conventional Olympus bronchofibrescopes (Type BF30, Olympus, Japan). The power of the violet excitation light at the distal tip of the bronchofibrescope was 130 mW. The endoscopic images were captured by the endoscopic camera and recorded on a digital video (DV) tape. A 475 nm high pass filter placed in the camera objective cut off all blue–violet excitation light. The spectral detection ranges for the three camera channels were 475 nm–490 nm (blue), 490 nm–580 nm (green), and 580 nm–650 nm (red).

The endoscopic optical reference

The endoscopic reference has been described in detail elsewhere [13]. Briefly, it was based on white opaque polymethyl methacrylate (PMMA) acrylic glass (Perspex Blanc Opal 1X20, Lucite Solutions, UK). A small cylinder (2 mm in diameter and 2 mm in length) was machined, provided with a central longitudinal drilling of 0.5 mm diameter and beaded onto a 0.5 mm surgical stainless steel guide wire (Unimed SA, Switzerland). The outer diameter of the cylinder was limited by the inner diameter of the bronchofibrescope working channel (2.2 mm). The optical properties of this PMMA resemble those of human bronchial tissues. More precisely, the fluorescence emission of the material and its reflectance in the red part of the spectrum are similar to those of human bronchial mucosa in the spectral conditions of the DAFE system. A detailed description of the optical properties can be found in [13]. An adjustable marker positioned at the proximal end of the guide wire ensured a constant distance of 7 mm between the bronchoscope tip and the reference during measurements. The position of the marker was adjusted prior to each session of bronchoscopy.

Patients

All 11 patients (five female and six male) involved in this study underwent diagnostic DAFE bronchoscopy in the ENT department of Centre Hospitalier Universitaire Vaudois (CHUV) the University Hospital in Lausanne, Switzerland. The mean age was 59±5.3 years (range 49 to 67 years). All patients were considered to be at high risk for head and neck or bronchial cancer, with nine patients being longtime smokers and two being non-smokers. The bronchoscopies were carried out under general anaesthesia using a 7.5 CH bronchoscope for intubation. The measurements were performed close to the optically healthy, i.e. tissues not suspicious under WL and AF bronchoscopy, main carina. The optical exclusion criteria were: areas of suspicion under WL or AF bronchoscopy in the proximity of the carina, and bleeding or mucous at the bronchoscopic site. The AFB

study was approved by the local ethics committee. All patients were asked to give informed consent prior to being enrolled in the study.

Clinical protocol

Following examination of the entire bronchial tree with both AF and conventional WL bronchoscopy, the flexible bronchofibrescope was positioned in front of the main carina. The visual aspect of the site was assessed for normality by both AFB and WLB. Then, the endoscopic reference was inserted into the working channel of the bronchofibrescope and positioned beside the main carina. As reported by Gabrecht et al.[13], the reference was positioned at a minimal distance from the bronchial wall to avoid a modification of the reference signal by the spatial irradiance coming from the bronchial wall. Images of the reference positioned close to the main carina were recorded in the AFB mode. The whole procedure took less than 2 min and did not interfere with the bronchoscopy. All AF bronchoscopies were performed according to the guidelines approved by the ethics committee of CHUV University Hospital.

Image analysis

AF images showing the reference close to the main carina were digitised in 24-bit red-green-blue (RGB) mode from the DV recordings using the IEEE1394 interface of the DV recorder and a portable personal computer (PC). Image analysis was performed with Adobe Photoshop 7.0 software (Adobe Systems, San Jose, CA, USA). In each image four areas were selected and analysed for the values of their red (R) and green (G) intensity levels: (1) the face side of the reference, i.e. the surface of the cylinder facing the observer, (2) a tissue area on the main carina, (3) and (4) an area on a red and a white stripe, respectively. The selected area on the reference typically included 1,000–1,500 pixels, corresponding to a surface of 2 mm^2. A corresponding area was selected on the tissue. The position of the reference close to the carina and the selection of the analysed areas are illustrated in Fig. 1. Saturated image areas as well as those showing specular reflections and surface abnormalities (secretion, airway crypts, etc.) were excluded from the analysis. All computed values of R and G intensity levels were corrected for the image background and the gamma factor of the camera system.

In order to quantify the inter-patient variations in intensity of the AF, we computed three green intensity ratios between (1) the reference area and the area on the carina, (2) the reference area and the area on the red stripes, and (3) the reference area and the area on the white stripes. In the following sections, these ratios will be referred to as

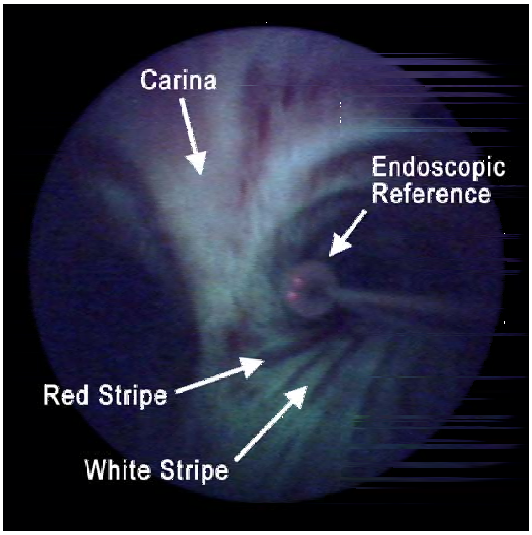

Fig. 1 DAFE image of the main carina, showing the endoscopic reference. The brightness and the chromatic aspect of the reference are similar to those of the bronchial wall. The striped structures on the dorsal wall (*bottom*) of the primary bronchi are clearly visible (A colour version of the image can be found in the online publication of this article)

the (G_{ref}/G_{tis}) ratios. The corresponding (R_{ref}/R_{tis}) ratios were computed accordingly.

Moreover, we computed the so-called normalised red-to-green ratio ($(R/G)_{norm}$), which is defined as the ratio between the red and the green intensity levels of the reference (R_{ref}/G_{ref}) divided by the ratio between the red and the green intensity levels from the bronchial wall (R_{tis}/G_{tis}). In other words,

$$\left(\frac{R}{G}\right)_{norm} = \left(\frac{R_{ref}}{G_{ref}}\right) \div \left(\frac{R_{tis}}{G_{tis}}\right)$$

The $(R/G)_{norm}$ ratio is of interest, as it is a monotonic function of the chromatic aspects of the image obtained with the DAFE system. It should be kept in mind that the green signal results from the tissue AF only, while the red signal is composed of both the tissue AF and the backscattering signal.

Typically, three different AF images per patient were digitised, analysed, and averaged. Our image analysis procedure was based on the selection of zones within an endoscopic image. To determine at which point the values of the computed (G_{ref}/G_{tis}), (R_{ref}/R_{tis}) and $(R/G)_{norm}$ ratios depend on the selections performed, the standard deviations were deduced from these measurements.

The error of the image analysis was deduced from the variation of the intensity levels computed from multiple tissue areas selected independently on the same bronchoscopic site.

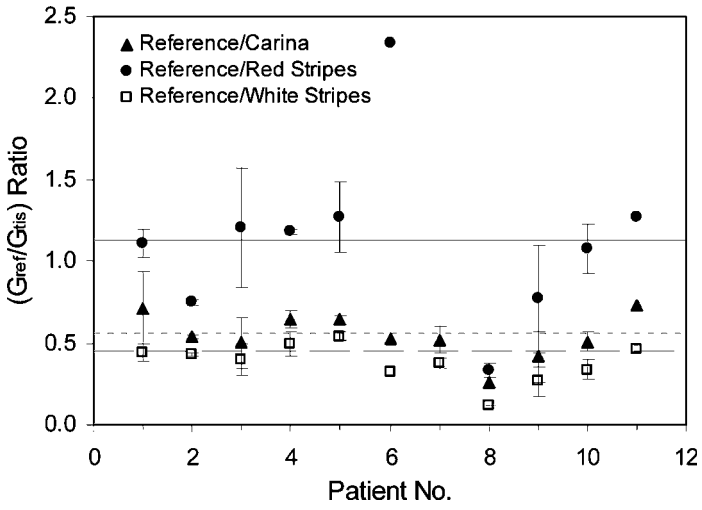

Fig. 2 Green intensity ratios of the reference and the bronchial tissues measured in 11 patients. The ratios are presented for the carina, the red stripes and the white stripes. The *horizontal lines* depict the mean ratios for the carina (*dashed line*), the red stripes (*continuous line*) and the white stripes (*large dashed line*). The *error bars* depict the standard deviations

Results

The results from the image analysis are shown in Figs. 2, 3 and 4 for (G_{ref}/G_{tis}), (R_{ref}/R_{tis}) and $(R/G)_{norm}$, respectively.

Figure 2 shows the (G_{ref}/G_{tis}) ratios between the reference and (1) the carina (triangles), (2) the red stripes (diamonds) and (3) the white stripes (squares) for all 11 patients. Each point represents the mean of three ratios computed from the three different images of a given patient, and the error bars depict the standard deviations. The mean (G_{ref}/G_{tis}) ratios between the reference and the tissue over all cases are 0.55±0.14 for the carina, 1.13±0.52 for the red stripes, and 0.38±0.12 for the white stripes. The mean ratios for each zone are depicted as dashed horizontal lines in Fig. 2. The corresponding (R_{ref}/R_{tis}) ratios are shown in Fig. 3. Depiction of the ratios and mean values are the same as in Fig. 2. The mean (R_{ref}/R_{tis}) ratios between the reference and the tissue are 0.77±0.25 for the carina, 1.27±0.68 for the red stripes, and 0.63±0.2 for the white stripes. It should be noted that the (G_{ref}/G_{tis}) and (R_{ref}/R_{tis}) ratios between the reference and the carina, as well as those between the reference and the white stripes, are all smaller than 1, while most of the corresponding ratios for the red stripes exceed 1.

The $(R/G)_{norm}$ ratios for the carina are shown in Fig. 4 for all 11 patients. As in Figs. 2 and 3, each datum point

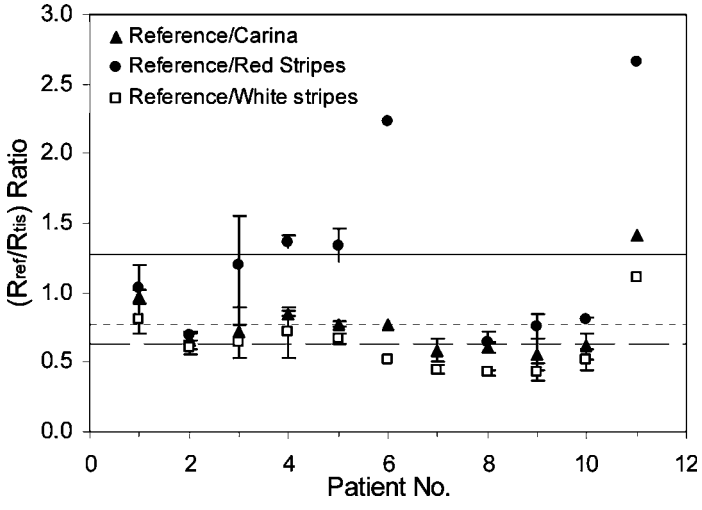

Fig. 3 Red intensity ratios of the reference and the bronchial tissues measured in 11 patients. The ratios are presented for the carina, the red stripes and the white stripes. The depiction is the same as in Fig. 2. The *error bars* depict the standard deviations

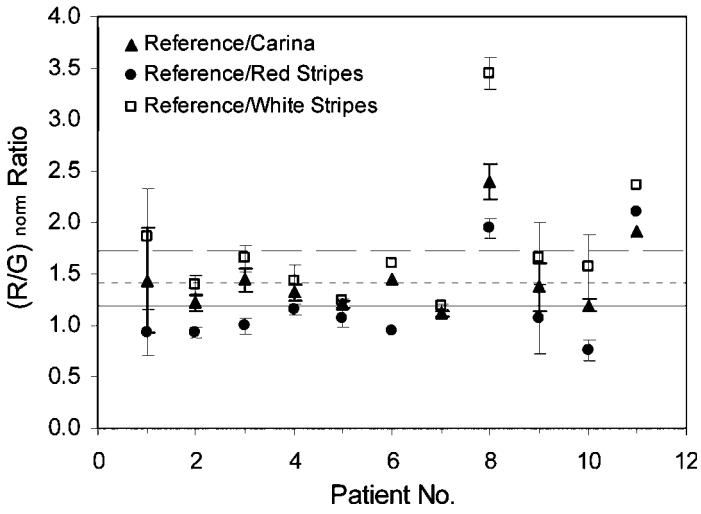

Fig. 4 Normalised (R/G) intensity ratios between the reference and the bronchial carina, the red stripes, and the white stripes, measured in 11 patients. The *error bars* depict the standard deviations

represents the mean of typically three ratios, and the error bars depict the standard deviations. The dotted horizontal line shows the mean $(R/G)_{norm}$ ratio. The mean $(R/G)_{norm}$ ratios were 1.46±0.38 (26%) for the carina, 1.19±0.45 (38%) for the red tracks and 1.76+/−0.65 (37%) for the white tracks.

The errors resulting from our image analysis procedure were approximately 15% for the (G_{ref}/G_{tis}) and (R_{ref}/R_{tis}) intensity level ratios and approximately 11% for the $(R/G)_{norm}$ ratios.

Discussion

The autofluorescence spectra of human bronchial tissue have been studied by several groups [12, 15–17]. However, the inter-patient variations of the AF intensity and spectral composition have hardly been studied quantitatively in vivo. Zellweger and co-workers [12] reported significant inter-patient variations of approximately 50% within the 67% confidence interval using 405 nm as excitation wavelength. Compared to those values, the inter-patient variations found in our study were surprisingly small. The inter-patient variations measured on the healthy carina were approximately 25% for the AF intensity in the green part of the spectrum (490 nm–580 nm) and only slightly higher (32%) in the red part of the spectrum. The relative ratio between the green and the red spectral parts of the AF varied by about 26%. Those values are nearly twice that of the error related to the image analysis method in this study. The differences between the inter-patient variations found by Zellweger et al. and those presented in this report most likely result from the measurement geometry used in the two studies. Zellweger et al. performed spectrofluorometric measurements using a fibre bundle and a spacer to keep a tissue–bundle distance of 3.5 mm [18]. This set-up offers a relatively small probing area for a given measurement. Consequently, local non-homogeneities of the tissue AF in the millimetre range may dramatically influence the AF signals measured from different spots in a given patient or between patients. Moreover, the AF intensities measured with this set-up are highly sensitive to slight changes in the tissue–probe distance. Our results were obtained using a broad field imaging technique. This measurement geometry is much less sensitive to non-homogeneities of the tissue AF in the millimetric range and to slight variations in the tissue–probe distance, since the tissue–endoscope distance is approximately 10 mm.

In this context, it is worth noting that the inter-patient variations observed in this imaging study were significantly higher (31% and 46%) on the white and red stripes, respectively, of the dorsal bronchial wall than on the carina (25%). As already pointed out in the introduction, the white stripes are formed by dense bundles of highly fluorescent elastic fibres that are closely juxtaposed to the epithelium. On the red stripes the fibre bundles are missing, resulting in a much lower AF intensity. Thus, the signal from the red stripes is dominated by the red backscattered light. The higher variations observed on the stripes are most likely due to the small size of both types of stripes (and consequently the small size of the analysed areas) making image analysis more sensitive to heterogeneities in the tissue's emission.

Though the inter-patient variations in the bronchial tissue AF observed in the this study were small, it is known from clinical practice with AFB that autofluorescence images obtained from different patients can show

clear differences in their chromatic compositions and intensities [3]. This is likely to be partly due to variations in the system's performance from one bronchoscopy to another, including variations of the excitation light intensity at the tip of the bronchoscope optics, the transmission quality of the imaging optics, and colour settings of the camera display unit, among others. Calibration charts or references used prior to the bronchoscopic examination can reduce these instrumental variations. Surprisingly, virtually no such test reference samples are provided by manufacturers producing AFB systems.

An additional approach to level out inter-patient variations in AFB is the use of automatic colour balance (ACB) procedures during bronchoscopy. Likewise the automatic white balance employed by nearly all conventional endoscopic imaging systems, the ACB will adjust the gains of the individual RGB colour channels to obtain a preset RGB signal. Performed on healthy tissue, this will allow compensation for potential colour shifts in the AFB image due to the inter-patient variations of the tissue AF.

This pioneering clinical study conducted with the endoscopic reference shows that its optical and fluorescence properties differ slightly from those of human bronchial tissue. As reported by Gabrecht et al. [13], the diffuse reflectance of the endoscopic reference is slightly higher than that of human bronchial mucosa at 675 nm. However, the AF emission spectrum of the reference was found to be slightly blue shifted relative to the tissue AF, resulting in a higher R/G ratio for the reference. This is confirmed by the fact that all $(R/G)_{norm}$ ratios computed for the carina in the study detailed here were greater than 1. Moreover, the mean (G_{ref}/G_{tis}) ratios computed for the main carina were 0.55. This indicates that the AF intensity emitted by the endoscopic reference in the green spectral part, i.e. between 490 nm and 580 nm, was approximately half the AF intensity typically emitted by healthy bronchial tissues. Although the AF of the tissue and that of the reference sample were about the same, this relatively low AF of the Perspex material was not ideal, in the sense that the reference emission was more affected by the environmental space irradiance induced by the tissues. The most reliable results will, therefore, be obtained with a brighter reference. Thus, for further clinical studies, the choice of a more fluorescent reference material than the one used in our study should be considered. It should be kept in mind that the procurement of material presenting optical and spectral properties similar to those of the bronchial wall, while being suitable for this clinical use, is very challenging. In addition, it is crucial to prevent saturation of the image, which will occur if the reference is too bright.

Apart from the inter-patient variations, the differences in the AF intensity and spectral composition within the bronchial tree of a given patient (the so-called intra-patient variations) are also very likely to influence the performance of AFB. Intra-patient variations result from morphological changes of the bronchial wall observed between the lower and higher level bronchi [3, 19]. These changes are, at least in part, due to variations in the epithelium thickness and complexity, the number and distribution of specific cells and the spatial distribution of smooth muscle and cartilage in the bronchial wall. A clinical study by our group, aiming to quantify these intra-patient variations using the endoscopic reference at different levels of the tracheo-bronchial tree, is currently in progress.

Conclusions

In this article we detailed the use of an endoscopic reference for the determination and quantification of inter-patient variations in the AF and reflectance of human bronchial tissue, using AFB imaging. The inter-patient variations in the bronchial AF intensity and spectral composition found on the carina with the AFB imaging system are small and, therefore, probably do not significantly affect the performance of AFB. The endoscopic reference described here presents a rapid and minimally invasive method to determine and quantify the intensity and spectral composition of bronchial AF during AFB.

References

1. Häußinger K, Stanzel F, Kohlhäufl M, Becker H, Herth F, Kreuzer A, Schmidt B, Strausz J, Cavaliere S, Müller K-M, Huber R-M, Pichlmeier U, Bolliger CT (2005) Autofluorescence bronchoscopy with white light bronchoscopy compared with white light bronchoscopy alone for the detection of precancerous lesions: a European randomised controlled multicentre trial. Thorax 60: 496–503
2. Lam S, MacAulay C, leRiche JC, Palcic B (2000) Detection and localization of early lung cancer by fluorescence bronchoscopy. Cancer Suppl 89:2468–2473
3. Wagnières G, McWilliams A, Lam S (2003) Lung cancer imaging with fluorescence endoscopy. In: Myceck M-A, Pogue BW (eds) Handbook of biomedical fluorescence, Marcel Dekker, New York, pp 361–396
4. Lam S, Kennedy T, Unger M (1998) Localization of bronchial intraepithelial neoplastic lesions by fluorescence bronchoscopy. Chest 113:696–702
5. Goujon D, Zellweger M, Radu A, Grosjean P, Weber B-C, van den Bergh H, Monnier P, Wagnières G (2003) In vivo autofluorescence imaging of early cancers in the human tracheobronchial tree with a spectrally optimized system. J Biomed Opt 8:17–25
6. Pierard P, Martin B, Verdebout J-M, Faber J, Richez M, Sculier J-P, Ninane V (2001) Fluorescence bronchoscopy in high-risk patients— comparison of LIFE and Pentay systems. J Bronchology 8:254–259
7. Leonhard M (1999) New incoherent autofluorescence/fluorescence system for early detection of lung cancer. Diagn Ther Endosc 5:71–75

8. Häußinger K, Stanzel F, Huber RM, Pichler J, Stepp H (1999) Autofluorescence detection of bronchial tumors with the D-Light/AF. Diagn Ther Endosc 5:105–112
9. Ikeda N, Honda H, Hayashi A, Usuda J, Kato Y, Tsuboi M, Ohira T, Hirano T, Kato H, Serizawa H, Aoki Y (2006) Early detection of bronchial lesions using newly developed videoendoscopy-based autofluorescence bronchoscopy. Lung Cancer 52:21–27
10. Hirsch FR, Prindiville SA, Miller YE, Franklin WA, Dempsey EC, Murphy JR, Bunn Jr PA, Kennedy TC (2001) Fluorescence versus white-light bronchoscopy for detection of preneoplasic lesions: a randomized study. J Natl Cancer Inst 93:1385–1391
11. Kennedy TC, Lam S, Hirsch FR (2001) Review of recent advances in fluorescence bronchoscopy in early localization of central airway lung cancer. Oncologist 6:257–262
12. Zellweger M, Goujon D, Conde R, Forrer M, van den Bergh H, Wagnières G (2001) Absolute autofluorescence spectra of human healthy, metaplastic, and early cancerous bronchial tissue in vivo. Appl Opt 40:3784–3791
13. Gabrecht T, Lovisa B, Borle F, Wagnieres G (2007) Design of an endoscopic optical reference to be used for autofluorescence bronchoscopy with a commercially available diagnostic autofluorescence endoscopy (DAFE) system. Phys Med Biol 52:N163–N171
14. Gabrecht T, Glanzmann T, Freitag L, Weber B-C, van den Bergh H, Wagnières G (2007) Optimised autofluorescence bronchoscopy using additional backscattered red light. J Biomed Opt (in press)
15. Alfano R, Tata D, Cordero J, Tomashefsky P, Longo F, Alfano M (1984) Laser induced fluorescence spectroscopy from native cancerous and normal tissue. IEEE J Quantum Electron 20:1507–1511
16. Alfano R, Tang G, Pradhan A, Lam W, Choy D, Opher E (1987) Fluorescence spectra from cancerous and normal human breast and lung tissues. IEEE J Quantum Electron 23:1806–1811
17. Qu J, MacAulay C, Lam S, Palcic B (1995) Laser-induced fluorescence spectroscopy at endoscopy: tissue optics, Monte Carlo modeling and in vivo measurements. Opt Eng 34: 3334–3343
18. Zellweger M, Grosjean P, Goujon D, Monnier P, van den Bergh H, Wagnières G (2001) In vivo autofluorescence spectroscopy of human bronchial tissue to optimize the detection and imaging of early cancers. J Biomed Opt 6:41–51
19. Gabrecht T, Andrejevic-Blant S, Wagnières G (2007) Blue-violet excited autofluorescence spectroscopy and imaging of normal and cancerous human bronchial tissue after formalin fixation. Photochem Photobiol 83:450–458

Bibliography

[Gabr06] T. Gabrecht. *Clinical fluorescence spectroscopy and imaging for the detection of early carcinoma by autofluorescence bronchoscopy and the study of the protoporphyrin IX pharmacokinetics in the endometrium.* PhD thesis, EPFL No 3537, 2006.

[Gabr07] T. Gabrecht, B. Lovisa, F. Borle, and G. Wagnières. Design of an endoscopic optical reference to be used for autofluorescence bronchoscopy with a commercially available diagnostic autofluorescence endoscopy (dafe) system. *Phys Med Biol*, 52(8):N163–N171, Apr 2007.

[Gabr09] T. Gabrecht, B. Lovisa, H. van den Bergh, and G. Wagnières. Autofluorescence bronchoscopy: quantification of inter-patient variations of fluorescence intensity. *Lasers Med Sci*, 24(1):45–51, Jan 2009.

[Gouj03] D. Goujon, M. Zellweger, A. Radu, P. Grosjean, B.-C. Weber, H. van den Bergh, P. Monnier, and G. Wagnières. In vivo autofluorescence imaging of early cancers in the human tracheobronchial tree with a spectrally optimized system. *J Biomed Opt*, 8(1):17–25, Jan 2003.

[Hirs01] F. Hirsch, S. Prindiville, Y. Miller, W. Franklin, E. Dempsey, J. Murphy, P. Bunn Jr, and T. Kennedy. Fluorescence versus white-light bronchoscopy for detection of preneoplasic lesions: a randomized study. *J Natl Cancer Inst*, 93(18):1385–1391, 2001.

[Kenn01] T. Kennedy, S. Lam, and F. Hirsch. Review of recent advances in fluorescence bronchoscopy in early localization of central airway lung cancer. *Oncologist*, 6(3):257–262, 2001.

[Zell01a] M. Zellweger, D. Goujon, R. Conde, M. Forrer, H. van den Bergh, and G. Wagnières. Absolute autofluorescence spectra of human healthy, metaplastic, and early cancerous bronchial tissue in vivo. *Appl Opt*, 40(22):3784–3791, Aug 2001.

[Zell01b] M. Zellweger, P. Grosjean, D. Goujon, P. Monnier, H. van den Bergh, and G. Wagnières. In vivo autofluorescence spectroscopy of human bronchial tissue to optimize the detection and imaging of early cancers. *J Biomed Opt*, 6(1):41–51, Jan 2001.

Chapter 10

Clinical evaluation of the AF imaging system

This chapter presents a clinical evaluation of a version of the AF-based imaging prototype, manufactured by Richard Wolf GmbH to detect early bronchial cancers. It implements the conclusions of Gabrecht *et al.* [Gabr08], that optimized the amount of detected blue backscattered light to improve specificity of AF detection method.

A second prototype — which allows online image analysis (*e.g.* thresholding based on the green/red ratio) — has also been evaluated clinically. The results are presented in Appendix A. This second study shows that an optimal thresholding procedure allows to dramatically reduce the false positive rate in head& neck (H&N) cancer patients.

10.1 Introduction

As mentioned in Chapter 7, lung cancer accounts for about 30% of the cancer deaths in the world, and the overall 5-year patient survival is less than 15%. Patient survival is strongly linked to the early detection of bronchial lesions. For instance, 5-year survival for stage Ia is 60%. Unfortunately, lung cancer is often asymptomatic. Consequently, about 66% of the patients already present a stage III/IV cancer at the time of diagnostic, which predicts a poor prognostic. Thus, a reliable detection method for early cancer would help to improve the patient prognostic.

Systematic screening by chest X-ray and sputum analysis has been proposed, but it is currently not implemented because it does not lower mortality [Cort83]. "Molecular screening" has undergone encouraging progresses in the recent years, but this procedure is not yet established in the clinical environment. The cancer guidelines advise the following : if atypical or cancerous cells are found during sputum analysis in absence of radio-visible lesions, a detailed examination of the full respiratory tract is strongly advised [Søre09]. Even if a primary cancer is already detected in the H&N region, one should not cancel the bronchoscopic examination, since these lesions are often multifocal [Sava91]. About 60% of radio-occult cancer are (pre-)neoplastic cancers (dysplasia, CIS, and micro-invasive carcinomas), but unfortunately only 30% of the CIS and 60% of the microinvasive carcinomas are visible in conventional white light bronchoscopy [Lam93].

Endoscopic fluorescence imaging (EFI) systems have been developed in order to improve the sensitivity of WL endoscopy. Indeed, AF bronchoscopy (AFB) has been shown to have a twice better sensitivity than conventional WL bronchoscopy (WLB) [Häuß05]. However, the AFB specificity remains limited, mainly due to high number of false positive. The AFB working principle has been described elsewhere in this manuscript (see Section 2.2.1.1).

In collaboration with Richard Wolf GmbH, a new flexible DAFE video-bronchoscope prototype had been developed. The chip-on-the-tip technology, that integrates a CCD detector at the distal end of the endoscope, had been implemented in this device. With this technical modification, the optical fibers for the image transmission could be spared, avoiding that fiber breakage and aging had an impact on image quality.

This clinical study aimed to assess the performances of this new prototype in a multicentric clinical study with a larger cohort of patients (about 150), since this system was already tested by the ENT unit in CHUV hospital with promising results.

The primary goal of this study was to determine the relative sensitivity and specificity of AFB with respect to WL bronchoscopy. The gold standard remained histopathological analysis of bronchial biopsies. AF photodetection served as a biopsy guide on patients with suspected early lesions.

The second goal was the determination of tumoral markers on pre-cancerous lesions. Genetic anomalies are observed in the course of neoplasia development. It is likely that an early detection of such alterations would be a diagnostic tool discriminating pre-neoplastic lesion with a proliferation rate. Thus, a molecular analysis was performed on 30 selected patients.

The official documents (study protocol, patient information sheet, and patient consent form) received approval by the local ethics committee.

10.2 Materials & Methods

10.2.1 Imaging system

The bronchoscopies were performed with the DAFE II prototype (6 mm diameter, Richard Wolf GmbH, Knittlingen, Germany). The system consists of a DAFE/PDD light projector (type 5138), a 1 CCD camera controller (type Endocam 5520) and a flexible DAFE video-bronchoscope (type 7270, outer diameter 6.0 mm, 2.2 mm working channel). The light projector is infrared-filtered and delivers both white and blue light (370–430 nm, see Figure 2.12). The video-bronchoscope is equipped with a long-pass filter that rejects most of the excitation light. In this device, some of the backscattered blue light is collected through the emission filter. The same bronchoscope allows to perform WLB and AFB. The images are recorded by a DVD recorder and displayed on a 19" LCD monitor, both also provided by Richard Wolf. Two of these systems (serial numbers 456145,456146) were delivered to Lausanne in November 2006. Before the start of the study in 2007, both light projectors were returned to Richard Wolf for technical revision and update. The revised light projectors arrived in Lausanne at the end of March 2007. A third one was delivered (serial number 5738) in March 2008.

With this setup, the lesions appear in blue over a greyish background. An *intelligent* color balance (iCB) procedure is performed at the beginning of each examination on healthy bronchial mucosa (*e.g.* main carina). It allows the camera controller to compensate for inter-patient AF variations (see Chapter 9). This procedure implements what will be discussed in Appendix F, namely that one option to achieve the best contrast would be to present a saturated color for the foreground over a greyish background.

Figure 10.1 shows a typical example, with a carcinoma *in situ* that is well-demarcated in AF mode, whereas it is nearly invisible with conventional white light illumination.

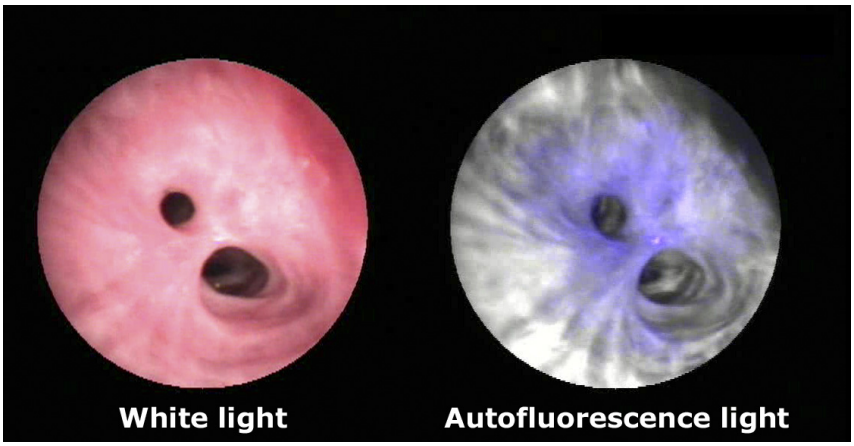

Figure 10.1: *Example of a CIS on a spur, with white and blue light illumination. The tumor margins are well-demarcated in AF mode.*

10.2.2 Patient population

The study was conducted in two medical locations: the CHUV university hospital in both pneumology (PNE) and ear-nose-throat (ENT) departments, as well as at Dr. François Heinzer's private practice. At the CHUV hospital, the study was supervised by Dr. Alain Sauty (PNE) and Dr. Philippe Pasche (ENT). At the end of 2008, Dr. Heinzer's setup was moved to Clinic Cecil in Lausanne for practical reasons (bronchoscopic examination sometimes require total anesthesia). At this point, we would like also to thank Marie Hofer for helping in collecting patient data and informed consent forms in CHUV hospital.

144 patients (mean age 61 years old, range 41–87) were recruited for this study between May 2007 and December 2009. Figure 10.2 shows the timeline of patient recruitment, with a mean patient number of 4–5 per month.

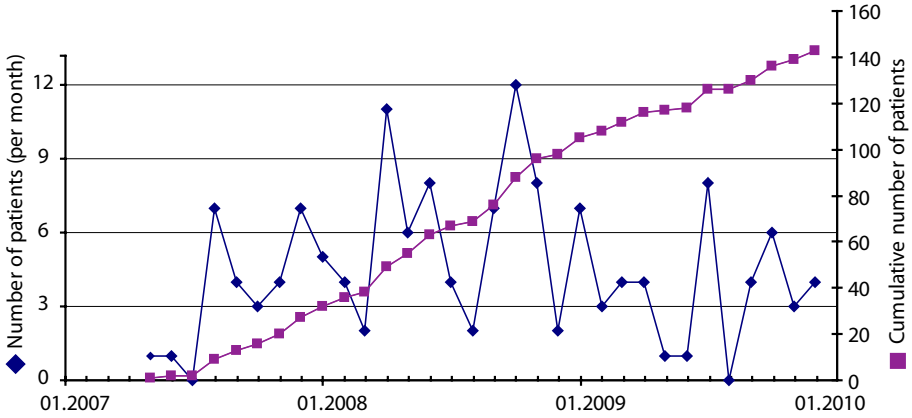

Figure 10.2: *Timeline of the patient recruitment in this clinical study.*

Most of the patients recruited for this study were at high risk of developing dysplasia or carcinoma in situ, because of their smoking history.

Inclusion criteria Patients older than 18 years old, that were subject to bronchoscopy or panendoscopy (before being recruited in the study) were recruited if they had :

- known endobronchial lesions suspicious for neoplasia
- pulmonary or ENT lesions suspect for neoplasia (as seen in chest X-ray or CT scan)
- post therapeutic control (follow-up of oncologic cases)
- pre therapeutic control (before laser, PDT, ...)
- samples (sputum, broncheoalveolar lavage, bronchial biopsy/brush) suspect for neoplasia
- previous suspect examination with/without AF
- smoker $>$ 20 UPA suspicious for endobronchial lesions

Exclusion criteria Patients were excluded from the protocol if they had, apart from the conventional contraindications for bronchoscopy:

- administration of a photosensitizer less than 4 weeks before
- treatment with chemo- or radiotherapy 3 months prior to the examination
- coagulation problems
- suspicion of carcinoid (because of high bleeding probability)
- severe hypoxemia
- pregnancy
- not signed the written informed consent.

10.2.3 Investigation protocol

All patients were examined following the same clinical protocol approved by the local ethics committee. Control biopsies sampled on healthy tissues allowed to determine relative sensitivity and specificity of the detection method.

The patients recruited for the study underwent endoscopic examination (flexible and/or rigid) following usual procedure, with local or general anesthesia. After the vocal cords, the tracheo-bronchial tree was reviewed for each lobe sequentially, first with WL, then with blue light, so that the suspicious lesions were recorded first in WL, and then in AFB. The physician proceeded with the remaining procedures (biopsy, brush, broncho-alveolar lavage) at the very end of the examination.

As a convention, it was stated in the protocol that the operator would take 2–3 biopsies per site if 1–2 sites were described to be suspicious (WL or AF), and 1 biopsy per site if more than 3 sites were described as suspicious. Additionally, he would take 2–3 biopsies on AF negative (AF−) tissue, with a maximum of 10 biopsies.

Suspicious regions in white light were described as areas where the bronchial mucosa lost his normal aspect (hyperemia, non-smooth mucosa with some surface irregularities, thickening and/or discoloration). The control biopsies on AF− tissues were sampled on interlobar or segmental spurs (because of easy access). The examination was recorded on DVD for documentation purpose.

Biopsies originating from areas suspects only under WL were excluded from this protocol (i.e. they were analyzed but simply labeled as *excluded from the protocol* in the Results part). Similarly, biopsies coming for exophytic masses were not considered because AF was irrelevant in this situation. A case report form summarized the patient information, the localization of the lesions, and their endoscopic appearance : fluorescence (AF+/AF−) and/or WL (WL+/WL−). If a biopsy was found to be as CIS or a micro-invasive carcinoma, the patient was informed and a local treatment was proposed (such as cryotherapy, brachytherapy, photodynamic therapy, or CO_2 laser cauterization).

10.2.4 Histopathological analysis

Each fluorescing positive site was cold-biopsied. Tissue samples were fixed in formalin and examined by experienced pathologists (Dr. Snezana Andrejevic Blant and Dr. Hanifa Bouzourene) who were blinded to the endoscopic result (AF+ or AF−) in order not to bias the examination. The slides were reviewed independently by both pathologists, until they reached a consensus. The biopsies were cut in 5 μm slides and stained with hematoxylin/eosin. Bronchial biopsies were graded according to the World Health Organization (WHO) classification 1999 [Bram01]. Fluorescence positive biopsies were then grouped into five categories: 1) normal bronchial mucosa; 2) reactive modifications (basal hyperplasia, squamous metaplasia); 3) low-grade dysplasia (light and moderate); 4) high grade dysplasia, carcinoma in situ; 5) micro-invasive carcinoma. In this study, classes 1, 2, and 3 are considered as non-cancerous lesions (Histo−), whereas 4 and 5 are cancerous (Histo+). Complementary observations (presence of inflammation, angiogenesis) were reported for each biopsy.

The biopsies that were taken on fluorescence positive (AF+) or white light positive (WL+) sites, but upon pathological analysis were described as non-cancerous biopsies (1,2,3), were characterized as false positives (AF/FP and WL/FP, respectively). Similarly, AF+ and WL+ regions of interest that demonstrated cancerous biopsies (4,5) were characterized as true positives (AF/TP and WL/TP, respectively).

10.3 Results

10.3.1 Histopathological results

As mentioned above, 144 patients were recruited in the study, among them 115 patients (80%) were not diagnosed with any fluorescence positive sites. In the following, an *occurrence* is defined as either a patient recruited in the study with no biopsy, or a biopsy taken in one particular patient (so that a patient with several biopsies could account for more than one occurrence). Similarly, an occurrence was said to be *excluded* from the study protocol, if either 1) no fluorescence positive (AF+) site was found in this particular patient, or 2) the histopathological analysis was unsuccessful (*e.g.* limited volume of biopsy, abraded epithelium).

The 144 patients recruited in the study yielded 175 occurrences, whose endoscopic appearance is listed in Table 10.1.

	AF+	AF–	total
WL+	9	8	17
WL–	23	135	158
total	32	143	175

Table 10.1: *Endoscopic appearance of the 175 occurrences*

The 143 AF– occurrences were described as follows: excluded from protocol study (n=126), normal (n=9), reactive modifications (n=6), low-grade dysplasia (n=2). All occurrences are true-negative.

The 32 AF+ occurrences were described as follows: excluded from protocol (n=8), normal (n=8), reactive modifications (n=8), low-grade dysplasia (n=2), high-grade dysplasia/CIS (n=3), micro-invasive carcinoma (n=1), non-small cell carcinoma, invasive (n=2). 18/24 (75%) of the AF+ are false-positive, whereas 6/24 (25%) are true-positive.

The 158 WL– occurrences were described as follows : excluded from protocol (n=128), normal (n=15), reactive modifications (n=11), low-grade dysplasia (n=2), high-grade dysplasia/CIS (n=2).

The 17 WL+ occurrences were described as follows: excluded from protocol (n=6), normal (n=2), reactive modifications (n=3), low-grade dysplasia (n=2), high-grade dysplasia/CIS (n=1), micro-invasive carcinoma (n=1), non-small cell carcinoma, invasive (n=2).

Table 10.2 summarizes the histopathological status of the 175 occurrences. The presence of inflammatory tissue in the biopsy is indicated in brackets.

	AF–	AF+	WL–	WL+
excluded from protocol	126	8 (2)	128 (2)	6
normal	9	8 (6)	15 (5)	2 (1)
reactive changes	6	8 (3)	11 (2)	3 (1)
low-grade dysplasia	2	2 (1)	2 (1)	2
high-grade dyplasia/CIS	0	3 (2)	2 (1)	1 (1)
micro-invasive carcinoma	0	1	0	1
invasive carcinoma	0	2	0	2
total	143	32	158	17
total (included)	17	24	30	11

Table 10.2: *Histopathological status of the 175 occurrences. Number in brackets indicate the number of occurrences containing inflammation.*

Inflammation is present in 10/18 (56%) of the AF+ false-positive sites. Table 10.3 summarizes the classification of the 41 occurrences that were not excluded from the protocol.

	AF–	AF+	total
Histo–	17	18	35
Histo+	0	6	6
total	17	24	41

	WL–	WL+	total
Histo–	28	7	35
Histo+	2	4	6
total	30	11	41

Table 10.3: *Summary of the 41 retained occurrences presented with respect to their endoscopic appearance.*

No false-negative (AF−/Histo+) were observed with AFB. Consequently, all the cancerous lesions were detected by AFB, whereas only 4/6 (66%) were detected with WLB only. The higher stage carcinomas (micro-invasive, invasive) were visible with both imaging modalities. AFB was more sensitive to pre-neoplastic changes of the bronchial mucosa than WLB (10/5).

10.3.2 Technical review

Since this instrumentation was an improved prototype, we also asked the physicians to comment about the new device. They positively reviewed the image quality in AF mode. The endobronchial stripes were well-defined, which can be of great help for the operator. Indeed, disruption in the stripes could be a hint for a pre-cancerous lesion. The bronchoscope handling was convenient (*e.g.* navigation was easy), even if the videobronchoscope was a little bit more rigid (less bendable) than the Olympus currently used in CHUV. The initial devices suffered from a lack of suction, which could impaired the broncho-alveolar lavage (*e.g.* difficulties to

recollect the fluid after it was squirted into the lung). This issue had been partly solved with Wolf's detailed explanations.

The intelligent color balance (iCB), as well as the non-intuitive false-color presentation, was not easy to teach to the operators. Secretions appearance was bright blue and could be disturbing to identify fluorescence positive lesions. A mucosa clearance with NaCl solution was sometimes required.

10.4 Discussion

In a review of fluorescence bronchoscopy data in a selected population of smokers and former smokers with sputum atypia (i.e. patients having a profile corresponding to the patients of the present study), prevalence rates of 6% and 1.6% were reported for severe dysplasia and CIS, respectively [Lam00]. The prevalence in the present clinical study is 6/144 (4.2%).

The number of biopsies taken on (WL+/AF−) sites with non-cancerous histopathological analysis is 3/7. Hence, AFB can potentially reduce the number of biopsies by 43%.

The number of false-negative is always difficult to assess extensively, because one could not take biopsies everywhere in the whole lung. In this study, the "theoretical" negative predictive value of AFB (directly linked to the numbers false-negative) is 100%. For this reason, some physicians do not take any biopsies on AF– areas, because they are pretty confident that a fluorescence negative area (AF–) won't turn out to be histopathologically positive [Ramo10].

The positive predictive value is only 25%, due to the high number of FP (n=18), which may be partly attributed to the high number of physicians involved in the study. It was foreseen that only 2-3 clinicians would be recruited as operators, but at the end, more than 20 physicians were active in this study due to rotations in the assistant team. Since they need a few patients to "steep" their learning curve, we can imagine that about 20% of the false positive could be discarded.

Despite the fact that they were built with the same architecture, some tiny differences in color rendering were observed between the three devices used in this study. However, we reviewed all the cases, and we could not show a significant difference in sensitivity and specificity between the three devices. However, it can not be excluded that some FPs may be attributed to these variations.

We observed a high number of inflammations associated with false-positive results (56%). It is likely that morphometric parameters (*e.g.* vascularization patterns underlying these AF+ areas) can reject a high proportion of these false-positive lesions [Shib10]. For that purpose, we developed *e.g.* high-magnification bronchoscopy (see Chapter 11) to help decreasing the false-positive rate.

Another source of AFB false positives is related to the biopsy sampling. Whenever possible, biopsies are taken in the fluorescence mode to ensure that the tissue sample is coming from a fluorescence positive area. Nevertheless, it cannot be excluded that a certain number of tissue samples are not taken from the fluorescence positive regions, but from fluorescence negative (AF−) neighboring tissue. Last, histopathologic examination is deemed as the "gold standard" for comparison with bronchoscopic findings in nearly all clinical studies reporting on autofluorescence bronchoscopy. Nevertheless, some authors report on significant inter-observer variability in histopathologic analysis [Kuri98, Venm00]. In a retrospective study of 343 bronchial tissue samples from AFB, Venmans *et al.* revealed inter-observer variability by a factor of 2 in the number of diagnosed preinvasive bronchial neoplasia [Venm00].

In this study, we used a strict definition of cancerous, resp. non-cancerous lesions. However, in a preventive examination, the first steps of carcinogenesis (such as reactive changes, squamous

metaplasia, low-grade dysplasia) can also be of interest, because the diagnosed patient can be told to avoid carcinogen exposure (*e.g.* smoking) to allow self-regression of the lesion.

Many patients have extra-bronchial lung tumors that can be visualized on the CT-scan, but since these tumors are not protruding in the endoluminal space, they remain invisible with bronchoscopic examination (even with AF). In the recent years, a new technology has been developed by Olympus Inc, namely the transbronchial needle aspiration guided by an endobronchial ultrasound (EBUS-TBNA) [Came10]. It allows the physicians to sample mediastinal lymph nodes and peribronchial lesions, and to stage the extrabronchial carcinoma.

Since bronchial cancer is an evolutive disease, we had in mind to follow-up the patients over the study timeline, in order to see if a pre-neoplasia (Histo−, but detected as AF+ with our device) could have been seen later on either with a self-regressed or a cancerous lesion. We reviewed all the patients files available at CHUV. Unfortunately, only few patients came back to the CHUV hospital for oncological treatment (chemo- or radiotherapy often for other non-bronchial primary cancer), but none of them were subject to a second bronchoscopy until end of 2009.

Summarily, we conclude that this new prototype is highly sensitive to pre-cancerous modifications of the bronchial wall. It also detects carcinoma *in situ* and micro-invasive lesions. Since it adds virtually no time to the conventional examination – barely a few minutes when used in parallel with WL examination –, it can be a great help for the physician.

Bibliography

[Bram01] E. Brambilla, W. D. Travis, T. V. Colby, B. Corrin, and Y. Shimosato. The new world health organization classification of lung tumours. *Eur Respir J*, 18(6):1059–68, 2001.

[Came10] S. E. H. Cameron, R. S. Andrade, and S. E. Pambuccian. Endobronchial ultrasound-guided transbronchial needle aspiration cytology: a state of the art review. *Cytopathology*, 21(1):6–26, Feb 2010.

[Cort83] D. A. Cortese, P. C. Pairolero, E. J. Bergstralh, L. B. Woolner, M. A. Uhlenhopp, J. M. Piehler, D. R. Sanderson, P. E. Bernatz, D. E. Williams, W. F. Taylor, W. S. Payne, and R. S. Fontana. Roentgenographically occult lung cancer. a ten-year experience. *J Thorac Cardiovasc Surg*, 86(3):373–380, Sep 1983.

[Gabr08] T. Gabrecht, A. Radu, P. Grosjean, B. Weber, G. Reichle, L. Freitag, P. Monnier, H. van den Bergh, and G. Wagnières. Improvement of the specificity of cancer detection by autofluorescence imaging in the tracheo-bronchial tree using backscattered violet light. *Photodiagnosis Photodyn Ther*, 5(1):2–9, Mar 2008.

[Häuß05] K. Häußinger, F. Stanzel, M. Kohlhäufl, H. Becker, F. Herth, A. Kreuzer, B. Schmidt, J. Strausz, S. Cavaliere, K.-M. Müller, R.-M. Huber, U. Pichlmeier, and C. Bolliger. Autofluorescence bronchoscopy with white light bronchoscopy compared with white light bronchoscopy alone for the detection of precancerous lesions: A european randomised controlled multicentre trial. *Thorax*, 60(6):496–503, 2005.

[Kuri98] J. Kurie, J. Lee, R. Morice, L. Garrett, F. Khuri, A. Broxson, Y. Jae, A. Wilbur, Y. Ren, and K. W. Hong. Autofluorescence bronchoscopy in the detection of squamous metaplasia and dysplasia in current and former smokers. *J Natl Cancer Inst*, 90(13):991–995, 1998.

[Lam93] S. Lam, C. MacAulay, J. Hung, J. LeRiche, A. E. Profio, and B. Palcic. Detection of dysplasia and carcinoma in situ with a lung imaging fluorescence endoscope device. *Journal of Thoracic and Cardiovascular Surgery*, 105(6):1035–1040, 1993.

[Lam00] S. Lam, C. MacAulay, J. C. leRiche, and B. Palcic. Detection and localization of early lung cancer by fluorescence bronchoscopy. *Cancer Suppl.*, 89(11):2468–2473, 2000.

[Ramo10] P. Ramon. Nécessité des biopsies sur des sites négatifs en autofluorescence. private communication, 2010.

[Sava91] M. Savary, P. Monnier, R. Pasche, E. Brossard, P. Pasche, and F. Lang. Multiple primary malignancies. *Adv Otorhinolaryngol*, 46:165–175, 1991.

[Shib10] K. Shibuya, T. Nakajima, T. Fujiwara, M. Chiyo, H. Hoshino, Y. Moriya, M. Suzuki, K. Hiroshima, Y. Nakatani, and I. Yoshino. Narrow band imaging with high-resolution bronchovideoscopy: A new approach for visualizing angiogenesis in squamous cell carcinoma of the lung. *Lung Cancer*, in press:NA, Jun 2010.

[Søre09] M. Sørensen, E. Felip, and E.S.M.O. Guidelines Working Group. Small-cell lung cancer: ESMO clinical recommendations for diagnosis, treatment and follow-up. *Ann Oncol*, 20 Suppl 4:71–72, May 2009.

[Venm00] B. Venmans, H. van der Linden, H. Elbers, T. van Boxem, E. Smit, R. Postmus, and T. Sutedja. Observer variability in histopathologic reporting of bronchial biopsy specimens - influence on the results of autofluorescence bronchoscopy in detection of preinvasive bronchial neoplasia. *J Bronchology*, 7(3):210–214, 2000.

Chapter 11

High magnification endoscopy in the bronchi

11.1 Introduction

Since several decades, the physicians are able to access hollow organs with endoscopic methods, which serve both as diagnostic and surgical means in a wide range of disciplines of the modern medicine (urology, gastroenterology, pneumology,...). Over the last years, various endoscopic instrumentations were developed. The original rigid optics were gradually replaced with new devices, including fibroscopes, videoendoscopes, and recently high magnification and high-resolution endoscopes. White light (WL) endoscopy displays a poor sensitivity to (pre-)neoplastic lesions. Autofluorescence bronchoscopy (AFB) was developed to overcome this limitation. Current endoscopic methods based on the detection of autofluorescence achieve high sensitivity, but still lack specificity.

High rates of false positive results negatively affect the outcome of the AF diagnostic technique, in particular in the tracheo-bronchial tree [Verm99, Venm99, Lam00]. This issue has already been addressed by other authors using commercial systems based on violet autofluorescence excitation [Häuß99, Horv99, Iked99]. Some categories of atypical but noncancerous tissues (such as scar tissue, inflammation, and bruised mucosa) often appear positive under AFB [Häuß99].

Section 2.2.1.1 present the origins of AF contrast in the bronchi between healthy tissue and early neoplastic lesions. Summarily, this contrast is mainly due to the epithelium thickening and the increased vessel density below the AF+ lesions [Kenn01, Chha05, Gabr07, Gabr08]. Indeed, several authors have reported increased microvessel density in the sub-epithelial layer of bronchial squamous dysplasia and carcinoma in situ (CIS) [F.-E96, Font99]. Vascular changes are also found in pre-neoplastic, i.e. inflammatory and metaplastic lesions, but are characterized by vessel sizes and distribution patterns different from those observed in neoplastic and early cancerous lesions [F.-E96]. Therefore, inflammation and metaplasia exhibit a minor increase in the number of vessels along with increased vessel cross section surface, while angiogenesis in dysplasia and CIS is characterized by a significant increase in the number of small diameter vessels [F.-E96]. Moreover, in a high number of dysplastic lesions, the presence of capillaries being closely juxtaposed or even projecting into the bronchial epithelium have been reported [Keit00, Hirs01].

These lesions, termed angiogenic squamous dysplasia (ASD), are suspected to have a higher probability to become squamous cell carcinoma than dysplasia or CIS.

All differences in the neovascularization pattern are associated with differences in blood volume, and thereby hemoglobin concentration in the tissue. This is also true for bronchial tissues, as described by Qu *et al.* [Qu94]. Therefore, it is likely that developing new imaging capabilities (including vascular imaging) will facilitate discriminating mucosal changes.

Gabrecht *et al.* showed that hemoglobin content of the tissue has a dramatic impact on spectral contrast [Gabr07]. Indeed, after formalin fixation, neither spectral measurements nor imaging revealed spectral contrast between healthy bronchial tissue and (pre-)neoplastic lesions in formalin. These results indicate that epithelial thickening and blood supply in the adjacent lamina propria are likely to play a key role in the generation of the AF contrast in bronchial tissues.

These results are confirmed by Uehlinger *et al.* , who performed time-resolved measurements of tissue autofluorescence excited at 405 nm with an optical-fiber-based spectrometer in the bronchi of 11 patients [Uehl09]. No significant change in the AF lifetimes was found, suggesting that the spectral contrast might be due to an enhanced blood concentration just below the epithelial layers of the lesion. The intensity contrast probably results from the thickening of the epithelium in the lesions.

Yamada *et al.* observed many ramifying subepithelial microvessels of large airways in intercartilage and membranous portions, whereas only a few microvessels were seen in cartilage portions. Histologically, these subepithelial microvessels were thought to be distributed within approximately 800 and 500 μm beneath the surface of the intercartilage portions and membranous portions, respectively [Yama05].

Shibuya *et al.* report the characterization of vessels with high magnification, using either narrow-band imaging or autofluorescence as a detection method [Shib02, Shib03]. All the biopsy specimens from 16 normal fluorescence sites were found to consist of normal bronchial epithelium. Biopsy specimens from 43 abnormal fluorescence sites were diagnosed as 22 bronchitis and 21 dysplasia. Of the 21 bronchial dysplasia specimens, 17 lesions had morphological changes characteristic of angiogenic squamous dysplasia reported by Keith *et al.* [Keit00]. Immunohistochemical stains for CD34 confirmed the presence of endothelial cells lining the capillaries in the core of the papillary projections and subepithelial lamina propria. In this study, they observed subepithelial vessels L1, L2, and L3 of calculated size 42.2–84.3 μm, 41.4–82.7 μm, and 50.3-100.6 μm, respectively, at an observation depth of 1-3 mm. In histopathological analysis, the diameter of capillary blood vessels C1, C2, C3, and C4 in ASD were 49.9 μm, 47.6 μm, 34.4 μm, and 26.5 μm, respectively. Thus, the actual diameters seen in the histopathological samples roughly matched the vessel diameters seen by high magnification bronchoscopy, especially at an observation depth of 1 mm.

In a very recent report, the same authors repeated the measurements on various histopathological types (ASD, CIS, microinvasive, and invasive carcinoma) [Shib10]. First, high-resolution bronchovideoscopy with WL was performed. Observations were repeated using NBI light to examine microvascular structures in the bronchial mucosa. Spectral features of the RGB (red/ green/ blue) sequential videoscope system were changed from a conventional RGB filter to the new NBI filter. The wavelength ranges of the NBI filter were: 400–430 nm (blue), 400–430 nm (green), and 520–560 nm (red). Increased vessel growth and complex network of tortuous vessels of various sizes were clearly observed in ASD, whereas some additional dotted vessels were observed in squamous cell carcinoma. Capillary blood vessel and/or tumor vessel mean diameters of ASD, CIS, micro-invasive and invasive carcinoma were 41.4$\pm$9.8 μm, 63.7$\pm$8.2 μm, 136.5$\pm$29.9 μm, and 259.4$\pm$29.6 μm, respectively. These results indicated a statistically signif-

icant increase of mean vessel diameters in the four groups ($p < 0.0001$). These authors even described a vessel morphology evolution during lung cancer pathogenesis.

	Squamous dysplasia	ASD	CIS	Micro-invasive	Invasive
Tortuous vessel networks	+	+	–	–	–
Dotted vessels	–	+	+	++	+++
Spiral and screw type vessel	-	-	+	++	+++

Table 11.1: *Vessel morphology during lung cancer pathogenesis established by NBI imaging using high-resolution bronchovideoscope (adapted from [Shib10].*

At this point, we can draw a parallel with urology, where we also performed high magnification vascular imaging. The observed vascular patterns were used to discriminate the false from the true positive lesions in the bladder (see Chapter 5, published in [Lovi10]).

In collaboration with Richard Wolf GmbH, we developed a new prototype to integrate high magnification capability in AF and standard bronchoscopes. Due to the high false-positive rate related to AFB, there is a high interest in characterizing positive spots observed during autofluorescence bronchoscopy. In this chapter, we present a clinical evaluation of the modified AF bronchoscope to provide a proof-of-concept for its future clinical usage. For this study, we recruited patients belonging to high risk groups, in order to have a higher probability of finding flat lesions.

The main objectives of the clinical evaluation were the following:

1. To determine the appropriate magnification to see the small vessels located at the surface of the bronchial wall.

2. To determine the optimal spectral design for the detection of backscattered light between WL, green light and violet light.

3. To determine if the found magnification is compatible with the standard DAFE or WL macroscopic observations.

11.2 Materials and Methods

11.2.1 HM bronchoscope optical and mechanical characteristics

Two slightly different bronchoscopes were tested in the clinics :

Bronchoscope **A** HM DAFE bronchoscope, filtered, outer diameter 6 mm.

Bronchoscope **B** HM bronchoscope, non-filtered, outer diameter 5.3 mm, used to detect backscattered violet light.

For comparison purpose, we used two regular DAFE bronchoscopes :

Bronchoscope **C** DAFE bronchoscope, filtered, outer diameter 6 mm.

Bronchoscope **D** DAFE bronchoscope, filtered, outer diameter 5.3 mm.

The CCD detector used in both endoscopes has a diagonal size of 1/10 inch with 330'000 pixels. It is equipped with a cyan-magenta-yellow-green (CMYG) mosaic filter. A dedicated video processing unit, that delivers RGB-PAL signals to a monitor, is attached to the CCD. The CCD itself is placed in bronchoscope **A** behind a long-pass filter (LP455nm, Richard Wolf GmbH, proprietary filter) to allow fluorescence visualization, and in bronchoscope **B** behind a neutral density glass window to protect it during machine cleaning process.

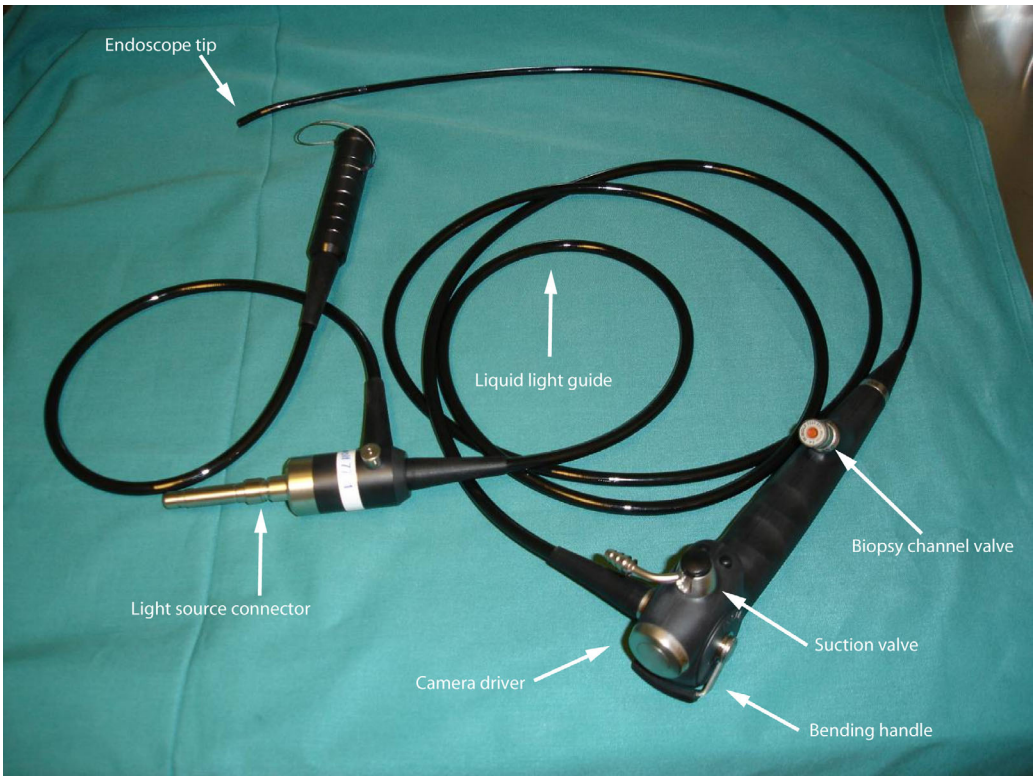

Figure 11.1: *Description of the HM bronchoscope assembly*

The two light channels convey the illumination light onto the tissue with the helps of embedded optical fibers. Both are placed symmetric relative to the CCD window.

The biopsy channel (2mm in diameter) allows the operator to: (i) spray liquid drug to induce local anaesthesia in the tracheo-bronchial tree (including pharynx, larynx, vocal cords and trachea); (ii) suck any secretion to avoid image blurring by mucous; (iii) insert instruments (e.g. biopsy forceps and brush) to assess histopathological status of the observed mucosa.

Similar to what was done in urology in order to enhance the contrast (see Appendix E), we placed bandpass filters in the light source in order to target the two hemoglobin absorption peaks. Sequentially, the flip-flop filter holder (with 3 positions) can be rotated to place the appropriate filters in front of the Xenon bulb. The three positions are filled with the following characteristics: a grid for white light (370–700 nm), a blue filter (405 nm FWHM 50 nm, proprietary AF filter, Richard Wolf GmbH) to excite AF and collect blue backscattered (BBS) images, and a green filter (550 nm, FWHM 50 nm, Chroma Technologies Inc.) to acquire green backscattered images (GBS). Images were collected either with the filtered (WL and GBS) or non-filtered HM bronchoscope (WL, GBS, and BBS).

Figure 11.1 depicts the HM bronchoscope with its connectors and valves, and Figure 11.2 depicts the main optical components at the distal end of the HM bronchoscope.

The resolution of the HM bronchoscope was assessed with the help of USAF target, in a similar manner to HM cystoscopy described in Section 5.2. Table 11.2 shows the comparison between conventional and HM bronchoscope. Unfortunately, the resolution is impaired when looking at the USAF target with blue light illumination (maybe due to chromatic aberrations in this wavelength range).

A direct comparison of the 5.3 mm and 6 mm bronchoscopes yields approximately the same

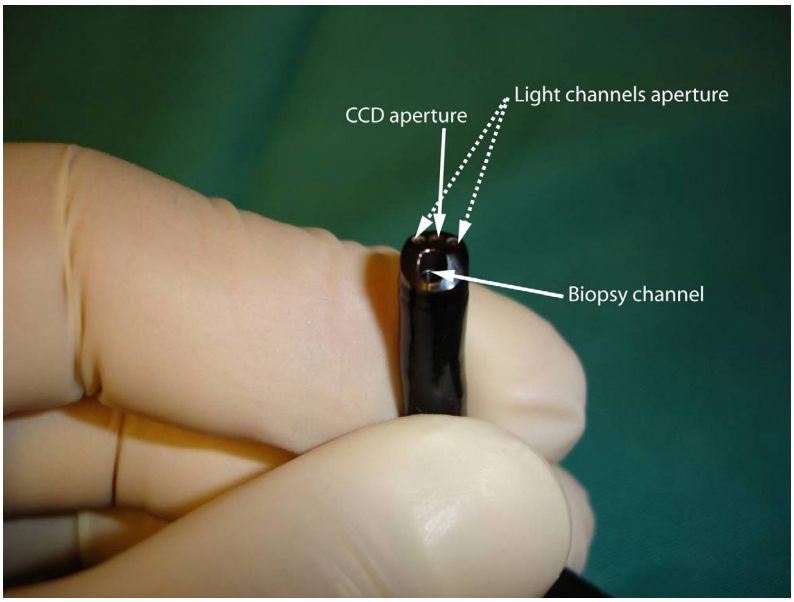

Figure 11.2: ***Distal end of the high magnification bronchoscope.*** *The white arrows show the main components (CCD, light channels, biopsy channel).*

	USAF Group & Element	line width [μm]	lp/mm
Conventional DAFE bronchoscope **C**			
White light	3-6	35.1	14.25
Blue light	3-3	49.6	10.08
HM bronchoscope **B**			
White light	5-1	15.6	32
Blue light	4-3	24.8	20.16

Table 11.2: *Resolution of the bronchoscopes*

FOV, despite the fact that they produce different apparent diameter on the screen (see Table 11.3). A full frame is assumed to be 720 pixels wide in the PAL video standard. The endoscope's magnification was increased by only shifting a lens inside the objective in order to get closer to the mucosa, without changing the focal length of the system [Webe10]. The relationship between the distance and the magnification is depicted in Figure 5.8 on page 100. The magnification — defined as the ratio between the real size and the size on 19" screen — ranged between 20–60× when the mucosa observed at 8 mm and 2 mm, respectively.

The angle of view is defined as follows, where the distance endoscope-USAF δ is 8.3 mm:

$$\alpha = 2 * \arctan\left(\frac{\mathrm{FOV}/2}{\delta}\right)$$

Endoscope type	Scope diameter [mm]	Screen diameter [pixels]	FOV [mm]	Angle of view
DAFE II **D**	5.3	331	11.86	71.10^o
DAFE II **C**	6	403	15.04	84.36^o
HM non-filtered **B**	5.3	513	15.14	84.73^o
HM filtered **A**	6	514	16.52	89.72^o

Table 11.3: *Field of view (FOV) of the bronchoscopes acquired at the same distance endoscope-USAF.*

11.2.2 Patient population

11 patients were recruited (mean age 68 years old, range 51–85). They were subject to routine fluorescence bronchoscopy (as a post-operative follow-up or pre-operative extension assessment). They were observed with the prototypes **A** and/or **B** in order to perform AFB and characterize the subepithelial vessels.

This clinical tests were hosted in CHUR Lille's endoscopy unit (lead by Dr. Philippe Ramon) and held on a two-days measurement campaign in April 2010. The procedure was done under local anesthesia to relax the throat muscles and diminish the coughing reflex. If needed, some relaxing medicine were given *per os* as a premedication (*e.g.* benzodiazepins). The patient remained sat for the whole procedure. The bronchoscope was usually inserted via the nose (exceptionally via the mouth when the nostrils were too small).

Unfortunately, no fluorescence positive areas were detected during this campaign. Therefore, the acquired images are not relevant for the characterization of any AF positive areas, but they can serve as a proof-of-principle of the high magnification bronchial imaging with our prototypes.

11.3 Results obtained in the clinics

The *in vivo* resolution is lower than that measured on the USAF target, but is sufficient to visualize small vessels. Indeed, the smallest observed vessel size was approximately 35 μm (see Figure 11.3). This lower resolution may be attributed to the non-ideal contrast observed between the bladder mucosa and the vessels, contrary to that measured on the USAF target's alternating black&white patterns observed (see Section 5.2.2).

We also directly compared the WL, DAFE, GBS, and BBS images (see Figure 11.4). The best contrast between the vessels and the *extravascular tissues* is obtained with green light, which is likely to be the optimal spectral design with the Wolf's bronchoscopes. WL images are not as contrasted but still "reasonable". Violet images are very bad due to the problems already identified in urology (see Appendix E). The latter are likely to be specific to this generation

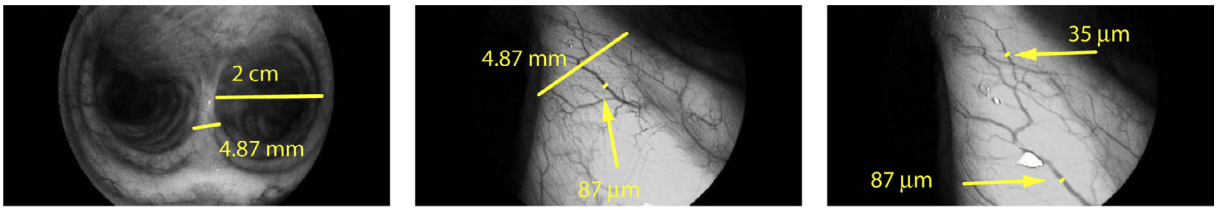

Figure 11.3: *Vessel resolution calculation based on the mean diameter of the main bronchi (2 cm). The images were acquired with green backscattered illumination, and are presented in grayscale.*

of the Wolf's instrumentations (poor overall sensitivity in the violet, optical aberrations, stray light, reflections on optical coatings ...).

We obtained similar results in all the patients that were investigated. Only few images are presented here, but the conclusions regarding resolution remain valid for all the observed areas.

11.4 Discussion

As it can be seen in the images presented above, the resolution is sufficient to visualize the reshaping of the vessel architecture due to early carcinogenesis. The observed vessel sizes are fairly compatible with those observed by Shibuya *et al.* [Shib10]. These preliminary encouraging results are clearly suggesting that, in the near future, we will be able to collect images on tissues corresponding to all kind of hystopathologic status to generate an "atlas" of images. In this atlas, we will record the optimal blood vessel features to be observed (tortuosity; vascular mesh density, loops, ... and other Shibuya's criteria) in order to differentiate true and false positives. The image analysis software developed for similar images obtained in the bladder will also be customized to describe qualitatively the observed vascularization patterns in the tracheo-bronchial tree.

Although the optical design is not the same between the 6 mm and 5.3 mm bronchoscopes, we observed that the field of view of bronchoscope **B** is almost the same than that of the bronchoscope DAFE **C**. In a next generation, we may implement a higher resolution chip to let the vessels be even better demarcated (due to the higher pixel density).

The color presentation has still to be improved in order to avoid intensity saturation in the color channels, since saturated channels do not contain any information. Color reallocation and digital scaling of the dynamic range may be effective in order to improve the vessel visualization. For instance, the two images presented in Figure 11.5 are two subsequent frames illuminated with green light. The two images differs by the camera controller mode. On the left part, the image is still in DAFE mode with the corresponding color balance. On the right part, the image is now in WL mode with a clear dazzling in the green channel (i.e. loss of information due to intensity saturation). One can clearly see the better vessel definition when the image color channels are not saturated. In the future, when design the color intensification patterns, we may bear this in mind.

These preliminary results with GBS and BBS showed a more contrasted and more superficial vascularization that is hardly invisible with standard WL. Therefore, we came to the conclusion that an objective of crucial importance is to identify the optimal wavelength to be used for this characterization of positive sites.

In conclusion, although this project was postponed to the last end of my thesis due to a manufacturing delay, we showed that this magnification is sufficient to identify vessel of interests,

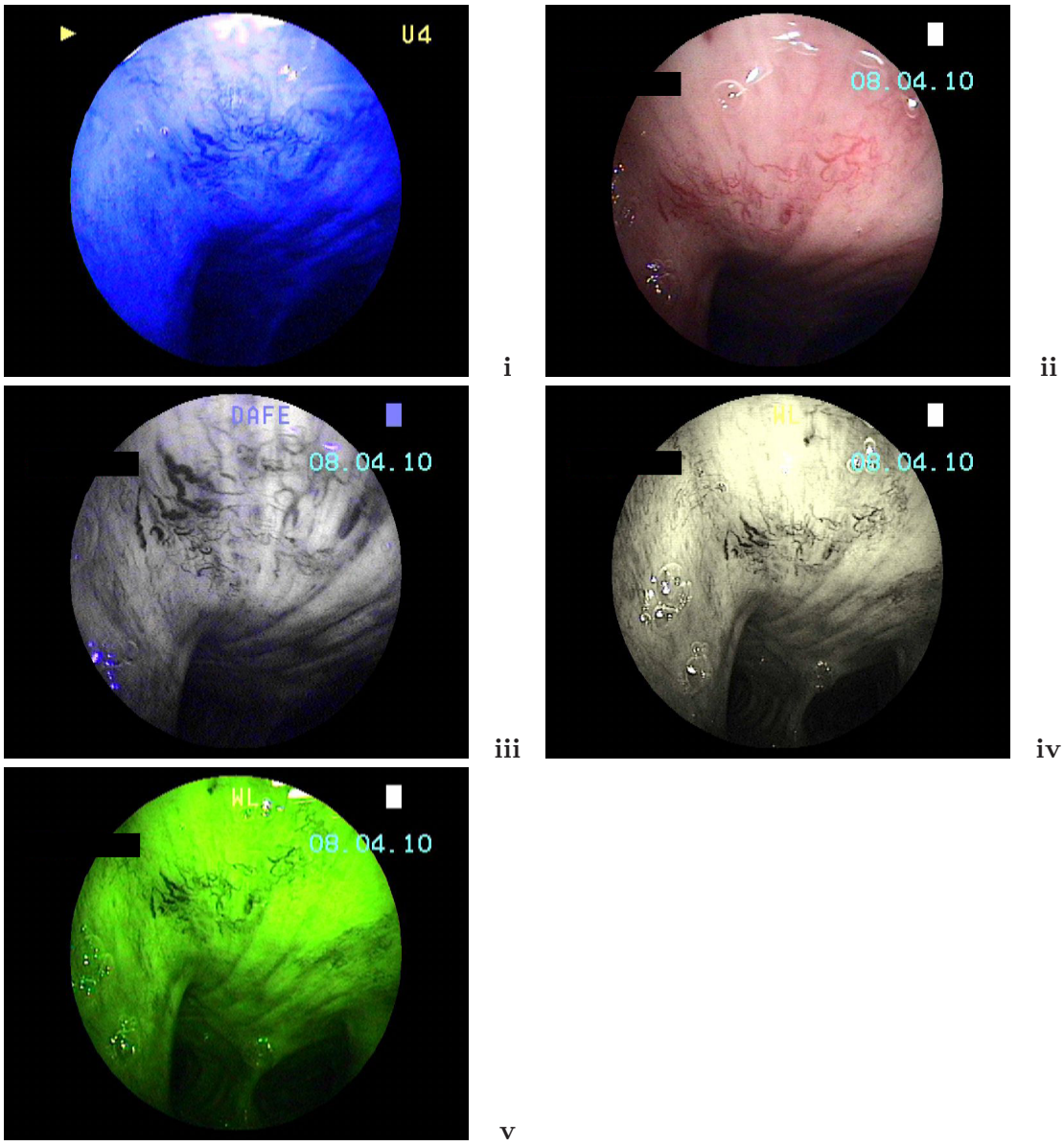

Figure 11.4: ***Comparison of different illumination modes while looking at the same suspicious site.*** *(**i**) BBS (bronchoscope B), WL mode; (**ii**) WL (A), WL mode; (**iii**) Blue light (A), DAFE mode; (**iv**) GBS (A), DAFE mode; (**v**) GBS (A), WL mode*

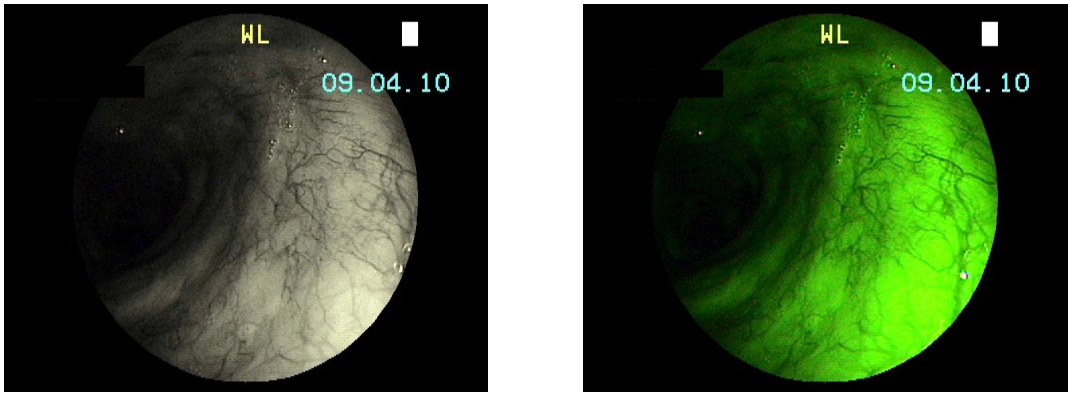

Figure 11.5: *Comparison of camera intensification mode. On the left, green illumination in WL mode. On the right, green illumination in DAFE mode.*

and that targeting hemoglobin peaks is a good approach the enhance the contrast vessel-to-background. Additionally, the physician did appreciate the better resolution as compared to the regular DAFE bronchoscope and was pleased to use the higher magnification, showing that this HM bronchoscope is fully compatible with the clinical routine.

Bibliography

[Chha05] P. Chhajed, K. Shibuya, H. Hoshino, M. Chiyo, K. Yasufuku, K. Hiroshima, and T. Fujisawa. A comparison of video and autofluorescence bronchoscopy in patients at high risk of lung cancer. *European Respiratory Journal*, 25(6):951–955, 2005.

[F.-E96] A. Fisseler-Eckhoff, D. Rothstein, and K. Müller. Neovascularization in hyperplastic, metaplastic and potentially preneoplastic lesions of the bronchial mucosa. *Virchows Arch*, 429(2-3):95–100, 1996.

[Font99] G. Fontanini, A. Calcinai, L. Boldrini, M. Lucchi, M. Mussi, C. Angeletti, C. Cagno, M. Tognetti, and F. Basolo. Modulation of neoangiogenesis in bronchial preneoplastic lesions. *Oncol Rep*, 6(4):813–817, 1999.

[Gabr07] T. Gabrecht, S. Andrejevic-Blant, and G. Wagnières. Blue-violet excited autofluorescence spectroscopy and imaging of normal and cancerous human bronchial tissue after formalin fixation. *Photochem Photobiol*, 83(2):450–458, 2007.

[Gabr08] T. Gabrecht, A. Radu, P. Grosjean, B. Weber, G. Reichle, L. Freitag, P. Monnier, H. van den Bergh, and G. Wagnières. Improvement of the specificity of cancer detection by autofluorescence imaging in the tracheo-bronchial tree using backscattered violet light. *Photodiagnosis Photodyn Ther*, 5(1):2–9, Mar 2008.

[Hirs01] F. Hirsch, W. Franklin, A. Gazdar, and J. Bunn P.A. Early detection of lung cancer: Clinical perspectives of recent advances in biology and radiology. *Clinical Cancer Research*, 7(1):5–22, 2001.

[Horv99] T. Horvath, M. Horvathova, F. Salajka, B. Habanec, L. Foretova, J. Kana, H. Koukalova, P. Pafko, F. Wurst, E. Novotna, J. Pecina, V. Vagunda, R. Vrbacky, R. Talac, H. Coupkova, and Z. Pacovsky. Detection of bronchial neoplasia in uranium miners by autofluorescence endoscopy (safe-1000). *Diagnostic and Therapeutic Endoscopy*, 5(2):91–98, 1999.

[Häuß99] K. Häußinger, F. Stanzel, R. Huber, J. Pichler, and S. H. Autofluorescence detection of bronchial tumors with the d-light/af. *Diagnostic and Therapeutic Endoscopy*, 5(2):105–112, 1999.

[Iked99] N. Ikeda, H. Honda, T. Katsumi, T. Okunaka, K. Furukawa, T. Tsuchida, K. Tanaka, T. Onoda, T. Hirano, M. Saito, N. Kawate, C. Konaka, H. Kato, and Y. Ebihara. Early detection of bronchial lesions using lung imaging fluorescence endoscope. *Diagnostic and Therapeutic Endoscopy*, 5(2):85–90, 1999.

[Keit00] R. Keith, Y. Miller, R. Gemmill, H. Drabkin, E. Dempsey, T. Kennesy, S. Prindiville, and W. Franklin. Angiogenic squamous dysplasia in bronchi of individuals at high risk for lung cancer. *Clinical Cancer Research*, 6(5):1616–1625, 2000.

[Kenn01] T. Kennedy, S. Lam, and F. Hirsch. Review of recent advances in fluorescence bronchoscopy in early localization of central airway lung cancer. *Oncologist*, 6(3):257–262, 2001.

[Lam00] S. Lam, C. MacAulay, J. C. leRiche, and B. Palcic. Detection and localization of early lung cancer by fluorescence bronchoscopy. *Cancer Suppl.*, 89(11):2468–2473, 2000.

[Lovi10] B. Lovisa, P. Jichlinski, B.-C. Weber, D. Aymon, H. van den Bergh, and G. Wagnières. High magnification vascular imaging to reject false-positive sites in situ during hexvix fluorescence cystoscopy. *Journal of Biomedical Optics*, 15(5):in press, 2010.

[Qu94] J. Qu, C. MacAulay, S. Lam, and B. Palcic. Optical properties of normal and carcinomatous bronchial tissue. *Applied Optics*, 33(31):7397–7405, 1994.

[Shib02] K. Shibuya, H. Hoshino, M. Chiyo, K. Yasufuku, T. Iizasa, Y. Saitoh, M. Baba, K. Hiroshima, H. Ohwada, and T. Fujisawa. Subepithelial vascular patterns in bronchial dysplasias using a high magnification bronchovideoscope. *Thorax*, 57(10):902–7, 2002.

[Shib03] K. Shibuya, H. Hoshino, M. Chiyo, A. Iyoda, S. Yoshida, Y. Sekine, T. Iizasa, Y. Saitoh, M. Baba, K. Hiroshima, H. Ohwada, and T. Fujisawa. High magnification bronchovideoscopy combined with narrow band imaging could detect capillary looops of angiogenic squamous dysplasia in heavy smokers at high risk for lung cancer. *Thorax*, 58(11):989–995, 2003.

[Shib10] K. Shibuya, T. Nakajima, T. Fujiwara, M. Chiyo, H. Hoshino, Y. Moriya, M. Suzuki, K. Hiroshima, Y. Nakatani, and I. Yoshino. Narrow band imaging with high-resolution bronchovideoscopy: A new approach for visualizing angiogenesis in squamous cell carcinoma of the lung. *Lung Cancer*, in press:NA, Jun 2010.

[Uehl09] P. Uehlinger, T. Gabrecht, T. Glanzmann, J.-P. Ballini, A. Radu, S. Andrejevic, P. Monnier, and G. Wagnieres. In vivo time-resolved spectroscopy of the human bronchial early cancer autofluorescence. *Journal of Biomedical Optics*, 14(2):024011, 2009.

[Venm99] B. Venmans, T. van Boxem, E. Smit, P. Postmus, and T. Sutedja. Results of two years experience with fluorescence bronchoscopy in detection of preinvasive bronchial neoplasia. *Diagnostic and Therapeutic Endoscopy*, 5:77–84, 1999.

[Verm99] P. Vermylen, P. Pierard, C. Roufosse, T. Bosschaerts, A. Verhest, J. P. Sculier, and V. Ninane. Detection of bronchial preneoplastic lesions and early lung cancer with fluorescence bronchoscopy: a study about its ambulatory feasibility under local anaesthesis. *Lung Cancer*, 25(3):161–8, 1999.

[Webe10] B.-C. Weber. Modifying a standard bronchoscope to allow high magnification imaging. private communication, 2010.

[Yama05] G. Yamada, H. Takahashi, N. Shijubo, T. Itoh, and S. Abe. Subepithelial microvasculature in large airways observed by high-magnification bronchovideoscope. *Chest*, 128(2):876–880, 2005.

Chapter 12

Conclusions and future prospects in bronchoscopy

The main aims of the second part of this manuscript were to optimize the photodetection instrumentation of bronchial cancer, and to find an efficient method to characterize the false-positive lesions associated with autofluorescence bronchoscopy. It consists basically of a translation into the tracheo-bronchial tree of the methods used successfully in the urinary tract. Despite the fact that the chromatic contrasts between the tumor and healthy background do not have the same origin (exogenously induced porphyrin fluorescence vs. autofluorescence), similar improvement methods can be implemented in bronchoscopy. For instance, high magnification vascular imaging is likely to be a reliable characterization method to evaluate the vascular patterns underlying (pre-)early neoplasia in the bronchi.

In this manuscript, several clinical and *ex vivo* imaging and spectrofluorimetric studies were performed to gain insight on the optical characterization of bronchial carcinoma, defining further possibilities to increase the sensitivity and specificity of photodetection.

In Chapter 8, we first evaluated whether a violet narrow-band (with a Krypton laser) excitation would improve the intensity contrast in the AF green spectral region. For each observed site *in vivo*, we showed that the healthy/tumor ratio in the green channel for the narrow-band excitation exceeds that for the broadband excitation, with a mean ratio equal to 1.43±0.20. However, in this study, since no red fluorescence intensity could be measured due to the red backscattered light, no valid statement about spectral contrast could be made. However, we may speculate that the red AF excited more superficially with narrow-band excitation is less absorbed by the epithelial thickening as would be the case with the broadband excitation. Similarly, the narrow-band violet light would not reach the increased vessel density, and would not yield a spectral contrast. Consequently, the red AF may not be modified by the excitation bandwidth. Since violet LEDs will be used in the future as endoscopic light source (see Chapter 6), this statement can be of interest for a technology transfer in the clinical environment.

In Chapter 9, we presented two studies aiming to quantify the intra- and inter-patient variations in the AF intensities in order to optimize the spectral response and the settings of the endoscopic fluorescence imaging (EFI) system. For this purpose, we developed a fluorescence

reference – with optical properties similar to the bronchial AF – to be placed endoscopically near the bronchial mucosa. The observed inter-patient variations for the AF intensity measured on the carina were in the order of 25–30%, which is less marked than in previously published spectroscopic studies (∼50%). Nevertheless, with this study, we obtained this good estimation of the AF variations, that helped to scale the dynamic range of future AFB systems.

Even if fluorescence endoscopy is a well established method for the detection of early carcinoma, instrumentation has still to be tested for its reliability over time. In Appendix D, we developed some fluorescence validation samples to assess the performance of the instrumentation. Several phantoms were developed. In the future, a validation procedure should be implemented on endoscopic clinical devices, because if a device is not functioning properly, it may reduce the clinical outcome of this imaging technology.

In Chapter 10 and Appendix A, we evaluated two generations of EFI prototypes. In Appendix A, we specifically reviewed what AFB can bring to H&N cancer patients. We were able to show that the additional use of AFB procedure induced a change of management in about 15% of the patients in our cohort of high-risk H&N cancer patients. Additionally, we showed that adding an online thresholding algorithm to the AFB procedure results in a rejection of about 90% of the AF false positive. In Chapter 10, we evaluated the clinical performance of the DAFE II prototype. No false-negative were observed with this AF bronchoscopy prototype. Additionally, more CIS were detected with AFB as compared with WL bronchoscopy. Since it has a negative predictive value close to 100%, this prototype can effectively reduce the number of biopsies on WL suspicious areas, that do not appear suspicious in autofluorescence (WL+/AF−). This new prototype has been shown to be very sensitive to early modifications of the bronchial mucosa, and may be considered as a serious candidate for an implementation in the clinical routine. Several physicians have reported that many biopsies can be spared thanks to AFB's very high negative predictive value. Additionally, the images acquired with the new system have a better texture than conventional WL images. For instance, when observing the alternating light and dark longitudinal stripes in the bronchial wall, they can better distinguish discrete irregularities, invisible in WL. Consequently, AFB can effectively serve as a guidance tool, even for the experienced bronchoscopist.

Lastly, we conducted some preliminary works in order to implement high magnification reflectance imaging in the tracheo-bronchial tree to characterize the false-positive lesions resulting from autofluorescence bronchoscopy. Chapter 11 shows some optical characterization of our high magnification bronchoscope. The preliminary measurement campaign showed that vessels with a diameter of about 30 μm could be resolved with this HM bronchoscope. This is likely to be sufficient to identify Shibuya's criteria (loops, meshes, dotted vessels) on AF positive lesions [Shib10]. In the future, we will characterize early cancers to see if this HM imaging procedure also allows to reject false positive lesions as it is the case in the bladder.

Concurrent groups have also added some backscattered light to their EFI system. It allows better discrimination of mucus, blood and mucosal alteration, but lowers the intrinsic red-green contrast.

All technical improvements already discussed in Chapter 6 will obviously also have an impact on bronchoscopy. Recent developments in OCT identified microstructures of normal bronchial mucosa, including epithelium and lamina propria. OCT features of malignancy included loss of normal, identifiable microstructures and subepithelial "optical fracture" of tissues [Mich10]. This OCT probe is also limited in resolution (10–20 μm, depth resolution, and 20–25 μm, a lateral resolution), but the imaging depth of 2.2 mm allow penetration through the upper layers of exposed tissues on airway surfaces, where many airway neoplasms may present, and are equivalent to the tissue sampling depth of conventional endobronchial forceps.

At this point, it should be noted that the development of patient screening procedures will have a dramatic impact on EFI's patient population. Indeed, current AFB inclusion criteria include smoking or ex-smoking patients, with known or suspected H&N lesions and/or known or suspected lung cancer. They may be narrowed down by an effective screening procedure (such as second generation sputum analysis, genetic testing or breath test). It is likely that patient benefit related to AFB will be even higher in high risks patients.

Bibliography

[Mich10] R. G. Michel, G. T. Kinasewitz, K.-M. Fung, and J. I. Keddissi. Optical coherence tomography as an adjunct to flexible bronchoscopy in the diagnosis of lung cancer: A pilot study. *Chest*, in press, May 2010.

[Shib10] K. Shibuya, T. Nakajima, T. Fujiwara, M. Chiyo, H. Hoshino, Y. Moriya, M. Suzuki, K. Hiroshima, Y. Nakatani, and I. Yoshino. Narrow band imaging with high-resolution bronchovideoscopy: A new approach for visualizing angiogenesis in squamous cell carcinoma of the lung. *Lung Cancer*, in press:NA, Jun 2010.

Remerciements

Au moment de rédiger ces quelques lignes, il me vient à l'esprit beaucoup de visages qui ont rendu ma thèse fascinante, beaucoup de discussions qui ont permis de pousser un petit peu plus loin le vaste navire de la connaissance, beaucoup d'amitiés qui sont nées au cours de ce temps passé entre l'EPFL et le CHUV.

Mes premiers mots vont naturellement vers ceux qui m'ont ouvert les portes de leur laboratoire, Prof. Hubert van den Bergh et Dr Georges Wagnières. Au sein de ce qui était encore à mon arrivée en 2005 un labo de pollution atmosphérique dans la faculté ENAC, ils ont mis en place une équipe pluri-disciplinaire, où la biologie féconde la physique, et la chimie engendre des progrès en médecine. Je les remercie ici pour les nombreuses discussions constructives, parfois dilatoires, souvent porteuses de solutions à mettre en oeuvre pour la conduite de mes projets de recherche. La route n'était pas toute tracée à l'avance, merci d'avoir orienté ma boussole lorsque cela fut nécessaire.

Merci au Prof. Jacques Moser, au Dr Walter Blondel, aux Profs Patrice Jichlinski et Christian Depeursinge d'avoir officié dans mon jury de thèse. Vos remarques et vos commentaires ont permis de faire positivement évoluer ce manuscrit. Soyez-en chaleureusement remerciés.

De nombreuses personnes ont contribué à ma thèse au sein de l'ex-LPAS. Un souvenir ému pour Jean-Pierre Ballini, décédé quelques jours avant mon dépôt de manuscrit. Sa disponibilité, son savoir inépuisable, son humour discret et notre gourmandise partagée ont marqué durablement ma mémoire. Puisse l'esprit qu'il a insufflé à notre groupe donner naissance à de nouveaux projets. Merci à Véronique, notre secrétaire à-tout-faire, grâce à qui tout fonctionne avec simplicité et efficacité. Merci à ses apprenties, Stefania, Gaëlle et Roxane, d'avoir rempli notre économat, nettoyé la machine à café, et surtout apporté un vent de fraîcheur juvénile à notre équipe. Merci à Flavio, notre mécanicien, qui a su transformer mes vagues brouillons en pièces magnifiques grâce à sa précision et son savoir-faire. Merci à André, électronicien, avec qui l'heure du café n'a jamais manqué d'animation, ni politique, ni internautique. Merci à Eddy, ardent défenseur de l'espéranto, pour les discussions humanistes qui ont souvent alimenté notre conversation.

J'ai également le plaisir de remercier mes collègues (post-)doctorants. Merci à Tanja d'avoir partagé son bureau, ses nuits blanches et sa longue expérience en bronchoscopie. Egalement d'avoir concocté pour nous d'innombrables merveilles culinaires, au gré des sorties et des anniversaires. Merci à Filippo, mon "Doktorbruder", pour sa bonne humeur revigorante, pour son envie de plein air, pour nos discussions enrichissantes pendant ces 5 ans partagés. Merci aux filles du CAM, Bernadette, Elodie et Patrycja, pour leur délicate amitié. Au fil des ans, elles ont su m'expliquer les subtilités de l'omelette. Merci à Jérôme, devenu épilateur professionnel, pour ses conseils appréciés en biologie et sucreries méridionales. Merci aux nouveaux arrivés Doris, Anna-Maria et Cédric pour les quelques mois que nous avons partagés, en attendant impatiemment la suite de votre carrière scientifique. Merci à nos indiens Santha et Senthil pour leur apport culturel indéniable. Merci à Céline et Martin pour votre coup de main apprécié lors de votre travail chez nous. C'était chouette de pouvoir converser avec toutes vos nouvelles idées. Merci aux anciens du labo, François, Pascal, Matthieu, Thomas et Nora, pour vos travaux qui ont permis l'émergence de mon sujet de thèse, ainsi que pour les moments d'amitié lors des repas partagés. Merci à Roland et Alain de Medlight SA pour leur disponibilité et leurs conseils appréciés pour la confection des fibres optiques. Merci à tous les anciens du grand LPAS d'avoir partagé le 5ème étage du CH: Carine, Mireille, Ari, Simone, Pascal, Federico, Michel, Todor, Valentin, Marian, Alain, Andrea, Erika, Clive, et tous ceux que j'oublie.

Mon travail n'aurait pas pu se faire sans une solide équipe clinique. Ma gratitude va tout d'abord aux Profs Philippe Monnier (ORL), Philippe Leuenberger et son successeur Laurent Nicod (Pneumologie), Hans-Jürg Leisinger et son successeur Patrice Jichlinski (Urologie) pour l'accueil réservé à votre serviteur et à nos dispositifs instrumentaux au CHUV. L'espace-temps du CHUV n'est pas incompressible et vous avez su m'y réserver une place. Un merci particulier au Prof. Jichlinski, pour m'avoir souvent ouvert son bureau le temps d'une discussion afin que notre recherche soit vraiment mise au service des patients. Pour l'étude DAFE, un merci spécial au Drs Alain Sauty, Philippe Pasche et François Heinzer pour leur enthousiasme initial.

Au risque d'en oublier, je remercie en bloc et dans le désordre tous les médecins cadres et assistants qui se sont prêtés de bonne grâce à mes investigations : Drs John-David Aubert, Florian Barras, Alessandro Bonetti, Christophe Brossard, Mohamed Cherif Ahmed, Yves Chollet, Lucie Cikirikcioglu, Arnaud Doerfler, Timothy Edney, Bernard Egger, Ziad El Lamaa, Jean-William Fitting, Pierre Grosjean, Barbara Hauler, Christos Ikonomidis, Etienne Jacot, Yves Jaquet, Florian Lang, Elisabeth Langenskiold, Igor Leuchter, Jesica Mazza Stalder, Yan Monnier, Bruno Naccini, Solange Nahum, Micaela Odman Jaques, Frédéric Olivier, Elsa Piotet, Valentin Praz, Alexandre Radu, Daniel Schroeder, David Sistek, Cécile Tawadros, Thomas Tawadros, Cédric Treuthardt, Yves Trisconi, Matieu Uffer, Laurent Vaucher, Jean-Frédéric Vodoz, Aurélia Wavre, Yassine Zarkik, Yannick Zaugg. Merci à la Dresse Snezana Andrejevic-Blant, ainsi qu'à toute l'équipe du Bugnon 25, pour leurs compétences pathologiques et microsopiques. Merci aux anesthésistes par la Dresse Madeleine Chollet, d'avoir bien voulu dilater leur chronomètre pour permettre mes mesures. Merci à l'équipe de la Clinique Cécil, par Isabelle Ansermet, pour leur accueil cordial. L'équipe clinique ne serait pas complète si j'oubliais tous ceux qui font que l'étage dédié à l'endoscopie (le zéro-sept) puisse fonctionner. Merci aux ICS et ICUS, Sylvie, Isabel et Petra d'avoir ouvert toutes les portes. Merci aux infirmières instrumentistes Brigitte, Assia, Noémie, Deborah, Marie-Hélène, Vanina, Marzia, Aurore, Doriana et les autres pour leur aide précieuse. Merci aux aides, en particulier l'infatigable Gianmarco, Giuseppe, Elsa, Aurea, Louise, Victorine, Claudio, pour leur savoir universel dans toutes ces petites choses qui m'ont grandement facilité la vie. Merci à Daniela, pour ses archives et son organisation très appréciés pour les études en urologie. Merci à Marie d'avoir collecté les documents DAFE à la volée.

Un merci à ceux qui ont contribué au financement de ma thèse: le Fonds National Suisse pour la Recherche Scientifique, au Dr. Julia Jacobi, ainsi que l'entreprise Richard Wolf GmbH, avec qui s'est installée une collaboration prometteuse. Dans ce contexte, merci au Dr Bernd-Claus Weber et Antoine Baur pour nos nombreux échanges en vue de l'amélioration de l'endoscopie de fluorescence.

Merci à Aurèle et Raphaël, pour leur clepsydre bienveillante dans nos voyages quotidiens et leurs encouragements alors que l'horizon de fin de thèse n'était pas très dégagé. Merci à tous ceux que j'ai pu côtoyer dans les murs extensibles de l'EPFL–CHUV et que j'oublie de citer ici.

Dans un registre plus personnel, j'aimerais rendre hommage à mes parents, que j'aurais tellement aimé pouvoir associer à cette fin de thèse. Ils furent tous deux emportés par le cancer, et je leur dois un amour tenace pour la vie avec de belles valeurs à défendre. Merci à toute ma famille, en particulier mes trois soeurs pour leur présence indispensable dans tous ces moments joyeux et tristes qui ont jalonné notre vie de famille ces dernières années. Merci à tous ceux avec qui j'ai fait de la montagne, de la musique chorale et d'autres aventures, d'avoir permis des respirations au milieu de ces années de thèse.

Enfin, je dis merci à Sophie, celle qui partage ma vie avec bonheur et amour depuis quelques années, ainsi qu'à Timothée, notre petit rayon de soleil virevoltant et éternel, qui m'a récemment soufflé à l'oreille du haut de ses deux ans: « Papa, fini thèse ? ».

Appendix A

Clinical experience in H&N cancer patients

Head and neck (H&N) cancer patients have a high incidence of second primary tumors in the tracheobronchial tree, which affects the patient prognosis and management [Sava91]. The prevalence of second primary lesions in H&N cancer patients is estimated to be between 7% and 21%, and about 63% of the metachronous second primary tumors are located in the lung and the esophagus [Stoe01].

Glanzmann *et al.* reviewed three different types of application of early cancer detection can be distinguished [Glan03]: (1) Large scale screening studies in high risk population; (2) tumor demarcation prior to surgery, and (3) patient follow-up in order to detect lung cancer recurrence and second primaries. The latter will be treated in this chapter with a special dedication on patients with a primary cancer in the H&N area.

Indeed, this chapter reviews the medical and therapeutic impact of AFB in a population of 21 (H&N) patients. This study showed that management of patients with H&N cancers can be dramatically altered using AFB. Indeed, 11 lesions in 8 patients were found with the combined autofluorescence-thresholding method. Two of these patients discontinued the medical follow-up in our medical facility. In the remaining six patients presenting a total of nine AF+ lesions, the clinical management was changed as a consequence of the observations with AFB. More precisely, all these patients were proposed additional treatment options for their second primary cancers in the tracheo-bronchial tree. Treatments proposed were radical surgery (n=2), CO_2 laser resection (n=1) and photodynamic therapy (PDT) (n=3). Of the nine lesions, four were invisible with the WL bronchoscopy. These four lesions were found in 3 patients. Consequently, the additional use of AF/T procedure induced a change of management in three of 19 (21-2 patients not followed up), i.e. about 15% in our cohort of high-risk H&N cancer patients.

Summarily, in addition to screening procedure in pneumology unit, AFB can be of great help also for patients with a primary H&N cancer, since the probability to develop a second meta- or synchronous bronchial cancer is high for these patients.

The work presented in the published article was mainly done by Tanja Gabrecht. The main role of the author of this manuscript was to help for clinical data acquisition, collect the patients data, and some offline statistical work to quantify the variations related the receiver-operator characteristics (ROC) curve.

Available online at www.sciencedirect.com
ScienceDirect
Medical Laser Application 22 (2007) 185–192
Medical Laser Application
www.elsevier.de/mla

Autofluorescence bronchoscopy: Clinical experience with an optimized system in head and neck cancer patients

Tanja Gabrecht[a], Alexandre Radu[b], Matthieu Zellweger[a], Blaise Lovisa[a], Didier Goujon[a], Pierre Grosjean[b], Hubert van den Bergh[a], Philippe Monnier[b], Georges Wagnières[a,*]

[a]*Swiss Federal Institute of Technology (EPFL), Laboratory of Photomedicine, SB ISIC-GE, Building CH, Station 6, 1015 Lausanne, Switzerland*
[b]*The CHUV University Hospital, Department of Otolaryngology and Head and Neck Surgery, 1011 Lausanne, Switzerland*

Received 31 August 2007; accepted 4 September 2007

Abstract

Head and neck (H&N) cancer patients have a high incidence of second primary tumors in the tracheobronchial tree, which affects the patient prognosis and management. Diagnostic autofluorescence endoscopy (AFB) has shown promising results in the detection of early neoplastic and pre-neoplastic changes in the bronchi. We have investigated the medical and therapeutic impact of AFB in a population of 21 H&N cancer patients using a modified commercially available AFB system. That allows both white light (WL) and autofluorescence (AF) observation. Endoscopic imaging of the tissue AF was combined with an online image analysis procedure improving the discrimination between true and false positive results. Forty-one biopsies were taken on macroscopically suspicious (WL or AF positive) bronchial sites. Histopathologic analysis confirmed pre- or early neoplastic changes in 11 of these biopsies taken from eight patients. All these lesions had been AF positive upon bronchoscopy. The sensitivity for the detection of these early lesions with the AFB was 1.6 times the sensitivity of WL bronchoscopy alone. The positive predictive value (PPV) for AF was 79% (33% for WL alone) while the PPV of both methods together was 100%. We could demonstrate that AFB is efficient for the detection of second primary lesions of the bronchi in H&N cancer patients. In conclusion, AFB can be used as a simple and minimally invasive additional procedure to pre-operative or follow-up examination in this patient population.

Keywords: Autofluorescence bronchoscopy; Early cancer; Head and neck cancer; ENT; Second primary carcinoma; Specificity; Sensitivity; Online image analysis; Therapeutic management

Introduction

Patients with head and neck (H&N) squamous cell carcinoma have a high risk of second synchronous and metachronous second primary carcinoma in the aero-digestive tract [1–3]. The prevalence of second primary lesions in H&N cancer patients is estimated to be

*Corresponding author. Tel.: +41 21 693 3120; fax: +41 21 693 5110.
E-mail address: georges.wagnieres@epfl.ch (G. Wagnières).

1615-1615/$ - see front matter © 2007 Elsevier GmbH. All rights reserved.
doi:10.1016/j.mla.2007.09.003

between 7% and 21% [4], and about 63% of the metachronous second primary tumors are located in the lung and the esophagus [4].

The presence, localization and characteristics of such lesions affect the patient prognosis and may modify the patient management. This is the reason why many authors recommend to examine the full upper aerodigestive tract prior to a definitive treatment decision, but also for follow-up examination in H&N cancer patients [4,5]. Detection of such neoplastic or pre-neoplastic conditions mostly relies upon chest X-ray, PET scan and upper aerodigestive tract endoscopy, i.e. the so-called panendoscopy. Among these detection methods, panendoscopy, i.e. more precisely bronchoscopy, is the only established method that allows detection and localization of central bronchial lesions and tissue sampling for histopathological examination. However, all these conventional detection methods frequently fail to detect pre-neoplastic and even early neoplastic lesions in the bronchi. Indeed, white light bronchoscopy (WLB) was reported to detect less than 40% of high-grade dysplasia in the central airways [6,7].

Diagnostic autofluorescence bronchoscopy (AFB) has shown the potential to significantly increase the number of detected lesions compared with conventional WLB increasing the sensitivity of bronchoscopy for pre-neoplastic and early neoplastic lesions by a factor of about 2 [7–10].

While conventional WLB is based on the detection of minimal alterations in tissue surface structure, AFB exploits the spectral and intensity contrast of the tissue intrinsic fluorescence (autofluorescence) between normal bronchial mucosa and pre-neoplastic or neoplastic tissue changes. This contrast consists in a general decrease in the AF intensity for (pre-)neoplastic tissue compared with normal mucosa [11] as well as in a change of the spectral shape. The latter results from the fact that the decrease in the autofluorescence intensity is more important to wavelength below 600 nm (green spectral region) than to wavelength above this transition wavelength (red spectral region) [11]. This decrease can be visualized by specific endsocopic imaging devices. In most cases, due to the three-dimensional geometry of the bronchi, a second background image is obtained in the red part of the spectrum, to perform a contrast enhancement procedure between the contrast bearing green and the non-contrast bearing red images. Several AFB systems are commercially available nowadays.

To date, diagnostic fluorescence bronchoscopy has mostly been used in H&N cancer patients as surveillance for metachronous neoplasia [12] rather than to detect synchronous primary lesions at the time of initial diagnosis.

Despite its potential, AFB is not widely used to detect synchronous disease at panendoscopy and its medical impact has not been reported in terms of its ability to change the patient's management. However, in a recently published study, Fielding et al. [13] reported the benefit of AFB panendoscopy in newly diagnosed and follow-up H&N cancer patients.

We present here the clinical results of a study conducted in a population of high-risk H&N patients to evaluate the benefit of AFB in this patient population. An online image analysis approach was used to improve the sensitivity of AFB.

Materials and methods

The diagnostic autofluorescence endoscopy system

Diagnostic autofluorescence bronchoscopy was performed with a modified AFB system (Richard Wolf GmbH, Knittlingen, Germany) illustrated in Fig. 1. The AFB system is described in details elsewhere [14]. Briefly, it was based on a filtered endoscopic 300 W Xenon light projector and a filtered 3 CCD endoscopic color camera. The light projector was equipped with a 2-step flip-flop filter holder containing a grid for conventional WL illumination and a custom-made bandpass filter (425 ± 35 nm) for the AF excitation. When the light projector was delivering conventional WL, all three color channels (red, green and blue) were activated, whereas in the AF excitation mode the blue color channel was suppressed. Consequently, the AF images contained only the red and green color information. Bronchoscopy was performed using rigid Hopkins optics (Richard Wolf GmbH, Knittlingen, Germany) and flexible fiberoptics (Olympus Corporation, Tokyo, Japan). The endoscopic images were displayed on a video monitor and recorded on a digital video tape (DVCAM SR-11, Sony Inc., Tokyo, Japan). With this system, the normal bronchial tissues appear greenish, and the early neoplastic or pre-neoplastic lesions appear red-brownish under the blue-violet AF excitation light.

Bronchoscopic procedure

Twenty-one patients with a history of squamous cell cancer in the H&N sphere were included in this study. They were relevant high-risk patients (history of cancer in the oral cavity, oropharynx, hypopharynx and larynx) scheduled for pre-therapeutic or follow-up panendoscopy. Exclusion criteria were endobronchial bleeding, severe stenosis in the tracheo-bronchial tree, and treatment with photosensitizing drug less than 3 weeks prior to the examination.

All bronchoscopies were performed under general anesthesia. State of the mucosa and the presence or absence of macroscopically visible lesions was first assessed with a rigid bronchoscope under WL. Care

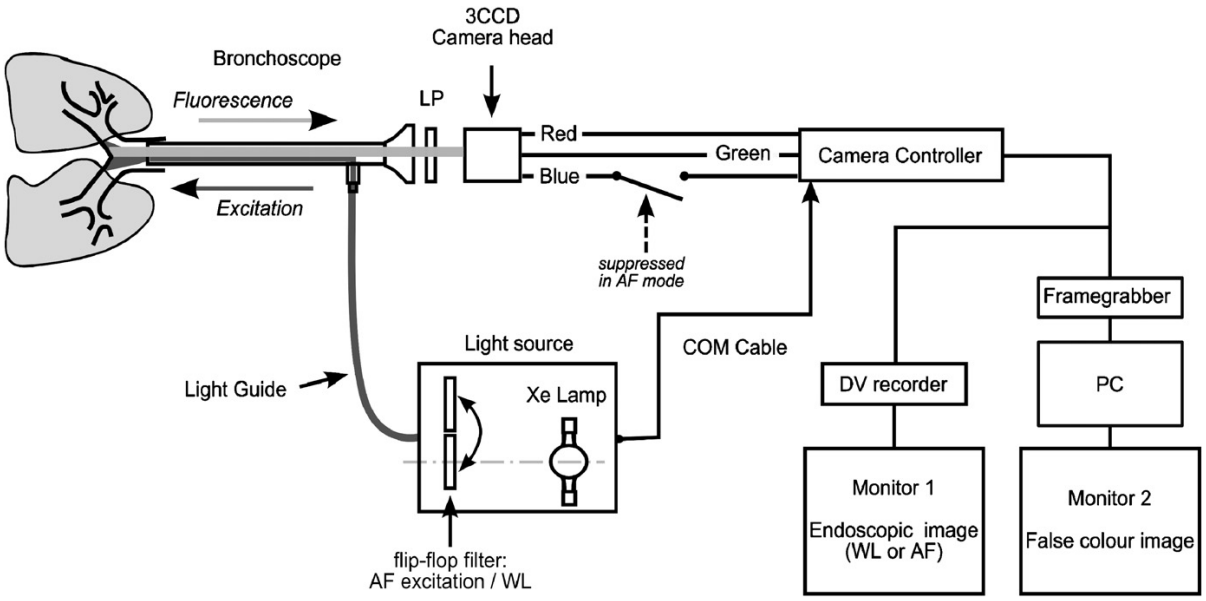

Fig. 1. The diagnostic autofluorescence bronchoscopy (AFB) system.

was taken not to damage the mucosa during this examination since blood can absorb the AF excitation light. The localization of suspicious areas was recorded. The tracheo-bronchial tree was then examined under AF excitation light in the same manner. During the bronchial observation in the AF mode, red-brownish sites were considered suspicious (AF positive), whereas greenish sites were considered non-suspicious (AF negative). A biopsy was taken on each suspicious (WL or AF) site and analyzed by a senior pathologist. Patients with suspicious and histopathologic positive lesions in the tracheo-bronchial tree were followed up during 4 years.

Online image analysis

We quantified the green and the red contribution in the endoscopic autofluorescence images to apply the threshold approach described by Goujon et al. [8], which allows to improve the sensitivity and specificity of AFB.

Basic principles of our image analysis method are the following [8]: the average green and red pixel intensities were computed on two areas, namely (1) the suspect, later-taken biopsy area (SUSP) and (2) the surrounding AF negative and presumably healthy tissue (REF). The green and red average intensities on the area (1) were normalized by (2), respectively, yielding a normalized green-to-red ratio:

$$R = (\mathrm{Green}_{\mathrm{SUSP}}/\mathrm{Red}_{\mathrm{SUSP}})/(\mathrm{Green}_{\mathrm{REF}}/\mathrm{Red}_{\mathrm{REF}}).$$

This procedure allows to correct the recorded intensities for interpatient fluctuations in the tissue AF and the color balance of the camera.

Goujon et al. used the threshold approach to analyze digitized still image off-line after the endoscopic procedure. We developed an online image analysis system that allows to enhance slight differences in the green-to-red intensity ratios and by this, to help the endoscopist to better discriminate true and false positive (FP) sites. Images were digitized using a RGB framegrabber (Matrox Meteor II, Matrox, Harefield, UK) and read out. A software algorithm was written in C++ code based on a commercial imaging library (Matrox Image Library MIL, Matrox, Harefield, UK). The software divided the green channel image by the corresponding red channel image. Each pixel value was further divided by the green-to-red ratio computed from a presumably healthy AF negative area defined manually by the endoscopist in the endoscopic image. The resulting images thus displayed the normalized R value for each pixel encoded in a color scale. The false color images were displayed on a separate monitor, to allow direct comparison of the original AFB images and the processed images.

The aim of such a computation is to determine an optimal threshold for this ratio R as an objective value to discriminate the pre-neoplastic and early neoplastic sites from non-neoplastic changes. The histopathological status of the biopsies were correlated with ratio R of the lesions and healthy tissue. Preliminary results relating the value of this ratio and the histopathologic

status, have been published in details elsewhere [8]. The AF positive sites were classified using our threshold approach as follows: AF positive tissue sites were considered as (i) normal when $R>0.85$, (ii) reactive changes when $0.85>R>0.66$ and (iii) (pre-)neoplastic when $R<0.66$. The results from the online image analysis were compared with the results from the histopathologic analysis.

Histopathologic analysis

Upon histopathologic analysis the biopsies were classified according to the WHO classification system [15,16] into six categories as follows: (1) normal tissue, (2) reactive changes including basal cell hyperplasia and squamous metaplasia, (3) mild dysplasia, (4) moderate dysplasia, (5) severe dysplasia or CIS and (6) invasive squamous cell carcinoma. For statistical purpose, we established a 3-group system as illustrated in Table 1: (I) normal tissue, (II) reactive changes and inflammation and (III) (pre-)neoplastic changes. Lesions in the groups (I) and (II) were considered as "False positives" if they were classified as "positive" during WL and/or AF bronchoscopy. Group (III) included the histopathologic categories (4) and (5). Lesions in this group having been classified as positive during bronchoscopy were considered as "true positives" (TPs).

Results

The mean time for a bronchoscopic procedure including examination with rigid and flexible optics was 30 ± 5 min. A total of 41 biopsies was taken on sites being suspicious under WL and/or AF mode, regardless of the results of the online image analysis. Eleven of them were confirmed to be AF TPs by histopathologic analysis whereas 30 were AF FP before application of the "threshold approach" mentioned above. Twenty-one of these 41 biopsies were positive in the WL mode, among them only seven turned out to be TPs. Four lesions belonging to the group III were positive with AF only. Table 1 summarizes the histopathological distribution of the 41 biopsies.

Table 1. Distribution of the histopathologic classes corresponding to the 41 biopsies with the corresponding groups

Histopathologic class	Number of biopsies	
Group I: normal tissue	4	False positives (FP)
(0) Normal tissue	4	
Group II: reactive changes	26	
Chronic inflammation	7	
(1) Metaplasia	19	
Group III: (pre-)neoplasia	11	True positives (TP)
(2) Mild dysplasia	1	
(3) Moderate dysplasia	3	
(4) Severe dysplasia/CIS	4	
(5) Invasive squamous cell carcinoma	3	
Total	41	

Application of the decisional threshold (called AF/T method in the following) on the results of the online image analysis reduced the number of FPs with the AF mode. After application of this criterion, only 14 of the 41 biopsies remained positive, thus 27 of the 30 AF FPs could be rejected using the decisional threshold. Consequently, together with the WL positives, a number of 28 biopsies taken on 16 patients corresponded to positive sites detected using both the WL mode and the AF/T method. The performances of these detection modes are summarized in Table 2. WL results have been considered positive when a biopsy would have been taken after the WL bronchoscopy. The 11 TP lesions were found in eight patients, with three patients presenting multiple lesions at different sites in the bronchi.

Table 2 shows that four pre-neoplastic and early neoplastic lesions have been detected by the AF/T mode only. Moreover, no TP (WL) sites were negative with the AF/T method. This indicates that the AF/T mode's sensitivity ($SENS_{AF/T}$) is higher than the WL's sensitivity ($SENS_{WL}$). Although it is not possible to assess a value for $SENS_{AF/T}$ (as the false negative rate is not measurable in this organ as explained by Wagnières et al. [17]), one can nevertheless estimate this parameter from $SENS_{WL}$ by the expression:

$$SENS_{AF/T} = SENS_{WL}\left(\frac{TP_{AF/T}}{TP_{WL}}\right).$$

According to the values given in Table 2, the sensibility of the AF/T mode exceeds the sensibility of the conventional WL bronchoscopy by a factor of 1.6.

The positive predictive value (PPV), defined as the ratio of the TP results over the overall positive results (true and FP), for AF/T and the WL bronchoscopy can be derived from the data in Table 2. The negative predictive value cannot be calculated, as the false negative rate is virtually unavailable, as mentioned above.

Table 2. Summary of the results obtained with AFB in combination with the decisional threshold approach

	FP	TP	
WL	14	7	0 with WL only
AF/T	3	11	4 with AF/T only
Total: 28 biopsies in 16 patients			

TP = true positives, FP = false positives.

Using the threshold values mentioned in the section "*Online image analysis*", AF/T and WL bronchoscopy yield the following PPVs:

$$\mathrm{PPV(AF/T)}: \ 11/(11+3) = 79\%,$$

$$\mathrm{PPV(WL)}: \ 7/(7+14) = 33\%.$$

The combination of WL and AF/T leads to an overall PPV of 100%, as the 3 FP lesions in the AF/T method were negative in the WL mode.

As already mentioned above, the 11 $TP_{AF/T}$ lesions were detected in eight patients. Two of these patients discontinued the medical follow-up in our medical facility on their own request. In the remaining six patients presenting a total of nine $TP_{AF/T}$ lesions, the clinical management was changed as a consequence of the observations with AFB bronchoscopy. More precisely, all these patients were proposed additional treatment options for their second primary cancers in the tracheo-bronchial tree. Treatments proposed were radical surgery in two cases, CO_2 laser resection in one case and photodynamic therapy (PDT) in three cases. Of the nine lesions, four were invisible with the WL bronchoscopy, and were thus only detected by AF/T. These four lesions were found in three patients. Consequently, the additional use of AF/T procedure induced a change of management in three of 19 (21–2 patients not followed up), i.e. about 15% in our cohort of high-risk H&N cancer patients.

Discussion

H&N cancer patients are at high risk to develop second primary cancers in the tracheo-bronchial tree [18]. Up to 30% of these patients having been cured of their primary H&N cancer eventually die from second primary lung cancer [13]. Early detection and treatment of these second primaries can significantly improve the patient 5-year survival rate. While the 5-year survival rate is about 15% [19,20] for bronchial cancer patients non-undergoing treatment, it increases to about 80% for patients with early stage cancer undergoing treatment (surgery, cryotherapy or PDT) when the cancer is still in an early stage [21].

It should be noted that AF imaging using blue-violet excitation light has proven to be a powerful tool for the detection of neoplastic lesions in the buccal cavity, larynx and the vocal cords [13,22,23]. The sensitivity of AF imaging for the detection of laryngeal neoplasia has been reported to be about 90–94% [22,23]. Most commercially available endoscopic AF imaging systems allow detection of early cancer in the bronchi as well as in the H&N sphere using dedicated endoscopes.

In this study, about 40% of the H&N cancer patients presented bronchial lesions. Improved performances of the AF/T method can help to limit the number of sites requiring biopsy in the bronchi, thus reducing the morbidity of diagnostic bronchoscopy. We have shown that conventional WL bronchoscopy combined with the AF/T procedure yields a PPV of 100%, even for early neoplastic and pre-neoplastic tissue changes, whereas 15% of the bronchial lesions were found only with the AF/T method. The addition of AFB bronchoscopy allows easy inspection of the bronchi in H&N cancer patients undergoing pre-therapeutic or follow-up panendoscopy. Our results can thus be considered as a proof of principle illustrating the possible benefits of adding AFB to routine examination in patients with H&N cancer. It is worth noting, that though all bronchoscopies performed in the study presented here were under general anesthesia, clinical routine has shown that AFB can be easily performed under local anesthesia, especially using the aforementioned flexible AFB videobronchoscopes. Flexible bronchoscopy performed under local anesthesia is less traumatic and requires less complex infrastructure (anesthesist, instrumentation) than rigid bronchoscopy, and may thus be conducted in outpatient conditions.

One drawback of commercially available AF imaging systems is the relative high number of FPs [14,24,25]. Since no method can completely avoid this problem at the present time, it is of utmost importance to minimize it. It is known from the literature that non-(pre-)neoplastic conditions such as reactive changes (i.e. metaplasia and hyperplasia) and inflammation of the bronchial tissue, but also scar tissue may produce FP findings with AFB [24–27]. Several authors have reported increased microvessel density in the subepithelial layer of bronchial dysplasia and carcinoma in situ [28,29] and vascular changes are also found in reactive tissue changes, inflammation and fresh scarring tissue. Recent ex vivo studies have attributed the AF contrast observed between healthy and pre-neoplastic bronchial mucosa at least partially to changes in the tissue blood circulation, including angiogenesis [14]. Indeed, the increase in blood volume, and thereby in hemoglobin concentration in the tissues with vascular changes is associated with a higher absorption of the blue-violet excitation light, resulting in a decrease in the AF intensity.

However, the vascular changes in reactive tissue changes, inflammation and freshly scarring tissue are characterized by vessel sizes and distribution patterns different from those observed in (pre-)neoplastic and early cancerous lesions. Inflammations and metaplasia exhibit an increased number of vessels along with increased vessel cross section, while angiogenesis in dysplasia and CIS is characterized by a significant increase in the number of vessels with small diameters. In this study, we demonstrated that the use of quantitative assessment of the color modifications of

the images could bring a significant improvement of AFB specificity. Our approach was based on the online computation of AF intensity ratios from selected tissue area and their classification using a three-way decisional threshold. Despite the online classification procedure, allowing the endoscopist to discriminate between true and FPs immediately during the exam, the manual selection of an AF negative reference area by the endoscopist may be cumbersome in clinical routine.

Other approaches to increase the specificity of AFB rely on the spectral optimization of the AFB system. For this purpose, additional techniques can be combined with imaging to improve AFB performance. Endoscopic optical spectrocopy has been reported recently by Bard et al. [30], Kusunoki et al. [31], Zeng et al. [32] and Tercelj et al. [33]. Bard's and Kusunoki's groups measured the autofluorescence and reflectance spectra during AFB. For this purpose, they inserted a fiber bundle through the biopsy channel of the bronchofibroscope and put it in smooth contact with the mucosa. This procedure can bruise the mucosa and provoke bleeding. To avoid this drawback, Zeng et al. and Tercelj et al. used a non-contact measurement system based on a modified Xillix's LIFE system with an integrated spectrometer unit. The AF and reflectance spectra were acquired from selected spots on the endoscopic sites. Thiberville et al. [34] developed a dual fibered confocal fluorescence imaging and spectroscopic system allowing to characterize modifications in the spectroscopy of (pre-)neoplastic bronchial lesions.

Other authors use the differences in the tissue vascular changes observed in inflammation, reactive changes and (pre-)neoplastic tissues to discriminated between false and TPs. Shibuya et al. [35,36] reported the use of a high-magnification videobronchoscope to visualize the vascular structures on WL and AF positive tissue sites. They observed the complex neo-vessels structure and tortuosity, and consequently were able to discriminate between (pre-)neoplastic tissues and inflammatory or reactive tissue changes. However, all these techniques require additional equipment, additional instrumental manipulation by the endoscopist or the staff, and prolong the bronchoscopic procedure [33]. A different approach relies on the spectral and optical optimization of the spectroscopic and optical conditions of the AFB imaging system itself. More precisely, the detection of specific wavelength bands, namely in the blue-violet wavelength range, helps to visualize the aforementioned differences in the tissue vascular structures. Detection of backscattered blue-violet light in addition to the tissue autofluorescence is thus likely to allow discrimination between tissues with different vascular structures [37]. This concept has been implemented in recent AFB videobronchoscope systems [38] and is now being under investigation in the clinics.

It is fairly difficult to assess the number of false negative results of an AF fluorescence detection method for bronchial (pre-)neoplasia. However, in this study the false negative rate of conventional WL bronchoscopy was adjusted with the help of AFB. In our preliminary study, it is striking to see that four lesions have only been detected in the AF mode. Therefore, the sensitivity of WLB has been improved with AF/T method proposed in this report. It is clear that this figure has to be considered with caution, as the overall number of lesions is small.

In summary, our study demonstrated that H&N cancer patients clearly benefit from the additional use of AFB in pre-therapeutic and follow-up examination. Further studies including a larger cohort of patients will be needed to confirm the trend observed in this preliminary study.

Acknowledgments

We grateful acknowledge the collaboration of the endoscopy staff of the CHUV hospital, the resident physicians of the Otolaryngology, Head and Neck Surgery Department at the CHUV hospital and the support from Richard Wolf GmbH, Knittlingen, Germany. This research was also supported by the Swiss National Fund for Scientific Research, Grant #205320 – 116556 and by the "Fonds de Service" of the Otolaryngology, Head and Neck Surgery Department at the CHUV hospital.

Zusammenfassung

Autofluoreszenz-Bronchoskopie: klinische Erfahrung mit einem optimierten System bei Kopf- und Halskrebspatienten

Patienten mit malignen Tumoren im Kopf- und Halsbereich haben ein stark erhöhtes Risiko, Zweit- und Mehrfachtumore, insbesondere im Respirationstrakt und in der Speiseröhre, zu entwickeln. Die Anwesenheit und der Charakter dieser Sekundärtumore beeinflussen stark die Prognose des Patienten und müssen im Therapieplan berücksichtigt werden. Diagnostische Autofluoreszenz-Bronchoskopie (AFB) hat vielversprechende Ergebnisse in der Detektion von Frühneoplasien und prä-neoplastischen Veränderungen der Bronchialschleimhaut gezeigt. Wir haben die medizinische und therapeutische Bedeutung von AFB in einer Population von 21 Kopf- und Hals-Krebspatienten untersucht. Die Studie wurde mit Hilfe eines abgewandelten kommerziell erhältlichen AFB Systems durchgeführt. Dieses System erlaubt sowohl die Durchführung von konventioneller Weisslicht- (WL) als auch von

Autofluoreszenz-(AF)bronchoskopie. Die endoskopische Untersuchung der Gewebeautofluoreszenz wurde mit einem Echtzeitbildanalyseverfahren kombiniert, welches die Unterscheidung zwischen falsch und echt positiven Ergebnissen während der Untersuchung vereinfacht. Insgesamt wurden 41 Gewebeproben an makroskopisch verdächtigen (WL oder AF positiven) Stellen in den Bronchien entnommen. Histopathologische Untersuchungen bestätigten die Anwesenheit von früh- oder prä-neoplastischen Veränderungen in 11 Gewebeproben von 8 Patienten. Die Sensibilität von AFB für diese frühen Veränderungen der Schleimhaut war 1,6 mal höher als die Sensibilität der Weisslichtbronchoskopie alleine. Wir konnten zeigen, dass AFB eine effiziente Methode zur frühzeitigen Erkennung von Zweit- und Mehrfachtumoren im Respirationstrakt bei Patienten mit Kopf- und Hals-Krebs darstellt. Zusammenfassend lässt sich sagen, dass AFB als eine einfache und minimal invasive Ergänzung zur präoperativen Diagnosestellung und zur postthera- peutischen Nachkontrolle in dieser Patientengruppe verwendet werden kann.

Schlüsselwörter: Autofluoreszenz-Bronchoskopie; Frühkrebs; Kopf- und Halskrebs; HNO; Primäre Zweitkarzinome; Spezifität; Sensibilität; Echtzeitbildanalyse; Therapieplan

Resúmen

Broncoscopía autofluorescente: experiencia clínica con un sistema optimizado en pacientes con cáncer de cabeza y cuello

Los pacientes con cáncer de cabeza y cuello tienen una alta incidencia de segundos tumores primarios en el árbol traqueobronquial que afecta el pronóstico y tratamiento de estos pacientes. La broncoscopía autofluorescente de diagnóstico (AFB) ha demostrado resultados prometedores en la detección de cambios neoplásicos tempranos y pre-neoplásicos en los bronquios. Hemos investigado el impacto médico y terapéutico de la AFB en una población de 21 pacientes con cáncer de cuello y cabeza, usando un sistema AFB comercialmente disponible modificado que permite la observación de luz blanca (LB) y autofluorescente (AF). El monitoreo endoscópico del tejido autofluorescente fue combinado con un procedimiento online de análisis de la imágen mejorando así la discriminación entre positivos verdaderos y falsos positivos. 41 biopsias fueron tomadas en sitios bronquiales macroscópicamente sospechosos (positivos para LB o AF). Los análisis histopatológicos confirmaron cambios pre o neoplásicos tempranos en 11 de estas biopsias tomadas a partir de 8 pacientes. Todas estas lesiones habían presentado AF positiva en la broncoscopía. La sensibilidad para la detección de estas lesiones tempranas con el AFB fue 1,6 veces mayor que la sensibilidad de broncoscopía con luz blanca. El valor predictivo positivo (PPV) para la AF fue de 79% y sólo del 33% para la LB, mientras que el PPV de ambos métodos junto fue del 100%. Pudimos así demostrar que la AFB es eficiente para la detección de las segundas lesiones primarias de los bronquios en pacientes con cáncer de cuello y cabeza. En conclusión, la AFB puede ser utilizada como un procedimiento adicional simple y mínimamente invasivo en el examen pre-operatorio o en el seguimiento de estos pacientes.

Palabras claves: Broncoscopía autofluorescente; Cáncer temprano; Cáncer de cabeza y cuello; ONG; Segundo carcinoma primario; Especificidad; Sensibilidad; Análisis de imagen online; Tratamiento terapéutico

References

[1] Laccourreye O, Veivers FD, Hans S, Brasnu FD, Garcia D, Laccourreye FL. Metachronous second primary cancers after successful partial laryngectomy for invasive squamous cell carcinoma of the true vocal cord. Ann Otol Rhinol Laryngol 2002;111:204–9.

[2] Morita M, Araki K, Saeki H, Sakaguchi Y, Baba H, Sugimachi K, et al. Risk factors for multicentric occurrence of carcinoma in the upper aerodigestive tract-analysis with a serial histologic evaluation of the whole resected-esophagus including carcinoma. J Surg Oncol 2003;83:216–21.

[3] Tabor MP, Brakenhoff RH, van Houten VM, Kummer JA, Snel MH, Snijders PJ, et al. Persistence of genetically altered fields in head and neck cancer patients: biological and clinical implications. Clin Cancer Res 2001;7: 1523–32.

[4] Stoeckli SJ, Zimmermann R, Schmid S. Role of routine panendoscopy in cancer of the upper aerodiaestive tract. Otolaryngol – Head Neck Surg 2001;124:208–12.

[5] Hujala K, Sipila J, Grenman R. Panendoscopy and synchronous second primary tumors in head and neck cancer patients. Eur Arch Oto-Rhino-Laryngol 2005;262: 17–20.

[6] Lam S, MacAulay C, leRiche JC, Palcic B. Detection and localization of early lung cancer by fluorescence bronchoscopy. Cancer Suppl 2000;89:2468–73.

[7] Wagnières G, McWilliams A, Lam S. Lung cancer imaging with fluorescence endoscopy. In: Myceck M-A, Pogue BW, editors. Handbook of biomedical fluorescence. New York: Marcel Dekker, Inc.; 2003. p. 361–96.

[8] Goujon D, Zellweger M, Radu A, Grosjean P, Weber B-C, van den Bergh H, et al. In vivo autofluorescence imaging of early cancers in the human tracheobronchial tree with a spectrally optimized system. J Biomed Opt 2003;8:17–25.

[9] Lam S, Kennedy T, Unger M. Localization of bronchial intraepitheloial neoplastic lesions by fluorescence bronchoscopy. Chest 1998;113:696–702.

[10] Sutedja TG, Condrigton H, Risse EK, Breuer RH, van Mourik JC, Golding RP, et al. Autofluorescence bronchoscopy improves staging of radiographically occult

lung cancer and has an impact on therapeutic strategy. Chest 2001;120:1327–32.
[11] Zellweger M, Grosjean P, Goujon D, Monnier P, van den Bergh H, Wagnières G. In vivo autofluorescence spectroscopy of human bronchial tissue to optimize the detection and imaging of early cancers. J Biomed Opt 2001;6:41–51.
[12] Venmans BJW, Van Boxem TJM, Smit EF, Postmus PE, Sutedja TG. Bronchial intraepithelial neoplastic lesions in head and neck cancer patients: results of autofluorescence bronchoscopy. Ann Otol Rhinol Laryngol 2001;110:635–8.
[13] Fielding D, Agnew J, Wright D, Hodge R. DAFE autofluorescence assessment of oral cavity, larynx and bronchus in head and neck cancer patients. Photodiagn Photodyn Ther 2006;3:259–65.
[14] Gabrecht T, Andrejevic-Blant S, Wagnières G. Blue-violet excited autofluorescence spectroscopy and imaging of normal and cancerous human bronchial tissue after formalin fixation. Photochem Photobiol 2007;83:450–8.
[15] Brambilla E, Travis WD, Colby TV, Corrin B, Shimosato Y. The new world health organization classification of lung tumours. Eur Respir J 2001;18:1059–68.
[16] Nicholson AG, Perry LJ, Cury PM, Jackson P, McCormick CM, Corrin B, et al. Reproducibility of the WHO/IASLC grading system for pre-invasive squamous lesions of the bronchus: a study of inter-observer and intra-observer variation. Histopathology 2001:202–8.
[17] Wagnieres G, Star W, Wilson B. In vivo fluorescence spectroscopy and imaging for oncological applications. Photochem Photobiol 1998;68:603–32.
[18] Grosjean P, Monnier P. Impact of diagnosis and treatment of early stage secondary tumors on outcome for the oncologic ORL patient [[Impact du diagnostic et du traitement au stade précoce des secondes localisations tumorales sur l'avenir du patient oncologique ORL.] Schweizerische Medizinische Wochenschrift]. J Suisse Med 2000;116:43S–6S.
[19] Henschke CI, Wisnivesky JP, Yankelevitz DF, Miettinen OS. Small stage I cancers of the lung: genuineness and curability. Lung Cancer 2003;39:327–30.
[20] Motohiro A, Ueda H, Komatsu H, Yanai N, Mori T. Prognosis of non-surgically treated, clinical stage I lung cancer patients in Japan. Lung Cancer 2002;36:65–9.
[21] Maziak D, Markman B, MacKay J, Evans W. Photodynamic therapy in nonsmall cell lung cancer: a systematic review [in process citation]. Ann Thorac Surg 2004;77:1484–91.
[22] Arens C, Reußner D, Woenkhaus J, Leunig A, Betz CS, Glanz H. Indirect fluorescence laryngoscopy in the diagnosis of precancerous and cancerous laryngeal lesions. Eur Arch Oto-Rhino-Laryngol 2007;264:621–6.
[23] Mostafa BE, Shafik AG, Fawaz S. The role of flexible autofluorescence laryngoscopy in the diagnosis of malignant lesions of the larynx. Acta Oto-Laryngol 2007;127:175–9.
[24] Hirsch FR, Prindiville SA, Miller YE, Franklin WA, Dempsey EC, Murphy JR, et al. Fluorescence versus white-light bronchoscopy for detection of preneoplasic lesions: a randomized study. J Natl Cancer Inst 2001;93:1385–91.
[25] Häußinger K, Stanzel F, Kohlhäufl M, Becker H, Herth F, Kreuzer A, et al. Autofluorescence bronchoscopy with white light bronchoscopy compared with white light bronchoscopy alone for the detection of precancerous lesions: a European randomised controlled multicentre trial. Thorax 2005;60:496–503.
[26] Chhajed PN, Shibuya K, Hoshino H, Chiyo M, Yasufuku K, Hiroshima K, et al. A comparison of video and autofluorescence bronchoscopy in patients at high risk of lung cancer. Eur Resp J 2005;25:951–5.
[27] Kennedy TC, Lam S, Hirsch FR. Review of recent advances in fluorescence bronchoscopy in early localization of central airway lung cancer. Oncologist 2001;6:257–62.
[28] Fisseler-Eckhoff A, Rothstein D, Müller KM. Neovascularization in hyperplastic, metaplastic and potentially preneoplastic lesions of the bronchial mucosa. Virchows Arch 1996;429:95–100.
[29] Fontanini G, Calcinai A, Boldrini L, Lucchi M, Mussi M, Angeletti CA, et al. Modulation of neoangiogenesis in bronchial preneoplastic lesions. Oncol Rep 1999;6:813–7.
[30] Bard MRL, Amelink A, Skurichina M, den Bakker M, Burgers SA, van Meerbeck JP, et al. Improving the specificity of fluorescence bronchoscopy for the analysis of neoplastic lesions of the bornchial tree by comvination with optical spectroscopy: preliminary communication. Lung Cancer 2005;47:41–7.
[31] Kusunoki Y, Imamura F, Uda H, Mano M, Horai T. Early detection of lung cancer with laser-induced fluorescence endoscopy and spectrofluorometry. Chest 2000;118:1776–82.
[32] Zeng H, McWilliams A, Lam S. Optical spectroscopy and imaging for early lung cancer detection: a review. Photodiagn Photodyn Ther 2004;1:111–22.
[33] Tercelj M, Zeng H, Petek M, Rott T, Palcic B. Acquisition of fluorescence and reflectance spectra during routine bronchoscopy examinations using the ClearVu Elite(TM) device: pilot study. Lung Cancer 2005;50:35–42.
[34] Thiberville L, Moreno-Swirc S, Vercauteren T, Peltier E, Cave C, Bourg Heckly G. In vivo imaging of the bronchial wall microstructure using fibered confocal fluorescence microscopy. Am J Respir Crit Care Med 2007;175:22–31.
[35] Shibuya K, Fujisawa T, Hoshino H, Baba M, Saitoh Y, Iizasa T, et al. Fluorescence bronchoscopy in the detection of preinvasive bronchial lesions in patients with sputum cytology suspicious or positive for malignancy. Lung Cancer 2001;32:19–25.
[36] Shibuya K, Hoshino H, Chiyo M, Iyoda A, Yoshida S, Sekine Y, et al. High magnification bronchovideoscpy combined with narrow band imaging could detect capillary loops of angiogenic squamous dysplasia in heavy smokers at high risk for lung cancer. Thorax 2003;58:989–95.
[37] Gabrecht T, Radu A, Grosjean P, Weber B, Reichle G, Freitag L, et al. Improvement of the specificity of cancer detection by autofluorescence imaging in the tracheobronchial tree using backscattered violet light. Submitted for publication.
[38] Richard Wolf Endoskope GmbH. Diagnostic Auto Fluorescence Endoscopy 〈www.richard-wolf.com〉, accessed September 2007.

Bibliography

[Glan03] T. Glanzmann. Rationale for autofluorescence bronchoscopy. private communication, 2003.

[Sava91] M. Savary, P. Monnier, R. Pasche, E. Brossard, P. Pasche, and F. Lang. Multiple primary malignancies. *Adv Otorhinolaryngol*, 46:165–175, 1991.

[Stoe01] S. J. Stoeckli, R. Zimmermann, and S. Schmid. Role of routine panendoscopy in cancer of the upper aerodiaestive tract. *Otolaryngology - Head and Neck Surgery*, 124(2):208–212, 2001.

Appendix B

Bladder cancer histopathology

B.1 Morphological criteria for bladder cancer classification

Tables B.1&B.2 give the histological characteristics (cell architecture, shape, ...) for both flat (reactive atypia, hyperplasia, dysplasia, CIS) and exophytic lesions (papilloma, PUNLMP, low- and high-grade papillary carcinoma) derived from [Mont08].

Table B.3 describes the weights used to calculate probability of recurrence and progression (Table B.4), first presented in [Sylv06]. It gives the physician a simple decisional help for bladder cancer management (*e.g.* whether to proceed to radical cystectomy or not, whether to give adjuvant chemotherapy).

Features	Reactive atypia	Hyperplasia	Dysplasia	CIS
Cell layers	Variable	>10	Variable	Variable
Polarization	Slightly abnormal	Normal	Disordered	Disordered
Cytoplasm	Often vacuolated	Homogeneous	Variable, homogeneous to granular	Variable
N/C ratio	Normal to slightly increased	Normal to slightly increased	Slightly increased	Increased
Nuclear size	Enlarged	Normal	Enlarged	Enlarged with variation in size
Nuclear borders	Regular/smooth	Regular/smooth	Notches/creases	Pleomorphic
Chromatin	Fine/dusty	Fine	Slight hyperchromasia	Coarse
Nucleoli	Large, single	Small/absent	Small	Large, often multiple
Mitotic figures	Variable	Absent	Rare, basal	Frequent, all levels
Umbrella cells	Uniformly present	Present	Present	May be present
Denudation	Variable	No	No	Variable

Table B.1: *Comparison of reactive atypia, hyperplasia, dysplasia and carcinoma in situ (CIS) [Mont08]*

Features	Papilloma	PUNLMP	Low-grade papillary carcinoma	High-grade papillary carcinoma
Architecture				
Papillae	Delicate	Delicate. Occasional fused	Fused, branching, and delicate	Fused, branching and delicate
Organization of cells	Identical to normal	Polarity identical to normal. Any thickness. Cohesive	Predominantly ordered,yet minimal crowding and minimal loss of polarity. Any thickness.Cohesive	Predominantly disordered with frequent loss of polarity.Any thickness. Often discohesive.
Cytology				
Nuclear size	Identical to normal	May be uniformly enlarged	Enlarged with variation in size	Enlarged with variation in size
Nuclear shape	Identical to normal	Elongated, round-oval, uniform	Round-oval. Slight variation in shape and contour	Moderate-marked pleomorphism
Nuclear chromatin	Fine	Fine	Mild variation within and between cells	Moderate-marked variation both within and between cells with hyperchromasia
Nucleoli	Absent	Absent to inconspicuous	Usually inconspicuous	Multiple prominent nucleoli may be present
Mitoses	Absent	Rare, basal	Occasionally at any level	Usually frequent, at any level
Umbrella cells	Uniformly present	Present	Usually present	May be absent

Table B.2: *Comparison of papilloma, papillary neoplasm of low malignant potential (PUNLMP), low-grade papillary carcinoma and high grade papillary carcinoma [Mont08]*

Factor	Recurrence	Progression
Number of tumors		
Single	0	0
2 to 7	3	3
≥8	6	3
Tumor size		
<3 cm	0	0
≥3 cm	3	3
Prior recurrence rate		
Primary	0	0
≤1 rec/yr	2	2
>1 rec/yr	4	2
T category		
Ta	0	0
T1	1	4
CIS		
No	0	0
Yes	1	6
Grade		
G1	0	0
G2	1	0
G3	2	5
Total score	0-17	0-23

Table B.3: *Weights used to calculate the recurrence and progression scores [Sylv06]*

Recurrence Score	**Prob Recurrence 1 Year (95% CI)**	**Prob Recurrence 5 Years (95% CI)**
0	15 (10, 19)	31 (24, 37)
1-4	24 (21, 26)	46 (42, 49)
5-9	38 (35, 41)	62 (58, 65)
10-17	61 (55, 67)	78 (73, 84)
Progression Score	**Prob Progression 1 Year (95% CI)**	**Prob Progression 5 Years (95% CI)**
0	0.2 (0, 0.7)	0.8 (0, 1.7)
2-6	1.0 (0.4, 1.6)	6 (5, 8)
7-13	5 (4, 7)	17 (14, 20)
14-23	17 (10, 24)	45 (35, 55)

Table B.4: *Probability of recurrence and progression according to total score. 95% Confidence Interval (CI) is indicated in brackets [Sylv06].*

Bibliography

[Mont08] R. Montironi, A. Lopez-Beltran, M. Scarpelli, R. Mazzucchelli, and L. Cheng. Morphological classification and definition of benign, preneoplastic and non-invasive neoplastic lesions of the urinary bladder. *Histopathology*, 53(6):621–633, Dec 2008.

[Sylv06] R. J. Sylvester, A. P. M. van der Meijden, W. Oosterlinck, J. A. Witjes, C. Bouffioux, L. Denis, D. W. W. Newling, and K. Kurth. Predicting recurrence and progression in individual patients with stage Ta T1 bladder cancer using EORTC risk tables: a combined analysis of 2596 patients from seven EORTC trials. *Eur Urol*, 49(3):466–5, Mar 2006.

Appendix C

Narrow-band excitation in the bladder

During fluorescence cystoscopy, the sharp fluorescence excitation peak of PpIX often interferes with the very strong and sharp absorption peak of hemoglobin contained in the tissues and in the liquid filling the bladder (see Figure 2.2&2.11). In the context of integrating a LED at the distal end of the endoscope, we have to investigate the best excitation wavelength to be chosen in the next endoscope generation.

To address this issue, we have injected light from a Krypton laser working in the multiline mode (407 nm and 413 nm) in the light guide attached to a flexible cystoscope (new prototype, PDD flexible cystoscope, Richard Wolf GmbH). We have then compared on the same flat lesions (n=2) the chromatic and visual contrast between the conventional filtered (370–430 nm) broadband Xenon light source (see Figure 2.12) and the narrowband excitation from the laser.

PpIX has an excitation peak at around 405 nm. Therefore, the excitation spectral power (in the violet range) was higher in the violet with the Krypton laser (20 mW violet light at the endoscope tip) than with the Xenon light source (30 mW for the whole bandwidth), leading to a better fluorescence excitation.

Images acquired with the narrow-band excitation (almost matching the PpIX excitation peak) showed an increased visual contrast between fluorescing lesions and healthy tissue. Typical images are shown in Figure C.1. Illumination pattern on the tissue is not homogenized yet and will be improved for clinical applications.

Regions of interest (ROIs) were defined as selected areas of pixels on tumors and normal tissues. Figure C.2 shows the red/green ratio ($R_1 = I_{red}/I_{green}$) and red/blue ratio ($R_2 = I_{red}/I_{blue}$) with both illumination modes on the selected ROIs.

Figure C.2 depicts the color channels ratio (R/G, R/B, G/B). It is likely that narrowband excitation improves the red/green contrast on tumors, whereas the red/blue ratio remains constant with both illumination modes. The green/blue ratio is close to 1 on healthy tissues with both narrow- and broadband excitation light. On cancers, this ratio lowers to 0.76 with broadband, and to 0.58 with narrowband. It suggests that the green autofluorescence alteration depends on the excitation bandwidth. More precisely, the use of shorter wavelength close to 405 nm will increase the tumor-to-background contrast.

If this trend is confirmed by other cases, the narrow-band excitation can be implemented in the next endoscope generation with the help of light-emitting diodes (LEDs) at the distal end of the endoscope.

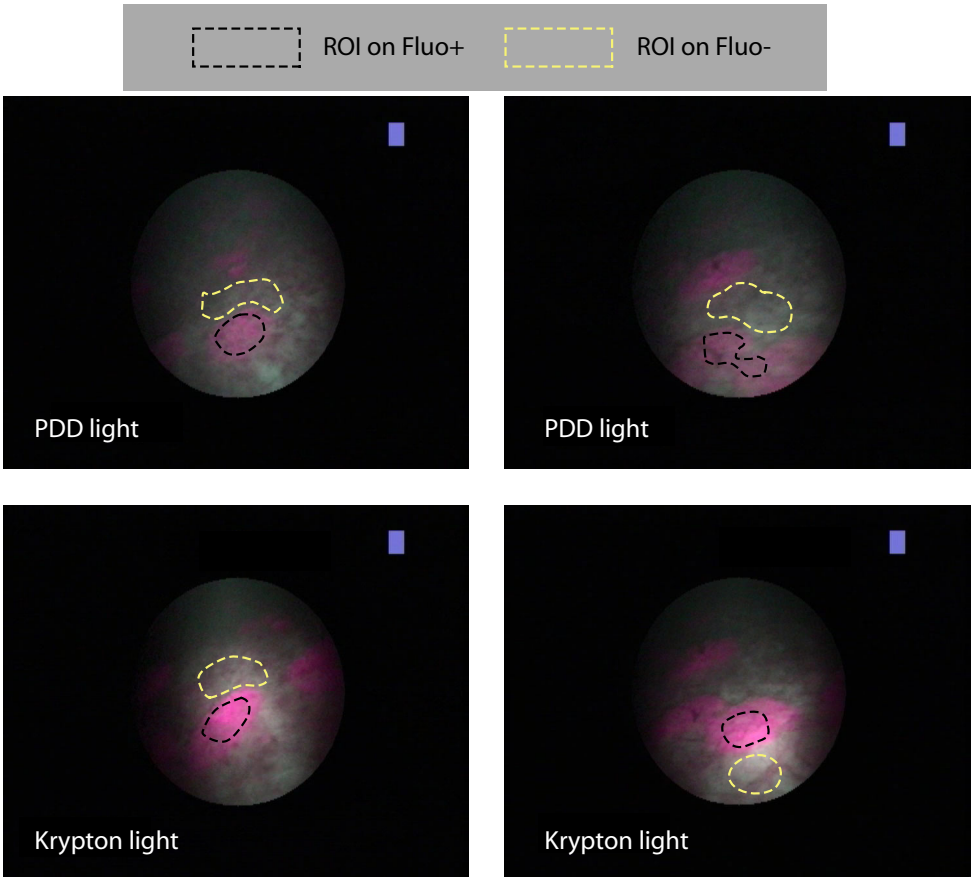

Figure C.1: *Comparison of broadband (PDD filtered Xe lamp) and narrow-band (Krypton laser) excitation in 2 patients*

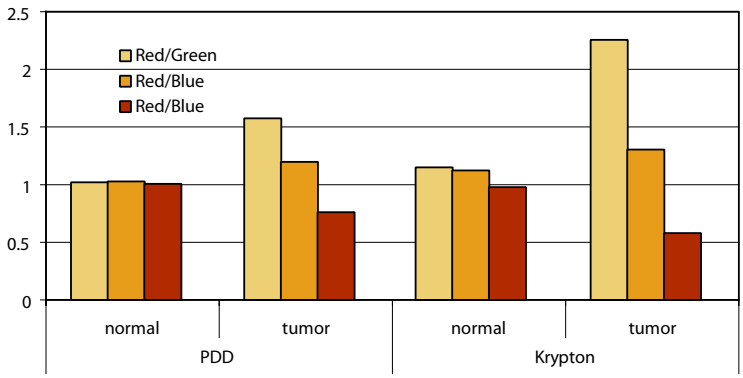

Figure C.2: *Red/green and red/blue ratios with the two illumination modes.*

Appendix D

Fluorescence validation sample to validate endoscopic imaging

D.1 Introduction

Even if fluorescence cystoscopy is a well established method for the detection of flat bladder carcinoma, instrumentation has still to be tested for its reliability over time. The same is valid for AF bronchoscopy. Several parameters such as illumination light power, excitation spectrum, overall transmission and detection system integrity are subject to variations over time. In the clinics, a regular check of these parameters is necessary. It helps to prevent misinterpretation of the obtained endoscopic images and avoid under/over diagnosis leading to an evident patient benefit.

In order to make it user-friendly, the validation procedure should be kept as simple as possible. It is not yet decided whether this validation routine will be implemented in the camera firmware with an integrated post-processing of the collected test pictures or if it has to be checked by an external technician. This issue has to be addressed separately, but it will undoubtedly play an important role on the design procedure.

Many phantoms mimicking tissue optical properties have been designed over the last 20 years, in parallel to the development of optical diagnostic and therapeutic applications. For instance, Bays *et al.* have design a three-dimensional (3D) optical phantom to characterize the PDT response of the tracheo-bronchial tree [Bays97]. Indeed, a very small isotropic light detector can be introduced into this phantom at several strategic positions to measure the radiant energy fluence rate. To produce the lung phantom, a negative imprint of the tracheo-bronchial tree was cast in wax. This imprint was then immersed in the silicone. After curing, the wax was removed by melting. With this technique, three-dimensional shapes can be accurately produced with only one mold (see Figure D.1). This phantom can also be used by physicians to practice the introduction and placement of the light distributor prior to clinical PDT to obtain an homogenous light distribution in the tissue.

Wagnieres *et al.* developed an optical phantom with tissue-like properties in the visible [Wagn97]. This phantom was designed to mimic the tissue fluorescence properties. Indeed, this phantom was built with an agarose base, in which several fluorophores were embedded: ink and blood as optical absorbers, silica powder and Intralipid as scatterers, bovine serum to mimic binding to

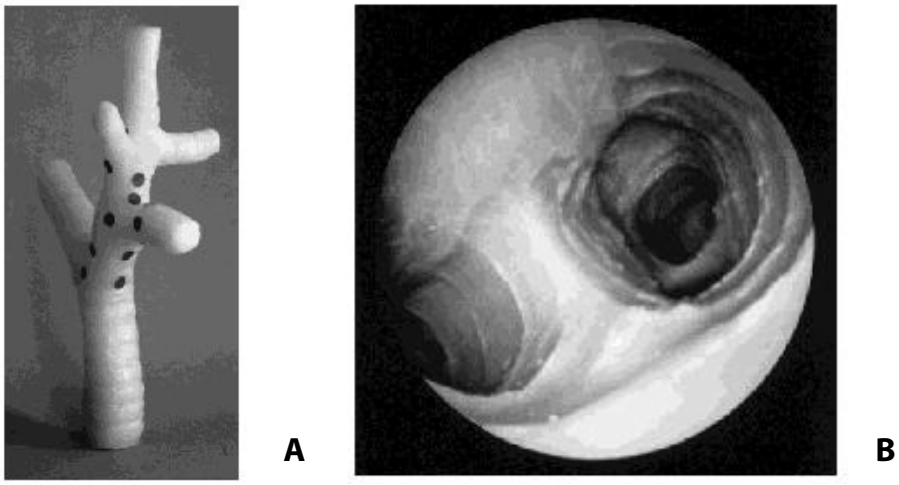

Figure D.1: ***A*** *Negative imprint in wax of the bronchial tree* ***B*** *endoscopic view of the lung phantom [Bays97].*

proteins. Interestingly, some penicillin were also added to ensure conservation of the phantoms over 2–3 weeks.

With the development of optical tomography, diffusely scattering and absorbing phantoms were required for developing experimental techniques as well as theoretical models of photon transport in biological tissues. Furthermore, phantoms with well-defined spatially varying optical properties are needed to compare different experimental methods of optical tomography. Firbank and Delpy reported on diffusely scattering solid phantoms made from titanium dioxide particles as scatterers embedded in polymer [Firb93]. Several authors improved the design of this first phantom by substituting monodisperses quartz glass spheres for the non-spherical titanium dioxide particles [Suko96].

In a recent paper, de Bruin *et al.* present the design and characterization of silicone elastomer-based optical phantoms [deB10]. Absorption is included by adding a green dye and scattering by adding TiO_2 or SiO_2 particles. They build up a layered phantoms (with thicknesses as small as 50μm) to mimic the human retina, and also embedded gold nanoparticles to assess the resolution of their optical coherence tomography (OCT) device. These homogenous phantoms exhibit well-defined and controllable thickness, refractive index, absorption, and scattering coefficients.

The tissue equivalent phantoms are also important for calibration and standardization of the new technique before putting it into clinical practice. For this purpose, many materials have been used as optical phantoms for optical imaging studies. Beck *et al.* reviewed the fabricating process of tissue phantoms [Beck98]. The most common tissue phantom system is based on Intralipid (Kabivitrium,Stockholm,Sweden) as a scattering medium, a standardized aqueous fat emulsion. It is usually combined with black Indian ink as absorber which itself contributes to scattering [Wagn97]. The scattering properties of diluted Intralipid correspond to those of tissue, apart from a relatively low scattering anisotropy of about $g = 0.8$. Other common scatterers are milk or micron-sized latex spheres.

While it is important to mimic the organ shape, semi-rigid and solid phantoms were built over time with different mechanical properties. Solid phantom samples have been made using either transparent hosts, like polymers, silicone or gelatin, or using inherently light-scattering materials such as wax. Polymer-based phantoms have been reported to crack if they are too large or to shrink during polymerization, which limit their applicability. Gels contain a solvent which

evaporates, changing the dimensions and optical properties of the sample within a short period. Steps towards realistic complex geometries have been layered samples, inserted inhomogeneities, and phantoms mimicking whole organs. Additionally, some phantoms have realistic properties over a wide wavelength range, and not only for laser-specific peaks.

We have prototyped some fluorescence charts ready to be used by technical staff in the hospital as so-called *validation* charts. They provide a visual test checking the correct functioning of the whole instrumentation chain. Our phantoms are based on a silicone matrix, loaded with different dyes to mimic absorption, scattering and fluorescence properties of the bladder wall. The overall goal of this subproject was 2-fold:

- Develop a validation/calibration chart to routinely assess the correct functioning of the endoscopic system in bronchoscopy (autofluorescence) and PDD system in urology (PpIX fluorescence).
- Design a reference sample for the PpIX fluorescence and the tissue autofluorescence, respectively.

D.2 Validation sample specifications

In the following, we designed solid phantoms to test one or more of the following parameters: Power and spectroscopy of the excitation/emission light, RGB balance and fluorescence contrast.

Power and spectroscopy : illumination and image acquisition

- leakage of the excitation filter (mechanical break, changes in the optical transmission characteristics);
- variation of the light power output of the Xenon bulb;
- transmission of the optics (aging of the light guide designed for violet light transmission, illumination optical fibers, image guide)

RGB color contrast (wrong settings, distorted visual appearance)

- individual channel intensification;
- leakage of the emission filter;
- contrast balance check between RGB channels (RG/RB/GB);
- distortion of the channel balance occurring during white and/or color balance (ACB)

Detectability of the fluorescence contrast

- **AF contrast** : the validation sample has to be designed with a drop in the green spectral region (to mimic AF drop on tumors).
- **PpIX contrast** : a fluorophore (that emits red when excited with blue light) should be present in the validation sample to check that the PDD setup can highlight the pseudo-tumor information.

D.3 Phantom Design

The assumptions in the next paragraph and the two next sections *Bronchoscopy* and *Urology* are depending on the endoscopic fluorescence imaging device. They are based on the commercial endoscopy setup manufactured by Richard Wolf GmbH, because it was part of our on-going research collaboration. Obviously, the test chart can be sized depending on the endoscope it is designed for.

During the test procedure, the endoscopic camera should operate with maximal intensification gain regulated by the automatic gain control (AGC) unit, even if amplified noise may interfere with a good visual check. Chromophores and fluorophores concentration in the matrix will have to be adapted to keep fluorescence signal and backscattered light intensities at a level similar to tissue. Additionally, it was assumed that frame integration time is continuously calculated to adapt for illumination variations. This calculation is based on the intensity of the pixels that are centrally located in the endoscopic images. It is to be noted that in the AF mode, tissue (or chart) appearance is seriously affected by the reflectance of the area illuminated at the time of intelligent color balance (iCB). iCB is an internal software procedure that creates a false color appearance to help visualization of the tumors with the DAFE II system. It sets the normal tissue to grayish appearance, whereas tumors are looking bluish, when illuminated in blue light.

D.3.1 Bronchoscopy

The bronchoscopic calibration chart is designed with 4 distinct areas: (i) white reflecting area to perform white balance procedure; (ii) a substrate backscattering blue light (10%), but non-fluorescing, that should appear blue with a normal functioning system; (iii) the same substrate loaded with a supplemental green fluorochrome, mimicking normal tissue autofluorescence (to check RGB color balance). iCB will be performed on this area, which should also backscatter the same amount of green light to visually detect green leakage; (iv) fluorescence contrast can be checked with two areas containing the same substrate, one of them containing less green fluorescent pigment to reproduce AF drop in the green spectral region.

Figure D.2 depicts a simplified version of the bronchial validation sample (without white reflecting coating). The spectral curves on the left show the good agreement between bronchial AF and sample emission spectra.

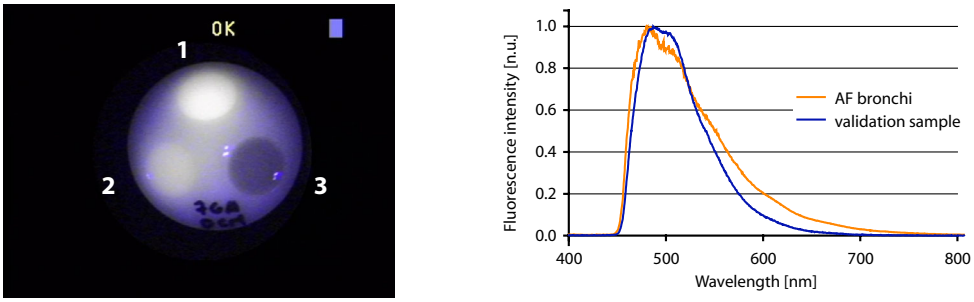

Figure D.2: ***Example for the bronchi.*** [left] *7.5µl fluorol 7GA ($10^{-3}M$) and 5µl DCM ($5 \cdot 10^{-4}M$). Additive : (1) no ink; (2) 12µl ink solution 2; (3) 48µl ink solution 2. iCB was performed on well 1.* [right] *comparison of the fluorescence emission spectra of normal bronchial mucosa and validation sample normalized at their maximum.*

D.3.2 Urology

This urologic calibration chart is similar to the one provided for bronchoscopy. However, the contrast tumor/normal is related to the PpIX detection (and the corresponding red channel intensification). The tissue AF is in this case used as a background image. The calibration chart is also designed with 4 distinct areas:(i) white reflecting area to perform white balance procedure; (ii) 10% grey reflecting area, non-fluorescing, to check color channels cross-talks;

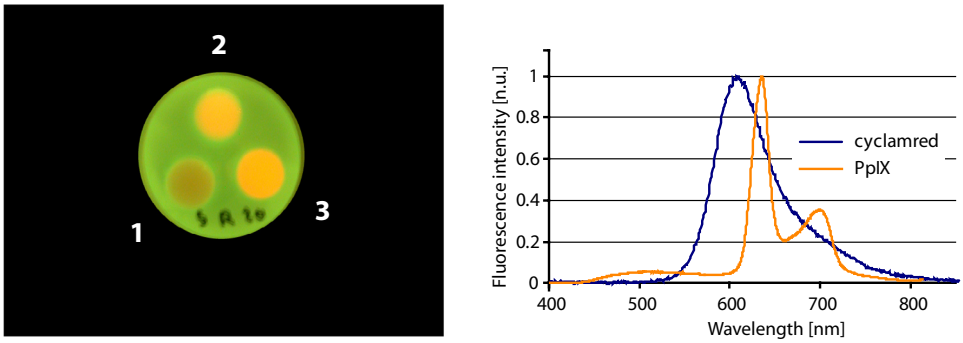

Figure D.3: ***Example for the bladder.*** [left] *5µl cyclamred. Additive : (1) no ink; (2) 6µl ink solution 2; (3) 12µl ink solution 2.* [right] *comparison of the fluorescence emission spectra of PpIX and validation sample normalized at their maximum.*

(iii) red fluorescing area to mimic tumor appearance and control red channel intensification; (iv) green AF to check level of background detection.

Figure D.3 depicts an early version of the urological sample with bright fluorescing spots. The emission was attenuated in the final version to drive the camera into the maximal intensification mode. Despite the non-exact overlap of the fluorescence peaks between PpIX and Cyclamred (as shown in Figure D.3), both display similar brightness and color appearance with the PDD imaging setup.

D.4 Phantom preparation

The silicone base material is transparent with a refractive index of about 1.4. The refractive index of soft tissues has been reported to be between 1.35 and 1.5 [Boli89] for soft tissues. In order to mimic absorption, scattering, and fluorescence properties of the tissue, we added chromophores, fluorophores, and scattering particles to the transparent matrix.

These phantoms were prepared in the framework of a Céline Dutruel's semester thesis. A detailed report about the recipes and the sample optical characterization (fluorescence, transmittance, reflectance) can be found in [Dutr07].

Our first matrix was built out of silicon A & B (100/10 for RTV 141 and 100/5 RTV121, Silitech AG, Switzerland). This material is very convenient to handle on workbench. A second variant was to include the dyes either in a metacrylate solution and to polymerize it into polymethylmetacrylate (PMMA, acrylic glass), or in a polyester matrix (Esprit Composite, France). The two latter materials are not easy to polymerize smoothly with standard lab equipment. The epoxy resin was also excluded because it emits a too strong autofluorescence signal in the green. As compared to other matrices (PMMA, polyester, epoxy), silicone was found to be the best candidates to incorporate various components with a spatially homogeneous distribution.

Scattering particles have to be added to the liquid solution (before polymerization) to mimic tissue optical properties (μ_s, scattering coefficient, μ_a, absorbing coefficient, and g, anisotropy). Candidates were TiO_2 and/or Al_2O_3 (1/1000 w/w with respect to silicone). Other variants included $BaSO_4$, ZnO, MgO.

We reviewed several fluorescing particles, also to be homogenously added before polymerization:

- Sphero^{TM} fluorescent particles (Spherotech Inc., USA). These fluorophores, once incorporated into the particles, do not bleach and their color and fluorescence remains stable for long periods of time under proper storage conditions. Not available at the time of testing.
- Dyes used for lasers : DCM $C_{19}H_{17}N_3O$ (emitting in the red when dissolved in MetOH) and Fluorol7GA (an efficient yellow-green dye for flashlamp-pumped laser). We retained them for the bronchoscopy validation model.
- Perspex^{TM} fluorescent PMMA (Lucite International Inc., USA) Different types of this material have been visually tested within the framework of the endoscopic reference design. They mimic the tissue optical properties (reflectance, effective attenuation coefficient, fluorescence spectrum) in a relatively good agreement (as shown in Chapter 9).
- Doped crytals with rare eath dopants (*e.g.* $NaYF_4$:Yb,Er), as for solid-state lasers, and fluorescent minerals (crystals), (*e.g.* FA-2036, Photon Technology International Inc., USA). Not tested.
- Industrial dyes for plastic like Hostasol red and Polysynthren blue (Clariant Inc., Switzerland). Used to backscatter blue and red light in urology and bronchoscopy samples.
- Leutalux^{TM} (Leuchtstoffwerk GmbH, Germany) as proposed by F. Borle [Borl06]. The main advantage of Leutalux pigments is that they all can be excited in the blue-violet and they have a broad band emission. We retained them to mimic the bright PpIX fluorescence.

In the following, we describe the *modus operandi* shortly, since it was thoroughly described in [Dutr07]. The components were first dissolved or dispersed in ethanol and the solution was carefully mixed with the silicone base. Ethanol was then removed by evaporation either in a fume hood or by gentle heating. Finally, after allowing the base to cool, the catalyst was added and the curing process could take place. A vacuum pump was used to extract air bubbles (due to mixing procedure) prior to curing. Methanol, dimethyl sulphoxide (DMSO), and water were also used successfully as solvents or dispersants instead of ethanol. The same technique of evaporation was been performed to remove these before the curing. Water appeared to be the most difficult liquid to mix with silicone though. Consequently, an homogeneous distribution of dye in the phantom was obtained only after complete evaporation of the water. Other solvents can certainly be used, but have not been tested so far.

Beside of their wide availability, liquid fluorescent dyes have the main disadvantage to photobleach rapidly and could thus not be considered as a stable reference. Therefore, solid pigments have been preferred until now.

D.4.1 Final recipes for the fluorescence phantoms

Various solid fluorescence phantoms were fabricated during this thesis work. The chosen shape was an epoxy mold (Polytec, Polymere Technologien, Germany) with 3 wells containing 3 different concentrations of pigments (fluorescing and non-fluorescing) embedded in a silicone matrix. Since it was a fully iterative process, we do not describe here all the attempts in details, but rather present the final mixture's recipe.

Three main components were separately prepared and then mixed at different concentrations:

- **Substrate A**: 5g of mixture with the proportions 10:1:1 (silicon/hardener/TiO2)
- **Solution B**: 4ml Ink diluted in 7.5ml EtOH
- **Solution C**: 0.4g Cyclamred diluted in 10ml EtOH

Bronchial reference
3 epoxy molded wells with a basic substrate of 5 g of **A** with the following adjuvants:
1st well: 5 μl green Leutalux solution
2nd well: 7.5 μl de Fluorol7GA 10^{-3}M, 5 μl DCM 5.10-4M, 48 μl **B** solution
3rd well: 5 μl Polysynthren blue and 12 μl **B** solution.

Figure D.2 depicts the bronchial validation sample. The bluish appearance in the 3rd well mimic the real tumor *in vivo*.

Bladder reference
3 epoxy molded wells with a basic substrate of 5g of **A** with the following adjuvants:
1st well: 5μl **C** solution
2nd well: 5μl **C** solution and 12μl **B** solution
3rd well: 20μl Hostasol red and 12μl **B** solution

Figure D.2 depicts one version urological validation sample (without the red backscattering part). The strong red emission can be further attenuated with Indian ink.

This mixture was also implemented in a "real" looking bladder model to serve as a demonstrator for fluorescence photodetection (see Figure D.4).

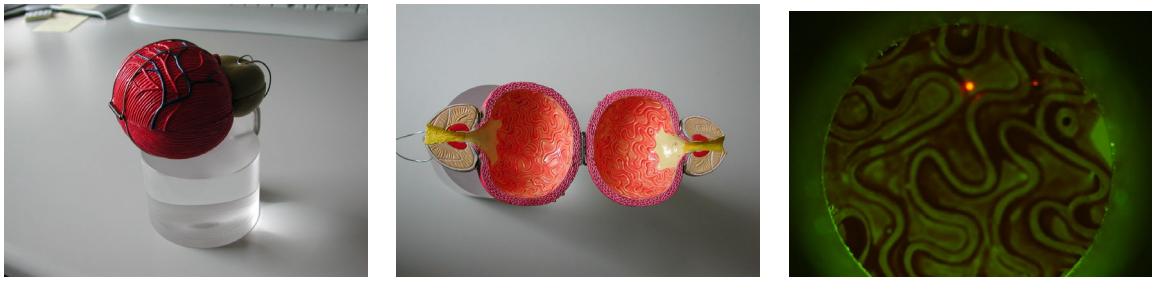

Figure D.4: *Bladder model with red fluorescing spots, invisible in WL illumination*

Bibliography

[Bays97] R. Bays, G. Wagnières, D. Robert, J. F. Theumann, A. Vitkin, J. F. Savary, P. Monnier, and H. van den Bergh. Three-dimensional optical phantom and its application in photodynamic therapy. *Lasers Surg Med*, 21(3):227–234, 1997.

[Beck98] G. Beck, N. Akgün, A. Rück, and R. Steiner. Design and characterisation of a tissue phantom system for optical diagnostics. *Lasers in Medical Science*, 13(3):160–171, 1998. cited By (since 1996) 12.

[Boli89] F. Bolin and L. Preuss. Refractive index of some mammalian tissues using a fiber optic cladding method. *Appl Opt*, 28:2297–2303, 1989.

[Borl06] F. Borle. Fluorescence phantoms based on leutalux pigments. private communication, 2006.

[deB10] D. M. de Bruin, R. H. Bremmer, V. M. Kodach, R. de Kinkelder, J. van Marle, T. G. van Leeuwen, and D. J. Faber. Optical phantoms of varying geometry based on thin building blocks with controlled optical properties. *J Biomed Opt*, 15(2):025001, 2010.

[Dutr07] C. Dutruel. Développement d'une référence de fluorescence quantitative pour des systèmes de détection du cancer par imagerie de fluorescence. Master's thesis, EPFL, 2007.

[Firb93] M. Firbank, M. Hiraoka, M. Essenpreis, and D. T. Delpy. Measurement of the optical properties of the skull in the wavelength range 650-950 nm. *Phys Med Biol*, 38(4):503–510, Apr 1993.

[Suko96] U. Sukowski, F. Schubert, D. Grosenick, and H. Rinneberg. Preparation of solid phantoms with defined scattering and absorption properties for optical tomography. *Phys Med Biol*, 41(9):1823–1844, Sep 1996.

[Wagn97] G. Wagnières, S. Cheng, M. Zellweger, N. Utke, D. Braichotte, J. P. Ballini, and H. van den Bergh. An optical phantom with tissue-like properties in the visible for use in pdt and fluorescence spectroscopy. *Phys Med Biol*, 42(7):1415–1426, Jul 1997.

Appendix E

Spectral optimization for HM endoscopy

In order to better visualize the vessels, we may improve their contrast with respect to the background. Since hemoglobin is a very strong absorber of green and blue light (see Section 2.1.1.1), it can be used as an intrinsic marker of the vessel, because it is contained almost exclusively in the red blood cells. Consequently, we moved towards a spectral optimization of our endoscopic observation system. This implementation is less invasive than the intravenous injection of a contrast dye (such as fluorescein or indocyanine green).

Since we did not exactly know which vessels at which depth to look at, we based our approach on the lesion depth profiling with different wavelength. Indeed, due to the tissue optical properties, different excitation wavelengths penetrate down to different tissue depths. For blue light excitation, only the first cell layers of the lesion emit fluorescence, because the light is not penetrating deeper. For green light excitation, several hundred microns in depth emit fluorescence, and for red light several millimeters [Dögn01].

In this study, we will adapt this principle to the blood vessels. Indeed, vessels located at different depths absorbs light of different wavelengths. The long penetrating wavelength may probe the whole depth, whereas the short wavelength may probe only the superficial vessels. It means that it is possible to follow a vessel with long wavelength to deeper layers of the mucosa, whereas we may observe vessels with abrupt ending at the penetration depth of blue violet light. In the final image, the vessel appearance may be affected by (i) the scattering and absorption characteristics of mucosa at different wavelengths, (ii) the oxygenation state of blood, which affects its absorption properties, (iii) the diameter and the depth of the vessels, and (iv) the visual perception process [Kien96].

To exploit this contrast, we placed bandpass filters in the light source in order to target the two hemoglobin absorption peaks. Sequentially, a grid for white light attenuation (370–700 nm), a blue filter (405 nm FWHM 50 nm, proprietary PDD filter, Richard Wolf GmbH), and a green filter (550 nm, FWHM 50 nm, Chroma Technologies Inc.) were placed in front of the Xenon bulb. Images were acquired with the unfiltered endoscopic camera (Telecam, Karl Storz GmbH & Co KG,Tuttlingen, Germany).

The original video sequences were digitized via IEEE1394. Individual frames were extracted with Adobe Premiere Pro. The 24-bit RGB color images were then split in three 8-bit grayscale

images, one for each color channel (ImageJ, NIH). Figure E.1 shows typical images acquired with this setup and the corresponding decomposition in the three video channels R(red), G(green), and B(blue). In this figure, the contrast and brightness were adjusted for legibility purpose. Whenever possible, images in the three excitation modes (WL, blue, green) should be acquired on the same lesion to allow direct comparison. However, for historical reasons, the number of patients observed with each illumination mode is not equivalent : WL (n≃60), GBS (n≃15), BBS (n≃5).

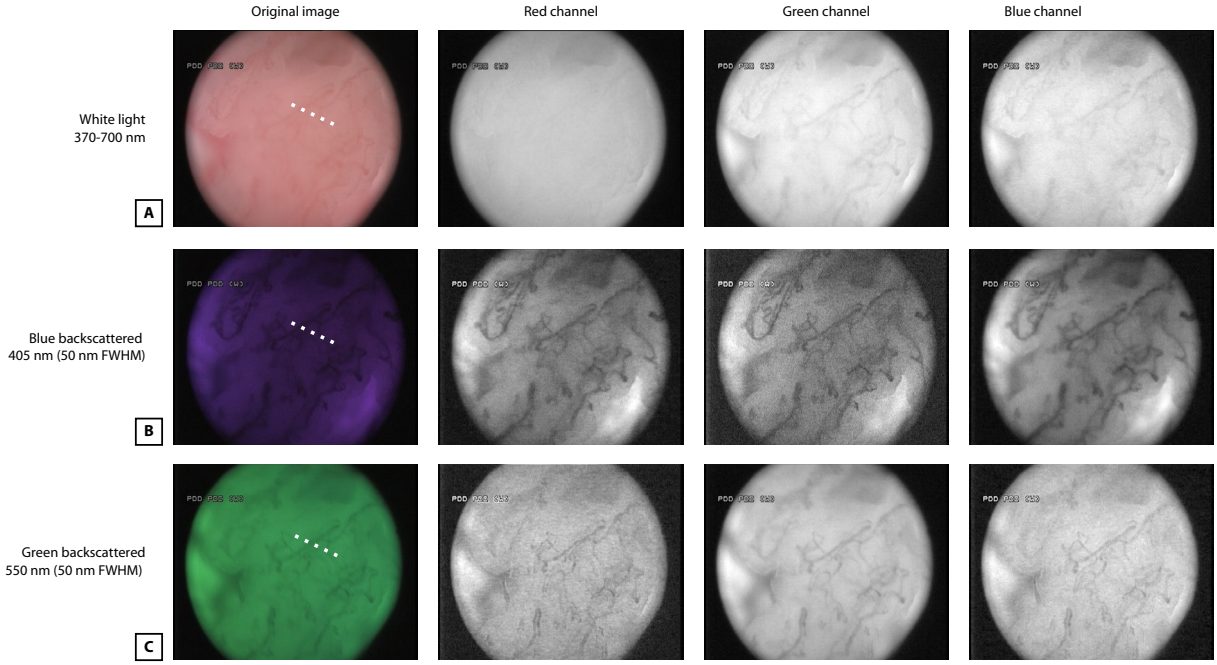

Figure E.1: *RGB channel decomposition for the three excitation modes (WL, blue backscattered, green backscattered). The white dashed line represent the place where intensity profile from Figure E.2 were measured. Grayscale intensities were adjusted to allow better visualization.*

First, we measured intensity profiles (4-pixels wide to minimize noise) in each individual color channel on a small portion of the image representative for vessel-background contrast (see the white dashed line in Figure E.1). These intensity profiles are shown in Figure E.2 with two columns. On the left part, figures A1, B1, C1 presents the overall intensity of each channel for each illumination light, whereas the mean intensity is subtracted from the overall intensity in figures A2, B2, C2. The dashed lines represent the position of the vessels. Obviously, the channel containing the highest intensity is depending on the excitation mode. Consequently, it yields a reddish (Fig.A under WL), a bluish (Fig.B under blue light), a greenish (Fig.C under green light) appearance to the RGB composite image.

If one observes these curves in details, it appears that the white light illumination yields poorly contrasted image. Indeed, the peak-to-peak intensity variation between vessel and background is less that 10 counts, and the vessel information is not really channel-specific (i.e. more important in one channel that in the two others). Conversely, the blue light illumination yields good contrast in all the channels (twice as high as with WL illumination). A major drawback would be the overall lower intensity of the image, but this may be compensated by electronic means. The green light illumination also yields a good contrast.

An other mean to evaluate the contrast is the evaluation of the color difference of the back-

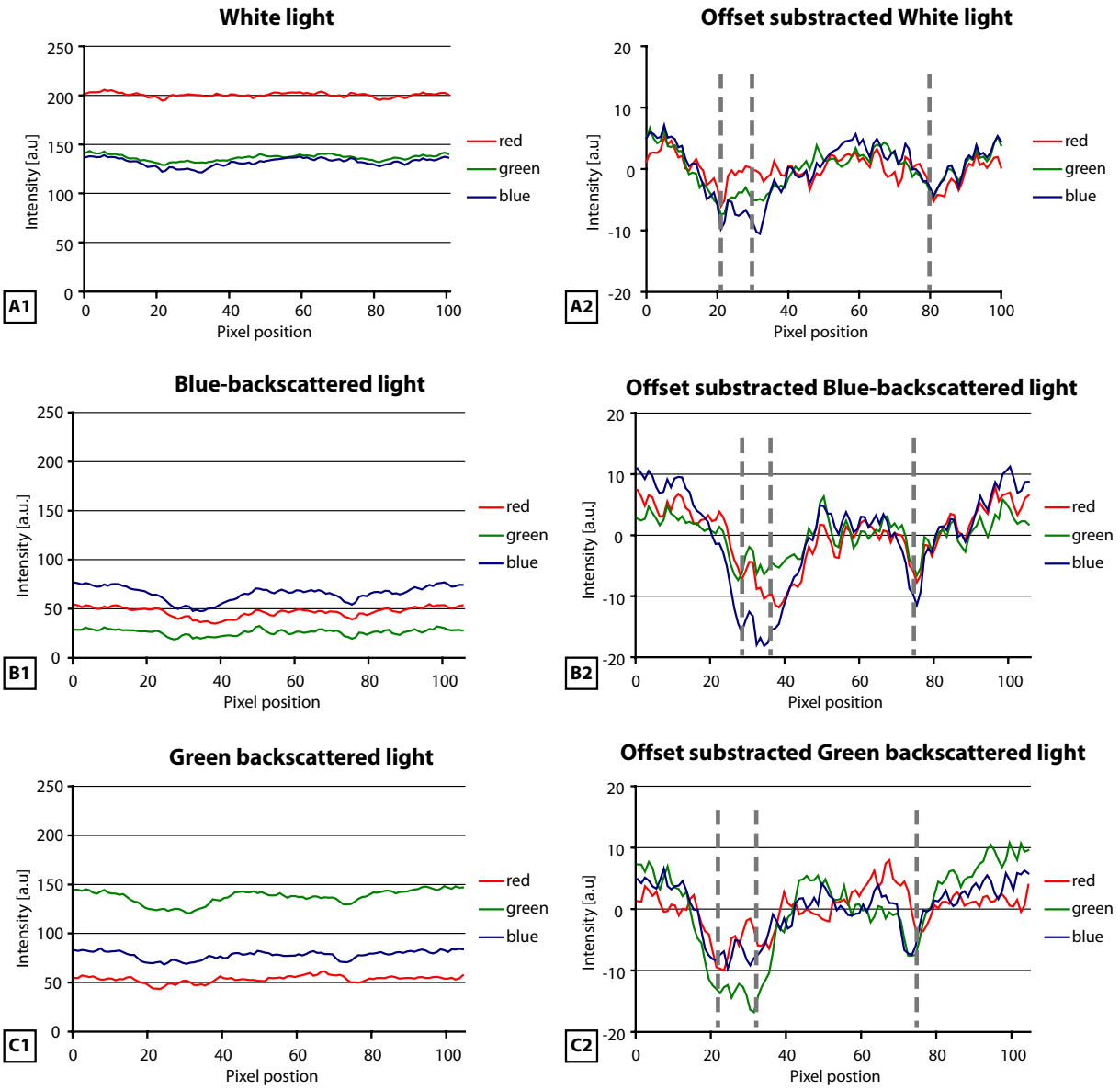

Figure E.2: *Intensity of the RGB channels for the three excitation modes (WL, blue backscattered, green backscattered). On the left, without mean substraction. On the right with mean substraction. The dashed lines represent the position of the vessels.*

ground vs. vessels. The color representation most commonly used in computers and other electronic systems is red-green-blue (RGB) color channels. However, there exist other color spaces that can be more effective in the context of reaching a specific goal, such as closeness to human perception (*e.g.* CIE-Lab) [Bosm10].

Consequently, we calculated the color difference in CIE 1976 $(L*, a*, b*)$ color space (CIELAB) [Kueh76]. In this color space, the color of endoscopic images was expressed in terms of three coordinate values $(L*, a*, b*)$, which located the object in a three-dimensional (3D) space. $L*$ is defined as lightness, $a*$ as the red-green component and $b*$ as the yellow-blue component. Regions-of-interest were selected on several zones appearing as background (resp. vessels). Typically, six analysis zones (three of each type) were selected per site to accommodate the illumination artifacts due to the bladder geometry. We defined here the Euclidean distance in the color space as follows, with L_i,a_i,b_i being acquired on background (b-index), resp. vessel (v-index):

$$\Delta(L, a, b) = \sqrt{(L_v - L_b)^2 + (a_v - a_b)^2 + (b_v - b_b)^2}$$

Figure E.3 shows the (L, a, b)-color space visualization for the 3 illumination lights (white, green, blue) for the background (resp. vessels) areas. The error bars represent variations across the image. A general trend that can be observed is that vessels have a lower lightness than background. This may be attributed to hemoglobin absorption, that results is less backscattered light. We observe high variations in the hue components (a and b) in the different illumination modes, originating from variations in channel intensities (see Figure E.2).

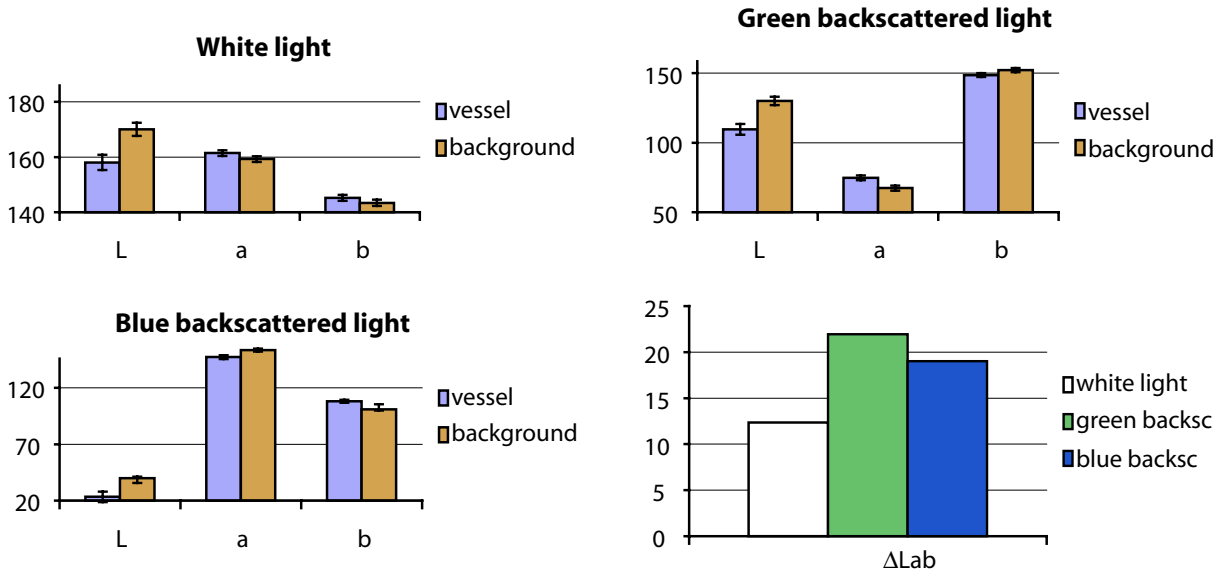

Figure E.3: *(L, a, b)-color space visualization and representation of the Euclidean distance $\Delta(L, a, b)$ for the 3 illumination lights (white, green, blue).*

The last histogram presents the value of the color distance ($\Delta(L, a, b)$ for the three illumination modes. It results that blue and green illuminations yield a much better contrast than white light illumination. It confirms the observed results on the intensity profiles.

Bibliography

[Bosm10] H. H. W. J. Bosman, N. Petkov, and M. F. Jonkman. Comparison of color representations for content-based image retrieval in dermatology. *Skin Res Technol*, 16(1):109–113, Feb 2010.

[Dögn01] N. Dögnitz. *Characterization of Vascular and Cancerous Lesions by Multispectral Excitation Fluorescence Imaging.* PhD thesis, EPFL Thesis Nr 2450, 2001.

[Kien96] A. Kienle, L. Lilge, A. Vitkin, M. Patterson, B. Wilson, R. Hibst, and R. Steiner. Why do veins appear blue? a new look at an old question. *Applied Optics*, 35(7):1151–1160, 1996.

[Kueh76] R. Kuehni. Color-tolerance data and the tentative CIE 1976 Lab formula. *J Opt Soc Am*, 66:497–500, 1976.

Appendix F

Color presentation in endoscopy

F.1 Introduction

The capability of an observer to take full advantage of a chromatic contrast presented on a monitor highly depends on its ability to differentiate colors and color patterns, depending on the background and surrounding environment.

With the help of his retinex model, Ewdin Land tried to sort out the mechanisms of color perception [Land64, Land71]. He described that the spectral composition of the light will depend on two factors: (i) the spectral reflectance of the object, its tendency to reflect some wavelengths more than others, and (ii) the spectral composition of the illuminate, the relative proportions of different wavelengths in the light that falls on the object. As we view an object under different conditions (distances, angles, and illuminations), important changes occur in the physical image on our retina, but our sensations prove much more stable than would be expected from our changeful retinal image [Land77, Land86].

One of the several 'constancies' that characterize our sensory experience is *color constancy*. Land *et al.* provided a particularly impressive and instructive demonstration of color constancy. He performed an experiment in which a single mixture of red, green, and blue light produced many different color sensations. Observers reported white, pink, green, red, brown, yellow, purple, blue, and black sensations from identical mixtures of red, green, and blue lights [Land77].

Land used his "Mondrians" cells to show that nearly the full gamut of color sensations can be produced from a single mixture of red, green, and blue light. In particular, he puts forward the fact that the foreground perception is mostly influenced by the color surrounding. For instance, in a famous experiment, he was able to adjust the illuminants so that a green and a white area were sending exactly the same triplet of radiant energies (RGB) to the eye. Under actual viewing conditions, white area continues to look white and green area continues to look green even though the eye was receiving the same flux triplet from both areas.

Humans perceive the three-dimensional (3D) world by a pair of two-dimensional (2D) retinas that react to visible light with a peak sensitivity near 550 nm. In a recent review, Cuschieri linked the physical and psychological aspects of visual perception [Cusc06]. After preliminary processing of the stimuli (including color) in the photoreceptors, the next event in the chain of visual perception involves transfer of electrical signals (retinal image information) via the optic nerves for resolution in the lateral geniculate nucleus and in the V1 region of the visual cortex.

Downstream, further secondary processing occurs in specialized areas of the visual cortex (e.g., V4 [color] and V5 [motion]). The resulting image recognized by the subject in the cognitive process is known as a *percept*, which determines the interpretation of the visual stimulation [Brid06]. Thus, the reality perceived is not absolute, but individual. Visual psychologists distinguish between two kinds of perception: *direct* (perception of objects in three-dimensional space) and *indirect* (perception of pictures/images of objects rather than the objects themselves).

Humans have trichromatic color vision based on three color receptors on the retinal cone cells: blue (β), or short wave (450 nm); green (γ), or medium wave (540 nm); and red (ρ), or long wave (580 nm) [Stoc99, Stoc00]. Hering was the first to suggest that the nature of the color perception process is the product of the opponent interaction between stimuli from the rods (respond to black and white) and the color sensing cones [Heri64].

It has been shown that different observers may observe the scene with a different perception due to the relative sensitivity of their color processing chain. Small perception are often negligible, but some form of color-blindness affects 1 in 12 individuals (8% of males and 0.4% females). Color-blindness (often called *daltonism*) types are classified after the involved cone types and the importance of visual trouble: (a) Monochromatism: no perception of colors (b) Dichromatism: absence of gene, thus lack of pigmentation. Only 2 colors are perceived. (c) Trichromatism: perception of 3 colors with abnormal intensity, due to gene hybridization, leading to important variations in chromatic sensitivity.

Even if the proportion of genetic daltonism is rather low, some subtle variations could have a great influence on the way physicians evaluate color contrast on a display. With fluorescence imaging, color presentation optimization is of high interest, since the information source is the color contrast itself.

In the endoscopic context, and thus in fluorescence cancer detection, color differentiation is the basis of every diagnostic approach. Indeed, fluorescence contrast often displays as a chromatic difference to be seen either directly through the eye piece of the endoscope or on the screen if a camera is connected to the endoscope. The latter allows a false-color presentation, which can be of great help to improve the contrast, but it has to be studied carefully before implementation. Little work has been done on aspects of visual perception and related defects as they affect the proficiency level for endoscopic surgery, in which the surgeon must operate from images rather than reality.

Unfortunately, little is known on the proficiency level of color-blind surgeons (anomalous trichromats and dichromats) in endoscopic surgery. Koningsberger *et al.* designed a study to assess the prevalence of color vision deficiencies amongst Dutch GI endoscopists and to determine whether color vision deficiency affects an endoscopist's diagnostic skill [Koni94]. The study did not show any effect of color vision deficiencies on endoscopic skills, nor does it show any deviant prevalence of color vision deficiencies amongst Dutch GI endoscopists.

In this preliminary study, we would like to identify which color presentation is best suited for endoscopic images. Observers were asked to classify images with different color settings for the foreground (tumor) and background. In a near future, the objective would be to implement in the endoscopic display a user-defined color presentation.

F.2 Color optimization in endoscopic fluorescence imaging

Preliminary tests performed by our group on charts designed for color blindness detection have been performed on a limited number of volunteers. The well-known Ishihara's tests can evaluate color blindness in individuals. Inter-observer variations lead us to the conclusion that an

observer-customized appearance is likely to increase observation comfort, and thus to benefit the diagnostic capability.

The current color presentation in endoscopic imaging devices is based on empiric observations. From a user point-of-view, it would be desirable to choose among a set of color presets corresponding to the eye's optimal color sensitivity. The latter could be determined with the help of pseudoisochromatic tests. It would result different color appearance independent from the raw spectral information. Figure F.1 depicts typical color appearance of endoscopic images.

a) Storz imaging system (tumor in red, background in blue)

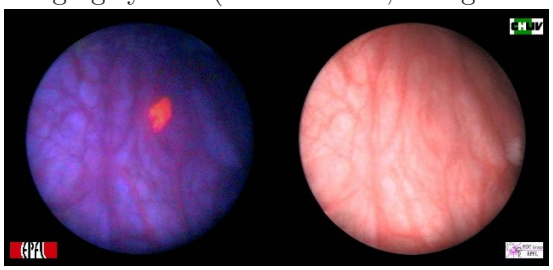

b) Wolf imaging system (tumor in magenta, background in blue-green)

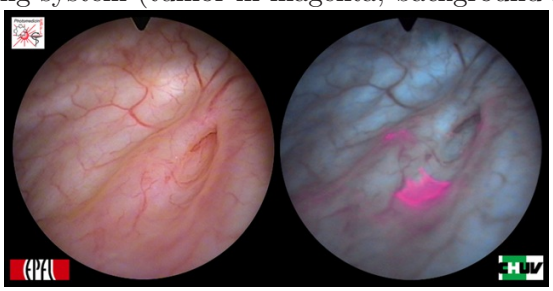

Figure F.1: *Comparison of the color presentation of two commercial devices*

In collaboration with Cédric Paulou, we performed some preliminary work on the visual sensitivity of chromatic contrasts [Paul10]. Basically, 11 naive subjects were asked to rank 8 images showing the same site, but with different color appearances, i.e. variations for the tumor and background, as depicted in Figure F.2. A small flat tumor is present in the middle of the picture; the ranking was based on tumor detectability.

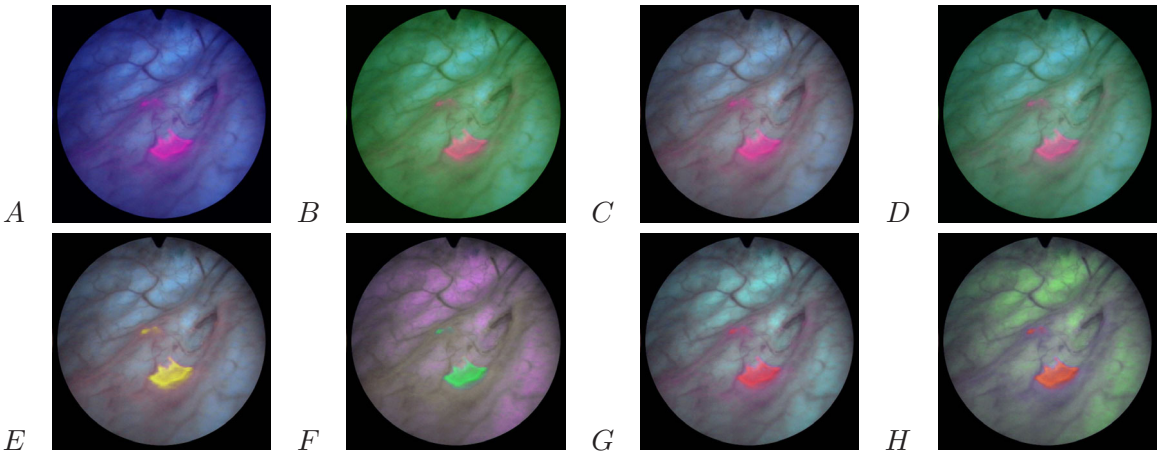

Figure F.2: *Images submitted to 10 observers*

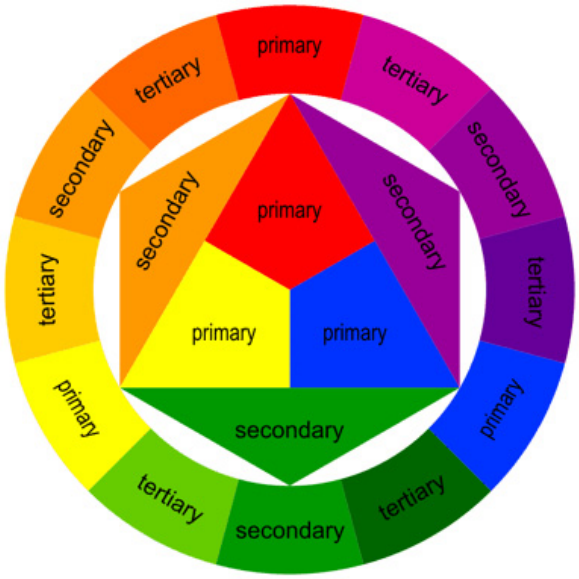

Figure F.3: *Simplified color wheel adapted from ArtFactory*

The colors in the images A, B, C and D were allocated with "arbitrary" color. Multiplicative factors of the Photoshop color balance procedure are listed in Table F.1. The images E, F, G, H were produced in such a way that the tumor and the normal tissues were presented in complementary colors (i.e. with opposite value in the color wheel, see Figure F.3).

The *total score* was computed as the ranking position (rank) weighted by the numbers of answers (n) : $S = \sum_i \text{rank}_i \cdot n_i$.

Arbitrary images		S	Complementary colors		S
A	blue 100	56	E	yellow vs. blue	12
B	green 100	72	F	green vs. magenta	33
C	original image	57	G	red vs. cyan	37
D	green100 blue50	81	H	orange vs. green	48

Table F.1: *Color allocation of the 8 images*

Figure F.4 clearly shows that images presented in complementary colors increased the detectability of lesions vs. background. The lowest score is obtained by E, maybe due to the fact that human's eye sensitivity is highest in the yellow-green spectral region. Additionally, the image F — which is classified in the 7th and 8th position for only one observer — illustrates that the most convenient color presentation for a majority of operators (yellow over blue, red over green) remain unsatisfactory for specific types of color sensitivity.

The diagonal in Figure F.4 is almost free of any point, meaning that their is a clear demarcation between complementary and arbitrary colors. For most of the images (even with the small sample size), we observe a Gaussian-like distribution, but, as already mentioned, the bi-modal distribution for image F suggests that color sensitivity is definitely not the same for each observer.

Brown *et al.* suggest that the perceived color at each point in a visual scene depends on the relationship between light signals from that point, and light signals from surrounding areas of the scene [Brow97]. In the well known phenomenon of simultaneous color contrast, changing the overall brightness or hue of an object's surround induces a complementary shift in the perceived

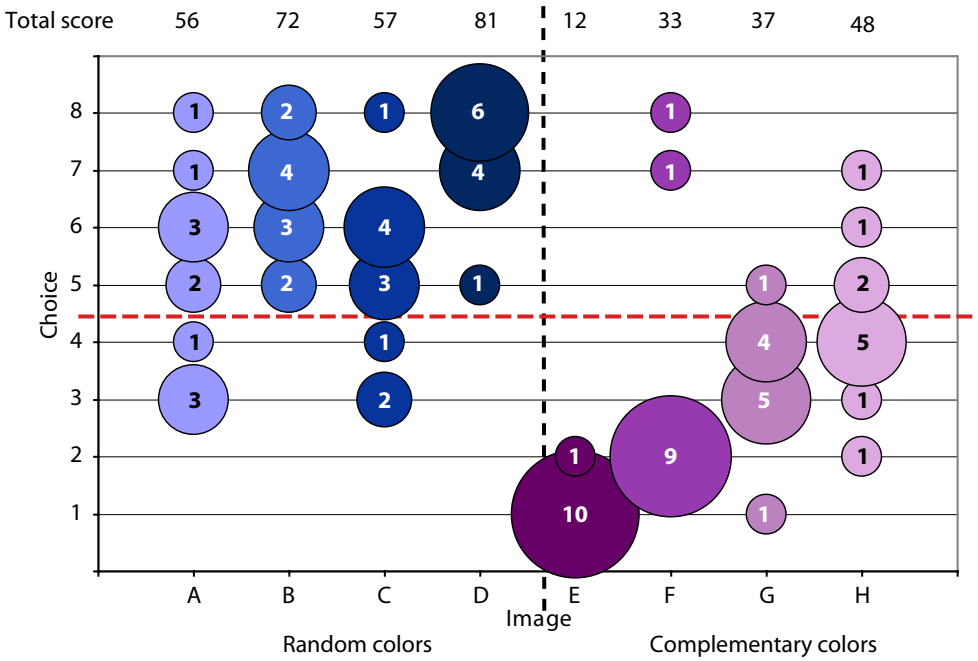

Figure F.4: *Graphical representation of the survey results. The circle sizes represent the number of answers corresponding to the choice.*

brightness or hue of the object's color. These authors also demonstrated a strong compression of the gamut of perceived colors depending on the background color. In other words, when a low-contrast rectangle is embedded in a high-contrast mosaic of richly colored squares, it appears as indistinct, washed-out shade of gray. But the same physically identical rectangles, when embedded in a uniform 50% gray background, appeared much more distinct and colorful.

For our endoscopic approach, it would mean that the best contrast would be achieved by setting the background to a complementary color related to foreground. In the bladder, the current color implementation with magenta-green is not too far from the ideal situation, except for people with specific red deficiency. An other option would be to set a grayish appearance for the background, and the tumor in a high-contrast saturated color. In collaboration with our industrial partner, we have implemented this approach in the bronchi (see Section 7.5).

In the future, we would like to implement color contrast adjustment directly in the imaging system. This would allow the system to be adapted to the subjective color perception of the user (this can to some extent combat color weaknesses of the user). Moreover, the color will also be adjusted in critical situations, when the initial tissue differentiation is not as clear as required, achieving the best possible distinction between healthy and diseased tissue.

Bibliography

[Brid06] H. Bridge and S. Clare. High-resolution mri: in vivo histology? *Philos Trans R Soc Lond B Biol Sci*, 361(1465):137–146, Jan 2006.

[Brow97] R. O. Brown and D. I. MacLeod. Color appearance depends on the variance of surround colors. *Curr Biol*, 7(11):844–849, Nov 1997.

[Cusc06] A. Cuschieri. Epistemology of visual imaging in endoscopic surgery. *Surg Endosc*, 20 Suppl 2:S419–S424, Apr 2006.

[Heri64] E. Hering. *Outlines of a theory of the light sense Harvard.* University Press, Cambridge, MA, 1964.

[Koni94] J. C. Koningsberger, D. van Norren, J. C. van Niel, and W. Dekker. Does color vision deficiency in the endoscopist influence the accuracy of endoscopic diagnosis? an anonymous study with dutch gastrointestinal endoscopists. *Endoscopy*, 26(6):549–553, Aug 1994.

[Land64] E. H. Land. The retinex. *American Scientist*, 52:247–264, 1964.

[Land71] E. H. Land and J. J. McCann. Lightness and retinex theory. *J Opt Soc Am*, 61(1):1–11, Jan 1971.

[Land77] E. H. Land. The retinex theory of color vision. *Sci Am*, 237(6):108–128, Dec 1977.

[Land86] E. H. Land. An alternative technique for the computation of the designator in the retinex theory of color vision. *Proc Natl Acad Sci*, 83(10):3078–3080, May 1986.

[Paul10] C. Paulou. Color vision optimization on endoscopic images. private communication, 2010.

[Stoc99] A. Stockman, L. T. Sharpe, and C. Fach. The spectral sensitivity of the human short-wavelength sensitive cones derived from thresholds and color matches. *Vision Research*, 39(17):2901–2927, 1999.

[Stoc00] A. Stockman and L. T. Sharpe. The spectral sensitivities of the middle- and long-wavelength-sensitive cones derived from measurements in observers of known genotype. *Vision Research*, 40(13):1711–1737, 2000.

Blaise Lovisa

Av. de l'Europe 41
CH-1870 Monthey
blaise.lovisa@alumni.ethz.ch
born July 13th 1981, married, Swiss citizen

Education

2005-2010 **Ecole Polytechnique Fédérale, Lausanne** (EPFL)
PhD, Biomedical optics

2000-2005 **Eidgenössische Technische Hochschule, Zürich** (ETHZ)
Electrical engineer ETH (dipl.el.Ing ETH) - Master of Science (MSc) Information Technology and Electrical Engineering (ITET)

2000 **Collège de l'Abbaye, St-Maurice**
High school diploma Type C (scientific & math)

Professional experience

2005-2010 **EPFL. Medical Photonics Group.**
Graduate Research Assistant

2005 **University of Arizona, Tucson, USA. Tissue Spectroscopy Lab.**
Graduate research assistant

Jul-Oct 2004 **Institute of Biomedical Technology (INBIT), Patras, Greece.**
Scientific trainee.

Mar-Jun 2004 **Unispital Zürich (USZ), Neonatology Department.**
Undergraduate research assistant.

Sep-Dec 2003 **ETHZ. Integrated Systems Laboratory.**
Undergraduate research assistant.

Publications and award

Author or co-author of 6 peer-reviewed publications, 2 invited talks, 11 oral presentations and conference proceedings, 6 posters.
Best poster award, Photonics Doctoral School, EPFL Research Day 2006

Languages

French (mother tongue), English (C1), German (C1), Swiss German, Italian (A1)

Hobbies

Choral music, baryton-bass (classical, Renaissance and contemporary music).
Mountaineering (ski touring, mountain hiking, climbing).
Member of steering committee of bilingual artistic association (3500 adults, 4000 children) with the editorial responsability of a quarterly publication about choral music (1000 subscriptions) and web editor of a collaborative platform.

List of publications

Peer-reviewed Publications

6. B. Lovisa, P. Jichlinski, B.C Weber, D. Aymon, H. van den Bergh, G. Wagnières, *High magnification vascular imaging to reject false-positive sites in situ during Hexvix® fluorescence cystoscopy*, Journal of Biomedical Optics, 15(5), 10149SSR (2010)

5. T. Gabrecht, B. Lovisa, H. van den Bergh, G. Wagnières, *In-vivo Quantification of the Inter-Patient Variations of the Tissue remitted Light Intensity during Autofluorescence Bronchoscopy*, Lasers in medical science, 24(1), 45–51 (2009)

4. P. Jichlinski, B. Lovisa, C. Erling, D. Aymon, H. van den Bergh, G. Wagnieres, *Fluorescence cystoscopy: Perspective in clinical practice and research*, Urologe - Ausgabe A, 47 (8), 975–977 (2008)

3. T. Gabrecht, B. Lovisa, F. Borle, G. Wagnières, *Design of an endoscopic optical reference to be used for autofluorescence bronchoscopy with a commercially available diagnostic autofluorescence endoscopy (DAFE) system*, Phys. Med. Biol. 52, N163-N171 (2007)

2. B. Lovisa, T. Gabrecht, S. Andrejevic, P. Grosjean, A. Radu, P. Monnier, H. van den Bergh,G. Wagnières, *Improvement of the contrast in cancer detection by autofluorescence bronchoscopy using a narrow spectral violet excitation: a preliminary study*, Biomed. Signal Processing and Control, 2 (3), 234–238 (2007)

1. T. Gabrecht, A. Radu, M. Zellweger, B. Lovisa, D. Goujon, P. Grosjean, H. van den Bergh, P. Monnier, G. Wagnières, *Autofluorescence bronchoscopy: Clinical experience with an optimized system in head and neck cancer patients*, Medical Laser Applications 22, 185–192 (2007)

Invited talks

- B. Lovisa, P. Jichlinski, D. Aymon, H. van den Bergh, G.A. Wagnieres, *Detection of early bladder carcinoma by fluorescence cystoscopy with Hexvix®: new perspectives with high magnification cystoscopy.*, CHUV surgery research seminar, 25.09.2007

- B. Lovisa, P. Jichlinski, D. Aymon, H. van den Bergh, G. Wagnières, *Detection of early bladder carcinoma by fluorescence cystoscopy with Hexvix®: new perspectives with high magnification cystoscopy.*, ECI conference, Naples/FL, 13.06.2007

Oral presentations & Proceedings

12. B. Lovisa, A.M. Novello, P. Jichlinski, H. van den Bergh, G. Wagnières, *Fluorescence of the bladder washout fluid following cystoscopy : a preliminary study*, Proceeding of SPIE, Volume 7548, San Francisco (2010)

11. B. Lovisa, P. Jichlinski, D. Aymon, B.-C. Weber, H. van den Bergh, G. Wagnières, *Bladder cancer detection by fluorescence imaging with Hexvix®: Image processing to help high magnification cystoscopy*, Proceeding of SPIE, Volume 7380, Article number 738047, IPA (2009).

10. B. Lovisa, P. Jichlinski, P. Monnier, B.C. Weber, H. van den Bergh, G.A Wagnières, *Development of high magnification endoscopy for the rejection of false positives observed in the bladder and the tracheo-bronchial tree during the detection of early cancers by endoscopic fluorescence imaging*, Photodiagnosis and Photodynamic Therapy, 2009, 6, 147-148, ESP Meeting, Wroclaw (2009)

9. B. Lovisa, P. Jichlinski, D. Aymon, B.-C. Weber, H. van den Bergh, G. Wagnières, *Bladder cancer detection by fluorescence imaging with Hexvix® : optimization of the excitation light during high magnification cystoscopy*, Proceeding of SPIE, Volume 7368, Article number 73681I, Munich (2009).

8. B. Lovisa, P. Jichlinski, D. Aymon, B.C. Weber, H. van den Bergh, G.A. Wagnières, *Detection of early bladder carcinoma by fluorescence cystoscopy with Hexvix®: Optical characterization of a high magnification cystoscope*, Proceeding of SPIE, Volume 7161, Article number 716118, San Jose (2009).

7. B. Lovisa, P. Jichlinski, D. Aymon, H. van den Bergh, G.A. Wagnières, *Detection of early bladder carcinoma by fluorescence cystoscopy with Hexvix®: Improvement of the specificity by microcystoscopy*, Progress in Biomedical Optics and Imaging - Proceedings of SPIE Volume 6842, San Jose (2008), Article number 684218

6. B. Lovisa, P. Jichlinski, D. Aymon, H. van den Bergh, G.A. Wagnières, *Cancer detection by fluorescence imaging: Characterization of suspicious sites by high magnification endoscopy*, EPFL Photonics Day, 17.10.2008

5. T. Gabrecht, A. Radu, M. Zellweger, B. Lovisa, D. Goujon, P. Grosjean, H. van den Bergh, P. Monnier, G. Wagnières, *Detection of early bronchial cancer by autofluorescence: results in patients with H&N cancer*, Proceedings of SPIE -Volume 6628, Diagnostic Optical Spectroscopy in Biomedicine IV, 66280C (2007)

4. B. Lovisa, P. Jichlinski, D. Aymon, H. van den Bergh, G.A. Wagnières, *Development of microcystoscopy for the characterization of lesions detected by fluorescence imaging with Hexvix® in the human bladder*, ESP Congress, Bath (UK), September 2007

3. B. Lovisa, P. Jichlinski, D. Aymon, L. Guillou, H. van den Bergh, G. Wagnières, *Détection de carcinomes précoces de la vessie par cystoscopie de fluorescence avec Hexvix® : amélioration de la spécificité par microcystoscopie*, OptDiag'07, Paris, France, 15-16 May 2007

2. B. Lovisa, T. Gabrecht, S. Andrejevic, P. Grosjean, A. Radu, P. Monnier, B.-C. Weber, H. van den Bergh,G. Wagnières, *Improvement of the contrast in cancer detection by autofluorescence bronchoscopy using a narrow spectral violet excitation: a preliminary study*, in Proceedings of the 6th IFAC Symposium, Reims, France, 20-22 September 2006

1. R. George, R. Krishnamurthy, B. Lovisa, N. D. Krikpatrick and U. Utzinger, *Clinical device for early detection of ovarian cancer using optical spectroscopy*, Proceedings of SPIE, Volume 6091, San Jose, CA (2006).

List of posters

6. B. Lovisa, P. Jichlinski, D. Aymon, H. van den Bergh, G. Wagnières, *Bladder cancer detection by fluorescence imaging with Hexvix®: Characterization of suspicious sites by high magnification cystoscopy*, Fisba Optik, Sankt-Gallen, Switzerland, June 2009

5. B. Lovisa, P. Jichlinski, D. Aymon, H. van den Bergh, G. Wagnières, *Fluorescence detection of bladder cancer with Hexvix®: New perspectives with high magnification cystoscopy*, Biomedical Photonics Network Annual Meeting, Beaulieu, Switzerland, June 2008

4. B. Lovisa, P. Jichlinski, D. Aymon, H. van den Bergh, G. Wagnières, *Detection of early bladder carcinoma by fluorescence cystoscopy with Hexvix®: New perspetives with high magnification cystoscopy*, Photonics Day, EPFL, November 2007

3. B. Lovisa, P. Jichlinski, D. Aymon, H. van den Bergh, G. Wagnières, *Development of fluorescence cystoscopy based on hexyl-aminolevulinic acid (h-ALA)*, CHUV Research Day, Cesar Roux Auditorium, 01.02.2007

2. B. Lovisa, P. Jichlinski, D. Aymon, S. Andrejevic-Blant, H. van den Bergh, G. Wagnières, *Développement de la cystoscopie de fluorescence basée sur l'utilisation de l'acide hexyl-aminolévulinique (hALA)*, Rencontre du Club Photonique et Sciences du Vivant de la Société Française d'Optique (SFO), Paris, 30.11.2006

1. B. Lovisa, P. Jichlinski, D. Aymon, S. Andrejevic-Blant, H. van den Bergh, G. Wagnières, *Development of fluorescence cystoscopy based on hexyl-aminolevulinic acid (hALA)*, EPFL Research Day 2006.

Award

Best poster award, Photonics Doctoral School, EPFL Research Day 2006
Prix de l'Association des Anciens du Collège de St-Maurice, 2000